Cellular integration of physical and biochemical damage signals in the generation of tissue-level wound responses

By

Aaron Christopher Stevens

Dissertation

Submitted to the Faculty of the

Graduate School of Vanderbilt University

in partial fulfillment of the requirements

for the degree of

DOCTOR OF PHILOSOPHY

in

Physics

September 30, 2022

Nashville, TN

Approved:

M. Shane Hutson, Ph.D.

Andrea Page-McCaw, Ph.D.

John Wikswo, Ph.D.

Sait Umar, Ph.D.

The reader not familiar with mathematical expressions should not be worried…

An equation is an unambiguous expression of what the hypothesis is.

- Hans Meinhardt

To my incredible wife April, my constant in an ever-changing world

and

To our children: the one we never met, the one we have now, and the one on the way

Acknowledgments

With everyone who has had an impact not only on the work presented here but also on myself, I hesitate to even call this work my own.

I want to thank Shane Hutson for being an incredible mentor. Despite having no clue of the direction I wanted to head in for my graduate studies, I was able to find a home in the Hutson lab because Shane is always able and willing to find a place for someone no matter their background or expertise. Rather than controlling how work gets done, Shane is able to trust his students' abilities to help them grow in the ways they need in order to succeed. I do not think I could have had a better experience working with anyone else.

I want to thank Andrea Page-McCaw along with her entire lab for fostering an inspirational collaboration as well as always showing interest in my own work beyond their own areas of expertise. I especially want to thank Erica Shannon and James O'Connor for allowing me to be a part of their own projects and for their eagerness to collaborate; quantitative modeling and analyses are nothing without the experiments from which they arise, so my work would not exist without them.

I want to thank the other members of my committee, John Wikswo, Bill Holmes, and Sait Umar, for their feedback and support in my work and for teaching all of my favorite classes while at Vanderbilt. I would not have had the tools and knowledge necessary to pull all of this off had it not been for them.

I want to thank those who laid a solid foundation in physics and math early in my career. To my high school physics teachers Ms. Parker and Mr. Heier who sparked my initial interest in physics by making it fun, engaging, and challenging all at the same time. To my Trevecca professors, Fred and Stephanie Cawthorne, Matthew Huddleston, and Sam Stueckle, for not only their in-depth education, but also for showing how to use that education to serve others in the upside-down kingdom of God.

I want to thank past and current members of the Hutson lab, especially Ty McCleery, Alex Auner, Kazi Tasneem, and Nate Hermann, for their willingness to provide feedback to and think critically about my own work even when it wasn't relevant to their own.

I want to thank my parents, my brother Spencer, my sister Anna, my in-laws, and my nieces and nephews for always supporting me and whose unconditional love allows me to pursue my goals without fear of failure.

Finally, I want to thank my wife April, whose strength surpasses my own in all areas. The slow burn of graduate school has not been the easiest, and yet she is still by my side ready to take on life and the new chapters ahead of us. I want to thank my son Camden for being a daily reminder that the best parts of life are intangible.

Table of Contents

List of Tables

List of Figures

List of Abbreviations

"Calcium"   always refers to calcium ions Ca^{2+}

ATP   Adenosine triphosphate
DAG   Diacylglycerol
DAMP   Damage-associated molecular patterns
ER   Endoplasmic reticulum
$G_{\alpha q}$ Subunit of a G-protein that activates PLC
Gbp   Growth-blocking peptide
GCaMP   A genetically encoded calcium indicator
GJ   Gap junction
GPCR   G-protein coupled receptor
Inx   Innexin, the proteins that make up gap junctions in *Drosophila*
IP_3 Inositol 1,4,5-triphosphate
IPR   Inositol triphosphate receptor
Mthl10   Methuselah-like 10
μT   Micro-tear
NCX Na^+ / Ca^{2+} exchanger
PIP_2 Phosphatidylinositol 4,5 bi-phosphate
PLC   Phospholipase C
PMCA   Plasma membrane Ca^{2+} ATPase
SERCA   Sarcoplasmic/endoplasmic reticulum Ca^{2+} ATPase
SOCC   Store operated Ca^{2+} channels
VGCC   Voltage gated Ca^{2+} channels

Chapter 1

Introduction

This work exemplifies mathematical modeling techniques applied to damage signals that arise around laser-induced epithelial wounds in *Drosophila* pupae. Chapter 1 provides an overview of necessary background information for understanding the context of the work presented here. First, a general overview of epithelial wounds followed by a specific look into laser-ablation wounds is provided (Sections 1.1 and 1.2). Second, key concepts of calcium signaling are reviewed (Section 1.3). And third, an overview of the types of mathematical models utilized in this work is provided (Section 1.4).

Chapters 2 - 4 are adaptations from either published work or work that has been submitted for review. Chapter 2 characterizes and quantifies calcium signals around laser-induced epithelial wounds. Chapter 3 identifies the signaling cascade components responsible for a delayed, distal calcium response around laser-induced epithelial wounds. Additionally, a reaction-diffusion model is developed that quantitatively validates the mechanism of the distal calcium response and provides new insights and predictions. Chapter 4 is a culmination of the previous chapters into a tissue-level mathematical model that replicates, explains, and predicts various aspects of calcium signals around laser-induced epithelial wounds.

Finally, Chapter 5 concludes the work presented here and offers promising future research that could arise.

1.1 Epithelial tissues and wounds

Epithelia are one of the basic yet important types of animal tissue. These tissues which form the lining of various organs and internal cavities consist of one to multiple sheets of cells that serve a variety of functions in a variety of contexts. Epithelial tissues regulate antigen exposure and immune health, secrete mucus to prevent exposure to pathogens, and form polarized, enclosed envelopes that serve as barriers to regulate nutrient exchange[1,2]. The barrier function of epithelia also serves as a physical boundary between whatever the epithelium encloses and the external environment[3]. Therefore, epithelial tissues are prone to external threats that disrupt their barrier function.

A threat of particular interest is when cells in an epithelial tissue are either damaged or destroyed following wounding. When an epithelial tissue is wounded, viable cells around the wound must react accordingly to restore the barrier function of the tissue. Cells farther from the wound undergo proliferation in order to replace destroyed cells, whereas cells closer to the wound migrate towards the wound to fill in the empty space[4]. How does a cell near an epithelial wound sense that a wound is present, and how does a cell "know" which wound healing response it needs to undergo in order to heal the wound?

In order to respond to a wound, cells must first detect the wound. Wound detection arises from the conversion of a wound signal into a specific physical or biochemical signal that is then propagated throughout the tissue. At the cellular level, wound detection can be mediated by the presence of DAMPs (Damage Associated Molecular Patterns) leaked from the lysis of damaged cells or by the presence of other

stress signals such as reactive oxygen species, mechanical stress, and calcium signals. At the tissue level, unconstrained epithelial edges and intercompartmental mixing due to loss of barrier function can serve as damage signals as well[5].

The various epithelial damage signals and responses discussed above have more or less importance depending on the type of wound that occurs as well as the type of epithelial tissue that is wounded. Nevertheless, study of one wounding system can still shed light on the wound signaling and wound healing processes of other systems. Here, we investigate laser-induced wounds of pupae and larval wing discs in of *Drosophila melanogaster* in order to probe the integration of physical and chemical damage signals.

1.2 Laser-induced wounding

For the purposes of the research presented here, pulsed laser ablation is any process of tissue incision or removal in which the laser pulse duration is on an order smaller than milliseconds, although many pulsed laser applications use pulses lasting femtoseconds to nanoseconds[6]. Laser ablation has many uses, from clinical applications such as laser surgery for the eyes[7] or skin[8], to research applications such as determining the tension and viscoelastic properties of a tissue[9]. Pulsed laser ablation of a tissue also creates a wound, and therefore, laser ablation can be used to study controlled and reproducible wounding events[10,11].

While the direct effect of pulsed laser ablation is to destroy the tissue within the immediate vicinity of the laser-disrupted region, there is an additional series of wounding events that results in the generation of individual damage signals. In the context of nanosecond ablations, the initiating event for cellular damage within the laser

3

focus radius on the order of microns is laser-induced plasma formation[12]. This plasma destroys macromolecules where it forms, but it also greatly raises the temperature in its vicinity, leading to vaporization of the surrounding cytosol as well as the formation of a cavitation bubble[12,13]. The cavitation bubble, initially consisting of a high-pressure gas, expands to a radius as large as hundreds of microns until the surrounding hydrostatic pressure forces it to collapse. The expansion and collapse of the cavitation bubble, which lasts on the order of microseconds, exerts hydrodynamic shear stresses on the surrounding tissue[12–14]. The peak shear stress decreases monotonically away from the wound center, and thus leads to a variety of cellular damage outcomes[13,14].

Hellman et al. 2008[14] related peak shear stresses to zones of cellular damage that vary with distance from the wound center, starting with cell lysis closest to the wound with the largest peak shear stresses, followed by necrosis, permeabilization due to plasma membrane damage, and then cell viability farthest from the wound experiencing the lowest peak shear stress. The spatial extent of these zones of cellular damage varied depending on the laser pulse energy and duration; however, further work by Compton et al. 2013[12] showed that the time integral of the shear stress at a given distance from the wound determines cellular outcome independent of the laser pulse parameters (more details on this method of analysis and its application to data presented in this work is presented in Appendix A). More recent work by O'Connor et al. 2021[11] has illuminated even more zones of damage within the zones of Hellman et al. 2013[12], including chromatin disruption and nuclear membrane damage. Ultimately, the effects of a pulsed-laser ablation wound extend far beyond the region of the laser-focus and cause a wide variety of cellular responses.

4

The cellular responses of particular interest for this work are plasma membrane permeabilization and cell lysis/necrosis. Plasma membrane permeabilization exposes otherwise viable cells to the extracellular environment practically immediately. This extracellular and intracellular mixing creates chemical imbalances that lead to cell death if not healed[15]. While smaller tears (≤ 0.2 μm in diameter) in the plasma membrane can heal on their own simply because closure is energetically favorable, larger holes require active changes in plasma membrane tension, cytoskeletal restructuring, and resealing from liposomes in order to be healed[16,17]. On the other hand, cell lysis and necrosis results in gradual release of DAMPs into the extracellular space. DAMPs can activate a variety of signaling cascades and initiate inflammation through the recruitment of immune cells[18].

While cell permeabilization and cell lysis initiate various cellular responses in the context of wounding, the signals they produce serve other purposes outside of wound signaling and wound healing[5]. Cells and tissues must be able to integrate various physical and chemical signals arising from a wound in such a way that identifies the combinations of signals as a wound rather than something else. How is this possible? One possible mechanism is through calcium, a ubiquitous second messenger that is known to integrate a wide variety of cellular signaling events.

1.3 Calcium as a signal integrator

Prolonged exposure to high calcium concentrations is toxic to cells and leads to cell death; therefore, calcium is highly regulated within cells with resting cytosolic calcium concentrations typically residing at ~0.1 μM. Calcium homeostasis is

maintained through a variety of pumps that move calcium against concentration gradients into either internal stores or the extracellular space. While organelles like the mitochondria or the Golgi apparatus have been shown to sequester and interact with calcium, the primary internal calcium store is the endoplasmic reticulum (ER). The ER, which contains calcium concentrations of ~100 µM, is filled by the high-affinity, low-capacity sarcoplasmic/endoplasmic reticulum calcium ATPases (SERCA pumps). Similarly, calcium is moved from the cytosol to the extra cellular space, which contains calcium concentrations of ~1000 µM, primarily by pumps similar to the SERCA pumps called plasma membrane calcium ATPases (PMCA pumps)[19].

The tight regulation of cytosolic calcium allows it to be an ideal second messenger. The conceptual framework of calcium signaling follows what is called a "bow-tie" motif in which many inputs fan into a specialized processing system (the "knot") which then regulates many possible outputs[20]. Therefore, a complete understanding of calcium signaling within any given system involves answering three questions: 1) what causes calcium signals, 2) how is information encoded in a calcium signal, and 3) how is a calcium signal decoded into downstream cellular behaviors. While the first of these three questions has primary importance in the work presented here, all three will be covered briefly below.

1.3.1 Initiation of a calcium signal

While cells expend energy to maintain cytosolic calcium concentrations, there are also various channels that utilize the calcium concentration gradient to momentarily yet quickly increase cytosolic calcium to initiate a calcium signaling event. On the ER,

calcium release is through the IP$_3$ receptors (IPRs), which are channels activated by the molecule IP$_3$ — a signaling molecule produced upon activation of a G-protein cascade by an extracellular agonist — as well as both activated and inhibited by calcium itself (IPRs are covered in more detail in Section 1.4.2.3). On the plasma membrane, a wide variety of channels allow for calcium entry from the extracellular space into the cytosol. Store operated calcium channels (SOCCs) open in a response to a calcium-depleted ER, receptor operated channels (ROCCs) open in response to agonist stimulation, and voltage gated calcium channels (VGCCs) open in response to cell depolarization; in contrast to previously mentioned pumps and channels, these three plasma membrane channels represent entire families of channels rather than a unique, single type of channel[19]. Calcium can also enter cells from other adjacent cells whose cytosols are in contact due to gap junction connections[21]. A variety of other pumps and channels on other internal stores and on the plasma membrane interact with calcium that are beyond the scope of this work.

The interplay between calcium pumps and calcium channels is what drives calcium signaling events. Cytosolic calcium is maintained at low concentrations due to calcium pumps, yet any number of signaling events can activate one or multiple calcium channel types, causing a brief calcium spike before calcium pumps bring the cytosol back to its resting state. Due to the spatial localization of calcium pumps and channels, as well as the large quantities of calcium buffers present in the cytosol that calcium readily binds to, many of these calcium signaling events occur in smaller regions of the cytosol; however, these local signals can build up to create global calcium signals that propagate across cells and even across entire tissues in what are called calcium waves.

Additionally, certain calcium channels, such as the IPRs or VGCCs, undergo cycles of activation and inhibition within a calcium signaling event. This leads to cytosolic calcium oscillations as these channels open and close while calcium pumps serve as a "force" back to equilibrium[21–23].

1.3.2 Information encoding and decoding in calcium signaling

The spatial and temporal regulation of cytosolic calcium allow it to be a dynamic and complex signal that can encode more information than a static signal. For nonexcitable cells, where calcium oscillations are primarily initiated by agonist stimulation, there are two main types of calcium oscillations: baseline spikes and sinusoidal oscillations. Baseline spikes are quick increases in cytosolic calcium concentration above a baseline concentration that is close to resting levels and that persists for a relatively long time between spikes, whereas sinusoidal oscillations look more like sine waves superimposed onto a calcium concentration that is higher than resting levels[24]. Similar to radio signals, information can be encoded by these signals in either their amplitude or frequency. For baseline spikes, agonist concentration determines the oscillation frequency without altering the amplitude, whereas for sinusoidal spikes the agonist concentration determines the average calcium concentration without altering the oscillation frequency[24,25].

Just as there are many possible input signals that can initiate a calcium signaling event, calcium signaling also regulates many possible output cellular behaviors. Indeed, calcium has been described as a "life and death" signal, regulating processes from fertilization and development, to cell migration and proliferation, to programmed cell

death[25]. Calcium signals are detected by various proteins that contain calcium-binding domains wherein the proteins' structure and function change upon calcium binding. These activated proteins can then in turn activate a variety kinases, phosphatases, and transcription factors which serve to initiate various cellular outcomes[20]. For example, upon calcium binding the protein calmodulin regulates the enzyme calmodulin-dependent protein kinase II (CaMK II) which can "count" calcium transients and is activated to varying degrees depending on the calcium oscillation frequency[25,26]. CaMK II then phosphorylates transcription factors that control cell differentiation and cell division[20,25,27].

1.3.3 Calcium signaling in the context of wound healing

Calcium has been shown to regulate many processes required for wound healing, and knockdown of calcium signals around wounds can cause abnormal healing[10,28]. Calcium has been shown to initiate inflammatory responses[29], regulate cell migration and proliferation[30,31], and initiate restructuring of the cytoskeleton[32]. Calcium signals also act in parallel with other wound-induced pathways such as the immune response[28].

For the work presented here, we will primarily be focused on the initiation and dynamics of calcium signaling events around epithelial wounds rather than the information encoded in such signals or the downstream effects they induce. This work looks at two main mechanisms that initiate calcium signals around epithelial wounds. First, direct damage to the plasma membrane causes contact between the cytosol and the extracellular space, allowing high levels of calcium to rush into cells[17]. Second,

damage signals released from the extracellular space stimulate G-protein cascades, eventually leading to the production of the molecule IP$_3$ which releases calcium from the ER into the cytosol[5].

These two calcium signaling mechanisms are separate wound responses (as one arises from a physical perturbation, and the other from a chemical signal), yet cells around epithelial wounds can experience both at the same time and are all equipped with the same machinery to interact with these signals regardless of the level of damage they undergo. While experimental work can tease apart the essential cellular components that respond to the mechanisms that produce calcium signals around epithelial wounds, mathematical modeling done in parallel is required in order to understand the complex spatiotemporal aspects of calcium signaling and how they arise from experimentally identified cellular components. The work presented here utilizes mathematical models of chemical reactions, diffusion, and intercellular calcium dynamics in order to replicate, explain, and predict the properties of damage signals arising from epithelial wounds.

1.4 Overview of relevant mathematical modeling concepts

The mathematical modeling presented here falls into two main categories: 1) reaction and diffusion models, and 2) calcium signaling models. Chapter 2 utilizes a simple diffusion model of calcium movement through plasma membrane damage, Chapter 3 utilizes a reaction-diffusion model of damage signals around epithelial wounds, and Chapter 4 uses the previously mentioned reaction-diffusion model as an

input into a tissue-wide calcium signaling model. A general overview of these categories of models is provided below.

1.4.1 Reaction and diffusion models

Systems which involve the diffusion of various molecular species that can also interact with each other to form composite species that may or may not also diffuse can be mathematically represented by a class of models called reaction-diffusion models. The general form of a reaction diffusion model is given by

$$\frac{\partial \boldsymbol{u}}{\partial t} = \boldsymbol{D}\nabla^2\boldsymbol{u} + \boldsymbol{R}(\boldsymbol{u}) \tag{1-1}$$

where $\boldsymbol{u} = \boldsymbol{u}(\boldsymbol{x},t)$ is a vector consisting of each species concentration over space $\boldsymbol{x}$ and time t, $\boldsymbol{D}$ is a diagonal matrix of diffusion constants, and $\boldsymbol{R}(\boldsymbol{u})$ contains any terms involving the reactions between species as well as sources or sinks for each species.

1.4.1.1 Quasi-steady state reduction of a reaction-diffusion model

While reaction-diffusion models exhibit a wide range of phenomena from spiral waves to self-organizing patterns[33], it is sufficient for the work presented here to cover the case of one diffusible species a that undergoes a reversible reaction with a non-diffusible species b to form a non-diffusible compound b_a. Then the set of reaction-diffusion equations from Eq. (1-1) then becomes

$$\frac{\partial a}{\partial t} = D\nabla^2 a + S + k_- b_a - k_+ ab \tag{1-2}$$

$$\frac{\partial b}{\partial t} = k_- b_a - k_+ ab \tag{1-3}$$

$$\frac{\partial b_a}{\partial t} = k_+ ab - k_- b_a \tag{1-4}$$

where k_+ and k_- are forward are reverse reaction rates respectively, and S is additional source or sink terms for a that can depend on various factors outside of the scope of the reaction-diffusion model itself. If a constant total amount of species b is defined as $b_T = b + b_a$, and if the reaction is assumed to be fast such that Eqs. (1-3) and (1-4) are each at equilibrium ($ab = Kb_a$ with $K = k_-/k_+$), b_a can be determined as a function of a

$$b_a = \frac{b_T \cdot a}{a + K} \tag{1-5}$$

From here, a differential equation for a can be determined that only involves "slow" dynamics by adding together Eqs. (1-2) and (1-4)

$$\frac{\partial}{\partial t}(a + b_a) = D\nabla^2 a + S \tag{1-6}$$

and then replacing b_a with Eq. (1-5) and solving for $\partial a/\partial t$

$$\frac{\partial a}{\partial t} = \left(1 + \frac{b_T \cdot K}{(a + K)^2}\right)^{-1} \cdot (D\nabla^2 a + S) \tag{1-7}$$

Therefore, by assuming a quasi-steady state reaction, we end up with a system where the remaining "slow" dynamics are altered by an effective term $\beta(a) = \left(1 + \frac{b_T \cdot K}{(a+K)^2}\right)^{-1}$. While quasi-steady state reduction can cause unintended side effects in certain models, such as the destruction of oscillations arising from Hopf bifurcations of "fast" variables[34], such a process is a necessary simplification when the dynamics of specific reactions are unknown for the system in question. The reaction-diffusion modeling of Chapter 3

utilizes derivations similar to the one above, just with a larger number of species and reactions between them, and calcium buffering present in the model of Chapter 4 assumes no diffusion so that $D = 0$ for all species present.

1.4.1.2 Diffusion from a constant point source

In the case where a single species is present, we move from a reaction-diffusion model to the diffusion equation with a source term

$$\frac{\partial u}{\partial t} = D\nabla^2 u + S \tag{1-8}$$

The Green's function for this system, which is the solution for an instantaneous point source at time $t = 0$ and location $x = x'$, is given by

$$G(r, r', t) = \left(\frac{1}{4\pi Dt}\right)^{3/2} \cdot \exp\left(-\frac{|r - r'|^2}{4Dt}\right) \tag{1-9}$$

and can be used to determine the general solution for u under a general source S as

$$u(r, t) = \int_{\substack{all \\ space}} \int_0^t G(r, r', t - \tau) \cdot S(r', \tau) \, d\tau \, dr' \tag{1-10}$$

Note that the above solution assumes an initial concentration of 0 everywhere, $u(r, 0) = 0$, and that the concentration goes to 0 at infinity, $\lim_{|r| \to \infty} u(r, t) = 0$

In Chapter 2, the diffusion of calcium from the extracellular space into the cytosol around laser-induced epithelial wounds is analyzed using the diffusion model of Eq. (1-8) assuming a constant point source at position r_0. In this case the source S is given by

$$S(\boldsymbol{r}, t) = S_0 \cdot \delta(\boldsymbol{r} - \boldsymbol{r}_0) \tag{1-11}$$

where S_0 is a constant source magnitude and δ is the Dirac-delta function. Eq. (1-10) with the source from Eq. (1-11) gives the concentration of calcium c in terms of an integral over time

$$\begin{aligned}
c(\boldsymbol{r}, t) &= \int_{\substack{\text{all} \\ \text{space}}} \int_0^t G(\boldsymbol{r}, \boldsymbol{r}', t - \tau) \cdot S_0 \cdot \delta(\boldsymbol{r}' - \boldsymbol{r}_0) \, d\tau \, d\boldsymbol{r}' \\
&= S_0 \cdot \int_0^t \left(\frac{1}{4\pi D(t - \tau)} \right)^{3/2} \cdot \exp\left(-\frac{r^2}{4D(t - \tau)} \right) d\tau
\end{aligned} \tag{1-12}$$

where $r = |\boldsymbol{r} - \boldsymbol{r}_0|^2$. The variable substitution $v = r^2 / 4D(t - \tau)$ puts this integral into the form of the incomplete Gamma function:

$$c(\boldsymbol{r}, t) = \frac{S_0}{4\pi^{3/2} D r} \int_{r^2/4Dt}^{\infty} v^{\frac{1}{2}-1} \cdot e^{-v} \, dv = \Gamma\left(\frac{1}{2}, \frac{r^2}{4Dt} \right) \tag{1-13}$$

1.4.2 Calcium signaling models

Calcium signaling regulates a wide variety of processes across a wide variety of systems and spatiotemporal scales, and as such a wide variety of calcium signaling models exist throughout the literature as well[35,36]. Nevertheless, calcium signaling models can fall into four major types, categorized by either deterministic or stochastic models as well as spatially homogeneous or spatially distributed models. While the latter of each type better-captures the physical reality of calcium signaling, as cells are spatially distributed and are driven by stochastic events, models that are deterministic and spatially homogeneous are still widely and successfully utilized[37–39]. Such models are described by systems of ordinary differential equations where calcium and other

14

relevant molecules move between compartments — typically the cytosol, internal stores, and neighboring cells — with uniform concentrations in each compartment at all times. A deterministic, spatially homogeneous model is what is utilized in the work presented here.

1.4.2.1 General framework of a compartmental model

The general form of such calcium signaling models determines the time derivative of the cytosolic calcium concentration for a single cell

$$\frac{\mathrm{d}c}{\mathrm{d}t} = \sum_i J_i - \sum_m \frac{\mathrm{d}B_m}{\mathrm{d}t} \tag{1-14}$$

where each J_i represents a calcium flux, either between internal stores, adjacent cells, or the extracellular space, and each B_m is the concentration of buffer m bound to calcium. The time derivative of the bound buffer concentrations accounts for calcium binding and unbinding events. If the calcium-buffer reactions are the same as those in Eqs. (1-2) - (1-4) and are assumed to be fast such that an expression similar to Eq. (1-5) can be obtained for each buffer, then effective fluxes are obtained similar to Eq. (1-7)

$$\frac{\mathrm{d}c}{\mathrm{d}t} = \left(1 + \sum_m \frac{B_{\mathrm{T},m} \cdot K_m}{(c + K_m)^2}\right)^{-1} \cdot \sum_i J_i \tag{1-15}$$

where $B_{\mathrm{T},m}$ is the concentration of total buffer m, and $K_m = k_{-,m}/k_{+,m}$ is the dissociation constant for buffer m.

With the rapid-buffer assumption, the main features of the model are therefore found in the choice of calcium fluxes to be included. This modular design allows calcium

15

signaling model development to be very flexible, as one can pick and choose the various sub-models to be used for each flux, and one sub-model can be switched out for another relatively easily. Many calcium flux sub-models can be found across the calcium signaling model literature, and choosing to include some fluxes over others comes down to many factors such as the questions being asked of the model, the system being modeled, experimental evidence, and hypothesized mechanisms required to produce desired calcium signaling dynamics. A brief overview of the sub-models used in this work is given below.

1.4.2.2 Calcium fluxes through pumps and channels

As covered in Section 1.3, Calcium pumps use energy to move calcium up its concentration gradient from the cytosol to either intracellular stores or the extracellular space, whereas calcium channels simply open to allow calcium to flow down its concentration gradient. While mathematical models of various calcium pumps and channels can be as complicated as multi-state, stochastic Markov models[36], simpler models based on reaction kinetics and simple diffusion are often sufficient for many purposes. Simple models of calcium pumps involve mathematical expressions for reactions similar to those in Eqs. (1-2) - (1-4), and thus take the form of Hill functions similar to that of Eq. (1-5):

$$J_{\text{pump}} = J_{\text{max}} \cdot \frac{c^n}{c^n + K^n} \tag{1-16}$$

where c is the cytosolic calcium concentration, J_{max} is the maximum capacity of the pump, n is the Hill coefficient that determines positive ($n > 1$) or negative ($n < 1$) cooperative binding between calcium and the pump, and K is the dissociation constant

16

of the calcium-pump reaction. Simple models of calcium channels assume that the

calcium flux is proportional to the concentration difference between the compartments

$$J_{\text{channel}} = \eta \cdot (c_{\text{ext}} - c) \qquad \textbf{(1-17)}$$

where η is the channel permeability, c_{ext} is the calcium concentration of the non-

cytosolic compartment, and c is the cytosolic calcium concentration.

1.4.2.3 The Li-Rinzel IPR model

The IPR channel on the ER is a primary driver of calcium waves and oscillations

in nonexcitable tissues. The IPR channels are activated by the signaling molecule IP_3

that is produced upon agonist stimulation; however, the IPRs are also both activated

and inhibited at low and high calcium concentrations respectively. Therefore, for a

constant IP_3 concentration, the open probability of the IPRs is a bell-shaped function of

calcium concentration[40]. The activation of the IPRs by calcium induces a process called

calcium-induced calcium release, which is a key mechanism in calcium wave

propagation[21]. The additional inhibition of the IPRs by calcium allows for calcium

oscillations at sufficiently high IP_3 concentrations: first, cytosolic calcium increases as

the IPRs open, which induces more calcium release; second, at sufficiently high calcium

concentrations the IPRs close, thus producing a net decrease in cytosolic calcium

concentration as calcium pumps work to remove calcium from the cytosol; and third, the

decrease in cytosolic calcium brings the calcium back to levels that activate the IPRs,

thus completing the cycle.

There is an extensive number of IPR models present in the literature ranging from simple, deterministic models to hierarchical and stochastic models[22,23,35–38,41]. However, Cao et al. 2014[38] showed that deterministic versions of stochastic IPR models can still make valid predictions. In the work presented here, we utilize the relatively simple yet effective IPR model of Li and Rinzel[42].

The Li-Rinzel model is a simplification of the model by DeYoung and Keizer 1994[43] in which each IPR consists of three independent subunits, and each subunit has three binding sites: a site for IP3, an activating calcium binding site, and an inactivating calcium binding site. Thus, in the DeYoung-Keizer model each IPR subunit can be in one of 8 possible states at a given time. Due to experimental evidence of IPR activation being much faster than IPR inactivation, Li and Rinzel simplified this model by assuming IP3 binding and calcium activation to be in a quasi-steady state (see Section 1.4.1.1), thus reducing the model to a two-state system of either active or inactive. The "fast" activation dynamics take the form of a product of Hill functions of IP3 (p) and calcium (c)

$$m_\infty = \left(\frac{p}{d_1 + p}\right)\left(\frac{c}{d_5 + c}\right) \tag{1-18}$$

whereas the "slow" inactivation dynamics are described by a differential equation for h, the fraction of receptors that are not inactivated, with a time constant τ_h

$$\frac{\mathrm{d}h}{\mathrm{d}t} = \frac{h_\infty - h}{\tau_h} \tag{1-19}$$

The open probability for a single subunit is then given by $m_\infty h$, and thus the expression for the entire calcium flux is given by

$$J_{\mathrm{IPR}} = \eta_{\mathrm{IPR}} m_\infty^3 h^3 (c_{\mathrm{ER}} - c) \tag{1-20}$$

Both h_∞ and τ_h are functions of calcium and IP$_3$ which are stated and utilized in

Chapter 4 (Eqs. (4-18) - (4-23)).

Chapter 2

Multiple mechanisms drive calcium signal dynamics around laser induced epithelial wounds

This chapter has been adapted from Shannon, E., Stevens, A., Edrington, W., Yunhua, Z., Jayashinghe, A. K., Page-McCaw, A., Hutson, M. S. Multiple mechanisms drive calcium signal dynamics around laser-induced epithelial wounds. *Biophysical journal* (in press).

My main contributions to this chapter are the mathematical modeling and fitting shown in Figure 2-6 and described in further detail in the Supplemental Methods (Section 2.7).

2.1 Abstract

Epithelial wound healing is an evolutionarily conserved process that requires coordination across a field of cells. Studies in many organisms have shown that cytosolic calcium levels rise within a field of cells around the wound and spread to neighboring cells, within seconds of wounding. Although calcium is a known potent second messenger and master regulator of wound-healing programs, it is unknown what initiates the rise of cytosolic calcium across the wound field. Here we use laser ablation, a commonly used technique for the precision removal of cells or subcellular components, as a tool to investigate mechanisms of calcium entry upon wounding. Despite its precise ablation capabilities, we find that this technique damages cells outside the primary wound via a laser-induced cavitation bubble, which forms and collapses within microseconds of ablation. This cavitation bubble damages the plasma membranes of cells it contacts, tens of microns away from the wound, allowing direct calcium entry from extracellular fluid into damaged cells. Approximately 45 s after this

20

rapid influx of calcium, we observe a second influx of calcium that spreads to neighboring cells beyond the footprint of cavitation. The occurrence of this second, delayed calcium expansion event is predicted by wound size, indicating that a separate mechanism of calcium entry exists, corresponding to cell loss at the primary wound. Our research demonstrates that the damage profile of laser ablation is more similar to a crush injury than the precision removal of individual cells. The generation of membrane micro-tears upon ablation is consistent with studies in the field of optoporation, which investigate ablation-induced cellular permeability. We conclude that multiple types of damage, including micro-tears and cell loss, result in multiple mechanisms of calcium influx around epithelial wounds.

2.2 Introduction

Epithelial wound healing is a multi-stage process. Cells must detect the presence of a wound, migrate and proliferate in a coordinated fashion to close the defect, and then successfully re-establish tissue-wide epithelial architecture.[5,44–47] An important early feature of the wound response is a rapid rise in cytosolic calcium. This rise initially occurs in cells near the wound margin and then spreads to more distant cells[10,28–30,48,49] to act as a potent signal that regulates several cellular responses around wounds: JNK signaling[50]; Rho GTPase activity[51]; and remodeling of the actin cytoskeleton[10,28,32,51]. Nonetheless, it is not yet clear how wound-induced calcium signals are initiated *in vivo*. In cell-culture wounding models, calcium signals are generated downstream of a diffusible ligand released by damaged cells into the extracellular space[52–54]. *In vivo* studies suggest another model, in which wound-induced changes in tissue tension open

stretch-activated calcium channels or activate other mechanosensitive proteins.[55] In support of this hypothesis, calcium waves can be generated in *Drosophila* wing discs by applying mechanical pressure[56] and are perturbed in both *C. elegans* and *Drosophila* wounding models after knocking out the putative stretch-activated calcium channel TRPM[10,28,29]. Importantly, the diffusible-ligand and altered-mechanics hypotheses are not mutually exclusive: both could be upstream initiators of wound-induced calcium signals *in vivo*, each acting through specific regulated receptors or channels.

Here, we use pulsed laser ablation to create repeatable and controllable wounds in epithelial tissues in *Drosophila* larvae and pupae, and carefully measure the dynamics of the induced calcium response in surrounding cells over time scales from milliseconds to hundreds of seconds. We observe a complex spatiotemporal response with multiple phases: initial calcium influx beginning within milliseconds at discrete loci as far as 70 µm from the wound site; a rapid, intercellular expansion of calcium away from these loci; and a second, slower expansion of high cytosolic calcium to additional cells as far as 150 µm from the wound. We show that the initial influx and subsequent expansion phases can be described by different diffusive processes – suggesting different expansion mechanisms – and can be linked to different aspects of cellular damage around laser-induced wounds.

Although laser energy can be precisely focused to remove single cells or even sub-cellular elements[57,58], additional cells near and far from the primary wound are affected through several mechanisms. The lasers typically used to investigate the mechanics of morphogenesis and wound healing *in vivo* are pulsed[9,59–61], with femtosecond to nanosecond pulse widths, and ablate tissue via plasma formation[62–64].

The plasma directly destroys macromolecules within the laser focus (radius < 1 μm), but recombination of the plasma leaves the targeted location extremely hot, leading to the vaporization of water and expansion of a cavitation bubble[62]. The bubbles associated with laser ablation vary with pulsewidth and fluence[62–64]; those measured for near-threshold *in vivo* ablation using ns-pulse lasers have lifetimes on the order of microseconds and inferred maximum radii of 10 to 100 μm.[64,65] In cell-culture studies, the rapid expansion and collapse of cavitation bubbles generates shear stresses that can lyse cells close to the ablation site, creating a primary wound, and can transiently permeabilize cells farther away[12–14] – a process known as optoporation.

Here, we show that two mechanisms of laser-induced damage, a tissue-level primary wound and cellular micro-tears, each drive distinct calcium signaling dynamics. By imaging wound-induced calcium dynamics with unprecedented time resolution, we show that calcium directly enters permeabilized cells 20-100 μm from the ablation site within milliseconds. This influx initiates a first calcium wave. In some cases, a second wave further expands the region of high cytosolic calcium, but the second wave is delayed by 30-60 s and its occurrence depends on the size of the primary wound. Through kinematic modeling of the calcium influx and expansion waves, we have identified parameters of the wave spread that narrow and inform the search for upstream mechanisms. Our findings have implications both specific to laser ablation and applicable to more general types of wounding. First, the precision lysis of laser ablation may be accompanied by cavitation bubble effects akin to a wider crush injury. Second, our general finding of two-phase initiation of calcium signaling is likely to be important for tissues sensing a wide range of traumatic damage.

2.3 Materials and Methods

Additional methods including fly genotypes, image processing, and computational analysis can be found in the Supplemental Methods (Section 2.7).

2.3.1 Laser Ablation and Live Imaging

White prepupae expressing *pnr-Gal4* and *UAS-GCaMP3, UAS-GCaMP6m* or *UAS-Arclight* were aged for 12-18 h After Puparium Formation (APF). Pupae were mounted with nota facing the coverslip. Wing discs expressing *tubP-Gal4* and *UAS-GCaMP6m* were dissected from 3rd instar larvae and immediately mounted on coverslips for imaging and ablation.

Laser ablation and live imaging were performed using a Zeiss LSM410 raster-scanning inverted confocal microscope with a 40X 1.3 NA oil-immersion objective. Laser wounding used single pulses of the 3rd harmonic (355 nm) from a Q-switched Nd:YAG laser (5 ns pulsewidth, Continuum Minilite II, Santa Clara, CA) at pulse energies ranging from 0.5 to 10 µJ. Kymographs were assembled and basic image measurements were taken in ImageJ (NIH, Bethesda, MD).

2.3.2 *Cavitation Experiments*

Pupae were mounted on coverslips in distilled water, and wing discs were mounted in calcium-free PBS. A small hydrophone (Onda, 0.5 mm aperture, <20 ns rise time, 2.24 V/MPa sensitivity) was mounted to the confocal stage and lowered into the aqueous medium approximately 1 mm from the focus of the laser. Bubble lifetime

measurements were taken from hydrophone pressure traces displayed on an oscilloscope.

2.3.3 FM 1-43 and Propidium Iodide analysis in wing discs

Wing discs were mounted on a coverslip 20 min prior to imaging. FM 1-43 (ThermoFisher #T35356) was diluted in PBS to 5 µg/ml and propidium iodide (PI, ThermoFisher #P3566) was diluted in PBS to 20 µg/ml. Each were added to wing discs immediately prior to imaging, and experiments were completed within 10 minutes of adding dye.

2.4 Results

2.4.1 Fast Ca^{2+} signal dynamics from 2 ms to 2 s.

To investigate wound-induced mechanisms of calcium release, we analyzed calcium dynamics in the *Drosophila* pupal notum (following procedures in Antunes et al. 2013[10]). At 12-18 h APF, the notum is a continuous epithelial monolayer of diploid cuboidal cells which exhibit apicobasal polarity and sit atop a basement membrane[66]. Pupae were wounded via laser ablation while imaged live simultaneously. Half of wounded pupae survive laser ablation and later eclose (data not shown and Antunes et. al.(Antunes et al., 2013)). Wound-induced calcium waves were visualized with a genetically encoded, intracellular GCaMP3 reporter[67].

Prior to ablation, cytosolic calcium remained at low basal levels (Figure 2-1A, $t = -2$ s), with single cells occasionally exhibiting transient calcium increases. In the first

frame (< 2 s) after ablation, a dramatic increase in cytosolic calcium was observed as bright GCaMP fluorescence both in cells along the wound margin and in surrounding cells up to seven cell diameters away (~ 50 μm) (Figure 2-1A). To analyze this initial response with improved temporal resolution, we performed line scans passing through the wound to increase our sampling rate to 2.1 ms/scan. For these experiments, we also employed a GCaMP6m calcium indicator since it has faster kinetics with an increased signal-to-noise ratio. These line scans were assembled into kymographs, an example of which is shown in Figure 2-1B (additional examples shown in Figure 2-2). Within milliseconds after ablation, calcium entered the cytoplasm and increased GCaMP6m fluorescence in multiple cells up to ~50 μm away from the ablated region. We call this rapid increase of intracellular calcium the "initial response".
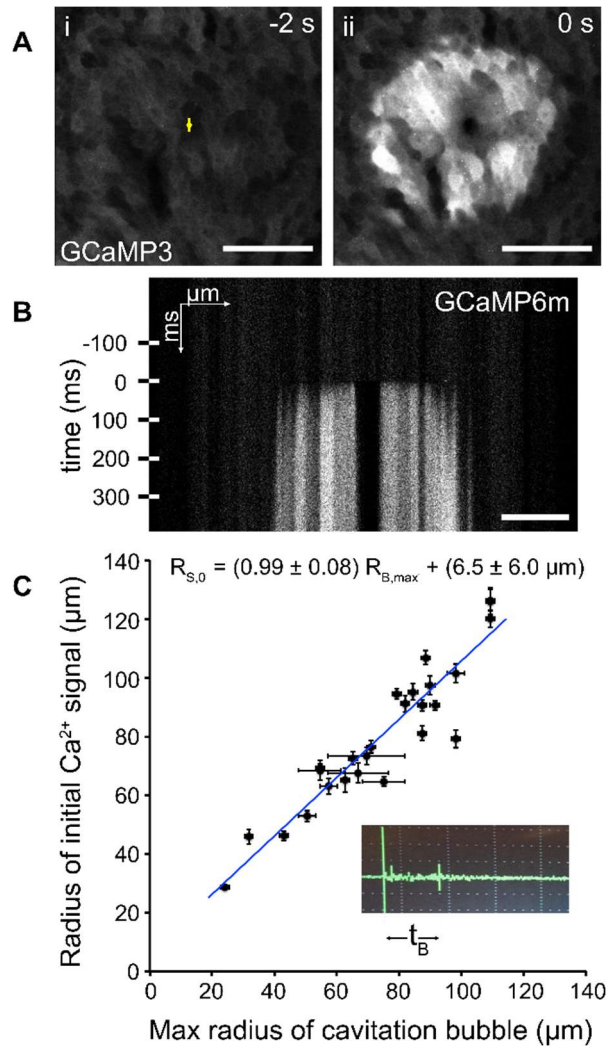
Figure 2-1: The initial response to wounding matches the radius of the cavitation bubble.

(A) Confocal images of the calcium reporter GCaMP3 in the pupal notum. Basal levels of cytosolic calcium are low before wounding (i), but rise rapidly after laser-ablation (ii). The rapid rise occurs in cells within 5-7 rows from the ablation site (crosshairs in i, central dark area in ii). Scale bar is 50 µm. **(B)** Confocal kymograph of GCaMP6m. Fluorescence is low before wounding (kymograph lines above t = 0 ms), but rises within milliseconds of laser ablation in cells distant from the wound site (central dark area for *t* > 0 ms). Scale bar is 50 µm. **(C)** The radius of the primary wound-induced Ca^{2+} signal ($R_{S,0}$) corresponds to the maximum radius of the laser-induced cavitation bubble ($R_{B,max}$). Linear regression yields a best fit with a slope of 0.99 (solid line; equation; R^2 = 0.87). Each data point corresponds to a single wound with initial Ca^{2+} signal radii measured from full frame confocal images (< 3 s after ablation) and bubble radii calculated from bubble lifetimes (t_B) measured via hydrophone (inset). Horizontal error bars represent estimated uncertainty in identifying the bubble collapse peak; vertical error bars are standard deviations of four radius measurements.
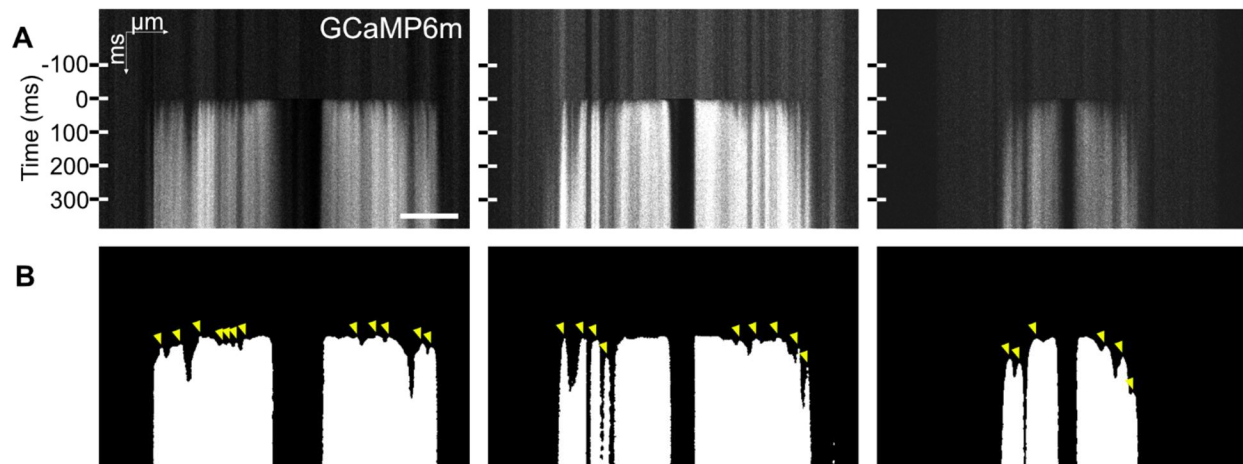
Figure 2-2: Kymographs show that increases in cytosolic calcium begin milliseconds after ablation, even tens of microns from the wound site.

GCaMP6m was expressed in the *pnr* domain using the Gal4-UAS system. Three separate samples are shown. Line scans were taken over the point of ablation and assembled into kymographs using ImageJ. **(A)** Kymographs show that intracellular calcium levels rise within a few ms at distances at least 50 microns away from the wound. **(B)** Identification of the initiation of calcium fluorescence in each pixel column (see Methods). Yellow arrowheads indicate calcium influx loci, or peaks. Scale bar is 50 μm.

Few biological signals could propagate away from the wound site quickly enough to drive this spatially-distributed initial Ca^{2+} response. For example, the kymograph in Figure 2-1B shows rises in intracellular Ca^{2+} that begin within 5 ms for cells up to 50 μm from the wound. To reach this far this fast, any ablation-induced diffusible signal would need a diffusion constant α ~1.3 x 10^5 μm^2/s, estimated from $(\Delta x)^2/4\Delta t$. This estimated diffusion constant is 2-3 orders of magnitude faster than that of a small molecule like ATP (adenosine triphosphate) (3.5 x 10^2 μm^2/s), or of small ions (0.8 to 2.0 x 10^3 μm^2/s), or of even the self-diffusion of water (2.3 x 10^3 μm^2/s). Thus, a diffusible signal cannot trigger the initial rapid response.

2.4.2 The initial Ca^{2+} response is driven by cavitation.

Pulsed laser ablation generates a plasma that completely destroys macromolecules in a nearly diffraction limited region (< 1 µm diameter) and generates a rapidly expanding cavitation bubble with high shear stresses that lyse cells in a variably broader region. Importantly, the region of macromolecular destruction and region of lysis are both much smaller than the initial GCaMP response region we observe. The cavitation bubble is short-lived but it can expand hundreds of microns beyond the region of lysed cells[12,14,65]. To investigate whether the initial Ca^{2+} response could be driven by cavitation, we simultaneously measured initial Ca^{2+} response radii and cavitation bubble radii.

We estimated cavitation bubble radii using a hydrophone to detect the acoustic transients associated with bubble expansion and collapse. For water at standard temperature and pressure, maximum bubble radii ($R_{B,max}$) are theoretically related to cavitation bubble lifetimes (t_B) according to $R_{B,max} \approx$ (5.46 µm/µs) t_B[65]. Validation of hydrophone measurements based on this relationship is provided by direct flash imaging of bubbles in *Drosophila* embryos as shown in Figure 2-3. For each experiment in pupae, we also collected full-frame confocal images of GCaMP6m fluorescence to record the initial Ca^{2+} response radius. With laser pulse energy intentionally varied to create both large and small cavitation bubbles, we found that cavitation radius matched the radius of initial response radius ($R_{S,0}$) with a slope very close to one: the best linear fit to the relationship was $R_{S,0}$ = (0.99 ± 0.08)$R_{B,max}$ + (6.5 ± 6.0 µm) (Figure 2-1C). Our initial response measurements are an overestimate as the calcium region can expand by as much as 17.6 ± 7.0 µm (mean radius ± s.d.) between the time of ablation and the

capture of images used to determine the radius of calcium influx (<2 s). Correcting for this overestimate would reveal a trend line that runs very close to the origin. We conclude that the cavitation bubble is tightly linked to the extent of the initial calcium response, and we explore the mechanism below.
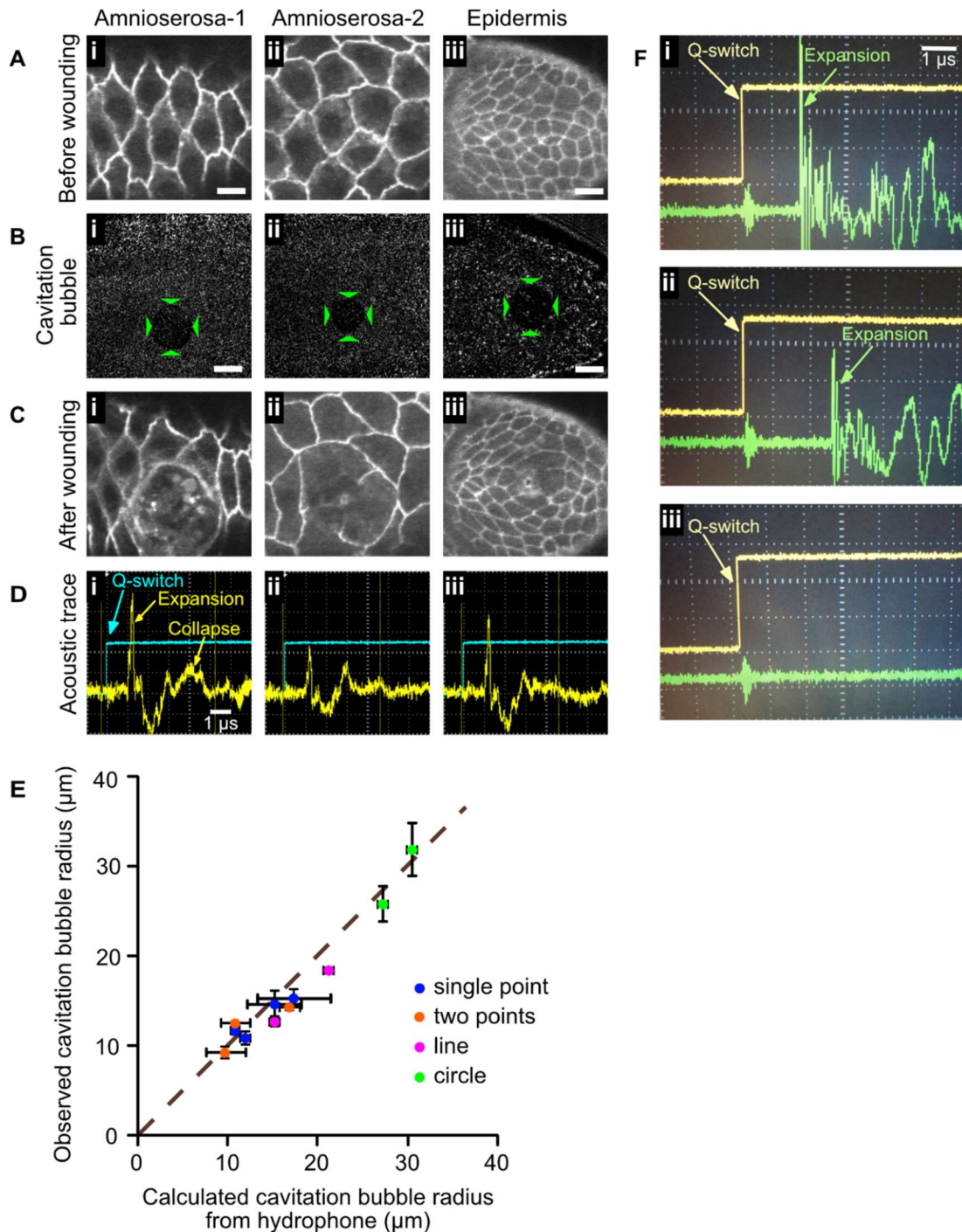
Figure 2-1: Acoustic data from a hydrophone can be used to measure

We validate the use of acoustic hydrophone data to measure laser-induced cavitation bubble radii in *Drosophila* embryos by comparison with direct bubble imaging. Three separate examples (i-iii) are shown in panels A-D: i-ii are from ablation of amnioserosa, a squamous epithelial tissue; iii is from ablation of columnar epithelial cells in the germband. **(A)** Cell borders are visualized before laser wounding via confocal images of embryos expressing *Ubi-p63E-shg.GFP*. **(B)** The cavitation bubble formed upon laser wounding (delineated by green arrowheads) is imaged by high-speed bright-field imaging. **(C)** Recoil of the cells observed in post-ablation confocal images indicates that a wound has been made that is much smaller than the cavitation bubble. **(D)** Acoustic traces from a hydrophone, overlaid with the ablation laser's Q-switch sync signal, show peaks corresponding to the initial rapid expansion and later rapid collapse of the cavitation bubble. The time between these peaks is used to calculate the maximum size of the bubble. All scale bars for A-D are 20 μm. **(E)** Comparison of cavitation bubble radii calculated from hydrophone measurements with those observed by direct imaging. Root-mean-square deviation from an exact match (brown dashed line) is ~12% even when considering multiple laser ablation patterns: single points, two points, lines, or circles. When cavitation bubbles were ellipsoidal, e.g., for two-point and line ablations, the reported radius is the geometric mean of the bubble's semi-major and semi-minor axes. The shape of the bubble did not affect our ability to assess cavitation radius with the hydrophone. Horizontal error bars represent propagation of uncertainty from our determination of bubble collapse times. Vertical error bars are the standard deviation among four radius measurements (for circular bubbles) or propagation of uncertainty in the ellipse parameters used to estimate the equivalent radius (for ellipsoidal bubbles). **(F)** Control experiments for hydrophone measurements: (i) when the hydrophone is located ~2.5 mm from the point of ablation, the first acoustic transient associated with bubble expansion is detected ~1.6 μs after the laser pulse, an appropriate time given the speed of sound in water (1,480 m/s); (ii) moving the hydrophone tip to 3.5 mm from the point of ablation appropriately delays the arrival of the first acoustic transient to 2.4 μs after ablation; (iii) allowing the laser to fire, but blocking the light from reaching the sample eliminates the acoustic transients associated with cavitation. In all cases, a small signal is present immediately after the laser fires and is likely attributable to electromagnetic interference from the capacitors that discharge in the ablation laser as its Q-switch is triggered.

2.4.3 The initial response begins at discrete loci.

Within milliseconds of ablation, kymographs of GCaMP6m fluorescence show the contemporaneous appearance of multiple high-Ca^{2+} loci (Figure 2-4A, arrowheads). This pattern cannot be due to Ca^{2+} flow from the wound margin through neighboring cells but instead indicates Ca^{2+} entering the cytosol at multiple distinct locations around

the wound. To quantify the spatial distribution of these Ca^{2+}-influx loci, we first identified

each kymograph's signal front – i.e., the time points when the fluorescence signal in

each kymograph column first exceeded the unwounded background by two standard

deviations (Figure 2-4A, solid white line). Considering this signal front as a function

$t_{front}(x)$, we identified influx loci as its local minima, which appear as peaks because of

the inverted time axis of our kymographs (Figure 2-4A, arrowheads). Although Ca^{2+}-

influx loci far from the wound appear as spatially distinct peaks, those close to the

wound blend together into a wide band of high fluorescence. For this wide band of

unresolved fluorescence near the wound, each pixel was counted as a Ca^{2+}-influx site.
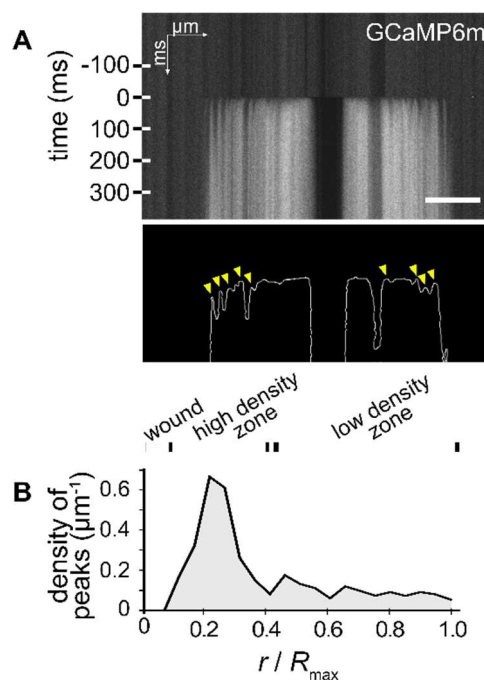
Figure 2-4: Early wound-induced calcium appears at discrete loci.

(**A**) Confocal kymograph of GCaMP6m showing discrete sites of cytosolic calcium entry in cells distant from the wound. These sites are marked by yellow arrowheads and were identified as local maxima along the signal front (outline in lower panel). Scale bar is 50 µm. (**B**) Density of Ca^{2+}-signal initiation sites as a function of relative distance from the wound center. Data were compiled from 25 kymographs with distances normalized to each kymograph's maximum signal radius (R_{max}). Broad regions near the wound with

rapid Ca^{2+} rise, but no discernable peaks, were treated as having one initiation site per kymograph pixel. Brackets above the plot demarcate different zones of initiation site density.

We plotted the radial density of influx sites around primary wounds by compiling

data from 25 kymographs and normalizing peak locations to each kymograph's

maximum signal radius (R_{max}). Figure 2-4B shows the primary wound plus two distinct

zones of Ca^{2+}-influx site density: a high-density zone corresponding to the fast,

unresolved band of high signal (0.1 R_{max} < r < 0.4 R_{max}); and a zone of lower density

corresponding to the region of distinct kymograph peaks (0.4 R_{max} < r < R_{max}). Although

the density in this latter region is ~ 1 site per 10 μm, which is close to one per cell, the

Ca^{2+}-influx sites do not fall in a regular pattern with respect to cell borders (Figure 2-5).
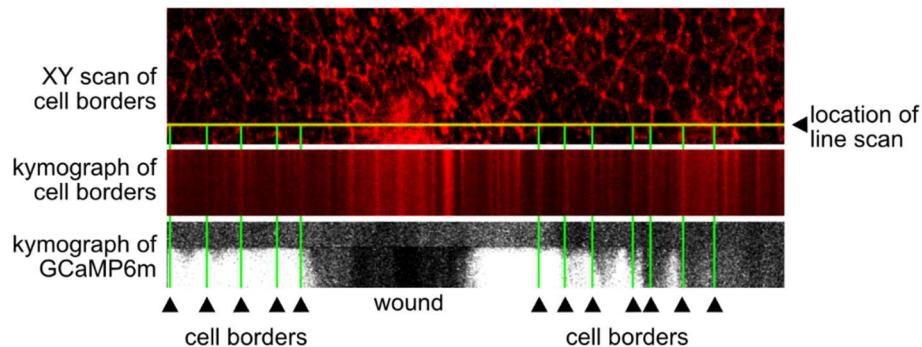
Figure 2-5: Calcium entry points appear randomly spaced with respect to cell borders.

The top panel shows an XY scan of *shg-tdTomato* (E-cadherin) used to label cell borders before ablation. The middle panel shows a kymograph of cell borders scanned along the yellow line before ablation. Because *shg-tdTomato* is present both at cell borders and in intracellular punctae, the determination of true cell borders (marked with green lines) required both the kymograph and the XY scan, registered for alignment. The bottom panel shows a kymograph of GCaMP6m upon wounding, with the cell borders shown as green lines from the top panel. Local maxima in the kymograph correspond to calcium entry points. The calcium entry points do not align with cell borders in any regular pattern.

The spatially distinct kymograph peaks show that Ca^{2+} enters the cytoplasm of cells around the wound at discrete loci and then spreads rapidly (Figure 2-6A). To quantify this spread, we individually fit 25 peaks to a three-dimensional diffusion model – i.e., the expected time-dependent signal along a sampled line due to diffusion from a point source of constant Ca^{2+} influx. An example fit for one peak is shown in Figure 2-6B, with selected temporal and spatial slices used to show overlays of the data and fit (Figure 2-6 C and D). The complete set of kymograph peak fits is shown in Figure B-1. From this complete set of fits, the interquartile range of estimated diffusion constants was 76 to 220 $\mu m^2/s$, with a median of 120 $\mu m^2/s$ (Figure 2-6E). This range lies between the diffusion constants of cytosolically buffered Ca^{2+} (13 $\mu m^2/s$) and free Ca^{2+} (220 $\mu m^2/s$)[68]. The breadth of the fitted diffusion-constant distribution can be attributed to a combination of expected random error, systematic errors based on using an infinitesimal point source equation that would slightly overestimate the diffusion constants from finite-sized influx sites, and cell-to-cell variations in the degree to which Ca^{2+}-influx levels saturate cytoplasmic and GCaMP6 buffering capacity.
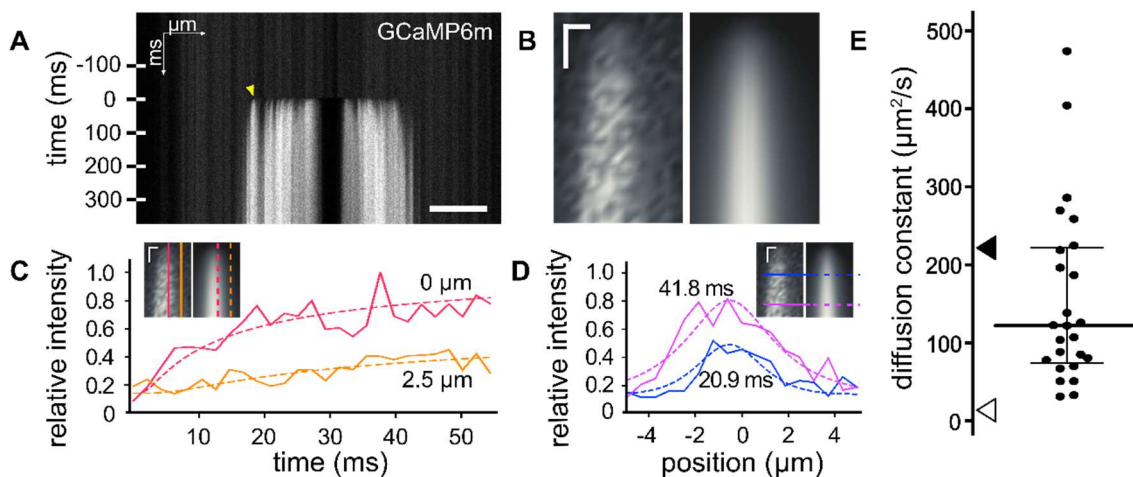
Figure 2-6: Wound-induced intracellular calcium diffuses from discrete loci at rates that appear to overcome cytosolic buffering capacity.

(**A**) Kymograph of GCaMP6m fluorescence upon wounding. A single peak (yellow arrowhead) is examined in more detail in B-D. Scale bar is 50 µm. (**B**) Enlarged view of an isolated kymograph peak (left) and the best fit of that peak to a diffusion model (right; see main text for details). Scale bar is 2 µm horizontal and 10 ms vertical. (**C**) Intensity versus time for two marked columns cutting through the selected kymograph section (at 0 and 2.5 µm from the center of the peak). (**D**) Intensity versus position for two marked rows cutting through the selected kymograph section (at 20.9 and 41.8 ms after laser ablation). (**E**) Box and whiskers plot of the diffusion constants from best fits of 25 isolated peaks. Bars show median and interquartile range. Arrowheads indicate diffusion constants of free calcium (black, 220 µm^2/s) and cytosolically buffered calcium (white, 13 µm^2/s) as measured by Allbritton et al. 1992[68].

2.4.4 The cavitation bubble creates plasma membrane micro-tears.

Our results thus far show that Ca^{2+} enters the cytoplasm from discrete loci spread throughout the maximum extent of the cavitation bubble. Previous reports show that cavitation bubbles induce cellular damage[69,70] and that this cellular damage is associated with rises in intracellular calcium[71–74]. Plasma membrane micro-tears would provide a simple direct mechanism for the inflow of calcium into the cytoplasm from its high concentration in the extracellular space (~10^{-3} M extracellularly vs ~10^{-7} M in cytoplasm). We thus tested for ablation-induced micro-tears in three types of assays described below: depolarization, dye internalization, and altered extracellular calcium.

A

i -3 s
Arclight

ii 60 s

B

$R_{Volt}=(0.96 \pm 0.12)R_{B,max}+ (3.0 \pm 8.2 \ \mu m)$

Depolarization Radius (μm) vs Max radius of cavitation bubble (μm)

C

i -2 s
FM 1-43

ii 60 s

D

$R_{Dye}=(0.93 \pm 0.05)R_{B,max}+ (2.1 \pm 2.7 \ \mu m)$

FM Dye Radius (μm) vs Max radius of cavitation bubble (μm)

E

$R_{Dye}=(0.93 \pm 0.09)R_{B,max}+ (2.1 \pm 4.2 \ \mu m)$

PI Dye Radius (μm) vs Max radius of cavitation bubble (μm)

F

i -3 s
ii 0 s
0 mM Ca^{2+}
GCaMP6m

G

$R_{2 \ mM}=(0.96 \pm 0.11)R_{B,max}+ (1.9 \pm 6.2 \ \mu m)$
$R_{0 \ mM}=(0.25 \pm 0.07)R_{B,max}+ (8.4 \pm 4.1 \ \mu m)$

2 mM Ca^{2+}
0 mM Ca^{2+}

Radius of initial Ca^{2+} (μm) vs Max radius of cavitation bubble (μm)

Figure 2-7: The cavitation bubble creates micro-tears in plasma membrane.

(**A**) Arclight fluorescence in the notum is high before wounding (i) and decreases around the wound afterwards, indicating depolarization (ii). The margin of depolarization is marked by red arrows. (**B**) The radius of wound-induced depolarization (R_{Volt}) corresponds to the maximum radius of the laser-induced cavitation bubble ($R_{B,max}$) with a best fit slope of nearly 1 (solid line; equation; $R^2 = 0.91$). R_{Volt} was measured from confocal images taken on the first frame (< 3 s) after ablation. (**C**) Fluorescent labeling of an *ex vivo* wing disc with FM 1-43 is modest before wounding (i), and increases around the wound afterwards, indicating a region of increased cell permeability and dye influx (ii). The outer margin of dye influx is marked by yellow arrows. Scale bar = 50 μm. (**D**) The radius of dye influx (R_{Dye}) also corresponds to $R_{B,max}$ with a best fit slope of nearly 1 (solid line; equation; $R^2 = 0.98$). The radius of dye influx was measured from confocal images taken 60 seconds after ablation. (**E**) Again, the radius of dye influx (R_{Dye}) corresponds to $R_{B,max}$ with a best fit slope of nearly 1 (solid line; equation; $R^2 = 0.92$). The radius of dye influx was measured from confocal images taken approximately 5 minutes after ablation. (**F**) Wing discs expressing GCaMP6m were ablated *ex vivo* in calcium-free media. Fluorescence is low before wounding (i) and only increases afterwards in cells close to the wound (ii). Scale bar is 50 μm. (**G**) The radius of the initial wound-induced calcium rise in calcium-free media ($R_{0 \ mM}$) is significantly smaller than $R_{B,max}$, with a best fit slope of 0.25 (red, open triangles; $R^2 = 0.60$). In

contrast, when wing discs are wounded in 2 mM calcium, the initial wound-induced calcium radius ($R_{2\ mM}$) corresponds to $R_{B,max}$ with a best fit slope of nearly 1 (blue, closed circles; $R^2 = 0.90$). Best-fit equations shown above graph. Horizontal error bars represent estimated uncertainty in identifying the collapse peak; vertical error bars are standard deviations of four radius measurements.

First, we measured electrical depolarization. Epithelial cells maintain an electrical potential or voltage difference across their plasma membranes and micro-tears would allow the free movement of Na^+, Cl^- and K^+ ions to eliminate this membrane potential and thus depolarize the cells. Ca^{2+} would also cross the plasma membrane, but Ca^{2+} ions do not contribute significantly to establishing or depolarizing the electrical potential[75]. We visualized cavitation-induced changes in membrane potential using a genetically encoded voltage indicator, Arclight, whose fluorescence decreases upon depolarization[76,77]. Although Arclight kinetics are slower than those of GCaMP6m, we observed a slight decrease in fluorescence in the first frame upon wounding in a region centered around the wound, and this decrease became more pronounced over the next 30 to 60 s (Figure 2-7A). As shown above for the initial Ca^{2+} signal, the radius of the depolarized region also matched the radius of cavitation (Figure 2-7B) – linking both to the maximum extent of the cavitation bubble. Over the course of ten minutes, damaged but un-lysed cells within the cavitation footprint repolarized, indicating that cells survive micro-tear damage (Figure 2-8).

Next, we used two robust and well characterized micro-tear assays based on two cell-impermeable fluorophores, the lipophilic dye, FM 1-43[70,78–84], and the DNA intercalating agent, propidium iodide (PI)[85–88]. FM 1-43 fluoresces only when bound to lipid membranes. Prior to wounding, dye binds only the outer leaflet of the cells' plasma

membranes. If wounding generates micro-tears, dye can then enter cells and label the inner leaflet of the plasma membrane, increasing its fluorescence intensity. We could not conduct these experiments in *Drosophila* pupae because they have an impermeable waxy cuticle that prevents dye from accessing notum cells and membranes. We thus used *Drosophila* wing discs, larval precursors of the pupal notum and wing that can be cultured *ex vivo*. We laser-wounded wing discs submerged in FM 1-43 while simultaneously imaging fluorescence and tracking cavitation with a hydrophone. After laser ablation, plasma membrane fluorescence increased, indicating inner-leaflet labeling and the presence of micro-tears in a circular region around the wound (Figure 2-7C). The radius of increased fluorescence matched the maximum radius of the cavitation bubble (Figure 2-7D) and did not expand with time. High-magnification imaging shows FM 1-43 preferentially labeling the plasma membrane with little labeling of endocytic vesicles, suggesting a route of entry that bypasses endocytosis (Figure 2-9). This route could be micro-tears, but since FM 1-43 has been observed to pass through some plasma membrane channels[89,90], we performed a similar experiment using the fluorophore PI. Upon laser ablation, the radius of PI positive cells also matched the radius of cavitation (Figure 2-7E). These results showing the internalization of two different fluorophores suggests a non-specific route of dye entry.
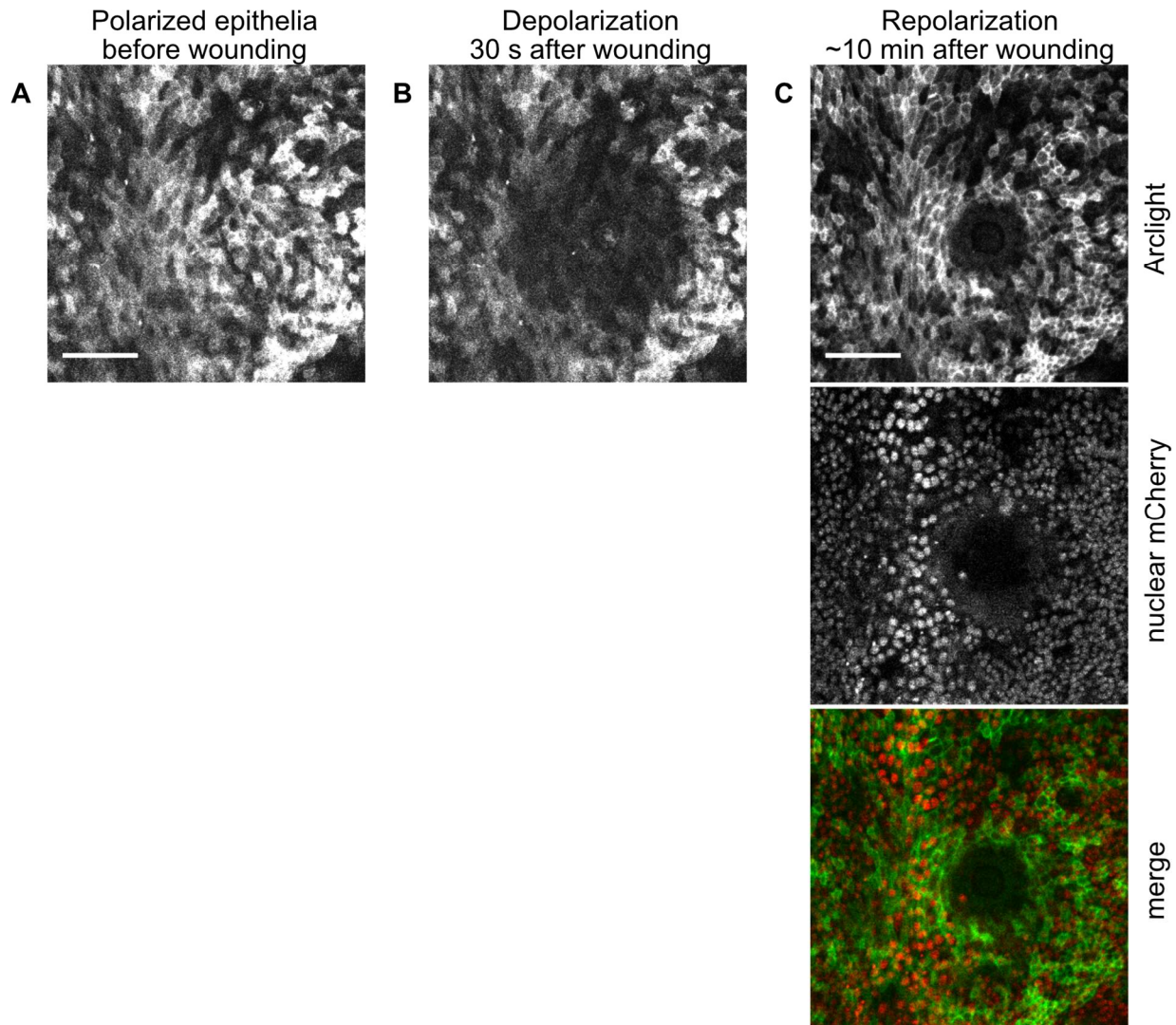
Figure 2-8: Cells in the cavitation footprint repolarize after wounding.

Panels show confocal images of electrical depolarization and repolarization over time after laser wounding of epithelial cells of the *Drosophila* notum. Cells express *pnr>Arclight* as a reporter of membrane electrical polarization. **(A)** Fluorescence intensity is high 10 seconds before wounding. **(B)** Fluorescence decreases after ablation, indicating depolarization in a region corresponding to the cavitation bubble footprint. **(C)** Approximately 10 minutes after wounding, cells in the affected area repolarize (Arclight), indicating their ability to survive micro-tear damage. The only area that remains dark is the primary wound itself, as indicated by the lack of nuclear-mCherry staining (nuclear mCherry panel and merge). Scale bar is 50 μm.
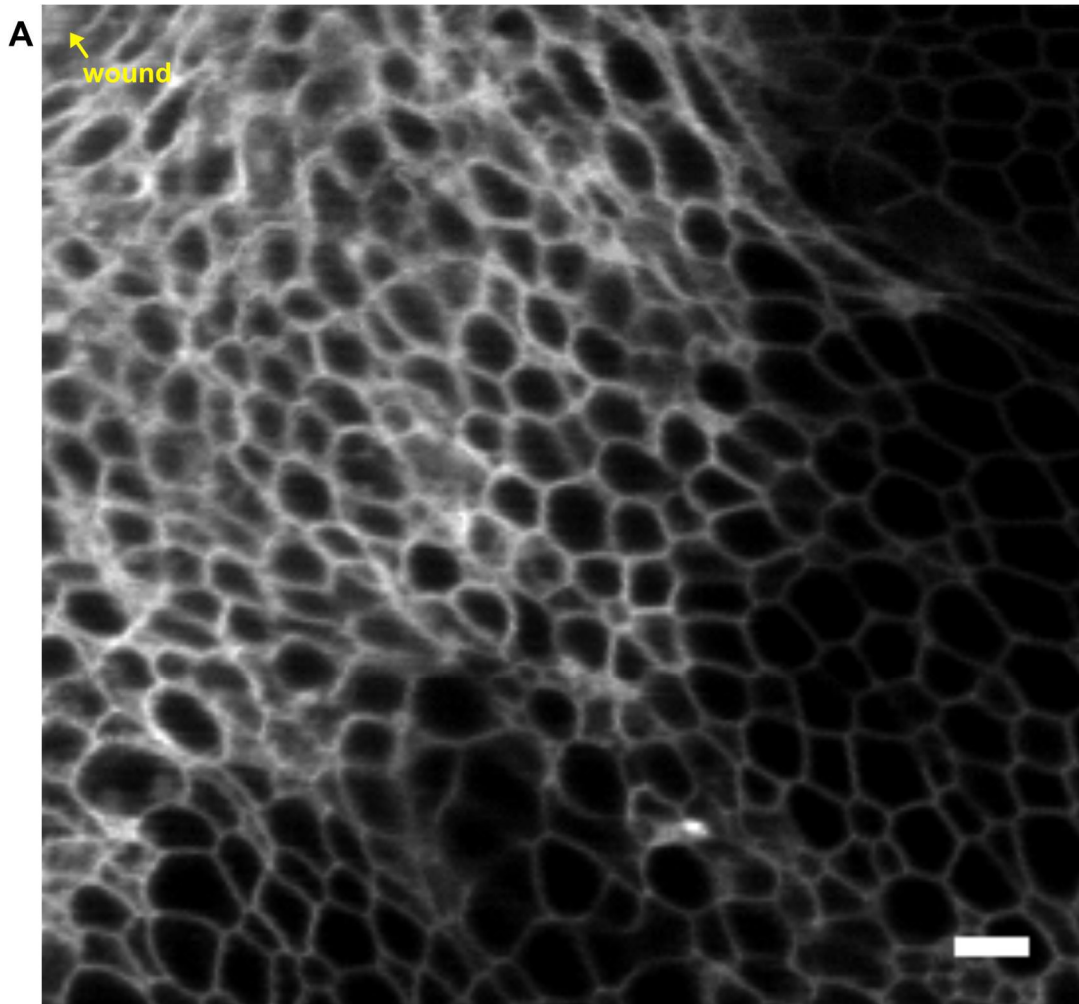
Micro-tear induced dye influx upon wounding labels plasma membranes of cells
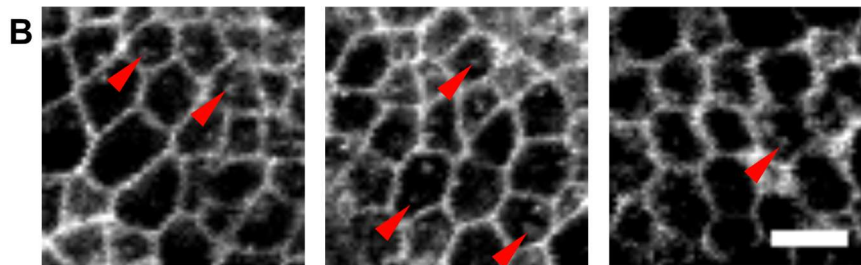
Endocytosis of dye appears as puncta in cells

Figure 2-9: Micro-tear induced dye influx labels plasma membranes.

FM 1-43 fluoresces upon binding lipid membranes. Prior to wounding, FM 1-43 cannot enter cells and labels the outer leaflet of the plasma membrane only. **(A)** When micro-tears occur, FM 1-43 will enter cells and is expected to label the inner leaflet of the plasma membrane, increasing its fluorescent intensity for cells with micro-tears. A high-resolution image of the apical cell surface of a wounded, wild-type wing disc taken within 10 minutes of dye application shows that FM 1-43 fluorescent intensity does

40

increase for plasma membranes within the cavitation footprint, but no dye-labeled endocytic vesicles are observed, confirming dye entry via micro-tears rather than endocytosis. Scale bar is 5 μm and the primary wound is out of frame, up and to the left of the image. **(B)** Three example images of dye uptake by endocytosis in an unwounded wing discs in two wild-type flies. Tissue was incubated in FM 1-43 for 30 minutes to allow normal endocytic processes to internalize dye in endocytic vesicles (red arrowheads). Such puncta are not observed in the cavitation footprint after wounding in (A). Scale bar is 5 μm.

Third, we removed extracellular Ca^{2+} and measured the effects on wound-induced Ca^{2+} signals. We could not alter extracellular calcium concentrations *in vivo* in the notum, so we ablated wing discs *ex vivo* as above, but in media with or without calcium. Wounding in the presence of physiological $[Ca^{2+}]$ (2 mM) resulted in a calcium influx radius that matched the cavitation radius (Figure 2-7G). Wounding in calcium-free media did not eliminate cytosolic calcium influx, but the radius of this influx was just ~ 1/4 the cavitation radius (Figure 2-7 F and G). We conclude that *in vivo,* most of the cavitation-induced calcium influx is derived from an extracellular pool. Interestingly, the small region of calcium influx observed in calcium-free media has similar dimensions to the zone of high influx-site density identified in kymographs *in vivo* in the notum (Figure 2-4B). We discuss this connection and possible explanations in the Discussion. Nonetheless, the strongly reduced extent of initial calcium signals in calcium-free media, in concert with the cavitation-linked changes in membrane potential and dye permeability shown above, combine to strongly support the hypothesis that most of the initial calcium influx comes through cavitation-induced micro-tears in the cells' plasma membranes.

2.4.5 Additional wound-induced Ca^{2+} signaling on timescales of seconds to minutes.

After the initial influx, the region of high intracellular Ca^{2+} around the wound typically undergoes two stages of radially symmetric expansion. The first stage follows directly from the micro-tears generated in the footprint of the cavitation bubble and expands the high-Ca^{2+} region radially outward ~20 μm over a period of 15-20 seconds (Figure 2-10A, i-ii). This first expansion is eliminated by expressing RNAi against the *Drosophila* gap junction proteins *Inx2* or *Inx3* (Figure 2-10 C and D), demonstrating signal propagation via gap junctions, consistent with some previous findings on other calcium waves[29,56,91]. The signal diffusing through gap junctions could simply be the leakage of Ca^{2+} from damaged to undamaged cells; alternatively, the first expansion could be mediated by IP3, similar to calcium waves in wing discs and in other wounding systems[28,56,91,92]. Cytoplasmic calcium buffering makes direct Ca^{2+} transport through gap junctions less common than IP3 transport[21], but the estimated diffusion constants in Figure 2-6E suggest the presence of saturating concentrations of Ca^{2+} that could overcome cytoplasmic buffering and thus flow directly through gap junctions. After the brief expansion, this high-Ca^{2+} region then shrinks modestly before a second expansion becomes evident 40 to 200 s after ablation (Figure 2-10A, iii-iv; Figure B-2). The second expansion is typically larger than the first and does not rely on gap junctions (Figure 2-10 C and D). After the second expansion, the high-Ca^{2+} region begins to shrink radially while sending off localized flares (Figure 2-10A, v-viii).

To further analyze the expansion of Ca^{2+} signals over time, we condensed each movie to a graph representing the expansion of the calcium wave with respect to time. This condensation involves radial averaging to identify the average edge of the calcium

wave (see Supplemental Methods Section 2.7), and is thus most appropriate for analyzing time periods in which the high-Ca^{2+} region is radially symmetric – e.g., during the first and second expansions, but not once flaring commences. A collection of Ca^{2+} signal radius graphs for 24 laser ablation experiments is shown in Figure 2-10B. All of these experiments have a first signal expansion, but the presence of a second expansion depends on the presence and size of the primary wound. Large wounds (> 35-µm diameter, blue) always exhibited a second expansion, and intermediate wounds (15-35 µm, green) sometimes did, but small wounds (< 15-µm diameter, magenta) either had no second expansion or an atypical weak one. Furthermore, some samples exhibited a first expansion but no visible wound likely due to slight mistargeting of the laser pulse, which could create cavitation without ablation; these samples never exhibited a second expansion. Thus, while the first expansion is tightly linked to cavitation-induced micro-tears, the second requires some cells to be damaged beyond repair and becomes more likely as the primary wound size increases.
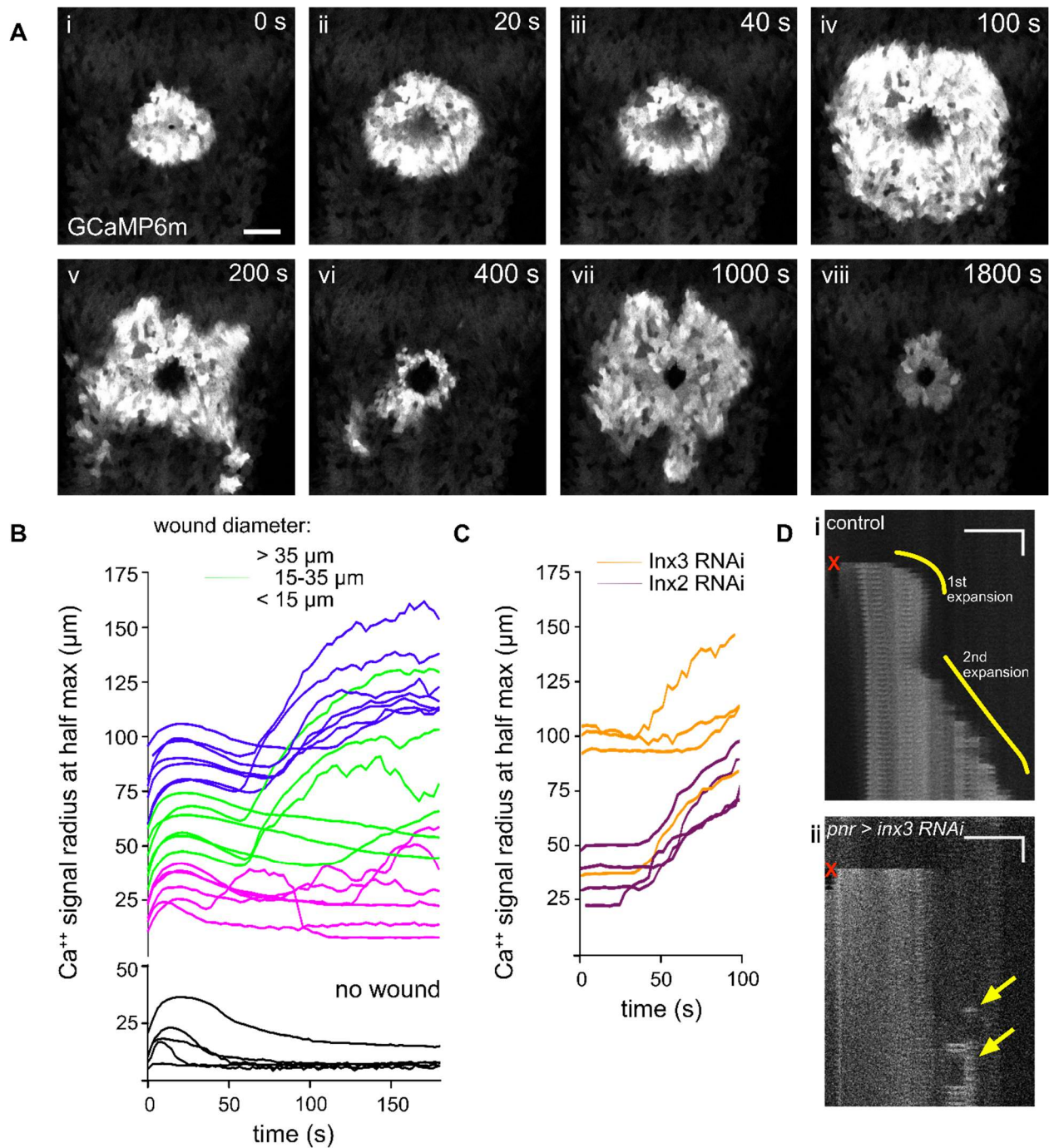
Figure 2-10: Two wound-induced calcium signal expansions occur on different timescales via different mechanisms.

(**A**) Stills of *in vivo* live imaging of GCaMP6m in the notum. In the first frame after laser ablation, an increase of cytosolic calcium is observed in a ~5-7 cell radius around the wound (i). Seconds after wounding, the region of increased fluorescence expands to adjacent cells (ii) before contracting slightly (iii). The region of increased fluorescence then expands concentrically again (iv) before breaking into propagating, anisotropic

calcium flares (v- viii). The flares continue initiating for >30 min after wounding while the central region cyclically expands and contracts. Scale bar is 50 μm. **(B)** The radial expansion of calcium signaling is plotted over time for 24 samples: each line represents a different sample with radii reported from the wound center. The initial region expands briefly in all samples before contracting. A second expansion may then occur and does so more frequently in larger wounds. No second expansion occurs when no wound is present. **(C)** The radial expansion of calcium signaling over time for representative samples expressing either *Inx2* or *Inx3* RNAi in the *pnr* domain. A similar pattern was seen with a second *Inx2* RNAi construct (data not shown). Knocking down gap junctions blocks the first expansion but not the second. **(D)** Kymographs showing the expansion of calcium signals over time for control (i) and *Inx3* knockdown samples (ii). The curved and straight yellow lines in controls indicate the normal shape of the first and second expansion. In *Inx3* knockdowns, the first expansion is absent; the second is perturbed but still occurs. Wound location and time are indicated by X, horizontal scale bar is 50 μm and vertical scale bar is 15 s.

We fit each expansion of the Ca^{2+} signal radius to a two-dimensional diffusion model to assess the kinematics and to begin to elucidate the signals driving each stage. This model assumes that some unknown signal X is released at a specific time (t_0) over a distributed area, given by an axisymmetric 2D Gaussian with $1/e^2$ radius σ_0 and total signal amount M. This signal diffuses with diffusion constant α and triggers a Ca^{2+} influx wherever the local concentration exceeds a threshold C_{th}. We acknowledge that the source likely is more complicated than a 2D Gaussian, but details of the distribution shape beyond its root-mean-square radius ($\sqrt{2}\sigma_0$) have no discernable effects over the time scales of our measurements. With this model, the time-dependent radius of the high-Ca^{2+} region (R_S) is thus given by

$$R_S^2 = 2\sigma^2 \ln\left[\frac{1}{2\pi\sigma(C_{th}/M)}\right] \text{ with } \sigma^2 = \sigma_0^2 + 2\alpha(t - t_0) \tag{2-1}$$

We fit models of this form to each expansion independently. The intervening and final shrinkage phases were not fit to this model because they involve additional

mechanisms and timescales governing the return to baseline Ca^{2+} levels. The model fit

the first expansion well with t_0 set to the time of laser ablation. This left three fit

parameters: σ_0, α and C_{th}/M. The second expansion could not be fit well with $t_0 = 0$, so

we instead set t_0 equal to the time at which each second expansion became apparent.

Example fits are shown in Figure 2-11A, with the first expansions highlighted in red and

the second in blue. The complete set of fits is shown in Figure B-2. Note that the fitted

equation has a degeneracy with respect to σ_0 and t_0, i.e., broadly distributed sources

releasing a signal at late times would be equivalent to narrowly distributed sources

releasing the same signal earlier. This becomes a particular issue when fitting the

second expansion because choosing earlier values for t_0 would lead to equivalent fits

with smaller values for σ_0. Considering this degeneracy, fits to the second expansion

have been back propagated (dashed lines in Figure 2-11A) to indicate that the driving

signal could have been released before the second expansion became apparent.

Notably, the back propagations do not go all the way back to $t = 0$. They instead

intersect the time axis at a median time of 47 s (interquartile range of 29 to 61 s),

strongly suggesting that the unknown signal driving the second expansion is either

released tens of seconds after ablation or has a delay introduced by cellular signal

transduction.

The best fit parameters for both expansions are compiled in the box-and-

whiskers plots of Figure 2-11B. The $1/e^2$ radii of the initial signal distributions are

comparable (24 versus 22 μm, assuming the second expansion starts when it first

becomes apparent). On the other hand, the second expansion yields significantly

smaller values for both the diffusion constant of the signal – median values for α of 53

versus 20 $\mu m^2/s$ (P = 1.5 x 10^{-5}; Mann-Whitney U test) – as well as for the relative signal threshold – median values for C_{th}/M of 2 x 10^{-5} μm^{-2} versus 6 x 10^{-6} μm^{-2} (P = 7 x 10^{-8}). These results suggest that each expansion is driven by a different diffusive signal.

Interestingly, the diffusion constants for both the first and second expansion increase with wound size (Figure 2-11C). In fact, for large wounds, the diffusion constant of the first expansion approaches the value for free diffusion of calcium. These observations suggest a model in which larger wounds release more of both signals and thus yield larger effective diffusion constants by overcoming more of the buffering or binding capacity of the environment.
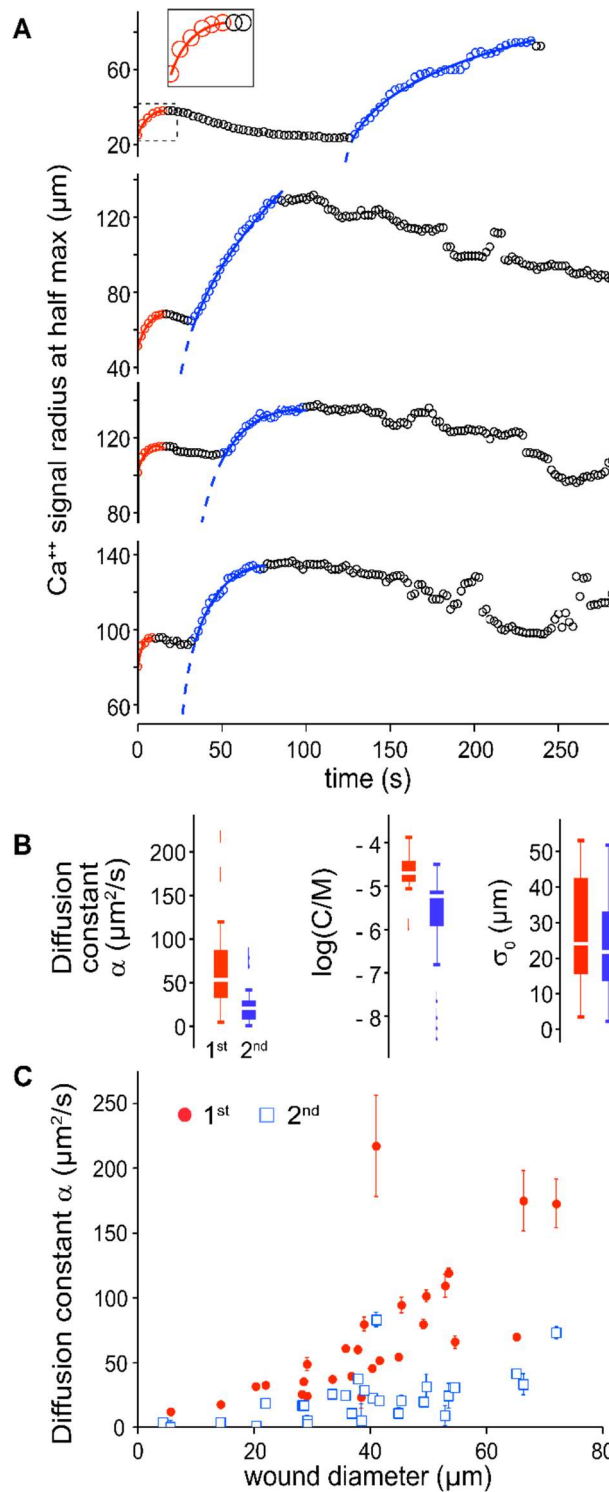
Figure 2-11: Parameterization shows distinct characteristics for each expansion.

(A) Four examples showing the expansion of calcium over time. The initial and secondary expansions are highlighted in red and blue respectively. The solid lines show diffusional fits to each expansion; the dashed blue lines show back-projections of fits to

the second expansion. The inset shows an expanded view of the fit to the data from the outlined region. The complete set of analyzed curves (N = 28) is shown in Figure B-2. As a measure of goodness-of-fit, the standard errors of the regression for the four fitted first expansions were (from top to bottom) 0.19 μm, 0.18 μm, 0.95 μm, 1.04 μm and for the four fitted second expansions were (from top to bottom) 1.62 μm, 1.76 μm, 1.21 μm, 1.30 μm. **(B)** Box-and-whiskers plots of the best-fit parameters for all first and second expansions: α is the diffusion constant; C/M is the ratio of the signal threshold to the amount released; and σ_0 is the $1/e^2$ radius of initial signal distribution. Median and interquartile range are displayed. **(C)** Variability among the fitted diffusion constants for each expansion is partially explained by a dependence on the wound diameter.

2.5 Discussion

When a pulsed laser creates wounds in the epithelium of the *Drosophila* pupal notum, these wounds trigger a complex series of calcium signaling dynamics: a rapid influx into nearby surviving cells that matches the footprint of the laser-induced cavitation bubble; followed by a spreading of the high-cytosolic-calcium region via two sequential and concentric waves. These dynamics and a model that explains them are summarized in Figure 2-12.

The initial calcium influx occurs at hundreds of distinct loci and spreads throughout the affected cells in < 0.1 s. It spreads intracellularly with diffusion constants near that of free calcium, suggesting that high concentrations of calcium are flooding the cells and overcoming cytosolic buffering capacity. We propose that each locus corresponds to a cavitation-induced, plasma membrane micro-tear that allows calcium influx from the extracellular environment. In support of this model, cells in the cavitation footprint also become electrically depolarized and permeable to entry of two cell-impermeable dyes. Further, wounding in calcium-free media strongly reduces the extent of the initial rise in cytosolic calcium. These results could also be explained by

cavitation-induced shear stresses opening mechanosensitive channels rather than micro-tears; however, the variety of observed effects implies a non-specific route of entry. We thus consider micro-tears more likely.
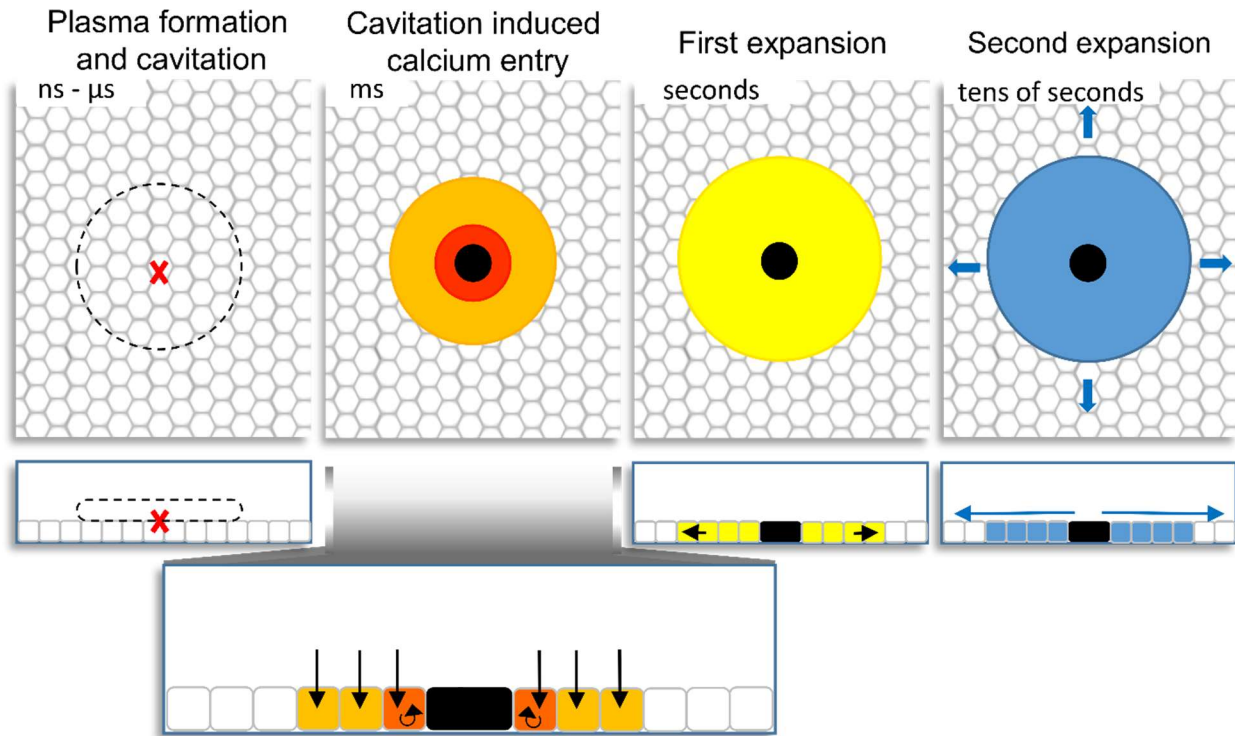
Figure 2-12: Summary of calcium signal dynamics after laser wounding.

Plasma formation and cavitation: Pulsed laser ablation generates a localized plasma at the laser focus (X), which then recombines and leads to expansion of a cavitation bubble (dashed black outline denotes maximum bubble radius).

Cavitation induced calcium entry: The cavitation bubble expands, damaging cells as it spreads. Close to the point of ablation, cavitation-induced shear stresses lyse cells, creating the primary wound (black). Cells close to the primary wound undergo extensive damage (dark orange). Micro-tears on the plasma membrane and in organelle membranes result in calcium influx from the extracellular space *and* internal stores <u>milliseconds</u> after wounding (black arrows). The shear forces applied to cells are attenuated as the cavitation bubble expands and slows. Cells far from the wound (light orange) exhibit plasma membrane micro-tear damage which allows calcium entry from the extracellular space (black arrows). Cells that were not lysed to create the primary wound survive cavitation damage.

50

First expansion: <u>Seconds</u> after wounding high concentrations of calcium that just entered the cells spreads intracellularly through gap junctions (black arrows) to neighbors (yellow).

Second expansion: After wounding a delayed second expansion of calcium spreads to cells distant from the wound (blue). This expansion is driven by extracellular ligand diffusion (blue arrows) but gap junctions may still have some role in generating a smooth wave front. Modeling of the second expansion shows it is characteristically different from the first expansion.

Membrane permeabilization is known to occur when laser-induced cavitation bubbles are used to introduce DNA, drugs or micro-particles into cultured cells via a process known as optoporation[93–98]. The shear stress associated with cavitation-bubble expansion and collapse can induce zones of acute cell lysis, cell necrosis, and membrane disruption[12,14]. We note similar zones of damage in our studies, observed as a primary wound surrounded by regions with a high and then low density of calcium influx sites (Figure 2-4B). This suggests more severe cellular damage close to the wound, which may be linked to the limited region of cytosolic calcium influx observed after wounding in calcium-free media. In fact, the radius of this limited region and the radius of high-density damage identified in kymographs represent similar fractions of the cavitation bubble radius (0.25 and 0.3 respectively). In this region proximal to the wound, the cavitation bubble and its shear stresses may generate additional micro-tears in organelle membranes that release calcium from the ER, mitochondria and Golgi or may trigger mechanosensitive GPCR (G-protein coupled receptor)-induced release of calcium from these same intracellular stores[99].

After the initial influx, the high-calcium region expands via two sequential waves. The first wave spreads with a diffusion constant of 32 to 87 $\mu m^2/s$, with faster diffusion observed in bigger wounds. These rates still exceed that of cytosolically buffered calcium and suggest a simple model for the first wave based on the diffusion of excess

calcium into neighboring cells through gap junctions. Indeed, variations in how well the excess calcium is buffered could explain this wave's wide range of fitted diffusion constants. Furthermore, this expansion is short-lived and short-ranged, which would be predicted as the calcium concentration decreases as it spreads and would thus be well buffered further from the wound. Although we favor this model in which the first expansion is caused by the direct diffusion of calcium to neighboring cells, the diffusion of IP3 has been identified as important for signal expansion in other wounding systems[28,56,91,92] and remains an alternative possibility.

The second wave begins ~45 seconds after wounding, but is not always present. The second wave occurs more frequently following larger wounds, suggesting its critical dependence on the extent of primary wound-induced damage. Interestingly, the second wave has a delayed start (at least 29 to 61 s after ablation) which may represent a delayed release of signal or time required for cells to transduce the signal into a calcium response. The second wave spreads with a diffusion constant of 7 to 30 μm^2/s, much slower than the first wave. This suggests distinct signals driving the two expansions, but further experiments are needed to identify the second wave's time delay and spread mechanism. After the second expansion, the high-calcium region begins sending off asymmetric directional flares, likely representing waves of calcium-induced calcium release moving throughout the tissue. Each flare lasts tens of seconds, but new ones continue starting for more than 30 minutes after wounding. These flares are similar to calcium oscillations reported after epithelial wounds in zebrafish[100,101] and fly embryos[29].

Previous studies have identified two models for wound-induced calcium wave initiation: mechanosensitive calcium channels[10,28,29,55,56,99,102] and extracellular diffusible

ligands[49,52,53,103–105]. In many cell culture models, the driving signal for the calcium wave propagates extracellularly and very fast, with speeds ranging from 4.6 to 49.3 µm/s[48,49,106]. This is much faster than the speeds of calcium signal spread in our *in vivo* experiments: the median speeds were 2.9 and 1.7 µm/s for the initial portions of the first and second expansions, and these slowed in a diffusive manner. These rates are more similar to other *in vivo* wound healing models in which calcium signals propagate via gap junctions and spread at rates of 0.4 to 6.9 µm/s[29,56,91]. Signal propagation via extracellular ligand diffusion may occur in the *Drosophila* notum during the second wave, as this expansion is not dependent on gap junctions, but the ligand would have to diffuse much more slowly than those identified in cell culture models.

Once calcium enters a cell, regardless of how, it is a master regulator of wound healing. Calcium regulates Rho[51,107,108] and the actin cytoskeleton[10,32], activates JNK signaling[50], prevents apoptosis[30], and increases hydrogen peroxide and inflammation around wounds[29]. Calcium waves alert cells to the presence of a wound and permit the activation of healing programs[101]. Given the variety of types of wounds that may need to be healed, multiple mechanisms may have evolved to initiate calcium signaling cascades. Our study of laser wounding has identified at least three different mechanisms. The first calcium response is extracellular calcium entering the cytosol through plasma membrane micro-tears. Although this effect is driven here by laser-induced cavitation bubbles, similar cellular and tissue damage are inflicted simultaneously during naturally-occurring trauma wounds[109,110]. In fact, pulsed-laser ablation is similar to a localized puncture accompanied by a wider crush injury. In either case, the calcium influx through micro-tears is in effect a single-cell response to cell-

level damage; it becomes a tissue-level response as high cytosolic calcium spreads to neighboring cells by diffusion through gap junctions. This so-called first wave thus involves a second distinct mechanism by which surrounding undamaged cells experience a rise in cytosolic calcium. Importantly, this expansion of a single-cell wound signal to neighboring cells suggests a continuum between single-cell and tissue-level wound responses.

Finally, if the region of ablated cells is large enough, an unknown signal initiates another wave of cytosolic calcium increases, which we term the second expansion. The unknown signal driving this wave represents a third mechanism governing calcium increases after wounding. Because this third mechanism occurs only after a discontinuity or hole appears in the epithelium, and not simply after cellular micro-tear damage, this signal may arise from cell mechanics or cell lysate or dying cells around the primary wound margin. It is noteworthy that separate, but overlapping calcium signals emanate from the wounded region due to both cell-level damage and tissue-level damage, albeit by different mechanisms. Our results suggest the interesting possibility that signaling from many types of damage may converge on increasing cytosolic calcium levels to regulate both single-cell and multicellular wound-healing programs.

2.6 Conclusions

Wounds created via laser ablation contain single-cell damage and tissue damage, similar to naturally occurring puncture or crush wounds. Each damage mechanism drives its own calcium signal dynamics. Single-cell damage arises from

cavitation-induced, plasma membrane micro-tears and results in direct calcium influx from the extracellular environment followed by diffusive expansion into neighboring cells. Tissue damage in the form of a primary wound at the ablation site results in a delayed calcium wave that expands well beyond the cavitation bubble footprint. This second wave occurs more frequently following larger wounds. Our kinematic analysis narrows and informs the search for calcium wave initiation and propagation mechanisms by showing that both expansion events fit diffusive models that are consistent with previously observed rates of calcium wave propagation *in vivo*, but are driven by different signals. Finally, this laser wounding model exhibits exaggerated, but controllable single cell damage and may be useful for future investigations at the intersection of single-cell wound healing and tissue wound healing.

2.7 Supplemental Methods

Fly Lines

     pnr-Gal4 (Fly Base ID: FBst0025758) was used to drive expression of *UAS-GCaMP3* (Fly Base ID: FBst0032236), *UAS-GCaMP6m* (Fly Base ID: FBst0042748), *UAS-Arclight* (Fly Base ID: FBst0051056), *UAS-Inx2 RNAi* (Fly Base ID: FBst0029306, data shown in Figure 5C), *UAS-Inx2 RNAi* (Fly Base ID: FBst0474063, data not shown) and *UAS-Inx3 RNAi* (Fly Base ID: FBst0060112) in the notum. *tubP-Gal4* (Fly Base ID: FBst0005138) was used to drive expression of GCaMP6m in the wing disc. *tubP-Gal80^{ts}* (Fly Base ID: FBst0007017) was used to suppression the expression of the RNAi lines during embryogenesis. *shg-tdTomato* (Fly Base ID: FBst0058789) and *Ubi-p63E-shg.GFP* (Fly Base ID: FBst0307577) were used to visualize cell borders. *Vkg-*

GFP^{454} (Fly Base ID: FBti0153267) was used to visualize cell architecture in wing disc experiments with propidium iodide. w^{1118} was used as wild-type.

Mounting pupae

  White prepupae expressing *pnr-Gal4* and *UAS-GCaMP3, UAS-GCaMP6m* or *UAS-Arclight* were identified and aged for 12-18 hours After Puparium Formation (APF). For imaging, a pupa was placed on a piece of double-sided tape (Scotch brand, catalog #665), ventral side down, and its anterior pupal case was removed with fine tipped forceps to reveal the notum epithelium. The entire piece of double-sided tape was gently lifted from the dissecting stage with the pupae still attached and adhered to a 45 mm x 50 mm coverslip (no. 1.5, Fisherbrand, 12-544F) so that the pupal nota were laid against the coverslip, with the pupae between the coverslip and the tape layer. It was not necessary to adhere all edges of the double-sided tape to the coverslip, only the edge at the anterior of the pupae. Then, an oxygen permeable membrane (YSI, standard membrane kit, cat# 1329882) was applied over the pupae and secured to the coverslip with additional double-sided tape so pupae would not become dehydrated.

Mounting wing discs

  For wounding experiments in the wing disc, *tubP-Gal4* was used to drive the expression of *UAS-GCaMP6m*. Wing discs were dissected from 3rd instar larvae in a drop of PBS (137 mM NaCl, 2.7 mM KCl, 10 mM Na_2HPO_4, 2 mM KH_2PO_4, pH 7.4) and immediately mounted on coverslips for imaging and ablation. Cell-Tak Adhesive (Corning, catalog #354240) was used to adhere wing discs to 45 mm x 50 mm coverslips (no. 1.5, Fisherbrand, 12-544F). 7 ug of Cell-Tak was used to coat a surface

area of 20 mm x 20 mm using the manufacturer's protocol. Because Cell-Tak was used, external forces were not applied to wing discs through mounting and imaging. A pap pen (RPI, catalog #50-550-221) was used to trace a hydrophobic barrier around the wing discs on the coverslip. Two wing discs were mounted on one coverslip. For calcium-free conditions, wing discs were mounted in a drop of PBS. For 2 mM calcium conditions, wing discs were mounted in a solution for which 200 mM $CaCl_2$ at pH 7.0, was diluted to 2 mM in PBS.

Laser ablation and live imaging

Laser ablation and live imaging were performed using a Zeiss LSM410 raster-scanning inverted confocal microscope with a 40X 1.3 NA oil-immersion objective. Scans were performed either every 2.14 seconds or every 3.0 seconds. Laser ablation used single pulses of the 3rd harmonic (355 nm) of a Q-switched Nd:YAG laser (5 ns pulsewidth, Continuum Minilite II, Santa Clara, CA). Laser pulse energies ranged from 0.5 µJ to 10 µJ, depending on the experiment. A separate computer-controlled mirror and custom ImageJ plug-in were used to aim and operate the ablation laser so that ablation could be performed without any interruption to live imaging. For kymograph experiments, line scans with a scan rate of 2.09 ms were taken at the wound site. Line scan data was assembled into kymographs using ImageJ.

Cavitation experiments

Pupae were selected and pupal cases were removed as described above. PBS was used to release pupae from double-sided tape. Fly glue, made of double-sided tape (Scotch brand, catalog #665) dissolved with heptane, was used to adhere each pupa to

the coverslip so its entire dorsal side was touching the glass. A pap pen (RPI, catalog #50-550-221) was used to trace a hydrophobic barrier around the pupae on the coverslip. Immediately prior to imaging, approximately 500 µl of distilled water was slowly dropped on top of the pupae on the coverslip so that the pupae were under a bubble of water. For wing disc cavitation experiments, discs were mounted as described above, in approximately 500 µl PBS or PBS with 2 mM calcium.

A small hydrophone (Onda, 0.5 mm aperture, <20 ns rise time, 2.24 V/MPa sensitivity), was mounted to the confocal stage and lowered into the bubble of water approximately 1 mm away from the focus of the laser. Hydrophone data were displayed on an oscilloscope. Samples were imaged and wounded as described above while the hydrophone measured the expansion and collapse of each cavitation bubble via their associated acoustic transients. Each cavitation bubble's maximum radius was calculated from its lifetime[65].

Cavitation bubble imaging

Drosophila embryos were collected approximately 2 hours after egg laying and aged at 18°C until germ band retraction. Prior to mounting, the chorion was removed using a 50% bleach solution. Fly glue, made as described above, was used to adhere each embryo to the coverslip. Embryos were immersed under a bubble of distilled water and the needle hydrophone was lowered into the solution as described above.

A second optical path was added to the Zeiss LSM410 microscope to image cavitation bubbles formed during ablation. This high-speed bright-field imaging system is built around a high-sensitivity CCD camera (Photometrics CoolSNAP EZ, Tucson, AZ; 1392×1040-pixel 12-bit sensor, >60% quantum efficiency in the range 450 to 650 nm)

and a pulsed diode laser (Coherent Cube, Santa Clara, CA; λ = 660 nm, maximum average power = 61 mW). The diode laser serves as a flash illumination source with a controllable pulse duration. The camera is triggered before ablation, and the illumination laser is used as a strobe light with an accurately adjustable delay. Signals for triggering the camera, the ablation laser's Q-switch, and the diode laser pulse (rise and fall) are controlled by a digital delay generator (Stanford Research Systems DG645, Sunny Vale, CA) using the ablation laser's flash-lamp sync as the master timing signal. The accuracy of the illumination pulse delay is limited by the approximately 2-ns jitter inherent to the electronics controlling the ablation laser. This system can image cavitation bubbles in liquid with illumination pulse durations as short as 7 ns. For imaging in fly embryos, longer pulses (~0.5 μs) are needed to obtain sufficient contrast. Note that images formed by the bright-field imaging system lack all depth information. Each is essentially a picture of the shadows cast by structures in the ~200-μm thick embryo.

To protect the photomultiplier tubes in the confocal system from inadvertent exposure to the illumination laser, the dichroic normally used to reflect collected fluorescence is removed during high-speed imaging. It can be reinserted to take confocal images of the embryos within a few seconds of ablation.

FM 1-43 and PI dye analysis in wing discs

FM 1-43 dye (ThermoFisher # T35356) was diluted in PBS to a final concentration of 5 μg/ml. Wing discs were mounted as described above and dye was added immediately prior to imaging. To limit pre-wounding dye internalization via endocytosis, wounding experiments were performed and completed within 10 minutes

of adding FM 1-43 dye. Since the kinetics of dye influx via micro-tears and its associated increase in dye-labeled membrane fluorescence are slower than GCaMP6m kinetics, measurements of the region of dye influx were taken from images collected 60 seconds after ablation. Despite this delay, we did not observe any spreading of increased dye fluorescence to neighboring cells. Simultaneous cavitation measurements were performed as described above.

PI (ThermoFisher #P3566) was diluted in PBS to a final concentration of 20 µg/ml. Wing discs were mounted as described above and dye was added immediately prior to imaging. Because PI does not fluoresce until after wounding a fluorescent marker was needed to identify the correct focal plane for laser ablation. Therefore, we used wing discs expressing *Vkg-GFP454* in a wild-type background to fluorescently label the basement membrane. Measurements of the region of dye influx were taken from images collected approximately 5 minutes after ablation.

Image processing and analysis

Quantitative data was extracted from images and kymographs of GCaMP fluorescence via routines implemented in Mathematica (Wolfram Inc., Champaign, IL).

To identify the initial Ca^{2+}-influx sites in kymographs, the signal front was first defined as the earliest time at which the GCaMP signal exceeded the mean pre-wounding signal plus two standard deviations. Each signal front was then smoothed using a 3rd-degree 17-point Savitzky-Golay filter to remove noise and the positions of its local minima were identified as the initial sites of Ca^{2+} influx.

To analyze the diffusion of calcium from these influx sites, all available kymographs were examined to identify sites whose kymograph peaks were symmetric, remained below saturation, and were spatially isolated for some time. These criteria identified 25 individual peaks that were separated from other regions of calcium influx for at least 43 ms and remained below saturation for at least 21 ms (all 25 peaks are shown in Figure B-1. These peaks were cropped in ImageJ to widths on the order of 10 μm and lengths on the order of 50 ms and then fit to a diffusion model for $t > 0$:

$$\phi(x, t; \alpha, q, x_0, y_0, \phi_0) = Min\left[1, \frac{q}{4\pi^{3/2}\alpha r}\Gamma\left(\frac{1}{2}, \frac{r^2}{4\alpha t}\right) + \phi_0\right] \tag{2-2}$$

where $\Gamma(a, p) = \int_p^\infty u^{a-1}e^{-u}du$ is the incomplete gamma function. The model assumes a single point source where calcium enters the cytosol at a constant rate q and diffuses with a diffusion constant α from a location that is at position x_0 along the kymograph line and a distance y_0 from this line. Therefore, $r^2 = (x - x_0)^2 + y_0^2$ is the squared distance from a position x on the kymograph line to the source location. Eq. (2-2) was obtained by integrating the equation of diffusion from an initial point source concentration, $\phi(x, t') = (4\pi\alpha t)^{-3/2}\exp\left(-\frac{r^2}{4\alpha t'}\right)$, over time from 0 to t, followed by a variable substitution $u = \frac{r^2}{4\alpha t}$. A more detailed derivation is given in Section 1.4.1.2. Due to the spatial symmetry of this model, there is no loss in generality in assuming the point source and the kymograph line are in the x-y plane and along the x-axis respectively.

This model further assumes that image intensity values are a linear function of calcium concentration, allowing for a constant non-zero intensity baseline ϕ_0, until image intensity saturates at a relative intensity value of 1. The fitted parameters were α,

q, x_0, y_0, and ϕ_0 as defined above. Note that on the time scales analyzed, the calcium signals have not yet spread completely through individual epithelial cells; therefore, three-dimensional diffusion was considered instead of two-dimensional diffusion.

To analyze longer term spread of calcium signals from full-frame time-lapse images, the ImageJ Radial Profile Angle Plot plug-in was used on each image to determine the average GCaMP intensity profile as a function of distance from the center of the wound. A custom MATLAB script was then used to determine the distance from the wound at which the intensity dropped to half its maximum. This distance corresponds to the radius of the radially-averaged calcium wave and plotting it for each video frame yields a graph of calcium signal expansion over time. Sections of these signal expansion curves were fit to 2D diffusion models (Eq. (2-1) in Section 2.4.5) using nonlinear regression in Mathematica.

Chapter 3

Proteolytic activation of Growth-Blocking Peptides triggers calcium responses through the GPCR Mthl10 during epithelial wound detection

This chapter is adapted from O'Connor, J. T., Stevens, A. C., Shannon, E. K., Akbar, F. B., LaFever, K. S., Narayanan, N. P., Gailey, C. D., Hutson, M. S., Page-McCaw, A. Proteolytic activation of Growth-Blocking Peptides triggers calcium responses through the GPCR Mthl10 during epithelial wound detection. *Dev Cell.* (in press).

My main contributions to this chapter are the reaction-diffusion modeling described in Section 3.5 with results presented in Section 3.3.6 and Figures 3-8 - 3-10 as well as the model predictions presented in Section 3.3.7, Figure 3-11, and Figure 3-12.

A full set of materials and methods for this chapter can be found in Appendix C.

3.1 Abstract

The presence of a wound triggers surrounding cells to initiate repair mechanisms, but it is not clear how cells initially detect wounds. In epithelial cells, the earliest known wound response, occurring within seconds, is a dramatic increase in cytosolic calcium. Here we show that wounds in the *Drosophila* notum trigger cytoplasmic calcium increase by activating extracellular cytokines, Growth-blocking peptides (Gbps), which initiate signaling in surrounding epithelial cells through the G-protein coupled receptor, Methuselah-like 10 (Mthl10). Latent Gbps are present in unwounded tissue and are activated by proteolytic cleavage. Using wing discs, we show that multiple protease families can activate Gbps, suggesting they act as a generalized protease-detector system. We present experimental and computational evidence that proteases released during wound-induced cell damage and lysis serve as the instructive signal: these

proteases liberate Gbp ligands, which bind to Mthl10 receptors on surrounding epithelial cells, and activate downstream release of calcium.

3.2 Introduction

When a tissue is wounded, the cells surrounding the wound rapidly respond to repair the damage. Despite the non-specific nature of cellular damage, there is remarkable specificity to the earliest cellular response: cells around the wound increase cytosolic calcium, and this damage response is conserved across the animal kingdom[10,28,29,49,100,101,106,111–115]. The calcium response is not limited to cells at the wound margin, but extends even to distal cells[10,29,100,101]. Multiple molecular mechanisms have been identified that regulate wound-induced gene expression or cell behavior downstream of calcium[10,17,29,50,51,100,101,116,117], but the upstream signals remain unclear. How exactly do cells detect wounds? Here we investigate the molecular mechanisms by which a wound initiates cytosolic calcium signals.

The immediate increase in cellular calcium in turn initiates repair or defense responses. Calcium has been well-established as a versatile and universal intracellular signal that plays a role in the modulation of numerous intracellular processes. Several calcium-regulated processes are required for proper wound repair, including actomyosin dynamics[10,32,51,118–120], JNK pathway activation[50], and plasma membrane repair (reviewed in Cooper and McNeil, 2015[121]). Unsurprisingly, an increase in cytosolic calcium is necessary for wound repair[17,28,49,51,100].

Nonetheless, there is less clarity on the mechanisms that trigger increased cytosolic calcium in cells near to and distant from the wound. In some cases, wound-

induced cytoplasmic calcium enters from the extracellular environment, either directly through plasma membrane damage[17,49–51,113,114] or through calcium ion channels like TrpM[10,28,29]. In others, calcium is released from the endoplasmic reticulum (ER) through the IP$_3$ Receptor[28,49,56,91,106,115] and initiated by an unknown G-Protein Coupled Receptor (GPCR) or Receptor Tyrosine Kinase (RTK). Further, calcium responses can be initiated by mechanical stimuli alone[56,122–124]. Elucidating the mechanisms by which calcium signaling is triggered *in vivo* is critical to understanding how wound information is transmitted through a tissue in order to change cellular behavior and properly repair the wound.

By live imaging laser wounds in *Drosophila* pupae, we previously showed that damaged cells around wounds become flooded within milliseconds by extracellular calcium entering through micro-tears in the plasma membrane[113]. Although this calcium influx expands one or two cell diameters through gap junctions, it does not extend to more distal cells. Strikingly, after a delay of 45-75 seconds, a second independent calcium response expands outward to reach a larger number of distal cells. Here we identify the relevant signal transduction pathway and receptor, the GPCR Mthl10. Downstream, signals are relayed through Gαq and PLCβ to release calcium from the ER. Upstream, Mthl10 is activated around wounds by the cytokine ligands Growth-blocking peptides (Gbps). Further, we provide experimental and computational evidence that the initiating event for the distal calcium response *in vivo* is a wound-induced release of proteases that activate the latent Gbp cytokines, cleaving them from inactive/pro-forms into active signaling molecules.

3.3 Results

To investigate the calcium responses after wounding, we analyzed *Drosophila* pupae (Figure 3-1A), which are amenable to live imaging *in vivo* because they are stationary throughout development. By partially removing the pupal case, we were able to access and wound the epithelial monolayer of the dorsal thorax, termed the notum (Figure 3-1A, white box). After wounding and imaging, nearly all wild-type pupae recovered to eclose as adults.

The calcium responses observed after wounding are temporally and spatially complex and somewhat variable[113], making it more difficult to identify underlying mechanisms by comparing wild-type and mutant animals. To circumvent this problem, we exploited the radial symmetry of the calcium response by manipulating gene expression on only one side of the wound, allowing us to assess symmetry in control versus experimental regions. We used the *Gal4/UAS* system to manipulate gene expression in the central region of the notum with *pnr-Gal4* (Figure 3-1A'), and then wounded on the margin between the control and knock-down region, so that half the wound served as an internal control (Figure 3-1B, C). We monitored the symmetry of the calcium responses with a ubiquitously expressed calcium reporter, *ActinP-GCaMP6m*, comparing the experimental (*pnr*) domain with the adjacent internal control. When no other genes are manipulated, the calcium signals remain radially symmetric about the wound (Figure 3-1D).
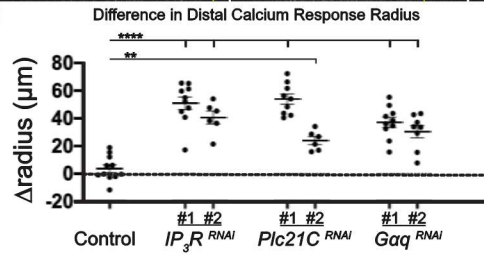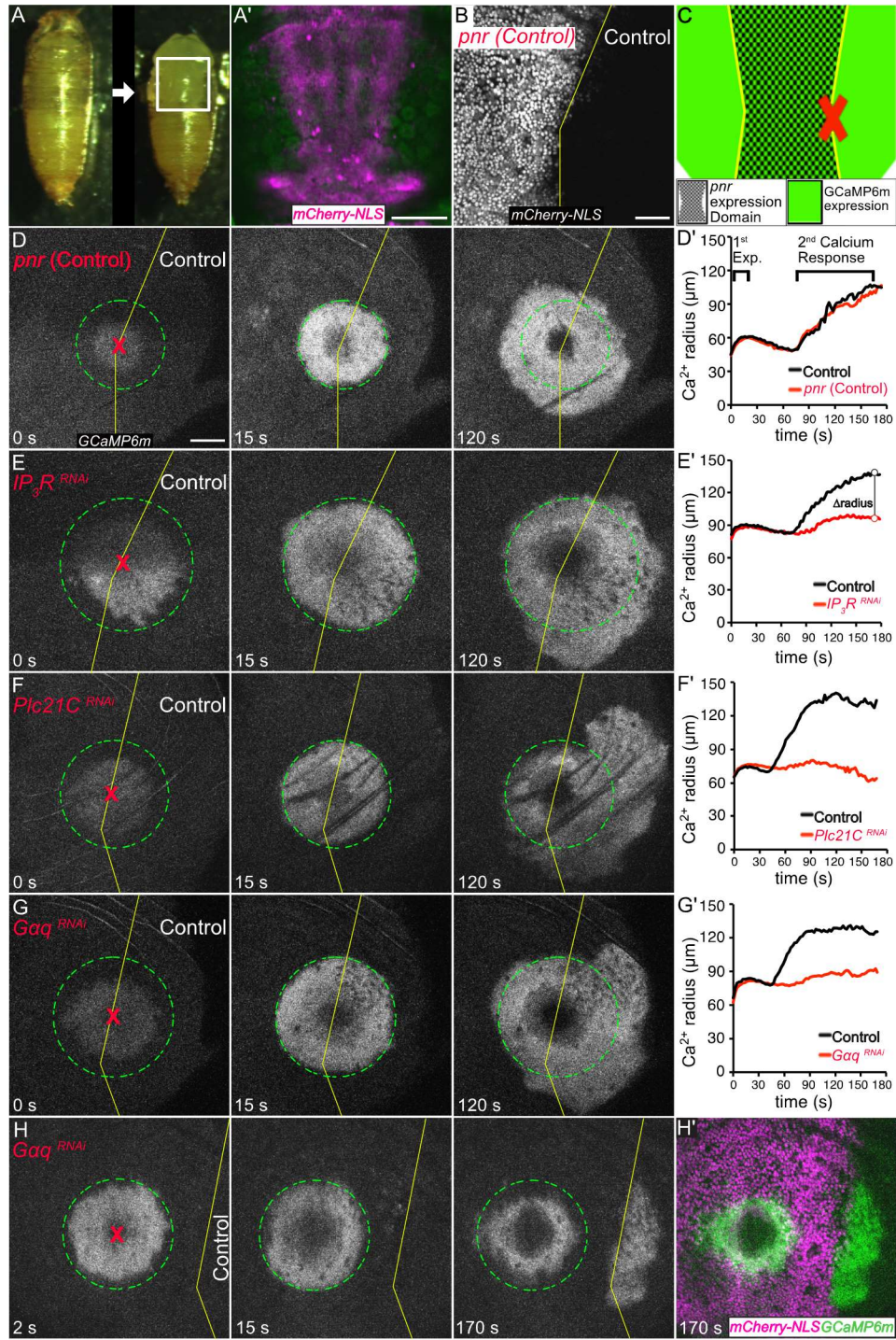
Figure 3-1: Wounds trigger calcium release via the Gq pathway.

(A) Experimental model, *Drosophila* pupa (left) with pupal case removed (right). Gene expression is controlled in the *pnr* domain, as delineated by mCherry-NLS (magenta in A', grayscale in **B**). (**B-C**) wounds (red X) are targeted at the *pnr* boundary (yellow line, **B, C**). (**D-H**) GCaMP6m calcium reporter. (**D, D'**) Calcium response to wounds in the absence of gene knock-down. The max radius of the rapid first calcium expansion is marked by green circle; the distal calcium response begins ~45-75 s after wounding. Analysis of the calcium radius with respect to time (**D'**) demonstrates that the response is symmetric on both sides of the *pnr* boundary. n = 11. (**E–G**) The distal calcium response requires G$_q$-pathway components knocked down on the left side (*pnr* domain) of each panel. *IP3R RNAi #1* n = 10, *IP3R RNAi #2* n = 6, *PLC21C RNAi #1* n = 9, *PLC21C RNAi #1* n = 6, *G□q RNAi #1* n = 10, *G□q RNAi #2* n = 8. (**D'–G'**) Quanti-fication of calcium dynamics for control (black) and *pnr* (red) sides of wounds. (**H**) Wound targeted within the G□q knock-down domain (left of yellow line) yields no distal calcium response until the initiating signal reaches the nearby control domain. (**H'**) Green shows calcium (*GCaMP6m*), magenta shows *pnr* domain where G□q is knocked down. (**I**) Δradius, difference in calcium signal radii at maximum extent of the distal calcium response for control minus *pnr* side of each wound (as shown in E'), with *pnr*-knockdown genotypes indicated; bars = mean ± SEM. Statistical analysis by one-way ANOVA, which included all genotypes from Figure 3-1, Figure 3-2, and Figure 3-3, multiple comparisons WRT control group, **p<0.01, ****p<0.0001. Scale bars = 200 μm (A'), or 50 μm (B–H'). See also: Figure 3-2.

3.3.1 The distal calcium response signals to release calcium via IP3.

We first used this internally controlled system to knock down gap junctions, which we have previously shown to be required for the first calcium expansion[113]. As expected, the first expansion did not occur in the gap junction knockdown region but did in the control region (Figure 3-2A). Importantly, the second distal calcium response still occurred in the gap junction knockdown region, although it appeared "speckled" because each cell transduced the signal independently of its neighbors (Figure 3-2A), as has been reported previously[56,92,113]. This result indicated that the initiation of the distal calcium response requires neither gap junctions nor the first (gap junction-dependent) expansion.
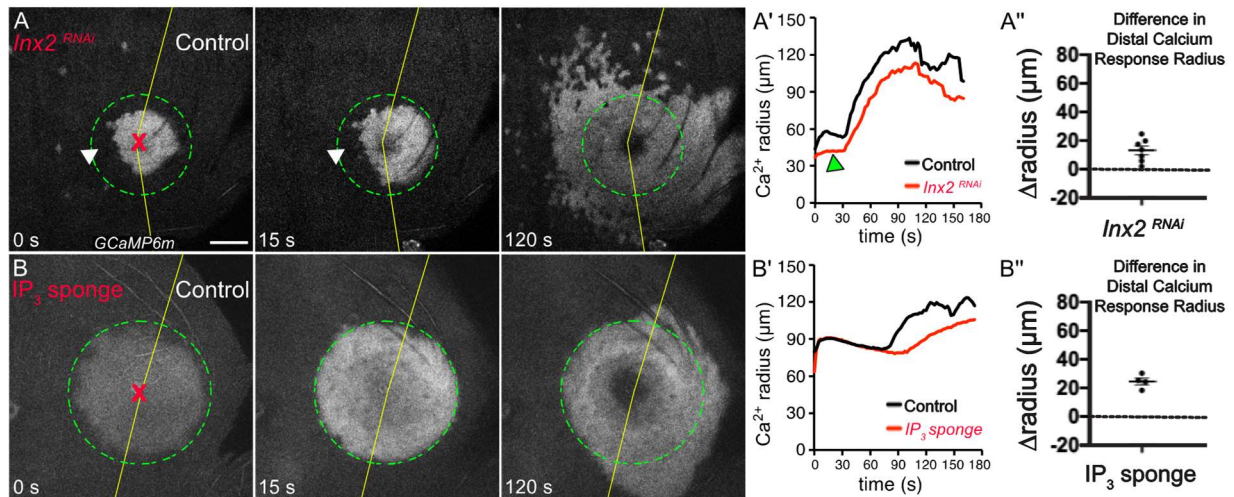
Figure 3-2: Wounds signal calcium to proximal cells through gap junctions and to distal cells through IP₃

(**A-B**) GCaMP6m reporter showing cytosolic calcium in representative samples of various knockdowns in the *Drosophila* notum. Gene manipulations are performed in the *pnr* expression domain (left side) and wounds (red X) are administered at the *pnr* domain boundary (yellow line). Maximum extent of first expansion is marked by dashed green circle. Scale bar = 50 μm. (**A**) Knockdown of gap junctions (*Inx2*[RNAi]) attenuates first calcium expansion (arrowheads) (n = 7); the distal calcium response still occurs in the knockdown domain, but with a "speckled" pattern, as reported previously (Balaji et al., 2017; Restrepo and Basler, 2016; Shannon et al., 2017). Although the *Inx2* knockdown appears to cause a slight reduction in calcium radius (**A'–A''**), the speckled nature of the signal would cause the automated algorithm that identifies the radius to underestimate it. (**B**) Expression of an IP₃ sponge has no effect on the first calcium expansion, but the distal calcium response is delayed (n = 4). (**A''–B''**) Difference in calcium signal radii (Δradius) at maximum extent of the distal calcium response for control minus pnr sides of each wound; pnr-side genotypes indicated. IP₃ sponge was statistically significant (*$p < 0.05$) by one-way ANOVA, which included all genotypes from Figure 3-1, Figure 3-2, and Figure 3-3, multiple comparisons WRT control group from Figure 3-1.

To determine whether the calcium of the distal response was coming from internal stores within the cell, we knocked down IP₃ Receptor (IP₃R), which controls calcium release from the endoplasmic reticulum. Knocking down IP₃R on one side of the wound using our internally-controlled system demonstrated that it is absolutely

required for the distal calcium response (Figure 3-1E). Importantly, the effect was limited to the experimental domain, while the control domain calcium response remained intact. We confirmed this result with two independent RNAi lines and an IP_3 sponge (Figure 3-2B) and concluded that calcium is released from intracellular stores in an IP_3-dependent manner.

The IP_3 signal transduction pathway has been well studied. IP_3 is generated via hydrolysis of phosphatidylinositol 4,5-bisphosphate (PIP2) into IP_3 and diacylglycerol (DAG), a reaction catalyzed by the enzyme phospholipase C beta (PLCβ). To test the role of PLCβ, we knocked it down on one side of the wound and found that PLCβ is required for the distal calcium response (Figure 3-1F). This result was obtained with two independent RNAi lines. As the next step upstream, PLCβ is most commonly activated through the G_q-signaling pathway; activation of a G-protein coupled receptor causes the α-subunit of the G_q-heterotrimer (known as Gαq) to dissociate from its β and γ subunits to activate PLCβ. Indeed, previous literature studying IP_3-mediated calcium responses following injury have also implicated Gαq[28,53]. To test the role of G_q-signaling, we knocked down Gαq on one side of the wound and found that it was also required for the distal calcium response (Figure 3-1G). These results demonstrate that the distal calcium response is transduced via the canonical G_q-signaling pathway.

Importantly, although all of the above experiments used laser wounding, we find that puncture wounds also had two distinct calcium waves: the first occurred immediately and required gap junctions; the second was delayed by tens of seconds and similarly required the G_q pathway. Thus, the mechanisms underlying the two

70

calcium responses appear to be general wound responses, not specific to laser ablation.

Interestingly, a modification of our internally controlled system suggests that wound-induced signals can diffuse in the extracellular space. Rather than wounding on the *pnr* domain border, we wounded in the middle of a *pnr* domain where Gαq was knocked down. As expected, no distal calcium response occurred within the knockdown domain, but the calcium response did jump the gap of knockdown cells to suddenly appear in the even more distal control domain (Figure 3-1H).

To quantify how gene knockdown alters the distal calcium response, we calculated the difference in maximum calcium-signal radius in the control and experimental regions (illustrated in Figure 3-1E'). Each G_q-pathway knockdown significantly inhibited the calcium response (Figure 3-1I). Taken together, the distal calcium response occurs through a G_q-signaling pathway likely activated by a diffusible signal.

3.3.2 The distal calcium response requires the GPCR Mthl10.

The requirement of G_q suggested that the distal calcium response is initiated by a GPCR; however, given previous reports that the TrpM ion channel could alter the intensity of wound-induced calcium responses in the pupal notum[10,28,29], we first knocked down TrpM with either of two previously-used functional RNAi lines. Neither had a discernible effect on the timing or range of the calcium response: the experimental domain remained symmetrical to its internal control (Figure 3-3A, D). Next,

we knocked down candidate GPCRs, prioritizing receptors with known epithelial expression and G_q activity[125]. Previous cell-culture studies have implicated ATP as a ligand activating calcium after wounding[53], and a recent study in mice implicated ADP in intercellular calcium waves following viral infection[126]. We thus knocked down *AdoR*, the only *Drosophila* adenosine receptor, but it had no effect on the calcium response (Figure 3-3B, D). We then knocked down the GPCRs *Tre1* or *TkR86C*, both implicated in wound responses[127,128], but they also had no effect on the calcium response (Figure 3-3D). Strikingly, we were able to completely eliminate the distal calcium responses by knocking down the cytokine-activated GPCR *Methuselah-like 10 (Mthl10)*[129] (Figure 3-3C, D). We confirmed this result with two independent RNAi lines. To test whether *Mthl10* is important for wound recovery, we measured pupal survival after large wounds and found that *Mthl10* knockdown throughout the notum decreased pupal survival by ~30% (Figure 3-3E).
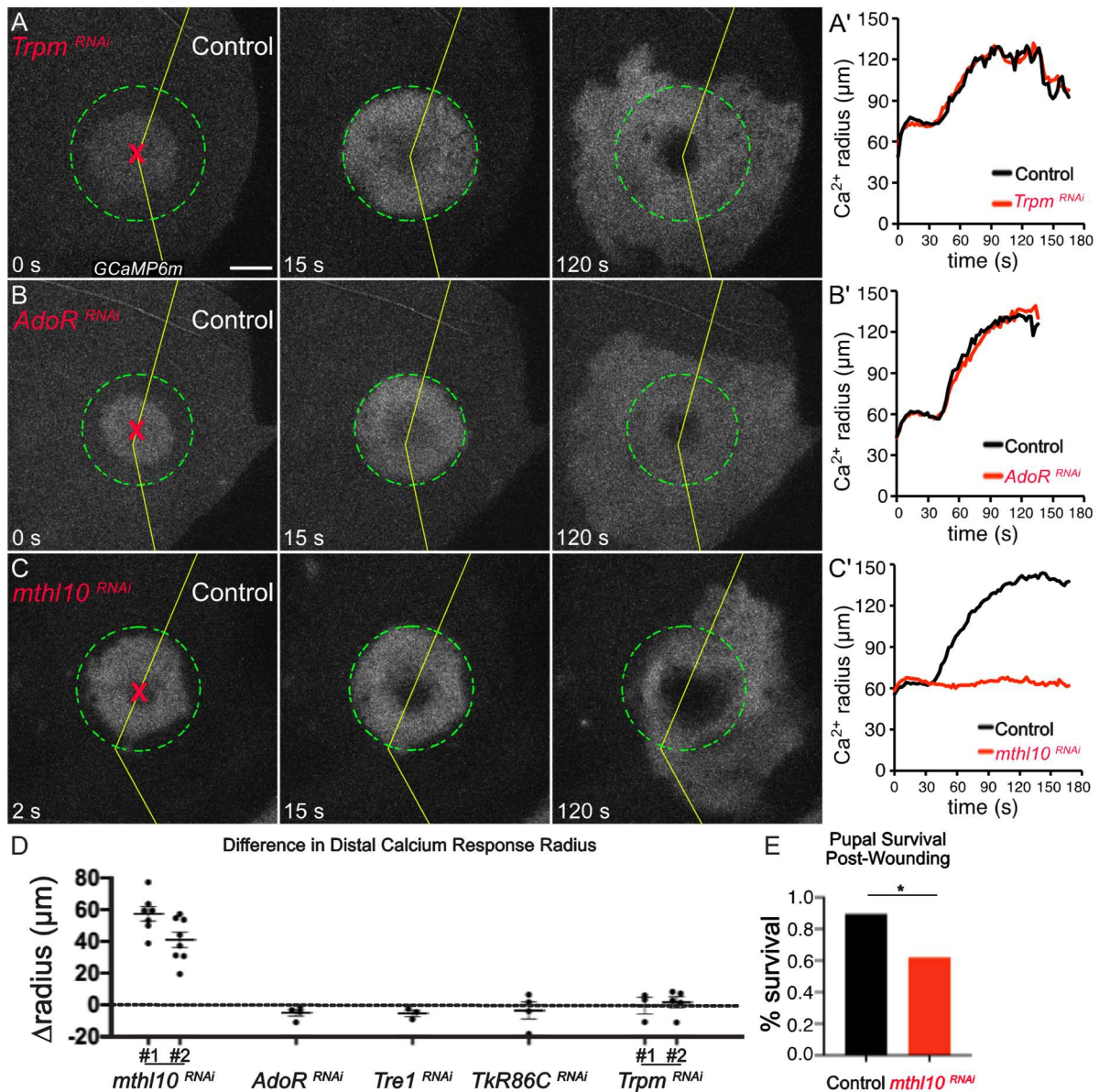
Figure 3-3: The distal calcium response requires the GPCR Methuselah-like 10 (Mthl10).

(**A–C**) GCaMP6m reporter showing cytosolic calcium in representative samples. RNAi of the indicated gene is limited to the *pnr* domain (left side), and wounds (red X) are administered at the *pnr* domain boundary (yellow line). Maximum extent of first expansion is marked by dashed green circle. (**A**) Knockdown of the calcium ion channel *TRPM* has no effect on either calcium response. *TRPM RNAi #1* n = 3, *TRPM RNAi #2* n = 5 (**B**) Knockdown of the GPCR Adenosine Receptor (*AdoR*) has no effect on either calcium response. *AdoR RNAi* n = 4. (**C**) Knockdown of the GPCR *Methuselah-like 10* (*Mthl10*) phenocopies the G_q-pathway knockdowns, with a dramatic decrease in the distal calcium response. *mthl10 RNAi #1* n = 7, *mthl10 RNAi #2* n = 8. (**A'–C'**) Quantification of calcium signal radius versus time in control (black) and *pnr*-expression

(red) sides of each wound. (**D**) Δradius between control and *pnr* sides, with *pnr*-knock-down genotypes indicated; bars = mean ± SEM. *Tre1 RNAi* n = 3, *TkR86C RNAi* n = 4. Both mthl10 RNAi lines were statistically significant (****p<0.0001) by one-way ANOVA, which included all genotypes from Figure 3-1, Figure 3-2, and Figure 3-3, multiple comparisons WRT control group from Figure 3-1. (**E**) Pupal survival to adulthood after large wounds. Quantification by Chi-Square, n=29 each, p=0.0141. Scale bar = 50 μm.

3.3.3 Mthl10 is activated by Gbp1 and Gbp2.

Mthl10 is known to be activated by a class of cytokines known as Growth-blocking peptides (Gbps), of which there are five in *Drosophila*[129,130]. Gbps are synthesized in the *Drosophila* fat body in a latent pro-peptide form, requiring proteolytic cleavage for activation[130–134]. Because Gbps are secreted (and thus not cell-autonomous), the internally controlled knockdown approach expressing an RNAi exclusively in epithelial cells would not be effective at testing their role; we instead needed to test homozygous Gbp knockout pupae. We used CRISPR to generate individual null mutants of *Gbp1* or *Gbp2* (hereafter referred to as Gbp1$^{\Delta}$ and Gbp2$^{3\Delta FS}$, respectively; Figure 3-4A), and obtained the previously generated and homozygous viable strain *Df(2R)Gbp-ex6*7, which has a small chromosomal deletion removing the neighboring genes *Gbp1* and *Gbp2*[135] (hereafter referred to as ΔGbp1,2; Figure 3-4A). Upon wounding these animals, we found the individual null mutants of *Gbp1* or *Gbp2* did not appear to have an altered calcium response compared to control (Figure 3-4B–D). However, the ΔGbp1,2 pupae lacked a normal distal calcium response in 13 out of 14 pupae (Figure 3-4E).

Because this method does not have an internal control, we analyzed the spatiotemporal dynamics of the distal calcium responses using the following metrics: (1) its relative spatial extent via $(R_{Max} - R_{1st})/R_{1st}$, where R_{Max} is the maximum calcium-

signal radius and R_{1st} is the radius of the first expansion (illustrated in Figure 3-4B'),

which provides normalization for wound size (Figure 3-4G); (2) its duration via the time

over which the calcium-signal radius remained greater than R_{1st} (Figure 3-4H); and (3)

its start time (Figure 3-4I). The spatial quantification showed that $\Delta Gbp1,2$ significantly

reduces the radius of the distal calcium response. The vast majority of $\Delta Gbp1,2$

samples actually had values at or near zero because there was no distal expansion. On

the other hand, the individual null mutants had robust distal expansions that were not

significantly different from controls (Figure 3-4G). We obtained similar results for

quantification of the distal calcium response duration: $\Delta Gbp1,2$ signal duration was

significantly reduced compared to control (Figure 3-4H), whereas that of the individual

nulls was either unchanged ($Gbp1^{\Delta}$) or even increased ($Gbp2^{3\Delta FS}$). In those samples for

which there was a distal calcium response, none of the nulls showed a significant

difference in the response start time (Figure 3-4I).

Taken together, this data shows that the absence of both *Gbp1* and *Gbp2*

significantly decreases the response radius and duration, while that of *Gbp1* or *Gbp2*

alone does not. Each extracellular ligand, Gbp1 or Gbp2, is independently sufficient to

relay wound information to surrounding cells.

A. Diagram showing Wild Type, $Gbp1^{\Delta}$, $Gbp2^{3\Delta FS}$, and $\Delta Gbp1,2$ gene structures with Active Gbp1 and Active Gbp2 regions labeled. Scale bar 250 bp.

B. Control, GCaMP6m, at 2 s, 15 s, 120 s.

B'. Graph of Ca^{2+} radius (µm) vs time (s) for Control, with R_{1st} and R_{Max} labeled.

C. $Gbp1^{\Delta}$ at 2 s, 15 s, 120 s.

C'. Graph of Ca^{2+} radius (µm) vs time (s) for $Gbp1^{\Delta}$.

D. $Gbp2^{3\Delta FS}$ at 2 s, 15 s, 120 s.

D'. Graph of Ca^{2+} radius (µm) vs time (s) for $Gbp2^{3\Delta FS}$.

E. $\Delta Gbp1,2$ at 2 s, 15 s, 120 s.

E'. Graph of Ca^{2+} radius (µm) vs time (s) for $\Delta Gbp1,2$.

G. Radius: $(R_{Max} - R_{1st}) / R_{1st}$ for Control, $Gbp1^{\Delta}$, $Gbp2^{3\Delta FS}$, $\Delta Gbp1,2$. **

H. Duration: time (s) for Control, $Gbp1^{\Delta}$, $Gbp2^{3\Delta FS}$, $\Delta Gbp1,2$. **, ***

I. Start Time: time (s) for Control, $Gbp1^{\Delta}$, $Gbp2^{3\Delta FS}$, $\Delta Gbp1,2$.

Figure 3-4: The distal calcium response requires either Gbp1 or Gbp2.

(**A**) Schematic showing the genomic region for *Gbp1* and *Gbp2*, the deletion $\Delta Gbp1,2$, and the *Gbp1* or *Gbp2* null mutants generated for this study (transcription proceeds from left to right). The $Gbp1^{\Delta}$ deletion allele is missing 282 bases within the coding region of *Gbp1*, removing most of the region encoding the Gbp1 active peptide (blue). The complex $Gbp2^{3\Delta FS}$ allele comprises 8 point mutations (asterisks) and 3 deletions, inducing frameshifts and premature terminations upstream of the Gbp2 active peptide (blue) (see Methods). (**B–E**) GCaMP6m reporter showing cytosolic calcium in representative samples of control or deletion mutants. Scale bar = 50 µm. (**B, B'**) The normal calcium response is present in controls (n = 9). (**C-D**) Homozygous $Gbp1^{\Delta}$ (**C**) or $Gbp2^{3\Delta FS}$ (**D**) each retain the distal calcium response (n = 14 and 11 respectively). (**E,E'**) A normal distal calcium response is absent after wounding homozygous $\Delta Gbp1,2$ in n=13/14. (**G**) Spatial quantification of each sample's maximum radius (R_{Max} in **B'**) normalized to its first expansion maximum radius (R_{1st} in **B'**). $\Delta Gbp1,2$ has a significantly decreased response compared to control, while the $Gbp1^{\Delta}$ and $Gbp2^{3\Delta FS}$ do not. (**H**) Duration that distal calcium response radius exceeded R_{1st}. $\Delta Gbp1,2$ has a significantly decreased duration compared to control, while surprisingly, $Gbp2^{3\Delta FS}$ was significantly increased. Movies cut off before the distal calcium response dipped below R_{1st} were excluded from **H**. (**I**) The start time, defined as the time when the calcium radius began consistently increasing for the distal calcium response, shows no significant differences. Samples where $R_{Max} = R_{1st}$ were excluded from **I**. Statistical analysis by one-way ANOVA, multiple comparisons WRT control group, **$p<0.01$, ***$p<0.001$.

If Gbps are wound-induced signals that direct cells to increase calcium, then ectopic Gbp would be expected to activate a calcium response, even without a wound. Unfortunately, the pupal notum is protected by an impermeable cuticle that makes it impossible to add Gbp directly to the tissue, and it cannot be removed without wounding. We thus turned to larval wing discs, sacs of epithelial tissue that have no cuticle. We applied synthetic active-form Gbp peptides directly to wing discs *ex vivo* at varying concentrations. Excitingly, we found that both Gbp1 and Gbp2 elicited a strong calcium response in wing discs when added *ex vivo* at 5 nM or 50 nM, respectively (Figure 3-5A, B). To test whether these responses were Mthl10-dependent, we mounted one control and one *Mthl10* knockdown disc side-by-side in a media bubble and added

Gbp peptide to both discs simultaneously. As expected, the calcium responses were absent from the *Mthl10* knockdown discs (Figure 3-5C, D). Finally, we asked whether the three other Gbps could elicit calcium in wing discs and found that Gbp4 and Gbp5 could elicit calcium consistently at 50 nM (and Gbp4 occasionally even at 5 nM), while Gbp3 was not effective, even at 50 µM, the maximum concentration tested (Figure 3-6). Despite the activity of these other Gbps *ex vivo*, the loss of the distal calcium response in the Δ*Gbp1,2* pupae indicates Gbp1 and Gbp2 are responsible for the calcium increase in the pupal notum.

A Gbp1

B Gbp2

Calcium imaging with GCaMP6m

C Control — + 5 nM Gbp1 — mthl10^{RNAi} — 0 s / 120 s

C' Gbp1

D Control — + 50 nM Gbp2 — mthl10^{RNAi} — 0 s / 120 s

D' Gbp2

E Gbp1 Gbp2

F Control — + Fly Extract — mthl10^{RNAi} — 0 s / 180 s

F' Fly Extract

G Control — + Larval Extract — mthl10^{RNAi} — 0 s / 180 s

G' Larval Extract

H Fly Extract Larval Extract
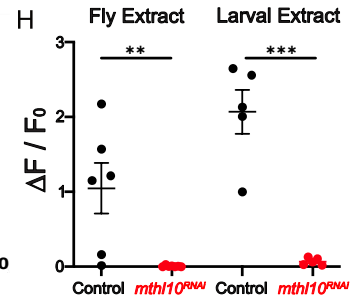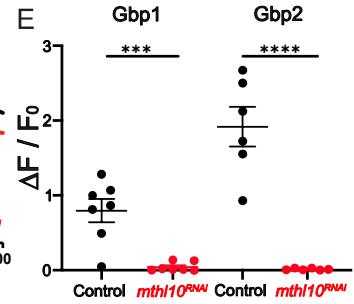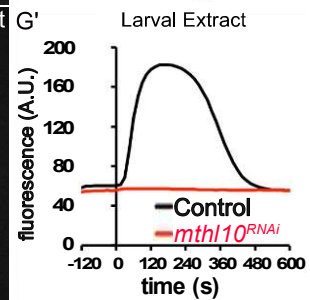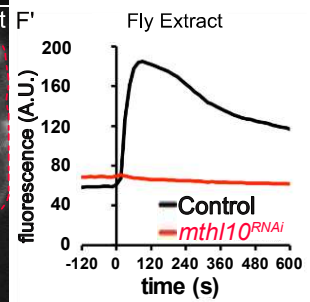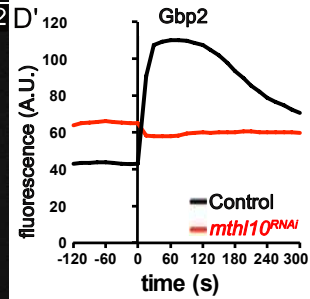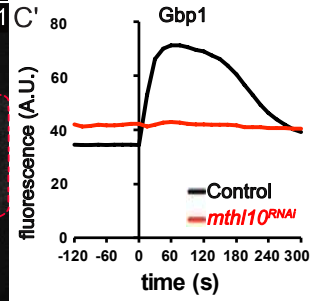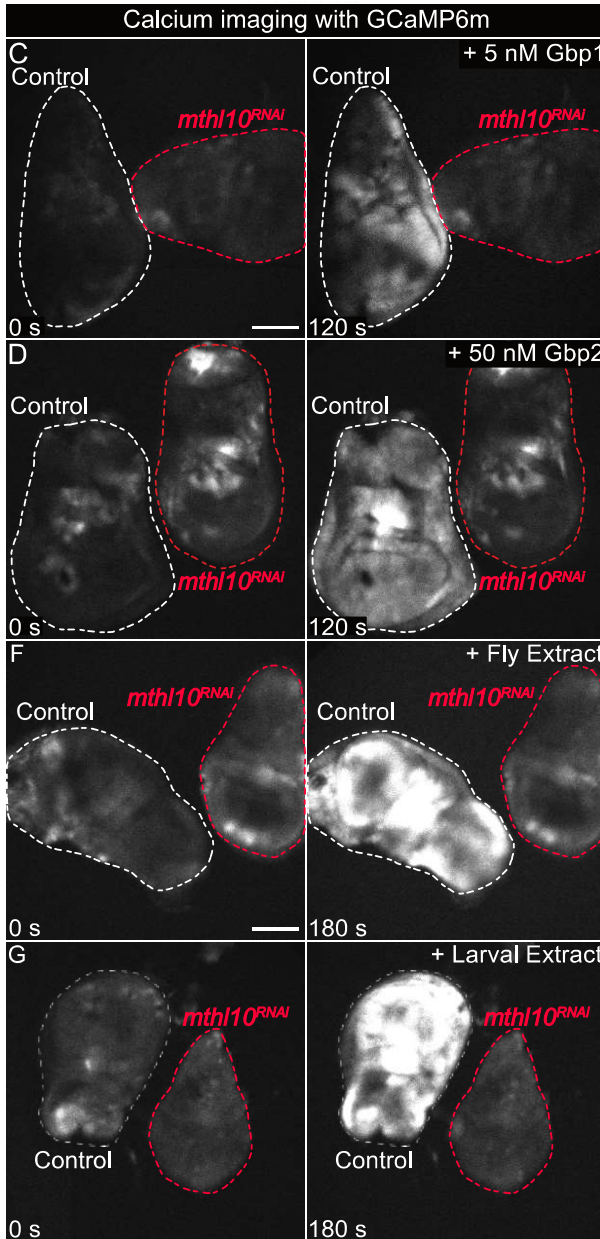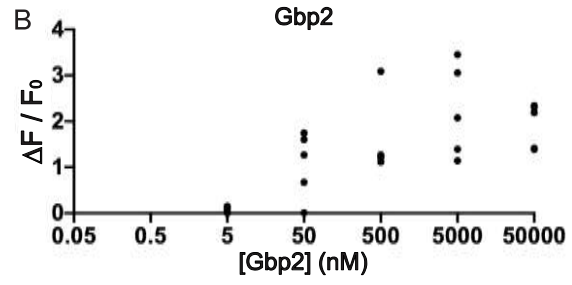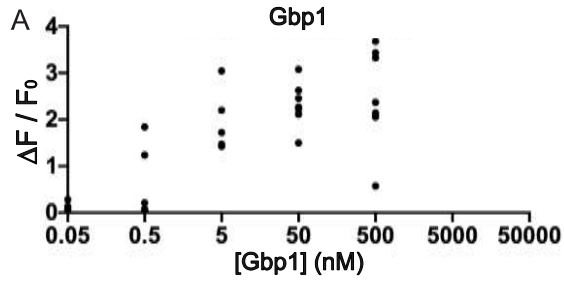
Figure 3-5: Gbp peptides and Drosophila extracts elicit calcium responses in wing discs through Mthl10.

(**A-B**) Gbp1 or Gbp2 peptides elicit a concentration-dependent calcium response in wing discs. Gbp1 additions n = 29, Gbp2 additions n = 21. 5 nM Gbp1 or 50 nM Gbp2 consistently elicits a calcium response. (**C-D, F-G**) Assays were performed with two wing discs (one control and one *mthl10* knockdown) mounted adjacently and activated simultaneously. *Mthl10* is required in wing discs for Gbp1 (**C**, n = 7) or Gbp2 (**D**, n = 6) to activate a calcium response. Change in GCaMP6m fluorescence over time for samples **C** and **D** is quantified in **C'** and **D'**, respectively. (**E**) Normalized change in fluorescence is quantified for all samples. (**F-G**) *Mthl10* is required in wing discs for 5% fly extract (**F**, n = 6) or 5% larval extract (**G**, n = 5) to activate a calcium response. Change in GCaMP6m fluorescence over time for samples **F** and **G** is quantified in **F'** and **G'**, respectively. (**H**) Normalized change in fluorescence is quantified for all samples in **F'** and **G'**. Scale bar = 100 μm. Graph bars represent mean and SEM. **p<0.01, ***p<0.001, ****p<0.0001 by Student's t-test. See also: Figure 3-6.
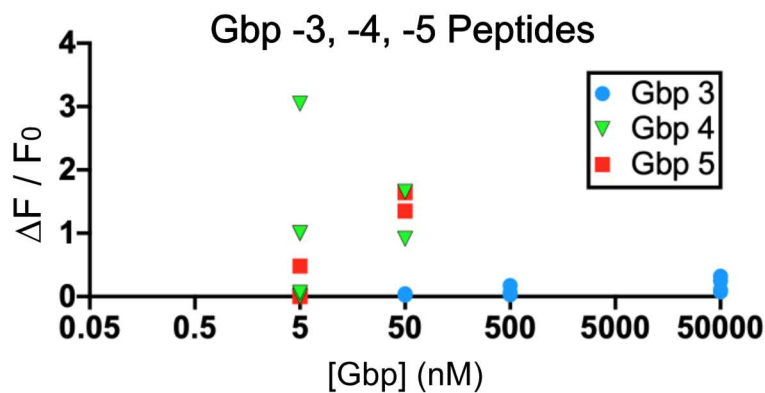
Figure 3-6: Gbps 4 and 5 are also sufficient to elicit calcium responses in wing discs.

Change in GCaMP6m calcium fluorescence when a given concentration of Gbp -3 (n = 15), -4 (n = 7), or -5 (n = 7) peptides is added to *Drosophila* wing imaginal discs. Even at 50 μM, Gbp3 (blue circle) does not elicit a calcium response. Gbp4 (green triangle) elicits an inconsistent response at 5 nM, and consistently when added at 50 nM. Gbp5 peptide elicits a calcium response at 50 nM.

3.3.4 Gbps and Mthl10 are required for calcium waves in wing discs.

Previous studies have shown that wing discs cultured *ex vivo* displayed potent calcium responses upon exposure to fly extract[56,92,124]. Because fly extract is created by lysing and homogenizing whole flies, we hypothesized that it contained wound-induced

signals that activate wound-detection pathways in wing discs to initiate calcium responses. Indeed, we observed the calcium response was *mthl10*-dependent by adding fly extract to control and *mthl10* knockdown wing discs simultaneously (Figure 3-5F, H). Since extract of adult flies is predicted to contain both Gbp4 and Gbp5, which may be confounding variables, we also tested extract made from larvae, a stage that expresses only Gpb1-3[130]; like adult extract, wild-type larval extract activated calcium responses in wing discs in an *mthl10*-dependent manner (Figure 3-5G, H). This shows that, in addition to the distal calcium response following wounding, Mthl10 mediates the lysate-induced calcium response in wing discs.

To determine whether the calcium-activating signal in the extract is Gbp, we added extract made from either wild-type or homozygous $\Delta Gbp1,2$ larvae to either control or homozygous $\Delta Gpb1,2$ wing discs (Figure 3-7A, B). We found that no calcium response occurs when Gbps are absent from both disc and extract (Figure 3-7B, C), demonstrating that the calcium response to larval extract does indeed require Gbp1 and/or Gbp2. Surprisingly, as long as Gbp was present in either the extract or the disc, the extract was able to elicit a calcium response. (Figure 3-7A-C). The former result is expected: extract made from wild-type larvae contains Gbp, which elicits calcium when applied to wing discs. The latter result is less intuitive and suggests that the wing discs themselves maintain a local supply of Gbp that can be activated by larval extract. If the discs already have Gbp, then what does the extract provide to activate calcium? This result suggested that proteases in the extract are necessary to cleave latent pro-Gbp from the disc to elicit the calcium response.
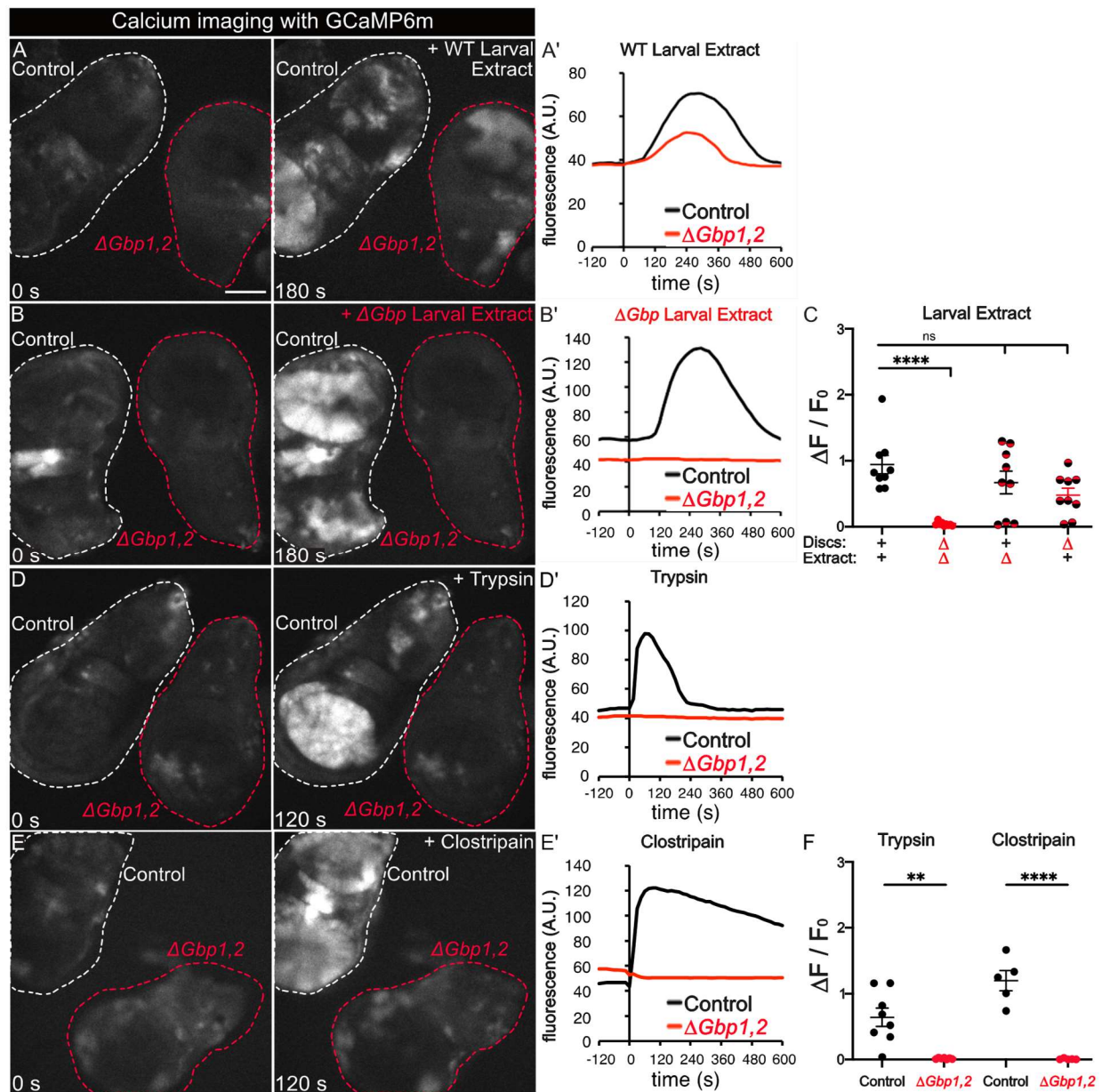
Figure 3-7: Drosophila extract and proteases require Gbps to elicit calcium responses.

(**A-F**) All assays were performed with two wing discs (one control and one Δ*Gbp1,2*) mounted adjacently and activated simultaneously. Scale bar = 100 μm. (**A-C**) Gbp is required for the larval extract-mediated calcium response, as no response occurs if Gbp is absent from both extract and wing disc (**A, A'**, n = 9). The signal can be supplied by either the wing disc (**A, A'**) or by the larval extract (**B, B'**, n = 9). Normalized change in fluorescence is quantified in **C**. (**D-F**) Serine protease trypsin (**D**, n = 8) or cysteine protease clostripain (**E**, n = 5) activate calcium in a Gbp-dependent manner. Normalized change in fluorescence is quantified in **F**. Graph bars represent mean and SEM. **p<0.01, ****p<0.0001 by two-way ANOVA in **C** and Student's t-test in **F**.

3.3.5 Gbps are activated by multiple proteases.

Bioinformatics analysis predicted that both pro-Gbp1 and pro-Gbp2 could release their active C-terminal peptides after cleavage by several unrelated proteases[136]. To confirm the activity of proteases in the lysate, we tried to inhibit them using broad-spectrum protease inhibitors, singly and in combination. Unfortunately, the inhibitors or the vehicle (DMSO) alone at high enough concentrations could themselves induce calcium responses in wing discs, stymieing our ability to use inhibitors in this experiment. As an alternative approach, we noted that the serine protease trypsin and the cysteine protease clostripain are both predicted to cleave Gbp1[136]. To test their ability to activate calcium in wing discs, we added trypsin or clostripain to wing discs and found that each was sufficient to elicit a calcium response in control but not ΔGbp1,2 wing discs (Figure 3-7D-F). Given that cell lysis is known to release multiple active proteases, our data suggest a model in which wound detection in the *Drosophila* notum depends on latent pro-Gbps in the extracellular space, acting as protease detectors, reporting the presence of wound-induced cell lysis via Mthl10 signaling.

3.3.6 Enzymatic generation of a diffusible signal explains wound-size dependence

This protease/Gbp/Mthl10 model is substantially more complex than the delayed-diffusion model of an unknown signal we presented previously[113]. That initial model was based on instantaneous release and diffusive spread of a single, unknown wound-induced signal. Although it lacked mechanistic detail, the prior model fit the data well and provided a useful parameterization of response dynamics: a total amount of signal released compared to its detection threshold (M/C_{th}), a back-propagated time delay $t_{0,min}$

at which calcium signals first become apparent, and an effective diffusion constant α_{eff} describing the rate at which signal spreads distally. A close look at these fitted parameters shows that the time delay and effective diffusion constant have definite trends with wound size (Figure 3-8F,F'; n = 26 wounds with diameters > 15 μm).

The delayed-diffusion model can describe these trends, but the description does not provide explanatory power. We find that α_{eff} increases linearly with wound diameter w: α_{eff} = (0.77 ± 0.26 μm/s) w - (8 ± 11 μm^2/s), whereas the trend for $t_{0,min}$ is better described by a linear dependence on $1/w$: $t_{0,min}$ = (1500 ± 700 μm s) w^{-1} + (12 ± 19 s).

The coefficients of the w or $1/w$ term are non-zero (with p-values of 0.006 and 0.04, respectively). Although one can postulate explanatory hypotheses, the delayed-diffusion model itself provides no reason for the wound-size dependence of the response dynamics. We thus wanted to explore whether the observed trends would fall out naturally from a more detailed model based on the protease/Gbp mechanism.

To do so, we constructed a computational reaction-diffusion model as outlined in Figure 3-8A, A'. In brief, wound-induced cell lysis releases proteases that enzymatically cleave extracellular pro-Gbps into their active forms, which then reversibly bind Mthl10 receptors. This abstraction treats all classes of proteases as a single pool of temporally and spatially varying protease activity. It also pools all Gbp family members, but does keep track of pro- and active forms. Because Mthl10 is membrane bound, and pro-Gbp2 physically interacts with collagen IV[137], both species are treated as stationary in the model, but released proteases and active Gbps are allowed to diffuse. The model is solved over time and a 2D radially symmetric space for six species – protease, free active Gbp, and receptor-bound Gbp (Figure 3-8B), as well as pro-Gbp, protease::pro-

Gbp complex and free receptor. Signaling downstream of the receptor is approximated as a threshold event that releases calcium from intracellular stores when a given fraction of receptors are bound by ligand (Figure 3-8C, dashed line). For complete mathematical details, see Section 3.5: Reaction-diffusion model of the distal calcium response.
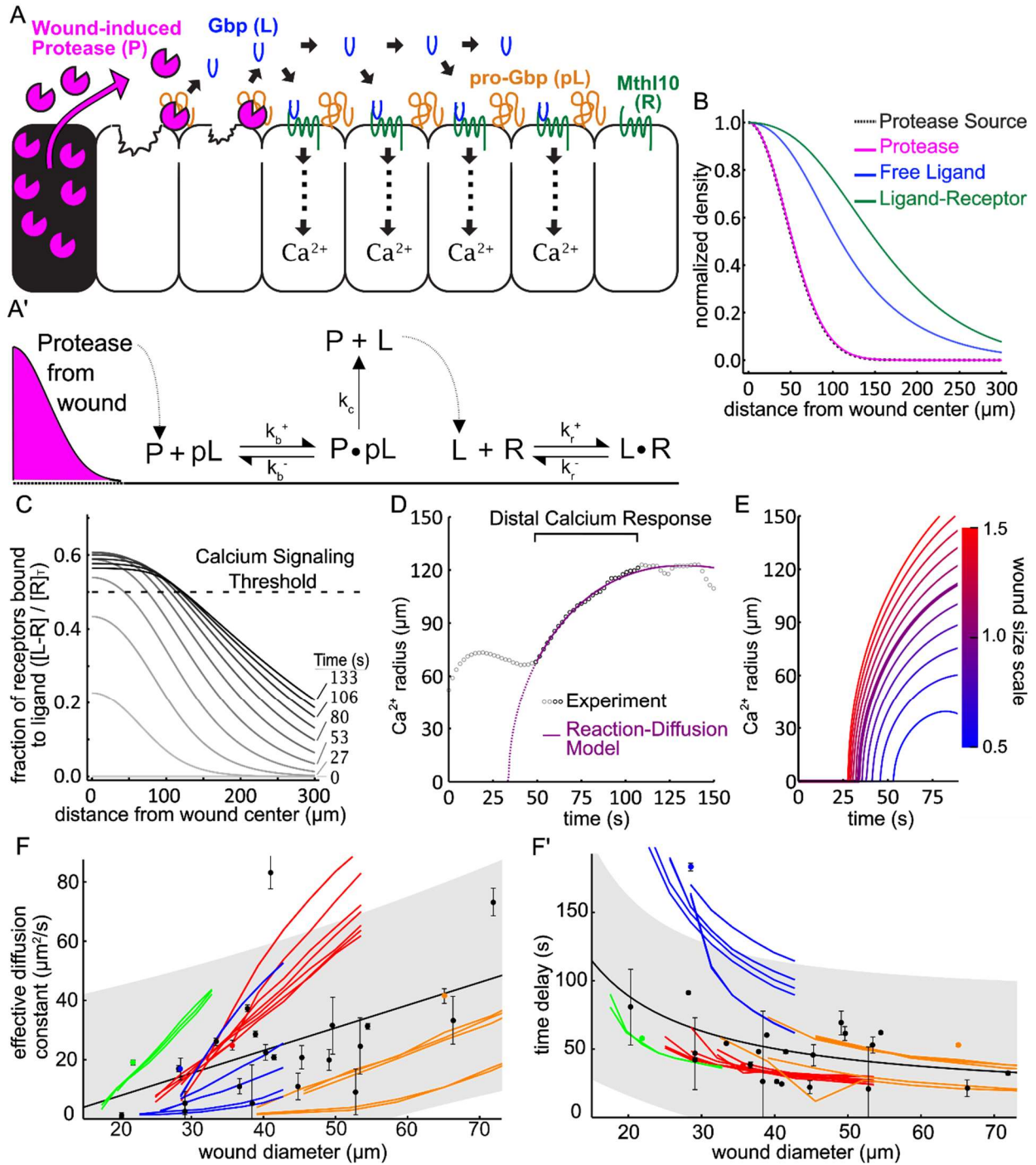
Figure 3-8: Reaction-diffusion (RD) model for epithelial wound detection.

(**A, A'**) Model schematic and reactions. Diffusible proteases (P) released from lysed and damaged cells cleave immobile pro-ligand (pL), releasing diffusible, activated ligand (L) that binds to its cognate cell-surface receptor (R). (**B**) RD model output of concentration of protease (pink line), free ligand (blue line), and ligand-receptor complex (green line) as a function of distance from the wound center 1 minute after wounding. Each line is

normalized by the component's maximum concentration over all space 1 minute after wounding. The spatial extent of the protease source (black dashed line) is normalized so that its maximum is 1. (**C**) Representative model output for the fraction of receptors bound to ligand as a function of distance from the wound at various times. Threshold for triggering calcium response is taken as 0.5 (dashed line). (**D**) Calcium signal radius versus time after wounding: experimental data (open circles), and RD model fit (purple line). (**E**) Calcium signal radius from the RD model for different simulated wound sizes; each line represents the impact of scaling the wound size for an otherwise fixed set of RD parameters determined from the best fit to an individual wound response. The bold line corresponds to a scale of 1.0 and matches the best fit line in panel D. **(F-F')** Experimental and modeled wound size dependence of the effective diffusion (F) and start time (F') of the distal calcium response. Experimental data (black dots) are taken from n = 26 wounds larger than 15 µm in diameter. Black line and shaded region indicate the best fit curve and single prediction 95% confidence interval respectively for a linear fit (F) and hyperbolic fit (F') to the data. Model results (colored lines) are determined by scaling the wound size from a best fit parameter set and then parameterizing the model outputs according to a delayed-diffusion model. Each color represents a fit to the same dataset (as in Figure 3-9 and Figure 3-10), and each line corresponds to a different best fit parameter set. See also: Figure 3-9, Figure 3-10, and Figure 3-12.

As constructed, this model has nine free parameters including protease release characteristics, initial component concentrations, diffusion constants, and reaction rates (see Section 3.5.5.2 and Figure 3-12). Given that experimental response dynamics are adequately fit by a simpler model using just three parameters, one should not expect fits of the more detailed model to place strong constraints on all parameters. Instead, the detailed model falls into the category of "soft" or "sloppy" behavior common in systems biology[138]: parameters are weakly constrained, often varying over orders of magnitude, but predictions of model output are nonetheless robust and useful. In an attempt to provide stronger parameter constraints, we did try simultaneous fitting of multiple experimental data sets using a set of nine shared parameter values. Such fits did not describe the data well (Figure 3-9A). As a second attempt, recognizing that wound size varied among experiments, we also tried simultaneous, multiple-data-set fits using

seven shared biochemical parameter values and two experiment-specific wound parameters; however, this additional flexibility was still insufficient (Figure 3-9B). We thus proceeded with fits of the full nine-parameter model to individual data sets and used the resulting parameter sets as the basis for comparing further model predictions with experimental data.
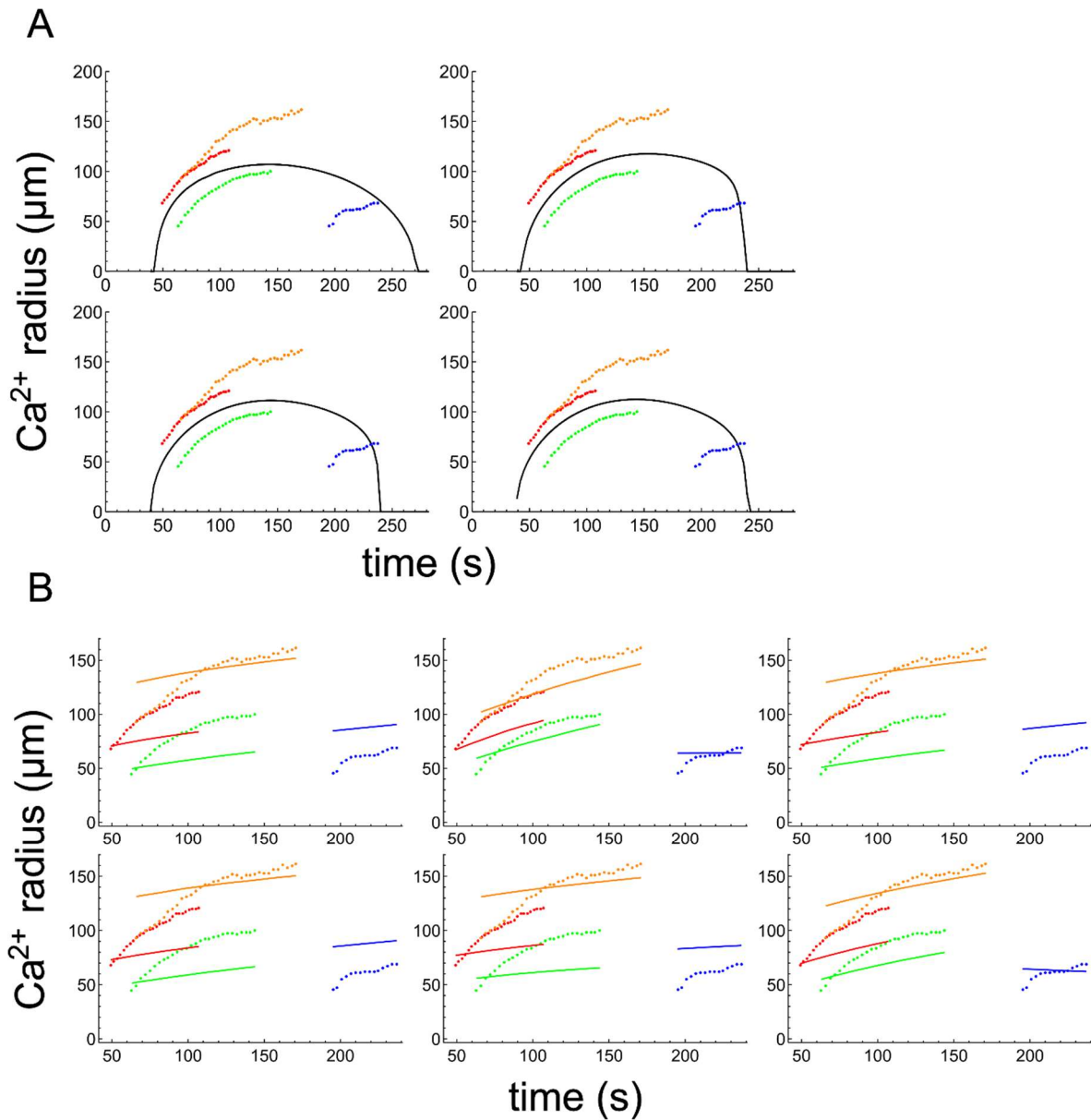
Figure 3-9: Results of simultaneously fitting the reaction-diffusion model to four selected experimental samples.

(**A**) Four results of running the fitting process trying to minimize the cost function for all data sets simultaneously with a single parameter set. Model output is given by the black line, and distal calcium response data (colored points) are color coded based on the colors in Figure 3-10. (**B**) Six results of running the fitting process trying to minimize the cost function for all data sets simultaneously with a single base parameter set that is scaled according to the wound size of each distal calcium response (See Section 3.5.11 for specifics on scaling parameters based on wound size). Model output (lines) and distal calcium response data (points) are color coded based on the colors in Figure 3-10. Colored lines correspond to model output given the wound size of the same colored distal calcium response data points.

We selected four typical distal calcium responses and fit each calcium signal radius versus time to the reaction-diffusion model using a constrained least-squares approach (see Section 3.5.10). For each experimental response, we conducted 32 fits with different randomly selected sets of initial parameter guesses. We used the single best fit to estimate the variance and kept all fits for which the chi-squared statistic indicated an equivalently good fit at the 95% confidence level (3-7 fits for each experiment). A single experimental response and model fit are shown in Figure 3-8D, and a full grid of all good fits is shown in Figure 3-10A. As expected for a "soft" model, the superset of parameter estimates from all good fits yields distributions for individual parameters that vary by orders of magnitude (Figure 3-10B).

A

B
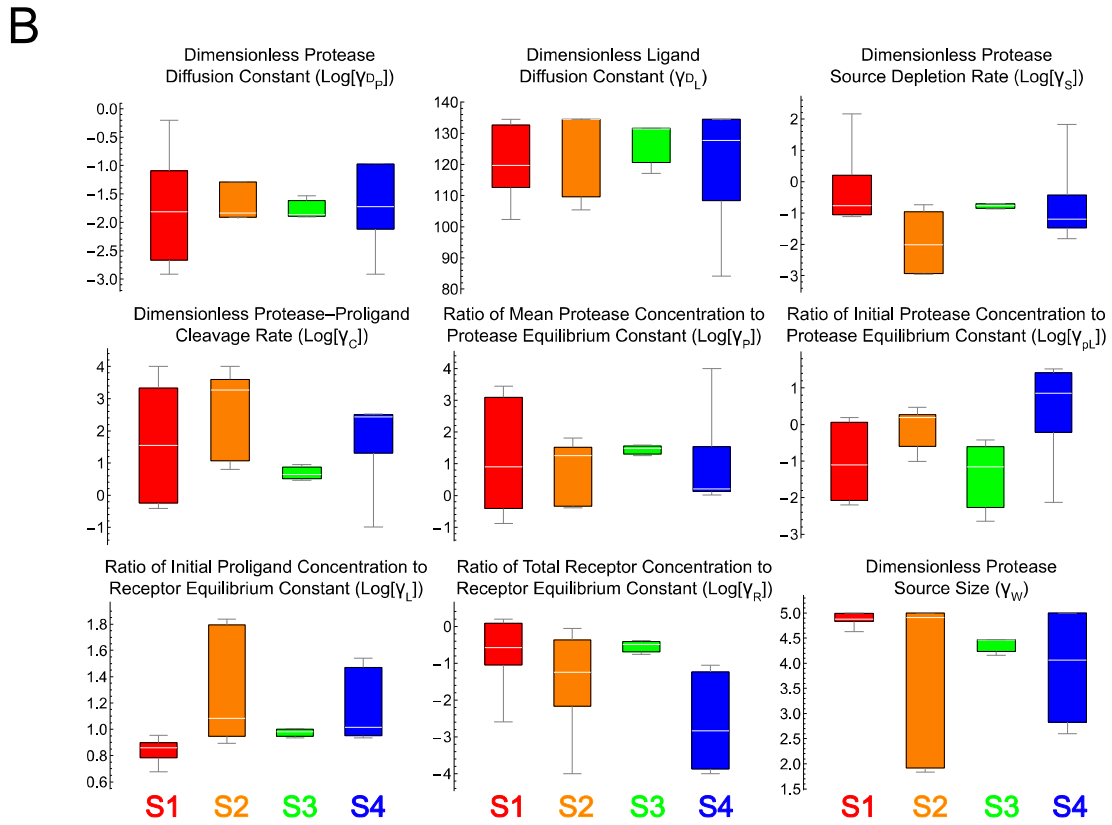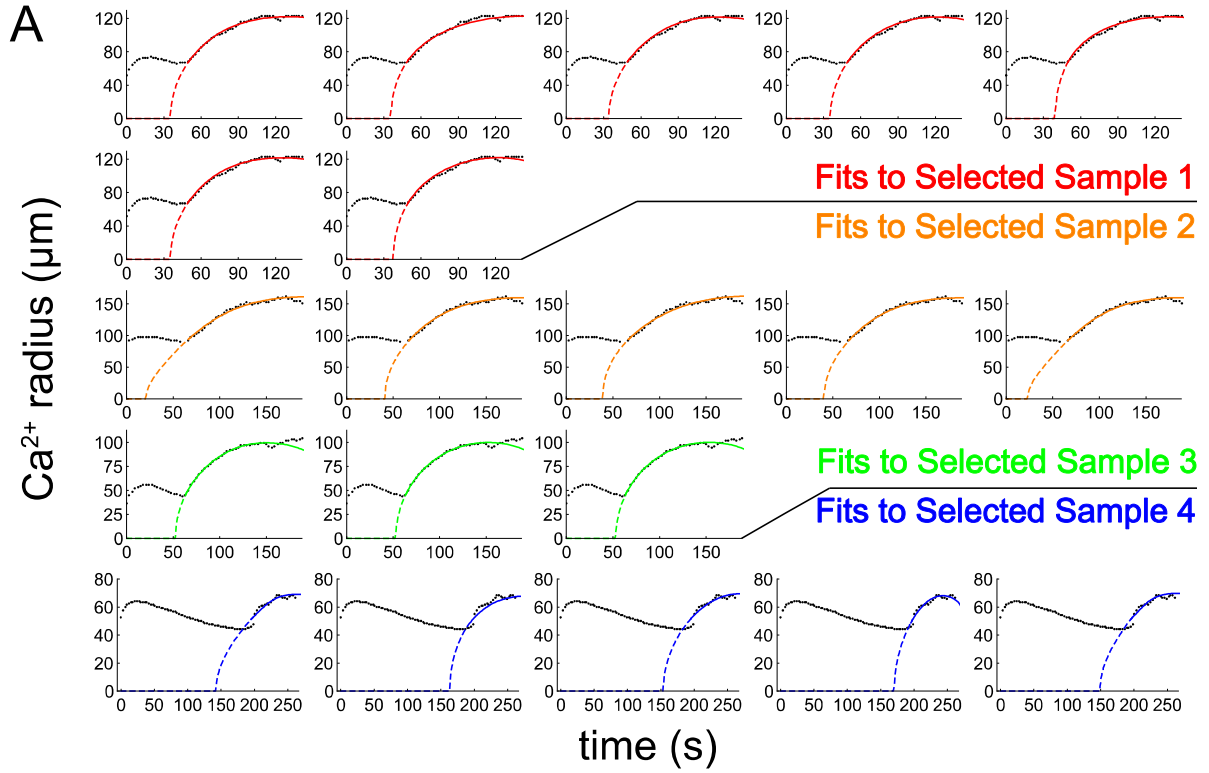
Figure 3-10: Results of fitting the reaction-diffusion model to four selected experimental samples.

(**A**) Calcium signal radius versus time after wounding: experimental data (black circles), and RD model fits (colored lines). Each graph is a different best RD model fit to the distal calcium response data. (**B**) Box and whisker plots of best fit parameters to each selected distal calcium response. Parameters are defined further in the Supplemental Text. Colors correspond to the colors in A. Note that some of the plots correspond to the logarithm of the parameters to emphasize spreads across orders of magnitude.

Despite these variations among best-fit parameters, the model makes robust predictions for its output's dependence on wound size. For each set of best fit parameters (a set being a group of nine parameters that yield a good fit), we solved the model with all parameters fixed, save two that scale with wound size: the $1/e^2$ radius of the protease source, which scales linearly with wound radius; and the total amount of protease activity released, which scales as wound radius squared. With these two parameters scaled in this manner, the peak density of the protease source (activity released per unit area) is held constant. As the example in Figure 3-8E shows, increasing wound size in the model yields smaller time delays and more rapid diffusion-like signal spread. To better compare to experimental trends, we parameterized the detailed model output in the same way as experimental data, i.e., by fitting its calcium signal radius versus time to the three-parameter delayed-diffusion model. The resulting wound-size dependencies fall out as two natural predictions of the detailed model. First, the parameterization shows that the effective diffusion constant in the detailed model output increases with wound size around every one of the widely varying best-fit parameter sets (each colored line in Figure 3-8F). Although individual curves flatten out as α approaches zero, the trends are mostly linear and the slopes are comparable or greater than the trend observed across all experiments. Second, the parameterization

shows that the signaling time delay in the detailed model varies in a roughly hyperbolic manner with wound size. These predicted trends are also similar to experiments (Figure 3-8F').

Within the detailed model, the wound-size-dependence for the time delay and spread rate of the distal response can be traced to a generalized mechanism with two key structural features. First, the signal (i.e., active Gbp) builds up gradually over time. Second, the signal diffuses rapidly enough during this build up to spread well beyond the spatial extent of its source. The first feature by itself provides both a time delay associated with reaching threshold and a diffusion-like spread associated with the threshold boundary moving further from the wound as signal builds; however, it does not yield a wound-size dependence. Even though smaller wounds produce smaller amounts of protease activity and thus smaller integrated signals, they do so over smaller areas to yield the same signal density as larger wounds. The second key structural feature, relatively rapid diffusional spread, ensures that signals from small or large wounds are spread over comparable areas, decreasing the signal density for smaller wounds, increasing it for larger wounds. This signal density difference yields the observed wound-size dependence for α and $t_{0,min}$.

Using the computational model, we are able to recapitulate key features of the calcium response. For example, we modeled the same parameters in a control vs a 70% reduction in Mthl10 levels (Figure 3-11A) and found this matches the observed response in our internally-controlled system where Mthl10 is knocked down on one side of the wound while an internal control is maintained (Figure 3-11B). We also modelled variations of extracellular pro-Gbp levels and found that, for the best-fit parameter sets,

decreasing pro-Gbp levels are predicted to decrease the spatial extent and duration of the calcium response (four model output examples shown in Figure 3-11C). In experiments, we observed similarly modified responses in the double null $\Delta Gbp1,2$, but not in the individual null mutants of *Gbp1* or *Gbp2* (Figure 3-4). Since the Gbp reduction in individual nulls was perhaps insufficient to measurably alter the calcium response, we revisited this experiment using trans-heterozygotes of the $\Delta Gbp1,2$ deletion and one of the individual null mutant alleles (*Gbp1*$^{\Delta}$ or *Gbp2*$^{3\Delta FS}$). The resultant pupae expressed only one allele of *Gbp1* and were null for Gbp2 $(\Delta Gbp1,2/ Gbp2^{3\Delta FS})$ or expressed one allele of *Gbp2* and were null for *Gbp1* $(\Delta Gbp1,2/ Gbp1^{\Delta})$. We wounded each of these pupae and compared their distal calcium responses to controls and found that the spatial extent was significantly decreased in both conditions compared to controls (Figure 3-11D). Furthermore, the response duration was decreased significantly in the pupae null for *Gbp1* and heterozygous for *Gbp2* (Figure 3-11E). Interestingly, the start times (Figure 3-11F) were not significantly different in either condition, which matches the very weak dependence of start time on Gbp levels in the model (Figure 3-11C). These results experimentally validate the model prediction that sufficient reduction in pro-Gbp prior to wounding can decrease the spatial extent and duration of the calcium response.

A. Mthl10 reduced 70% / Control — normalized [L-R] vs distance from wound center (μm); Calcium Signaling Threshold; Time (s): 165, 132, 99, 66, 33, 0

B. mthl10 RNAI / Control, 120 s, GCaMP6m

C. [L-R]/[R]T threshold radius (μm) vs time (s); relative [pro-Gbp] 50% to 100%

D. Radius: (RMax − R1st) / R1st; ** , *
Gbp1: +/+, Δ/Δ, Δ/+
Gbp2: +/+, Δ/+, Δ/Δ

E. Duration: time (s); ** , ns
+/+, Δ/Δ, Δ/+
+/+, Δ/+, Δ/Δ

F. Start Time: time (s)
+/+, Δ/Δ, Δ/+
+/+, Δ/+, Δ/Δ

G. log[1/k_c] vs log[1/k_s]

H. pnr > mCherry.NLS; -15 s, 2 s, 15 s, 30 s, 90 s
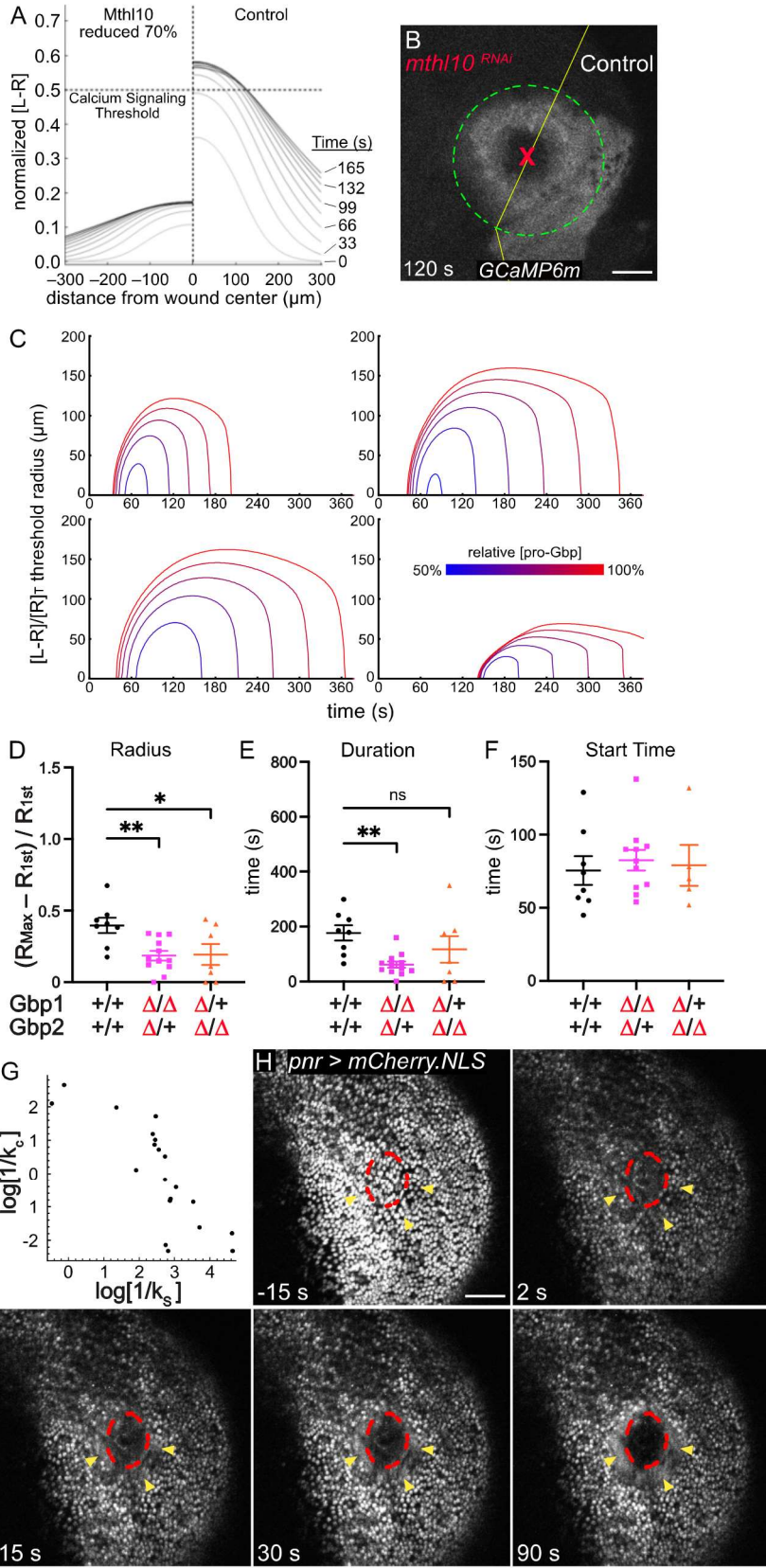
Figure 3-11: Reaction-diffusion (RD) model predictions and experimental validations.

(**A**) Representative RD model output for the normalized fraction of receptors bound to ligand as a function of distance from the wound at various times, with Mthl10 reduced on one side of the wound. The threshold for triggering calcium response is taken as 0.5 (dashed line). Negative distances (left side) correspond to the side with a reduced receptor level, and positive distances (right side) show the response on the control side with an unaltered receptor level. The signal does not reach the threshold on the side where Mlth10 is reduced, matching *in vivo* experimental data where *mthl10* is knocked down on one side (**B**). Scale bar = 50 µm. (**C**) Model output for four parameter sets with varying initial concentration of extracellular pro-Gbp, showing sufficiently decreased levels of pro-Gbp are predicted to decrease the radius and duration of the calcium response, a result not observed in Figure 3-4. (**D–F**) Post-hoc experiments performed on trans-heterozygous pupae expressing one allele of either *Gbp1* or *Gbp2* while null for the other. The distal calcium response radius is significantly decreased in both conditions (**D**), while the signal duration is decreased in the condition lacking both copies of *Gbp1* (**E**). Interestingly, the start times (**F**) were unchanged, as predicted in **C**. Statistical analysis by one-way ANOVA, multiple comparisons WRT control group, *p<0.05, **p<0.01. (**G**) Time constant of pro-ligand cleavage ($1/k_c$) is inversely correlated with the time constant of protease release and activation ($1/k_S$). The model predicts that a rapid pro-ligand cleavage will only occur if the protease is released and activated slowly over time, or in rare cases a rapid protease release can occur but only if the pro-ligand cleavage occurs slowly. In both cases, the triggering signal must build up slowly, indicating that cells lyse and protease accumulates progressively over time after wounding, rather than all at once. (**H**) The black region devoid of mCherry.NLS signal corresponds to the region of fully lysed cells. Cells lyse progressively over time during the first 90 s following wounding, expanding to a region indicated by the red dotted circle. Yellow arrowheads indicate cells with damaged nuclear membranes, which release nuclear-localized mCherry from nuclei into the cytosol, a process which also appears to occur progressively. Scale bar = 50 µm.

3.3.7 Computational model identifies key role for cell lysis over time

In the detailed model construction used here (Figure 3-8A), the rate of signal spread is controlled largely by the rate of signal accumulation plus the diffusion constant of active Gbp. Diffusive spread of the protease itself is minimal (Figure 3-8B). The rate of signal accumulation itself is controlled by the rate constant for the release of protease activity via cell lysis, k_S, and the enzymatic rate constant for proteolytic cleavage of pro-Gbp, k_C. Among the set of best fits, these two model parameters can compensate

95

for one another, as shown by their inverse correlation (Figure 3-11G). One can be fast

so long as the other serves as the sufficiently slow rate-limiting step in generating active

Gbp. In most best-fit parameter sets, the rate-limiting step had a corresponding time

constant ($1/k$) of 50-500 s. Interestingly, only a few of the best fits had a quick release of

protease activity after wounding ($1/k_S < 1$ s) and modifying the model to force an

instantaneous release of this activity failed to fit the experimental data. In other words,

the model predicts that extracellular protease release occurs progressively over time

after wounding, rather than all at once. Given that laser-induced wounds are made very

rapidly – cavitation bubble generation and collapse occur within microseconds – the

best-fits' requirement for much slower protease release was an unexpected prediction.

We hypothesized that the key step may not be an instantaneous release of proteases

from all damaged cells, but rather slow and progressive cell lysis. This led us to

reexamine live imaging of nuclear-mCherry-labeled cells around wounds. Although a

small number of cells were destroyed immediately by the ablation process, a much

larger group of surrounding cells were observed to lyse progressively over ~90 seconds,

validating the model's prediction that the wound-induced cell destruction is not

instantaneous (Figure 3-11H).

Quantitative modeling based on the protease/Gbp mechanism thus provides

explanations for the distal calcium response's wound-size dependencies, makes verified

predictions regarding required extracellular pro-Gbp concentrations, and makes an

unanticipated prediction about slow protease release that matches a reexamination of

experimental data. Further model predictions are provided by the sensitivity analysis

shown in Figure 3-12. Several parameters have a strong impact on the timing and reach

of the distal calcium response, including all those related to the release of protease activity, plus the rate constant for pro-Gbp cleavage, and the initial amount of pro-Gbp present in the extracellular space. It is especially interesting that the amounts of pro-Gbps have a strong impact on the calcium response, as these are known to vary with environmental conditions[135]. The inclusion of an extracellular enzymatic step in the wound-detection pathway provides both signal amplification and multiple options for regulation. Quantitative modeling provides a set of potentially experimentally testable predictions for how this regulation could function *in vivo*.
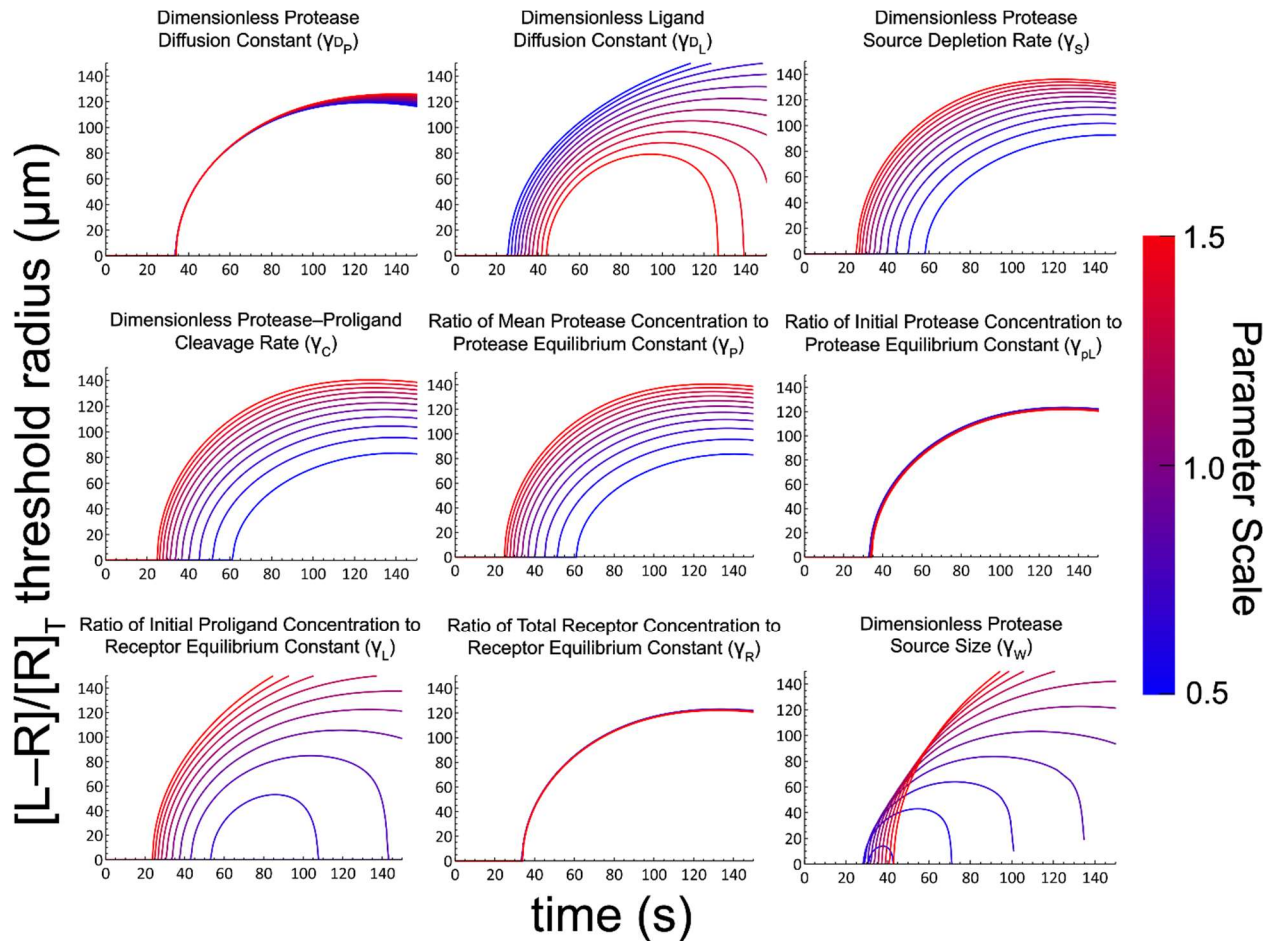
Figure 3-12: Parameter variation effect on RD model output.

Calcium signal radius when varying a single parameter from a set of RD parameters determined from the best fit to an individual wound response (Purple line, Figure 3-8D). Parameter scale indicates by how much the corresponding parameter was scaled to obtain lines of the corresponding color.

3.4 Discussion

This study traces the induction of the repair process back to the wound itself. We find that for epithelial wounds in the *Drosophila* notum, the cell-surface receptor Mthl10 responds to Gbp ligands in the extracellular environment, triggering a cell-autonomous increase in cytoplasmic calcium. It was already known that Gbps are synthesized in an inactive pro-form, requiring proteolytic cleavage for activation, and that they are secreted by the fat body. We find that although Gbps are present in unwounded tissues, they activate Mthl10 only in the presence of a wound. Interestingly, Gbps have cleavage consensus sequences for multiple protease families. Further, the addition of cell lysate or the addition of the unrelated proteases trypsin or clostripain to unwounded tissue is sufficient to generate a calcium signal in wing discs through Mthl10/Gbp signaling. These results lead us to a model in which the lysis of cells inherent in wounding releases non-specific cellular proteases into the extracellular environment. These proteases cleave and activate extracellular Gbps, which in turn activate the Mthl10 GPCR on cells around the wound, initiating wound-induced calcium signaling. Such cell lysis and protease release should be a general feature of cell destruction, whether caused by trauma, pathogen-induced lysis, or a lytic form of cell death such as pyroptosis or necroptosis (immunologically silent apoptosis may well be an exception[139]). A variety of epithelial damage mechanisms may thus converge through

the Gbps to signal via the GPCR Mthl10 and alert surrounding cells to the presence of a nearby wound. This molecular mechanism is supported by a computational model which accurately describes the pattern and timing of wound-induced calcium, predicted its dependence on wound size and initial levels of Gbps, and directed us to observe that cell lysis is not immediate but rather takes place over 10s of seconds. Thus, we offer a model for how surrounding cells detect the damage of cell lysis, utilizing a Gbp-based protease detector system.

3.4.1 Two superimposed mechanisms increase cytoplasmic calcium levels around wounds.

Laser-wounds generate complex yet reproducible patterns of increased cytoplasmic calcium, and the complexity of this pattern has undoubtedly made it difficult to unravel its underlying mechanisms. Within the first ~90 seconds after wounding, two mechanisms drive the increase of calcium, and the complexity is generated by the temporal and spatial superimposition of these two mechanisms. Previously, we reported that a different type of cellular damage initiates a different mechanism for increasing cytoplasmic calcium[113]. In that report, we identified wound-induced micro-tears in the plasma membranes of surviving cells, and these micro-tears provided an entry for extracellular calcium to flood into the cytoplasm and then flow out to neighboring undamaged cells via gap junctions. This direct entry of calcium through damaged plasma membranes is evident within milliseconds after wounding. In this report we describe a second mechanism that extends to more distal cells, initiated by cell lysis at wounding. The dynamics of protease release from lysed cells, along with the gradual

99

accumulation of active Gbp and its rapid diffusion, all contribute to the appearance of this distal calcium response 45-75 s after wounding. The earliest and closest cells to be activated by Mthl10/Gbp signaling cannot be identified visually because the initial flood of calcium through micro-tears takes time to subside.

Three tools allowed us to decipher these superimposed mechanisms. The first tool was the laser itself, which generates a highly stereotyped pattern of damage within a circular wound bed. Although cell lysis and plasma membrane damage are features of nearly every wound, their reproducible pattern in a laser wound allowed us to distinguish the signaling mechanisms each type of damage potentiated. The second tool was a spatiotemporal analytical framework to measure radius over time, which clearly identified two peaks, the first induced by micro-tears and the second induced by cell lysis. The third tool was experimental, using RNAi-knock down of genes in a limited region and comparing it with an internal control. The ability to identify asymmetry between the control and experimental sides of wounds allowed us to bypass concerns about variable wound sizes, which otherwise would have made it difficult to recognize patterns and interpret data. Complex overlapping patterns may have obscured the mechanisms upstream of wound-induced calcium in other systems as well as ours.

3.4.2 Other upstream regulators of wound-induced calcium

Previous studies identified other molecules and phenomena upstream of wound-induced calcium. Studies in cell culture found that wound-generated cell lysis releases ATP, which diffuses extracellularly to bind to purinergic receptors and activate calcium release from intracellular stores[5,53,102,140–142]. Although reproducible in many types of

cultured cells, there has been little evidence to support ATP signaling from lytic cells *in vivo*, likely because extracellular ATP is rapidly hydrolyzed by nucleotidases *in vivo*[143]. Interestingly, ATP does appear to signal damage and promote motility in response to injuries associated with cell swelling in zebrafish, animals that inhabit a hypotonic aqueous environment; however, even in this wounding paradigm, ATP does not signal from lytic cells at an appreciable level[141]. We did not find evidence for ATP signaling upstream of calcium in our wounding experiments, as knockdown of the only fly adenosine receptor did not alter the calcium pattern around wounds.

Some *in vivo* studies have implicated a TrpM ion channel upstream of calcium release. This role of TrpM was first identified in laser-wounding studies of the *C. elegans* hypodermis[28], a giant syncytial cell where we would expect great overlap in the spatial extent of micro-tear-initiated calcium, which would diffuse quickly throughout a syncytium, and receptor-mediated calcium released from the ER. In the hypodermis, loss of TrpM reduced by half the intensity of wound-induced calcium signaling, but without spatial and temporal analysis, the exact contribution of TrpM is not known. In the *Drosophila* notum, a previous study identified TrpM as a regulator of wound-induced actin remodeling, and a slight reduction in wound-induced calcium intensity over time was noted in *TrpM* knockdowns[10]. In contrast, we did not observe any change in the spatial or temporal aspects of the calcium response in *TrpM* knockdown cells compared to the internal control, and given wound-to-wound variability it would have been hard to identify a small effect without an internal control. A study in the fly embryo determined that wound-induced calcium originates from both the external environment and internal stores[29], suggesting to us that two superimposed calcium response mechanisms may

have been at play in these experiments. They found when *TrpM* was knocked down, calcium intensity was reduced by half, but again without spatial and temporal analysis or an internal control, it is difficult to know what pathway TrpM regulates.

Tissue mechanics are upstream of increases in cytoplasmic calcium in a non-wounding context. Several labs have reported calcium flashes and waves in unwounded wing discs, dissected from larvae and cultured *ex vivo*[56,91,92]. Cell and organ culture requires serum to support metabolism outside the organism, and in fly culture, this "serum" is generated by grinding whole adult flies and collecting the supernatant. Because such serum would undoubtedly contain secreted signals from wounded cells, calcium signaling in wing discs *ex vivo* is probably a wound response; indeed, we found it to be transduced by the same mechanism as wound signals, requiring protease, Gbps, and Mthl10. One aspect of calcium signaling in wing discs that we have not tested in our wounding model, however, is the role of mechanical tension. In carefully controlled mechanical experiments, fly serum was found to induce calcium flashes in wing discs specifically on the release of mechanical compression, indicating that tension is a requirement for calcium signaling in these wing discs[124]. It is interesting to consider the TrpM results in light of these mechanical studies, as some TrpM channels can be mechanosensitive. Together, these data suggest that there may be a role for mechanical tension in wound-induced calcium responses.

3.4.3 Functions of the Gbp/Mthl10 induced calcium increase around wounds.

We have found two independent mechanisms that increase cytoplasmic calcium, and in the cells at the wound margin these mechanisms would appear to act

redundantly. Such redundancy indicates that the role of calcium in these cells is very important for wound healing. One biological pathway that may be downstream of calcium in these cells is recruitment of actin and myosin to the wound margin[10,32,144] to form an actomyosin purse-string that cinches the wound closed[10,144,145]. What about calcium in the distal cells, regulated by Gbp/Mthl10? There are many possible functions, but at the moment, all of them are speculative. One possibility is that the cytosolic calcium response initiates distal epithelial cells to modify their cellular behavior from a stationary/non-proliferative state to a migratory and/or proliferative state necessary to repair the wound. Alternatively, an increase in cytosolic calcium may act to modulate an inflammatory response through DUOX leading to the formation of hydrogen peroxide to recruit inflammatory cells to the wound[29] or through the calcium-dependent activation of cytoplasmic Phospholipase A_2 leading to the rapid recruitment of immune cells to tissue damage[101]. This possibility is intriguing because Gbp is known to activate an immune response leading to the upregulation of antimicrobial peptides[130] and to increased activity of phagocytic plasmatocytes in a calcium-dependent manner[146]. Interestingly, loss of Methuselah-like (Mthl) GPCRs results in increased lifespans[129,147,148], and Gbps are nutrition-sensitive peptides whose expression is reduced under starvation conditions[135]. Increased lifespan, caloric restriction and decreased inflammation have all been linked[149–152], and Gbp/Mthl10 activation at wounds may be part of this link.

Although the cytokine and GPCR families are widely conserved, Gbp and Mthl10 do not have direct orthologs in chordates. Nonetheless, similarities exist between the Gbp/Mthl10 mechanism and wound responses in other organisms. Damage- or pathogen-induced activation of proteins by proteolytic cleavage has been well

documented in the cases of spätzle in the Toll pathway[153–155], thrombin and fibrin in the blood coagulation pathway[156–158], and IL-1β and IL-18 in the pyroptosis pathway[159–161]. Additionally, wound-defense signaling in plants relies on an immunomodulatory plant elicitor peptide that is cleaved into its active form by cysteine proteases upon damage-induced cytosolic calcium[116], and the plant defense hormone systemin is cleaved into its active form by phytaspases in response to damage or predation[162]. Because the basic circuitry is similar across kingdoms, our study suggests an ancient strategy for wound detection based on proprotein cleavage, activated by proteases released via cell lysis. As these examples make clear, proteases are already known to play critical roles in blood clotting and immune signaling, and this study finds that proteases are also instructive signals in epithelial wound detection.

3.4.4 Limitations of the Study

As noted above, the Gbp ligands and Mthl10 receptor are not present in mammals, so the extent of mechanistic conservation is unclear. Further, we have not experimentally tested this wound-detection mechanism in other developmental stages of *Drosophila*. For the computational model, several simplifications were made: the use of one variable for all proteases and one variable for all Gbps, rather than having separate Gbp1 and Gbp2; the use of simplified receptor/ligand dynamics that do not include uptake or recycling; and the use of a ligand-receptor binding threshold rather than inclusion of the signal transduction cascade between receptor-binding and calcium release. Finally, this study does not describe or address the mechanism behind the calcium flares that continue for at least an hour after wounding.

3.5 Reaction-diffusion model of the distal calcium response

3.5.1 The extracellular space

While the extracellular space in the pupal laser wound experiments is a three-dimensional space, arguments can be made to reduce it to a one-dimensional space. First, a cuticle that exists just above the tissue essentially limits the extracellular space to a two-dimensional plane. Second, due to the radial symmetry of the distal calcium response around the wound, we can assume that the system is radially symmetric about the wound center. Therefore, the relevant molecular components in the model can be assumed to only depend on two dependent variables: one spatial variable r that is the distance from the center of the wound, and one temporal variable t that is the time since wounding.

3.5.2 The protease source

Since the extent of the damage decreases farther from the wound center, it is reasonable to assume that the source of active protease follows this same trend. Therefore, the active protease source initiated by the wound is taken to be a Gaussian in space whose maximum is at the wound center. The source is also taken to decay exponentially in time to represent the depletion of protease from the total amount released from the wound. The protease source term then takes the form

$$S(r,t) = \frac{P_0 k_S}{2\pi\sigma_w^2} \exp\left(-\frac{r^2}{2\sigma_w^2} - k_S t\right) \tag{3-1}$$

where P_0 is the total number of protease molecules released from the source, k_S is the

rate constant for the source, and σ_w determines the spatial extent of the source.

It is worth noting that, while active protease could arise from various

mechanisms, the model remains agnostic as to how we get to a final, activated form of

the protease. Therefore, the Gaussian form of the protease source just represents

where we would expect to find active protease after various activation mechanisms

have occurred.

3.5.3 The protease-proligand model

The protease-proligand interactions are modeled as a simple reaction, where one

protease molecule reversibly binds to one proligand molecule to form a complex. This

complex is then irreversibly converted into a protease molecule and a ligand molecule

upon cleavage of the proligand. These processes can be modeled with the scheme

shown in Figure 3-8A' with rate constants k_b^+, k_b^-, and k_c.

3.5.4 The ligand-receptor model

The ligand-receptor interactions are modeled as a simple reaction, where one

ligand molecule reversibly binds to one receptor molecule to form a complex. This

process can be modeled with the scheme shown in Figure 3-8A' with rate constants k_r^+

and k_r^-. While the ligand-receptor dynamics upstream of calcium signaling can be

modeled in a more detailed way, as in Lemon et al. 2003[163], these processes most likely

do not influence the calcium signals on the timescale of the distal calcium response, so

they are not considered here.

3.5.5 Reaction-diffusion model equations

Using the law of mass action, the model reactions above can be turned into a set of coupled partial differential equations. The model assumes that all molecular components exist in a radially symmetric, two-dimensional plane where protease and ligand can diffuse with diffusion constants D_P and D_L respectively. All other molecular components are assumed to be immobile. This leads to the following set of six differential equations

$$\frac{\partial [P]}{\partial t} = D_P \nabla^2 [P] + S - k_b^+ [P][pL] + k_b^- [P \cdot pL] + k_c [P \cdot pL] \tag{3-2}$$

$$\frac{\partial [pL]}{\partial t} = -k_b^+ [P][pL] + k_b^- [P \cdot pL] \tag{3-3}$$

$$\frac{\partial [P \cdot pL]}{\partial t} = k_b^+ [P][pL] - k_b^- [P \cdot pL] - k_c [P \cdot pL] \tag{3-4}$$

$$\frac{\partial [L]}{\partial t} = D_L \nabla^2 [L] + k_c [P \cdot pL] - k_r^+ [L][R] + k_r^- [L \cdot R] \tag{3-5}$$

$$\frac{\partial [R]}{\partial t} = -k_r^+ [L][R] + k_r^- [L \cdot R] \tag{3-6}$$

$$\frac{\partial [L \cdot R]}{\partial t} = k_r^+ [L][R] - k_r^- [L \cdot R] \tag{3-7}$$

where brackets denote the concentration of a molecular component in terms of number of molecules per unit area, and the Laplacian operator ∇^2 is expressed in terms of the polar coordinate r as $\nabla^2 = \frac{\partial^2}{\partial r^2} + \frac{1}{r} \cdot \frac{\partial}{\partial r}$.

In order to simplify this set of equations, it is assumed that ligand production is described by Michaelis-Menten kinetics and that ligand-receptor binding is at equilibrium on fast timescales. Therefore, we have

$$[P][pL] = K_b[P \cdot pL] \tag{3-8}$$

$$[L][R] = K_r[L \cdot R] \tag{3-9}$$

where $K_b = \frac{k_b^- + k_c}{k_b^+}$ and $K_r = \frac{k_r^-}{k_r^+}$. Additionally, by defining the total proligand concentration

as $[pL]_T = [pL] + [P \cdot pL]$ and the constant total receptor concentration as $[R]_T = [R] +$

$[L \cdot R]$, we obtain the following equations:

$$[P \cdot pL] = \frac{[P][pL]_T}{K_b + [P]} \tag{3-10}$$

$$[L \cdot R] = \frac{[L][R]_T}{K_r + [L]} \tag{3-11}$$

By adding together specific pairs of equations from Eqs. (3-2) - (3-7) we obtain

$$\frac{\partial}{\partial t}([pL] + [P \cdot pL]) = \frac{\partial [pL]_T}{\partial t} = -k_c[P \cdot pL] \tag{3-12}$$

$$\frac{\partial}{\partial t}([R] + [L \cdot R]) = \frac{\partial [R]_T}{\partial t} = 0 \tag{3-13}$$

$$\frac{\partial}{\partial t}([P] + [P \cdot pL]) = D_P \nabla^2 [P] + S \tag{3-14}$$

$$\frac{\partial}{\partial t}([L] + [L \cdot R]) = D_L \nabla^2 [L] + k_c[P \cdot pL] \tag{3-15}$$

Then, by combining Eqs. (3-10) - (3-15) we end up with a set of three differential

equations and four algebraic equations

$$\frac{\partial [P]}{\partial t} = \left(1 + \frac{K_b[pL]_T}{(K_b + [P])^2}\right)^{-1} \cdot \left[D_P \nabla^2 [P] + S + k_c \left(\frac{[P]}{K_b + [P]}\right)^2 [pL]_T\right] \tag{3-16}$$

$$\frac{\partial [pL]_T}{\partial t} = -k_c \cdot \frac{[P] \cdot [pL]_T}{K_b + [P]} \tag{3-17}$$

$$\frac{\partial [L]}{\partial t} = \left(1 + \frac{K_r[R]_T}{(K_r + [L])^2}\right)^{-1} \cdot \left[D_L \nabla^2 [L] + k_c \cdot \frac{[P] \cdot [pL]_T}{K_b + [P]}\right] \tag{3-18}$$

$$[P \cdot pL] = \frac{[P] \cdot [pL]_T}{K_b + [P]} \tag{3-19}$$

$$[pL] = [pL]_T - [P \cdot pL] \tag{3-20}$$

$$[L \cdot R] = \frac{[R]_T[L]}{K_r + [L]} \tag{3-21}$$

$$[R] = [R]_T - [L \cdot R] \tag{3-22}$$

3.5.5.1 Initial and boundary conditions

Due to diffusive terms in the equations, the mobile molecular components require both boundary conditions and initial conditions, whereas the immobile molecular components only require initial conditions. We assume that there is initially no protease or ligand in the extracellular space, and that a uniform proligand concentration $[pL]_0$ is present in the extracellular space. This gives the following initial conditions

$$[P](r,0) = 0 \tag{3-23}$$

$$[pL]_T(r,0) = [pL]_0 \tag{3-24}$$

$$[L](r,0) = 0 \tag{3-25}$$

The initial conditions of the other molecular components can be obtained from the algebraic equations above, although these are not important in solving the differential equations.

For each mobile molecular component, the same boundary conditions are applied: far from the wound the concentrations should go to 0, and in order to impose radial symmetry there needs to be no flux at the origin. This leads to the following boundary conditions

$$\lim_{r \to \infty}[P] = \lim_{r \to \infty}[L] = 0 \tag{3-26}$$

$$-D_P \frac{\partial [P]}{\partial r}\Big|_{r=0} = -D_L \frac{\partial [L]}{\partial r}\Big|_{r=0} = 0 \tag{3-27}$$

3.5.5.2 Non-dimensionalization

To reduce the number of parameters in the model, as well as simplify the model further, the independent variables are scaled in the following way:

$$r = r_d \rho \tag{3-28}$$

$$t = t_0 \tau \tag{3-29}$$

where $r_d = 10\ \mu m$ is the average ablation radius following wounding, $t_0 = 47\ s$ is the median time after wounding before the distal calcium response occurs, and ρ and τ are dimensionless variables for space and time, respectively. Additionally, the dependent variables are scaled in the following way:

$$[P] = [P]_0 x \tag{3-30}$$

$$[pL] = [pL]_0 y \tag{3-31}$$

$$[P \cdot pL] = [pL]_0 y_x \tag{3-32}$$

$$[pL]_T = [pL]_0 y_T \tag{3-33}$$

$$[L] = [pL]_0 \ell \tag{3-34}$$

$$[R] = [R]_T w \tag{3-35}$$

$$[L \cdot R] = [R]_T w_\ell \tag{3-36}$$

where $[P]_0 = \dfrac{P_0}{2\pi r_d^2}$, and $x, y, y_x, y_T, \ell, w,$ and w_ℓ are dimensionless variables.

By applying these scales (3-28) - (3-36) to the model equations Eqs. (3-16) - (3-22) one arrives at the following non-dimensionalized equations

$$\frac{\partial x}{\partial \tau} = \left(1 + \frac{\gamma_{pL} y_T}{(1 + \gamma_P x)^2}\right)^{-1}$$
$$\cdot \left[\gamma_{D_P} \nabla_\rho^2 x + \frac{\gamma_S}{\gamma_w^2} \exp\left(-\frac{\rho^2}{2\gamma_w^2} - \gamma_d \tau\right) + \gamma_c \cdot \frac{\gamma_{pL}}{\gamma_P} \cdot \left(\frac{\gamma_P x}{1 + \gamma_P x}\right)^2 \cdot y_T\right] \tag{3-37}$$

$$\frac{\partial y_T}{\partial \tau} = -\frac{\gamma_c \gamma_P x}{1 + \gamma_P x} \cdot y_T \tag{3-38}$$

$$\frac{\partial \ell}{\partial \tau} = \left(1 + \frac{\gamma_R}{(1 + \gamma_L \ell)^2}\right)^{-1} \cdot \left[\gamma_{D_L} \nabla_\rho^2 \ell + \frac{\gamma_c \gamma_P x}{1 + \gamma_P x} \cdot y_T\right] \tag{3-39}$$

$$y_x = \frac{\gamma_P x y_T}{1 + \gamma_P x} \tag{3-40}$$

$$y = y_T - y_x \tag{3-41}$$

$$w_\ell = \frac{\gamma_L \ell}{1 + \gamma_L \ell} \tag{3-42}$$

$$w = 1 - w_\ell \tag{3-43}$$

where we now have nine dimensionless parameters (see also Figure 3-12, which

highlights the influence of each of these parameters on model output)

$$\gamma_w = \frac{\sigma_w}{r_d} \tag{3-44}$$

$$\gamma_{D_P} = \frac{t_0}{r_d^2} D_P \tag{3-45}$$

$$\gamma_{D_L} = \frac{t_0}{r_d^2} D_L \tag{3-46}$$

$$\gamma_S = t_0 k_S \tag{3-47}$$

$$\gamma_c = t_0 k_c \tag{3-48}$$

$$\gamma_P = \frac{[P]_0}{K_b} \tag{3-49}$$

$$\gamma_{pL} = \frac{[pL]_0}{K_b} \tag{3-50}$$

$$\gamma_L = \frac{[pL]_0}{K_r} \tag{3-51}$$

$$\gamma_R = \frac{[R]_T}{K_r} \tag{3-52}$$

Additionally, the scaled initial and boundary conditions are

$$x(\rho, 0) = 0 \tag{3-53}$$

$$y_T(\rho, 0) = 1 \tag{3-54}$$

$$\ell(r, 0) = 0 \tag{3-55}$$

$$\lim_{\rho \to \infty} x = \lim_{\rho \to \infty} \ell = 0 \tag{3-56}$$

$$-\gamma_{D_P} \frac{\partial x}{\partial \rho}\Big|_{\rho=0} = -\gamma_{D_L} \frac{\partial \ell}{\partial \rho}\Big|_{\rho=0} = 0 \tag{3-57}$$

where, once again, initial conditions for the other scaled molecular components can be determined from the algebraic relations, although these are not important for solving the differential equations.

3.5.6 Method of solution

Due to the $1/\rho$ dependence of the Laplacian operator in polar coordinates, the boundary condition at $\rho = 0$ cannot be handled numerically in a simple fashion. Therefore, the boundary conditions were imposed at a small radial distance of $\Delta\rho = .001$, and the protease source was shifted this distance as well so that the scaled source term becomes $s(\rho, \tau) = \frac{\gamma_S}{\gamma_w^2} \exp\left(-\frac{(\rho - \Delta\rho)^2}{2\gamma_w^2} - \gamma_d \tau\right)$. Additionally, the boundary condition at infinity must be imposed at a finite value ρ_{far}. A value of $\rho_{far} = 100$ ($r_{far} = 1000 \ \mu m$) was chosen for simulations since values of ρ_{far} larger than this do not cause large changes in the model output on the timescale of interest.

The software Mathematica was used to solve the above set of model equations. Since the system of equations is nonlinear and the equation for y_T does not contain derivatives with respect to ρ, the method of lines was chosen to solve the set of

differential equations. Because the spatial region is one-dimensional, the "Tensor Product Grid" method was used to discretize the spatial variable. The number of grid points for this discretization was chosen to be the smallest value so that use of a larger number of points did not yield a significantly different solution. A more detailed description of the numeric solution algorithms and settings can be found in the Mathematica documentation.

3.5.7 Model output and signal radius

Solving the set of non-dimensionalized model equations along with a set of parameter values yields scaled molecular component concentrations as functions of $\rho = r/r_d$ and $\tau = t/t_0$. The model assumes that for a given spatial coordinate ρ, calcium will first be released into the cytosol when at least half of the receptors are bound to a ligand molecule. This sets a threshold for the scaled variable w_ℓ as $w_{thres} = 0.5$. By solving for the radial distance ρ_{thresh} such that $w_\ell(\rho_{thres}, \tau) = w_{thresh}$, we can then determine the signal radius as a function of time $\rho_{thresh}(\tau)$. Therefore, it is assumed that $\rho_{thresh}(\tau)$ is equal to the calcium radius during the distal calcium response.

After the distal calcium response, the calcium dynamics are determined by processes not covered in the current model. Therefore, it should be noted that the proposed model is not valid past the distal calcium response, as the ligand is not the sole factor in determining the calcium dynamics past this point.

3.5.8 Estimate of the Gbp diffusion constant

To estimate the free diffusion constant of the ligand Gbp, we assume that the ligand of molecular weight as 2.79 kDa $\approx$ 4.63 x 10^{-21} g (based on the peptide sequence described in Appendix C) is spherical with a typical protein density of 1.37 g/cm^3. This results in an estimated effective radius of 0.93 nm. Using the Stokes-Einstein relation at a temperature of 293 K in water results in an estimated diffusion constant of about 260 µm^2/s, which is 122.2 in scaled units. This estimate is only used to approximate the free Gbp diffusion constant; this parameter was still allowed to vary during the fitting process.

3.5.9 Initial guess selection

Initial guesses for each selected distal calcium response were obtained by randomly searching parameter space for parameter sets that produced model outputs that met two criteria. First, the parameter set had to produce a distal calcium response that did not extend past the maximum of the distal calcium response to be fit to. Second, the parameter set had to produce a distal calcium response that had a sum of squares error that was 10% or less than the sum of squares error of a no-response model output (where the fraction of receptors bound to ligand never crosses the 50% threshold). Sum of square errors are determined according to step 2 of Section 3.5.10 below. For each of the four selected data sets to fit to, 32 initial guesses were obtained.

3.5.10 Fitting the model to the data

The first goal of the model is to reproduce the distal calcium response data. This is done by fitting the model output of $\rho_{thresh}(\tau)$ to the data by varying the nine dimensionless parameters mentioned earlier. Due to a possibly large space of feasible parameter values, a fitting method is desired that searches a sufficient amount of the parameter space without taking too much time or biasing one region of parameter space over another. Therefore, the fitting method is based on orthogonal array sampling. The fitting steps are outlined below:

1. A distal calcium response dataset is chosen that the model will be fit to. In order to prevent $\rho_{thres}(\tau)$ from increasing to ρ values past the distal calcium response at later times, additional "constraint points" are appended to the dataset that are equal to the maximum extent of the distal calcium response. The number of constraint points is equal to the number of experimental data points in order to equally weigh fitting the distal calcium response with not extending past its maximum extent.

2. A fitting function to be minimized is defined in two parts. For the original data points, the fitting function is just a sum of squares difference between the data and the model. For the constraint points, the fitting function is also a sum of squares difference between the model and the data, but it is 0 if $\rho_{thres}(\tau)$ is less than the corresponding constraint point. This way there is only a penalty when the model output extends past the maximum extent of the distal calcium response. The goal of the fitting procedure is then to find a parameter set that minimizes the fitting function. More explicitly, we want to minimize the following

piecewise function for data points (original and constraint) $d(\tau_i)$ and model

output points $\rho_{thres}\ (\tau_i) = m(\tau_i)$

$$f(d, m) = \sum_i \begin{cases} (m(\tau_i) - d(\tau_i))^2 & \text{for original data points} \\ Max\ [m(\tau_i) - d(\tau_i), 0]^2 & \text{for constraint points} \end{cases}$$

3. In order to vary the dimensionless parameters across desired ranges, some of
   which span orders of magnitude, the dimensionless parameters are replaced in
   the following way

$\gamma_{D_P} \rightarrow 12.22 \times 10^{\Gamma_{D_P}}$
$\gamma_{D_L} \rightarrow 122.2 \times \Gamma_{D_L}$
$\gamma_S \rightarrow 10^{\Gamma_S}$
$\gamma_c \rightarrow 10^{\Gamma_c}$
$\gamma_P \rightarrow 10^{\Gamma_P}$
$\gamma_{pL} \rightarrow 10^{\Gamma_{pL}}$
$\gamma_L \rightarrow 10^{\Gamma_L}$
$\gamma_R \rightarrow 10^{\Gamma_R}$
$\gamma_w \rightarrow \Gamma_w$

Therefore, we have created a new dimensionless parameter set $\Gamma = $

$\{\Gamma_{D_P}, \Gamma_{D_L}, \Gamma_S, \Gamma_c, \Gamma_P, \Gamma_{pL}, \Gamma_L, \Gamma_R, \Gamma_w\}$ to use for the fitting method.

4. An initial set of parameter values Γ_0 is determined as explained in the section
   "Initial Guess Selection" above.

5. An orthogonal array A is created with 729 runs, 9 factors, 3 levels, a strength of
   5, and an index of 3. The levels are set to be {-1, 0, 1}. i.e. A is a 729 x 9 matrix
   with the three entries -1, 0, or 1 such that every 729 x 5 subarray of A contains
   every 5-tuple based on {-1,0,1} exactly 3 times.

6. For each row A_i of the orthogonal array A, a new parameter set Γ_i is obtained by
   adding A_i to the initial parameter set Γ_0. Each of these parameter sets are then

applied to the model, thus resulting in a set $\{\rho_i(\tau)\}$ of 729 different $\rho_{thres}\ (\tau)$ functions.

7. For each $\rho_i(\tau)$, the fitting function from step 2 is evaluated. The parameter set Γ_i that results in the best fit $\rho_i(\tau)$ now becomes Γ_0.

8. Steps 6 and 7 are repeated until the best fitting parameter set is Γ_0

9. Steps 6 – 8 are repeated with entries $\{-1,0,1\}$ in the orthogonal array replaced with entries $\{-1/2^n, 0, 1/2^n\}$ for n values 1, 2, 3, and 4. The final set Γ_0 is then determined to be the parameter set that best fits the data for the given initial parameter set.

3.5.11 Wound-size scaling of the model

The distal calcium response has two characteristics of interest: its time delay $t_{0,min}$ and its effective diffusion constant α_{eff}. We previously showed that the distal calcium response can be fit to an empirical "delayed diffusion equation" where $t_{0,min}$ and α_{eff} are independent parameters that are chosen to fit the data[113]. As shown in Figure 3-8F-F', these measures appear to have a wound size dependency.

The parameters in the model that are affected by the wound size are the total amount of protease that is released and the spatial extent of the protease source. However, it is assumed that the protease per cell (area) should remain constant with respect to wound size. More specifically, in order to keep the protease density constant as the wound size changes, it must be that if σ_w is scaled by some factor λ, then P_0 must be scaled by λ^2. These parameters appear in the dimensionless parameters

117

$\gamma_P = \frac{[P]_0}{K_b} = \frac{1}{K_b} \cdot \frac{P_0}{2\pi r_d^2}$ and $\gamma_w = \frac{\sigma_w}{r_d^2}$. Therefore, scaling the wound size by a factor λ in the model corresponds to scaling γ_w by λ and scaling γ_P by λ^2.

Starting with a best fit parameter set, the wound size was then varied using scaling factors of λ from 0.5 to 1.5 in step sizes of 0.1. An example of the calcium signal radius for each scaling factor is shown in Figure 3-8E. Values of $t_{0,min}$ and α_{eff} were then determined for each new parameter set by fitting the delayed diffusion model to the RD model output. The delayed diffusion model, discussed in more detail in[113], describes the calcium signal radius by the equations

$$R_S^2 = 2\sigma^2 \ln\left[\frac{1}{2\pi\sigma^2 (C_{th}/M)}\right] \tag{3-58}$$

$$\sigma^2 = \sigma_0^2 + 2\alpha(t - t_0) \tag{3-59}$$

The effective diffusion constant α was obtained by directly fitting the RD model output to the delayed diffusion model, while the time delay $t_{0,min}$ was obtained from

$$t_{0,min} = t_0 - \frac{\sigma_0^2}{2\alpha} \tag{3-60}$$

In other words, the time delay is the time when σ from Eq. (3-59) is equal to 0 given the best fit parameters to the delayed-diffusion model.

3.5.12 Mthl10-reduction internally-controlled expression model

In order to simulate an internally-controlled system where Mthl10 is reduced on half of the tissue, the model must be modified in the following ways:

1. Unlike the original model, which assumes a uniform initial tissue, the internally-controlled system no longer has rotational symmetry. Therefore, the species in the model need to be expressed as functions of both distance from the wound center r as well as the polar angle θ, and periodic boundary conditions are implemented so that for each diffusible species x_i, $x_i(r, 0, t) = x_i(r, 2\pi, t)$. The periodic behavior of the non-diffusible species is not explicitly implemented, as it follows automatically from the diffusible species' periodic boundary conditions.

2. The total amount of receptor is reduced on half of the tissue by reducing the parameter $\gamma_R = [R]_T/K_r$ for $\pi/2 < \theta < 3\pi/2$. Therefore, the parameter γ_R now becomes a piecewise function in space

$$\gamma_R = \begin{cases} \lambda \cdot [R]_T/K_r & \text{for } \pi/2 < \theta < 3\pi/2 \\ [R]_T/K_r & \text{otherwise} \end{cases} \tag{3-61}$$

Where $0 \leq \lambda \leq 1$

3. In order to compare the $[L \cdot R]/[R]_T$ output between each side of the tissue, $[L \cdot R]/[R]_T$ on the MthI-10 reduction side needs to be multiplied by λ so that the fraction is relative to $[R]_T$ on the control side.

An example of the $[L \cdot R]/[R]_T$ output of the above model is shown in Figure 3-11A.

3.5.13 Initial pro-Gbp concentration scaling of the model

In addition to wound size, the reaction-diffusion model can be scaled in terms of other system parameters as well. More specifically, the model can be used to investigate how the system behaves due to a reduction in pro-Gbp levels . The initial

pro-ligand concentration appears in the dimensionless parameters $\gamma_{pL} = \frac{[pL]_0}{K_b}$ and

$\gamma_L = \frac{[pL]_0}{K_r}$. Therefore, scaling the initial pro-ligand concentration by a factor λ in the

model corresponds to scaling both γ_{pL} and γ_L by λ. Results of this scaling are shown in

Figure 3-11C.

Chapter 4

A mathematical model of calcium signals around laser-induced epithelial wounds

This chapter is adapted from Stevens, A. C., O'Connor, J. T., Pumford, A. D., Page-McCaw, A., Hutson, M. S. A mathematical model of calcium signals around laser-induced epithelial wounds. (draft has been submitted for review in *Mol. Biol. Cell.*)

Apart from experiments performed by James O'Connor (Figure 4-3A and Figure 4-5A, C) and the micro-tear distribution determined by Andrew Pumford (Figure 4-2), all of the work presented in this chapter is my own.

4.1 Abstract

Cells around epithelial wounds must first become aware of the wound's presence in order to initiate the wound healing process. An initial response to an epithelial wound is an increase in cytosolic calcium followed by complex calcium signaling events. While these calcium signals are driven by both physical and chemical wound responses, cells around the wound will all be equipped with the same cellular components to produce and interact with the calcium signals. Here, we have developed a mathematical model in the context of laser-ablation of the *Drosophila* pupal notum that integrates tissue-level damage models with a cellular calcium signaling toolkit. The model replicates experiments in the contexts of control wounds as well as knockdowns of specific cellular components, but it also provides new insights that are not easily accessible experimentally. The model suggests that cell-cell variability is necessary to produce calcium signaling events observed in experiments, it quantifies calcium concentrations during wound-induced signaling events, and it shows that intercellular transfer of the molecule IP$_3$ is required to coordinate calcium signals across distal cells around the

wound. The mathematical model developed here serves as a framework for quantitative studies in both wound signaling and calcium signaling in the *Drosophila* system.

4.2 Introduction

Wound healing is an essential mechanism that allows an epithelial tissue to maintain its barrier function [1,2]. As a first step, cells must be alerted to the presence of a nearby wound [4,47,165]. Among early wound-induced signals is an increase in cytosolic calcium – a "life and death signal" that is essential for a wide variety of biological processes [10,25,28,29]. Previous work has shown that multiple physical and chemical mechanisms initiate calcium signals around epithelial wounds, some starting as fast as milliseconds, others reaching more distal cells in minutes [113,164]. Here, we develop a mathematical model for wound-induced calcium signaling across an epithelium of thousands of coupled cells. The model incorporates two key triggering mechanisms – plasma membrane damage and protease-based activation of latent pro-peptides – which then regulate calcium fluxes across cells' plasma membranes, between cells' cytosol and intracellular endoplasmic reticulum (ER) stores, and through gap junctions with neighboring cells. The resulting model yields rich calcium-signaling dynamics that reproduce those observed in experiments, recreate the results of several genetic perturbations, and provide insights not directly accessible through experiments.

The mechanisms included here are those observed using the genetically encoded calcium indicator GCaMP6m to follow calcium signals around laser wounds in the *Drosophila* pupal notum. Those experiments showed that the initial calcium influx begins within milliseconds and is initiated by cavitation-induced shear stresses that

physically create micro-tears in the cells' plasma membranes. The radius of this damaged region ranged from 30-120 µm, depending on laser energy, and corresponded to 70-1000 cells (not all of which will survive). Over the next 10-20 s, this initial influx spreads through one to two rows of surrounding undamaged cells [11]– a process blocked by knocking down gap junctions [113]. In parallel, proteases released by cell lysis near the wound cleave and activate cytokines called growth blocking peptides (Gbps). The activated Gbps diffuse through the extracellular space and bind to the cell surface receptor Methuselah-like 10 (Mthl10), a G-protein coupled receptor, to trigger a canonical $G_{\alpha q}$/PLCβ/IPR cascade that releases calcium from the ER. These distal calcium signals appear ~40 s after wounding and spread as far as 150 µm from the wound [164]. Stochastic calcium waves or flares then extend even further away from the wound.

These separate damage events drive different aspects of intra- and intercellular calcium signaling. To understand how they are integrated into a collective tissue-level wound response, we implement the damage signals as inputs into an ordinary differential equation (ODE) model for calcium signaling that is operable in every cell in the epithelium – generating a large set of coupled ODEs. Calcium signaling has been previously modeled in a wide range of systems, from the excitation of muscles and neurons to non-excitable cells such as hepatocytes and *Xenopus* oocytes, and from the kinetics of single calcium channels all the way to signal propagation across entire tissues [37,166–170]. These wide-ranging models nonetheless have a modular design: specific components of a calcium signaling "toolkit" can be included or excluded based on the system in question [36]. From this toolkit, we include gap-junction fluxes, plasma-

123

membrane fluxes (leak currents, store-operated channels (SOCs), the plasma membrane calcium ATPase (PMCA) calcium pump, and a generalized high-capacity pump), and regulated cytosol-ER fluxes through the IP3 receptor and SERCA pumps. On top of this toolkit, we apply a spatial distribution of micro-tears that add another plasma-membrane flux, and we couple in a previously published reaction-diffusion model for protease-driven activation of Gbps, and their binding to cell-surface receptors.

4.3 Methods

Our mathematical model represents the monolayer epithelium of the *Drosophila* pupal notum as a Voronoi mesh of tightly packed cells. Upon wounding, each cell is subjected to a different degree of damage and experiences different time-dependent levels of active GBP signaling through the G-protein coupled receptor Mthl10. The cell-specific damage and GBP-Mthl10 signaling then couples into each cell's common calcium signaling machinery: fluxes across the plasma membrane; fluxes through gap junctions with neighboring cells; and IP3-mediated fluxes between the cytoplasm and intracellular ER stores. This coupling of wound-induced damage, extracellular signals, and intracellular signaling pathways gives rise to the rich calcium signaling dynamics observed in experiments. A schematic of the model is shown in Figure 4-1, and each part is described in detail below.
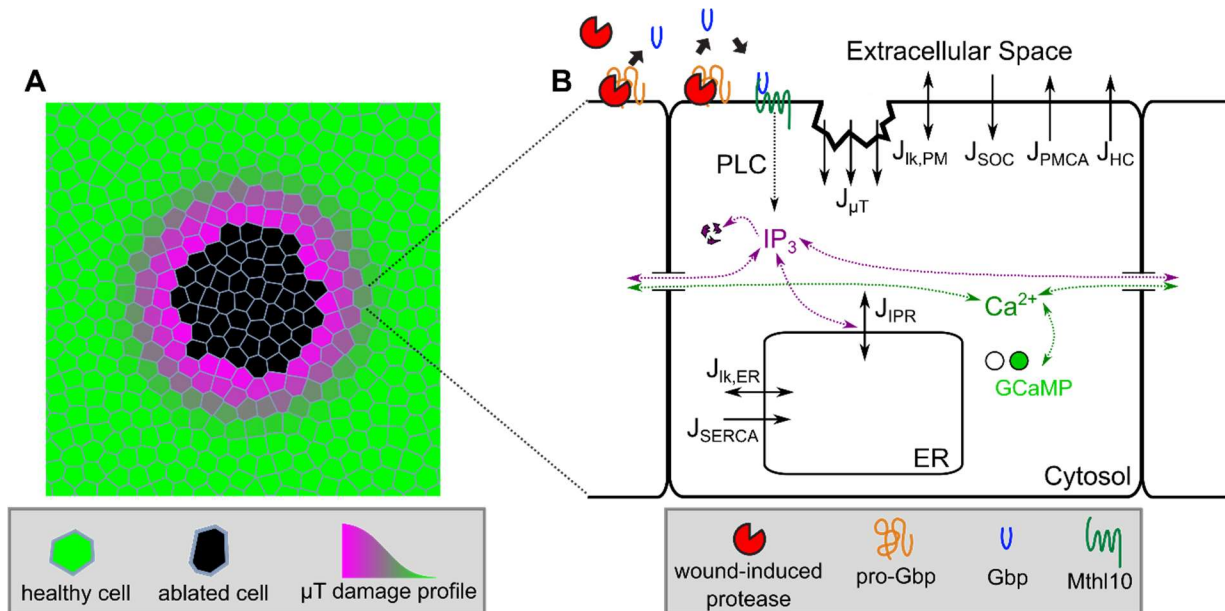
Figure 4-1: Schematic diagram of the complete wound-induced calcium signaling model.

A) 160 x 160 µm section of the tissue mesh centered around the wound. Cells are color-coded according to their physical damage level. **B)** Reactions and fluxes included in the single-cell model and its connection to the extracellular model of biochemical damage signals. Solid black arrows show directions of calcium fluxes.

4.3.1 Tissue-level model

The *in silico* tissue is a 2D Voronoi mesh constructed from a set of 4826 seed points confined to a 450 by 450 µm square. The seed points were initially placed at random and then redistributed more uniformly by simulated annealing with an inverse-square-distance repulsion between all seed pairs. A similar force repulsed each seed from the closest boundary of the square. After Voronoi tessellation, each Voronoi cell represents one modeled biological cell. The chosen parameters yield an average cell area of 42 µm^2 that matches experimental images. A 160 µm x 160 µm section of an example tissue mesh is shown in Figure 4-1A.

4.3.2 Wound-induced damage signals

4.3.2.1 Plasma membrane micro-tears

The wounds we model are those caused by pulsed laser ablation[113]. Such wounds locally destroy some cells – those labeled as "ablated" in Figure 4-1A – and permeabilize others further out through damage to their plasma membranes, so called micro-tears. This damage is caused by shear stress created through the rapid (< 100 μs) expansion and collapse of a laser-induced cavitation bubble[6,171]. We previously found that the radius of the region of calcium influx at ~2 s after wounding was well matched to the maximum bubble radius. By imaging even faster, we find that a central region of calcium influx still appears within the first frame (17 ms after wounding), but more distal influx proceeds from discrete sites that fill in the cavitation-bubble footprint over 1-2 seconds. Analysis of the density of discrete calcium entry sites provides an estimate for the distribution of plasma-membrane damage (Figure 4-2). We find that this distribution can be heuristically described by

$$s_{\mu T}(r; r_{max}) = \begin{cases} A \cdot \left[\text{erf}\left(-\frac{r/r_{max} - B}{C} \right) + 1 \right] & , 0 \leq r \leq r_{max} \\ 0 & , r > r_{max} \end{cases} \qquad \textbf{(4-1)}$$

where $s_{\mu T}$ is the local plasma-membrane permeability due to micro-tears, erf is the error function, r_{max} is the maximum radius of the cavitation bubble, and A, B, and C are fitting parameters with values shown in Table 4-1. This heuristic function provides a means to scale the damage distribution for wounds with different sized cavitation bubbles.
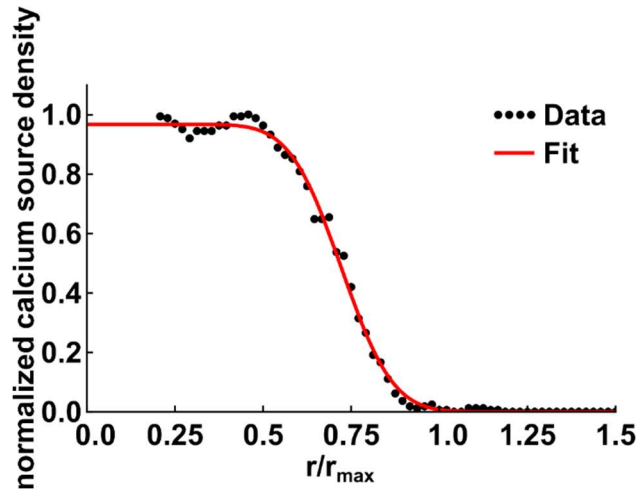
Figure 4-2: Calcium source density is fit to a heuristic function.

Image analysis of GCaMP fluorescence 17 ms after wounding yields a radial density of calcium entry sites as a function of distance from the wound (black points). The data is fit to Eq. (4-1) (red line, parameters in Table 4-1). The vertical axis is normalized so that the maximum density is 1, and the horizontal axis is scaled relative to the maximum radius of the cavitation bubble.

4.3.2.2 Extracellular Gbp-Mthl10 signaling

After the initial calcium influx, there is a second delayed calcium response driven by an extracellular signaling cascade: proteases released from lysed and damaged cells cleave latent, extracellular proGbps into their active forms, which diffuse in the extracellular space and bind to the cell-surface receptor Mthl10, which initiates calcium release from the ER. This Mthl10 response extends even more distally than the first calcium response caused by damage to the plasma membranes. As done previously, we model that process as a set of coupled reaction-diffusion equations. The scaled equations (Eqs. (4-2) - (4-5) below) determine w_ℓ, the local fraction of Mthl10 receptors that have bound Gbp as a function of time and distance from the wound. The independent variables ρ and τ are scaled distance and time; the dependent variables

127

$x, y_T,$ and ℓ represent local, scaled concentrations of protease, proGbp, and active Gbp respectively. At t=0, there is no protease and all Gbp is in the pro-form. A no-flux boundary is imposed at the origin, and all species go to zero at infinity. Parameters for downstream intracellular signaling (see Table 4-1) were selected so that a distal calcium response occurs at a threshold of $w_\ell = 0.05$. Further details of the parameters and scaled model equations can be found in O'Connor et al. 2021[164] or Section 3.5

$$\frac{\partial x}{\partial \tau} = \left(1 + \frac{\gamma_{pL} \cdot y_T}{(1 + \gamma_P \cdot x)^2}\right)^{-1}$$

$$\times \left[\gamma_{D_P} \nabla_\rho^2 x + \frac{\gamma_S}{\gamma_w^2} \exp\left(-\frac{\rho^2}{2\gamma_w^2} - \gamma_S \cdot \tau\right) + \gamma_c \cdot \frac{\gamma_{pL}}{\gamma_P} \cdot \left(\frac{\gamma_P \cdot x}{1 + \gamma_P \cdot x}\right)^2 \cdot y_T\right]$$

(4-2)

$$\frac{\partial y_T}{\partial \tau} = -\frac{\gamma_c \cdot \gamma_P \cdot x}{1 + \gamma_P \cdot x} \cdot y_T$$

(4-3)

$$\frac{\partial \ell}{\partial \tau} = \left(1 + \frac{\gamma_R}{(1 + \gamma_L \ell)^2}\right)^{-1} \cdot \left[\gamma_{D_L} \nabla_\rho^2 \ell + \frac{\gamma_c \gamma_P x}{1 + \gamma_P x} \cdot y_T\right]$$

(4-4)

$$w_\ell = \frac{\gamma_L \ell}{1 + \gamma_L \ell}$$

(4-5)

Table 4-1: Parameter values for the damage models.

Symbol	Definition	Value
Plasma Membrane Damage Distribution		
A	Damage distribution parameter	0.48
B	Damage distribution parameter	0.72
C	Damage distribution parameter	0.16
Extracellular GBP-Mthl10 Signaling		
γ_{D_P}	Scaled protease diffusion constant	0.012
γ_{D_L}	Scaled Gbp diffusion constant	134
γ_S	Scaled protease release rate	0.019
γ_c	Scaled protease cleavage rate	487
γ_P	Scaled total protease amount	1.15
γ_{pL}	Scaled total Gbp amount	0.025
γ_L	Scaled total Gbp amount	1.17
γ_R	Scaled total Mthl10 amount	0.023
γ_w	Scaled protease release radius	2.41

The parameters for the plasma membrane damage distribution are determined through fits to data as explained in the text. The parameters for the extracellular GBP-Mthl10 signaling model are described in more detail in O'Connor et. al. 2021 (Section 3.5.10), but are obtained assuming a calcium signaling threshold of $w_\ell = 0.05$ rather than 0.5.

4.3.3 Single-cell model

For each cell in the tissue mesh, the local micro-tear permeability and fraction of GBP-bound Mthl10 receptors is determined as above and coupled into a single-cell model that uses ordinary, nonlinear differential equations to represent a common set of calcium signaling machinery. The single-cell model tracks cytosolic calcium c, ER calcium c_{ER}, cellular IP3 levels p, and the IP3 Receptor (IPR) inactivation parameter h. At the most general level, the ODEs for cytosolic and ER calcium concentrations are based on fluxes and buffering:

$$\frac{dc}{dt} = \beta \cdot \left(J_{\mathrm{ER}} + J_{\mathrm{PM}} + J_{\mathrm{GJ,Ca^{2+}}} \right) \tag{4-6}$$

$$\frac{dc_{ER}}{dt} = -\epsilon \cdot J_{ER} \tag{4-7}$$

where J_{ER}, J_{PM}, and $J_{GJ,Ca^{2+}}$ are respectively calcium fluxes between a single cell's cytosol and ER, between a cell's cytosol and the extracellular space across its plasma membrane, and between adjacent cells through gap junctions. The parameter ϵ is the ratio of cytosolic to ER volume, which is needed to express the rate of change of ER calcium concentration in terms of cytosolic calcium fluxes. The variable β represents rapid buffering of cytosolic calcium:

$$\beta = \left(1 + \frac{K_e \cdot B_e}{(K_e + c)^2} + \frac{n_x \cdot K_x^{n_x} \cdot B_x \cdot c^{n_x - 1}}{\left(K_x^{n_x} + c^{n_x}\right)^2}\right)^{-1} \tag{4-8}$$

where K_e and B_e are the dissociation constant and total concentration of endogenous buffers, and K_x and B_x are corresponding parameters for the exogenous, genetically encoded calcium indicator GCaMP6m. Eq. (4-8) follows from the derivation in Wagner et al. 1994[172] but with the exogenous buffer term modified to reflect GCaMP6m's experimentally determined Hill coefficient of n_x = 2.96[173].

The value of 5 µM for the total GCaMP concentration (B_x) was chosen in order to be a substantial concentration value without disallowing calcium oscillations completely. Values for the other parameters in this section are taken from various literature sources, and all parameter values and justifications for the single-cell model can be found in Table 4-2.

Calcium movement across the plasma membrane of a single cell is modeled by five fluxes: a micro-tear flux present only in damaged cells, a leak flux, and fluxes through store operated channels, PMCA pumps, and a generalized high-capacity pump.

$$J_{PM} = J_{\mu T} + J_{lk,PM} + J_{SOC} - J_{PMCA} - J_{HC} \tag{4-9}$$

The micro-tear and leak fluxes are modeled as proportional to the difference in calcium concentration across the plasma membrane:

$$J_{lk,PM} = \eta_{lk,PM} \cdot (c_{ext} - c) \tag{4-10}$$

$$J_{\mu T} = \eta_{\mu T}(r,t) \cdot (c_{ext} - c) = \eta_{\mu T,0} \cdot s_{\mu T}(r) \cdot \exp\left(-\frac{t}{\tau_{heal}}\right) \cdot (c_{ext} - c) \tag{4-11}$$

where the leak permeability $\eta_{lk,PM}$ is constant and the initial micro-tear permeability $s_{\mu T}(r)$ varies with distance from the wound to represent the spatial distribution of membrane damage (see Section 4.3.2.1). The micro-tear permeability decays exponentially with time constant τ_{heal} to represent membrane damage repair. For each cell in the tissue mesh, r is the distance from the wound center to the centroid of the cell.

The PMCA and high-capacity pump fluxes are modeled as Hill functions dependent on cytosolic calcium:

$$J_{PMCA} = J_{PMCA,max} \cdot \frac{c^{n_{PMCA}}}{K_{PMCA}^{n_{PMCA}} + c^{n_{PMCA}}} \tag{4-12}$$

$$J_{\text{HC}} = J_{\text{HC,max}} \cdot \frac{c^{n_{\text{HC}}}}{K_{\text{HC}}^{n_{\text{HC}}} + c^{n_{\text{HC}}}} \tag{4-13}$$

The PMCA is needed to regulate resting calcium levels as well as the calcium flares at lower concentrations, and the high-capacity pump term is needed in order for the first expansion to retract. The model is agnostic as to the what the high-capacity pump represents; however, the typical counterpart to the PMCA that is responsible for maintaining cytosolic calcium levels is the sodium-calcium exchanger (NCX) which has been shown to indirectly regulate cell migration in epithelial tissues [174]. A complete model of the NCX would require the inclusion of sodium dynamics that are beyond the scope of the model, and so a general calcium-dependent Hill function is used.

The SOC flux is represented as a Hill function dependent on ER calcium[175]

$$J_{\text{SOC}} = J_{\text{SOC,max}} \cdot \frac{K_{\text{SOC}}^{n_{\text{SOC}}}}{K_{\text{SOC}}^{n_{\text{SOC}}} + c_{\text{ER}}^{n_{\text{SOC}}}} \tag{4-14}$$

In Eqs. (4-12) - (4-14), each J_{max} represents a maximum flux value, each K represents the calcium concentration at half-maximal activity, and each n controls the steepness of the switch from low to high activity. Note that the directionality of these three fluxes is represented directly by the sign preceding each in Eq. (4-9) (negative for outward fluxes).

Values for parameters $\eta_{\text{lk,pm}}$, $J_{\text{PMCA,max}}$, and $J_{\text{SOC,max}}$ were chosen to give desired resting cytosolic calcium concentrations ($\sim$ 0.1 µM) for single cells as well as to produce propagative calcium waves in the tissue model. Values for parameters τ_{heal} and $\eta_{\mu\text{T},0}$ were chosen such that an isolated cell with a micro-tear permeability of $0.95 \cdot \eta_{\mu\text{T},0}$ would reach half of maximum fluorescence in 25 seconds given all other model

parameters, consistent with experimental data (not shown). Values for parameters $J_{HC,max}$, K_{HC}, and n_{HC} were chosen such that the time and spatial extent of the first expansion matched experimental data.

4.3.3.2 ER calcium fluxes

Calcium exchange between the cytosol and the ER is determined by three fluxes: a leak flux plus fluxes through the SERCA pump and IP3 receptors:

$$J_{ER} = J_{lk,ER} - J_{SERCA} + J_{IPR} \qquad \text{(4-15)}$$

Similar to above, the leak flux simply follows the difference in calcium concentrations between ER and cytosol,

$$J_{lk,ER} = \eta_{lk,ER} \cdot (c_{ER} - c) \qquad \text{(4-16),}$$

and the SERCA pump is modeled as a Hill function dependent on cytosolic calcium levels,

$$J_{SERCA} = J_{SERCA,max} \cdot \frac{c^{n_{SERCA}}}{K_{SERCA}^{n_{SERCA}} + c^{n_{SERCA}}} \qquad \text{(4-17).}$$

For the IPR flux, We use the relatively simple, effective and widely used model from Li and Rinzel 1994[42] for which channel inactivation through low-affinity calcium binding sites is assumed to be much slower than activation through IP3 and high-affinity calcium binding. The overall form is

$$J_{IPR} = \eta_{IPR} \cdot m_\infty^3 \cdot h^3 \cdot (c_{ER} - c) \qquad \text{(4-18)}$$

where m_∞ and h are respectively fast activation and slow inactivation variables. They are cubed because channel opening requires the coordination of three active IPR subunits. The "fast" activation variable m_∞ depends on cytosolic IP3 levels p and calcium levels c

$$m_\infty = \left(\frac{p}{d_1 + p}\right) \cdot \left(\frac{c}{d_5 + c}\right) \tag{4-19}$$

where d_1 and d_5 are the concentrations at which p and c respectively have half-maximal effects. The "slow" inactivation variable h evolves with time according to

$$\frac{\mathrm{d}h}{\mathrm{d}t} = \frac{h_\infty - h}{\tau_h} \tag{4-20}$$

$$\tau_h = \frac{1}{a_2 \cdot (\xi + c)} \tag{4-21}$$

$$h_\infty = \frac{\xi}{\xi + c} \tag{4-22}$$

$$\xi = d_2 \cdot \frac{p + d_1}{p + d_3} \tag{4-23}$$

Although more sophisticated models have been published for the IPR flux[176,177], the Li and Rinzel 1994 model is sufficient for our system.

Values for parameters $\eta_{\mathrm{lk,ER}}$, $J_{\mathrm{SERCA,max}}$, and η_{IPR} were chosen so that resting cytosolic calcium concentrations were ~ 0.1 µM for single cells as well as to produce propagative calcium waves in the tissue model.

4.3.3.3 IP₃ dynamics

IP3 is generated downstream of GBP binding to Mthl10, a G-protein-coupled receptor. This is a multi-step process in which ligand-receptor binding activates the $G_{\alpha q}$-protein, which then binds to and activates PLCβ in a calcium-dependent manner, and this complex then cleaves PIP₂ into diacylglycerol (DAG) and IP₃. Although detailed models for this type of signaling cascade have been published[163], we do not have sufficient data to determine those model parameters for our experimental system and have therefore opted for a simpler model of the IP₃ production rate (V_{PLC}) that uses a product of Hill functions to represent the cascade's activation by cytosolic calcium c and the fraction of GBP-bound Mthl10, w_ℓ (as described in Section 4.3.2.2)

$$V_{\mathrm{PLC}} = \alpha \cdot \left(\frac{c}{K_{\mathrm{PLC}} + c} \right) \cdot \left(\frac{w_\ell{}^{n_\ell}}{K_\ell{}^{n_\ell} + w_\ell{}^{n_\ell}} + w_0 \right) \tag{4-24}$$

where α is the maximum IP₃ production rate, n_ℓ is a Hill coefficient that controls how sensitive IP₃ production is to damage-induced GBP-signaling, and w_0 serves to keep a base-line rate of IP₃ production in the absence of a wound. Following Lemon et al. 2003[163], the Hill exponent for the calcium dependence was set to one.

IP3, levels also change due to degradation, assumed to be first order, and flux through gap junctions, yielding

$$\frac{dp}{dt} = V_{\mathrm{PLC}} - V_{\mathrm{deg}} + J_{\mathrm{GJ,IP_3}} \tag{4-25}$$

where p is the cytosolic concentration of IP₃, and

$$V_{\mathrm{deg}} = k_{\mathrm{deg}} \cdot p \tag{4-26}$$

with k_{deg} constant.

Values for parameters α, n_ℓ, and w_0 were chosen to allow for propagative calcium waves in the tissue-level model as well as to match the time and spatial extent of the distal calcium response to experimental data.

4.3.3.4 Gap junction transfer of calcium and IP₃

Adjacent cells are connected by gap junctions that permit intercellular diffusion of both calcium and IP₃. We use a simple model that does not include any gating effects. Therefore, for cell j, the gap junction flux terms for calcium and IP₃ are given respectively by

$$J_{\mathrm{GJ,Ca^{2+}}} = \eta_{\mathrm{GJ,Ca^{2+}}} \cdot \sum_{i \in \mathrm{adj}} \frac{A_0}{A_j} \cdot \frac{L_{i,j}}{L_0} \cdot (c_i - c_j) \tag{4-27}$$

$$J_{\mathrm{GJ,IP_3}} = \eta_{\mathrm{GJ,IP_3}} \cdot \sum_{i \in \mathrm{adj}} \frac{A_0}{A_j} \cdot \frac{L_{i,j}}{L_0} \cdot (p_i - p_j) \tag{4-28}$$

where each sum is over all cells adjacent to cell j. A_j is the 2-dimensional area in the plane of the tissue covered by cell j, and $L_{i,j}$ is the length of the shared edge between cell i and cell j. Parameters A_0 and L_0 are a reference area and length respectively, and the ratios A_0/A_j and $L_{i,j}/L_0$ are explicitly included so that the gap junction permeabilities $\eta_{\mathrm{GJ,Ca^{2+}}}$ and $\eta_{\mathrm{GJ,IP_3}}$ are the same for every cell in the tissue and have comparable dimensions to other η parameters in the model corresponding to fluxes due to concentration differences. For cells on the wound margin, a residual gap junction

connection to the wound ($0.025 \cdot \eta_{\text{GJ}}$) was maintained to reproduce the long-term, high calcium observed around the wound.

The value for parameter $\eta_{\text{GJ,Ca}^{2+}}$ was chosen to match the time and spatial extent of the first expansion to experimental data. The value for parameter $\eta_{\text{GJ,IP}_3}$ was chosen to allow for propagative calcium waves in the tissue model. The value for parameters A_0 and L_0 were measured from segmented tissue images as the average cell area and perimeter respectively; however, the exact values of these parameters are irrelevant; the full gap junction parameter is $(A_0/L_0) \cdot \eta_{\text{GJ}}$ for both calcium and IP3.

4.3.4 Resting levels and initial conditions

Initial conditions for each cell were determined by running the tissue model with no micro-tears ($\eta_{\mu T}(r) = 0$) and no Mthl10 activation ($w_\ell(r, t) = 0$) for up to 300 s. Model parameters were selected to ensure that resting cytosolic calcium and IP3 concentrations did not deviate too far from 0.1 μM and 10 nM respectively, and that resting ER calcium concentrations were on the order of 100 μM. The cytosolic calcium concentration within the wound was set to be constant and equal to extracellular calcium concentration c_{ext} = 1 mM.

4.3.5 GCaMP fluorescence

GCaMP fluorescence F is obtained from the model using a Hill function of the free calcium concentration as specified by Chen et al. 2013[173]

$$F - F_{\min} = (F_{\max} - F_{\min}) \cdot \frac{c^{n_x}}{c^{n_x} + K_x^{n_x}} \qquad \text{(4-29)}$$

where $F_{\min}$ is the fluorescence when $c = 0$, and $F_{\max}$ is the fluorescence at saturation

when $c \gg K_x$. However, with our *in vivo* system we are not able to determine the

GCaMP fluorescence when no calcium is present. Therefore, with the assumption of the

resting calcium concentration being $c_0 = 0.1~\mu\text{M}$, we can express the fluorescence F in

terms of the resting fluorescence F_0 as

$$F = \frac{\left(c^{n_x} - c_0^{n_x}\right) \cdot F_{max} + \left(c_0^{n_x} + K_x^{n_x}\right) \cdot F_0}{c^{n_x} + K_x^{n_x}} \qquad \text{(4-30)}$$

Since GCaMP is a cytosolic reporter, the wound is treated as having no GCaMP, and

thus appears black in figures below.

Values for parameters F_0 and $F_{\max}$ were obtained from GCaMP fluorescence

images after wounding from average fluorescence values in regions of resting cytosolic

calcium and high cytosolic calcium respectively.

Table 4-2: Single-cell model parameter values.

Symbol	Definition	Value	Notes
Ca²⁺ dynamics			
ϵ	Ratio of cytosolic to ER volume	5.4	Wagner and Keizer (1994)
B_e	Concentration of endogenous buffer	150 μM	Wagner and Keizer (1994)
K_e	Endogenous buffer dissociation constant	10 μM	Wagner and Keizer (1994)
B_x	Concentration of GCaMP	5 μM	See text
K_x	GCaMP dissociation constant	0.167 μM	Chen et al. (2013)
n_x	GCaMP Hill coefficient	2.96	Chen et al. (2013)
Plasma membrane Ca²⁺ fluxes			
c_{ext}	Extracellular Ca²⁺ concentration	1 mM	Kusters et al. (2005)[178]
$\eta_{lk,PM}$	Plasma Membrane leak permeability	$2.5 \times 10^{-6}~\text{s}^{-1}$	See text
$\eta_{\mu T,0}$	Maximum micro-tear permeability	$0.411~\text{s}^{-1}$	See text
τ_{heal}	Micro-tear healing time constant	5.25 s	See text
$J_{PMCA,max}$	Maximum PMCA Ca²⁺ flux	$1.2~\mu\text{M s}^{-1}$	See text
K_{PMCA}	PMCA dissociation constant	.1 μM	Dupont et al. (2016)
n_{PMCA}	PMCA Hill coefficient	2	Dupont et al. (2016)
$J_{HC,max}$	Maximum high-capacity pump Ca²⁺ flux	$10~\mu\text{M s}^{-1}$	See text
K_{HC}	High-capacity pump dissociation constant	1.6 μM	See text

Symbol	Definition	Value	Notes
n_{HC}	High-capacity pump Hill coefficient	2.5	See text
$J_{SOC,max}$	Maximum SOC Ca^{2+} flux	1.5 µM s^{-1}	See text
K_{SOC}	SOC dissociation constant	187 µM	Dupont and Sneyd (2017)
n_{SOC}	SOC Hill coefficient	3.8	Dupont and Sneyd (2017)
ER Ca^{2+} fluxes			
$\eta_{lk,ER}$	ER leak permeability	0.01 s^{-1}	See text
$J_{SERCA,max}$	Maximum SERCA Ca^{2+} flux	5 µM	See text
K_{SERCA}	SERCA dissociation constant	.1 µM	Wagner and Keizer (1994)
n_{SERCA}	SERCA Hill coefficient	2	Wagner and Keizer (1994)
η_{IPR}	IPR channel permeability	4 s^{-1}	See text
d_1	IPR channel kinetic parameter	0.13 µM	Wagner and Keizer (1994)
d_2	IPR channel kinetic parameter	1.05 µM	Wagner and Keizer (1994)
d_3	IPR channel kinetic parameter	0.943 µM	Wagner and Keizer (1994)
d_5	IPR channel kinetic parameter	0.0823 µM	Wagner and Keizer (1994)
a_2	IPR channel kinetic parameter	0.2 µM^{-1} s^{-1}	Wagner and Keizer (1994)
IP$_3$ dynamics			
α	Maximum rate of IP$_3$ production	0.9 µM s^{-1}	See text
K_{PLC}	Dissociation constant of PLC	0.4 µM	Lemon et al. (2003)
K_ℓ	EC$_{50}$ of Gbp-Mthl10 activity	0.05	O'Connor et al. (2021)
n_ℓ	Hill coefficient of Gbp-Mthl10 activity	5	See text
w_0	Baseline Gbp-Mthl10 activity	0.1	See text
V_{deg}	IP$_3$ degradation rate	1.25 s^{-1}	Lemon et al. (2003)
Gap junction fluxes			
$\eta_{GJ,Ca^{2+}}$	Gap Junction Ca^{2+} permeability	2 s^{-1}	See text
η_{GJ,IP_3}	Gap Junction IP$_3$ permeability	4 s^{-1}	See text
A_0	Average two-dimensional cell area	43 µm^2	See text
L_0	Average cell perimeter	23 µm	See text
GCaMP fluorescence			
c_0	Ideal resting Ca^{2+} concentration	0.1 µM	Lemon et al. (2003)
F_0	GCaMP fluorescence before wounding	0.0997 a.u.	See text
F_{max}	GCaMP fluorescence at saturation	0.142 a.u.	See text

4.3.6 Method of solution

The Gbp-Mthl10 signaling model equations are solved over a radially symmetric, continuous space and over time. Further details on the method of solution can be found in Section 3.5.6. The initial conditions for each cell in the single-cell model are obtained by running the model for an extended time with no wound ($\eta_{\mu T,0} = 0$ and $w_\ell = 0$). All numerical solutions of the model equations are performed in Mathematica version 12 on the ACCRE cluster at Vanderbilt University. A single model run along with output video production takes roughly 1.5 to 2.5 hours.

4.3.7 Experimental methods

Full experimental methods including fly genetics, fly preparation and mounting for laser ablation, the laser-ablation process, and live imaging follow those from the work presented in Chapter 3 and can be found in Appendix C.

4.4 Results

4.4.1 Model validation

4.4.1.1 Control calcium signaling dynamics

Applying Eqs. (*4-1*) - (*4-5*) across the entire tissue and Eqs. (*4-6*) - (*4-28*) for each cell in the tissue, the model can calculate cytosolic calcium concentration as a function of time for each cell in the tissue. Applying Eq. (*4-30*) then yields expected GCaMP fluorescence for direct comparison to experiments. Using the parameters in Table 4-2 for every cell, the model yields uniform resting levels of cytosolic calcium, ER calcium, and IP_3 that match expected ranges: 0.09 μM, 220 μM and 13 nM, respectively.

A key measure of model validity is its reproduction of wound-induced calcium signaling on similar spatial and temporal scales as observed *in vivo*. A comparison of model and experiment is shown in Figure 4-3, with still images at key times shown in Figure 4-3A-C and the corresponding calcium signal radius versus time graphs shown in Figure 4-3A'-C'. Similar to experiments, the model yields a first expansion that reaches roughly 60 μm from the wound center within ~20 s, and then recedes. It also yields an appropriate distal calcium response that becomes apparent 50-90 s after wounding and reaches cells 120-150 μm from the wound center. Finally, as in

experiments, the model produces transient calcium waves or flares that extend further into the tissue. Nonetheless, the model with uniform parameters in every cell yields a calcium response that is too uniform and too radially symmetric (Figure 4-3B). Adding some cell-to-cell variability provides a much closer match to experiments (compare Figure 4-3A and Figure 4-3C).
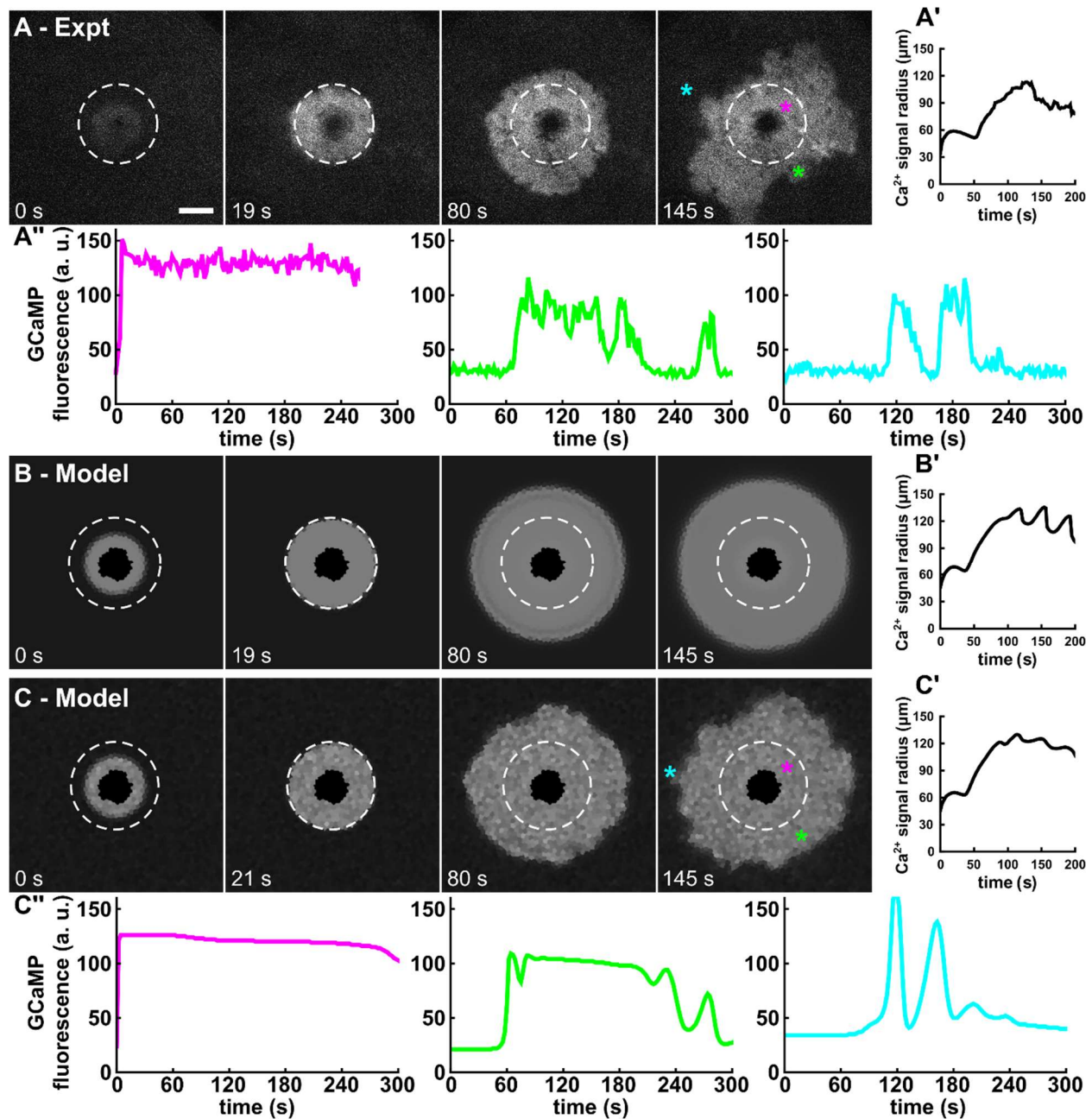
Figure 4-3: Matching the model to experiments.

(A) Experimental wound-induced calcium response in control/wild-type tissue. Maximum radius of the first calcium expansion occurs at 19 s after wounding in this example and is marked by a white circle. Scale bar is 50 μm and applies to all images. **(B)** Model response when uniform parameters are used for all cells. **(C)** Model response when the GCaMP parameter B_x and the IP$_3$ production parameter α varies from cell to cell by sampling from a log-normal distribution. Such variation is needed to break radial symmetry of the calcium oscillations. **(A'-C')** Corresponding quantifications of the

calcium signal radius as a function of time. **(A'', C'')** Dynamic calcium signals at select locations that demonstrate matching single-cell dynamics in model and experiment.

4.4.1.2 The role of cellular variability

We investigated the impact of cellular variability across the tissue by running the model where a single parameter varied from cell to cell. Variability was imposed by multiplying a given base parameter from Table 4-2 with a cell-specific random number chosen from a log-normal distribution (associated normal distribution mean of 1 and variance of 0.2). From these single-parameter variation runs, two parameters stood out. First, varying the total GCaMP concentration within each cell, B_χ, results in a minimal change in calcium signaling dynamics, but produces fluorescence variation as seen in experiments. Second, varying the IP₃ production rate parameter, α, breaks the radial symmetry of the calcium waves around the wound and produces stochastic flaring behavior that matches experiments. The model output with variation in both of these parameters is shown in Figure 4-3C,C' and will be taken as the base control model from here forward. Additionally, each subsequent run of the model with parameter variation utilizes a different random seed to generate a different set of randomly determined parameters for each run.

Single-parameter variability runs were performed for model parameters that do not have a set, referenced value in Table 4-2. These runs divide the parameters into five main groups based on the qualitative model output they produce upon variation. Variation of α or η_{IPR} produces an "ideal" response where radial symmetry is broken and calcium flares are produced. In contrast, variation of B_x, $\eta_{GJ,Ca^{2+}}$, η_{GJ,IP_3}, $J_{HC,max}$,

$\eta_{\text{lk,PM}}$, $\eta_{\mu\text{T}}$, or τ_{heal}, many of which only deal with the first expansion, produces no qualitative differences in the model output as compared to the no-variation model. Variation of w_0 n_ℓ, or K_{PMCA} produces spiral waves that branch off from the region of high calcium. Spiral waves are also produced upon variation of K_{HC}, n_{HC}, $J_{\text{PMCA,max}}$, $J_{\text{SOC,max}}$, $\eta_{\text{lk,ER}}$, $J_{\text{SERCA,max}}$, or K_{SERCA}; however, the initial conditions vary greatly from cell to cell, indicating that these parameters serve to control resting calcium levels in the model. Finally, variation of K_ℓ results in calcium oscillations that arise independently of the region of high-calcium around the wound; regions of cells that are highly sensitive to the damage signal are produced in this case. Examples of these model outputs can be found in Figure 4-4.
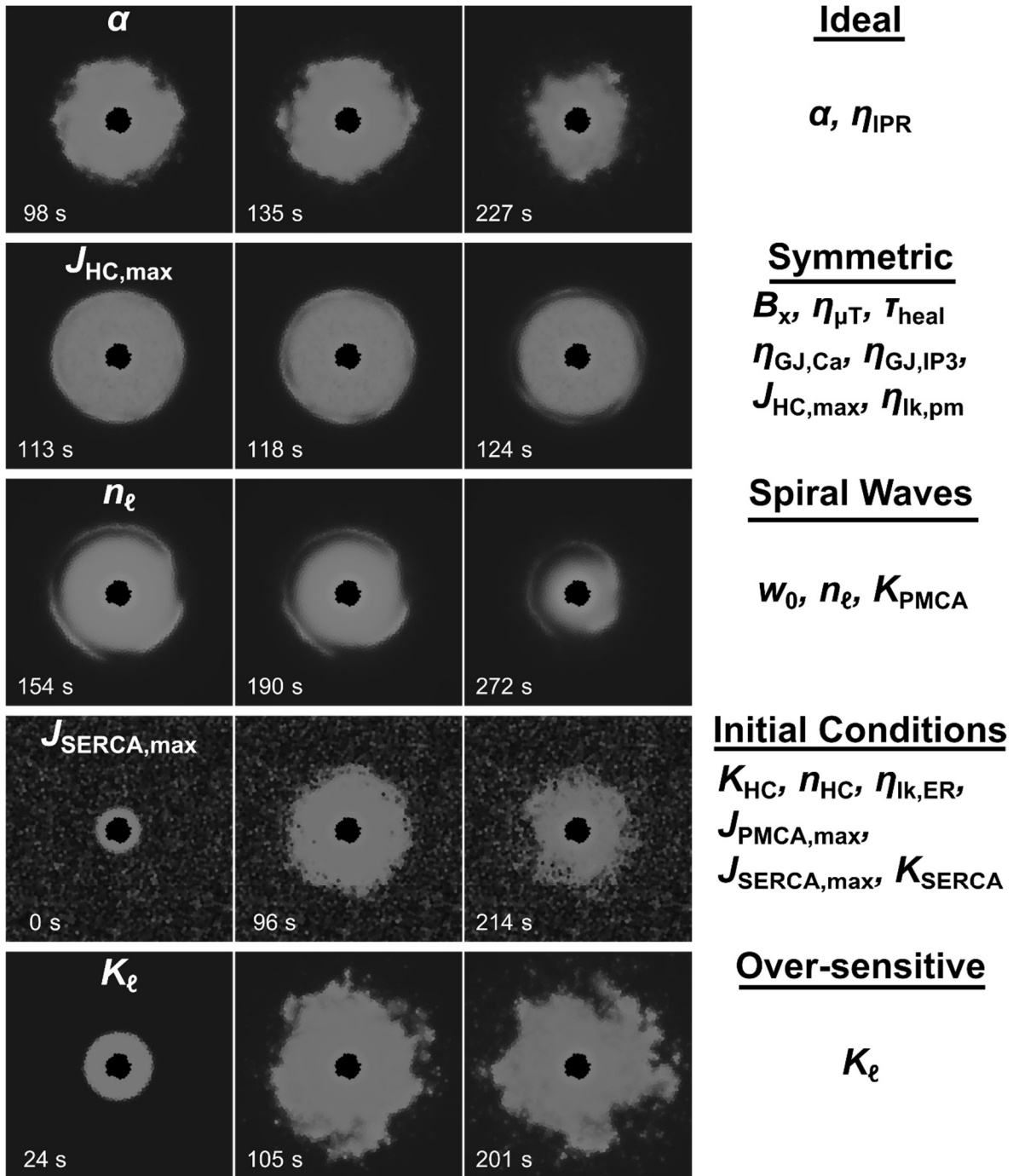
Figure 4-4: Examples of single-parameter variation model outputs.

Parameters are grouped based on the model output when only that parameter varies
from cell to cell by sampling from a log-normal distribution. One example output of each
group is shown in each row, with the full list of parameters in each group in the right-
most column. Frames were chosen that best show the group behavior. "Ideal": model
outputs where radial symmetry is broken and calcium flares are produced. "Symmetric":

model outputs where calcium oscillations are radially symmetric, similar to having no parameter variation (Figure 4-3B). "Spiral Waves": Model outputs where spiral waves emerge around the high-calcium region. "Initial Conditions": model outputs where initial conditions have large variations; spiral waves are also present. "Over-sensitive": model output where flares and calcium oscillations arise independently of the high-calcium region.

4.4.1.3 In silico *knockdowns*

As a second validation step, we performed *in silico* knockdowns and compared them to *in vivo* genetic knockdown experiments. Following methods from O'Connor et al. 2021[164] (given in Appendix C), experiments were run using an internally controlled experimental system: a Gal4-driven RNAi was used to knock-down a gene of interest in one section of the *Drosophila* pupal notum known as the pannier (*pnr*) domain, and a wound was made on the *pnr*-domain boundary. The wound response would thus be asymmetric, with a knockdown on one side and an internal control on the other. We generated similar *in silico* knockdowns in the model by reducing appropriate parameters for cells in just one section of the tissue mesh.
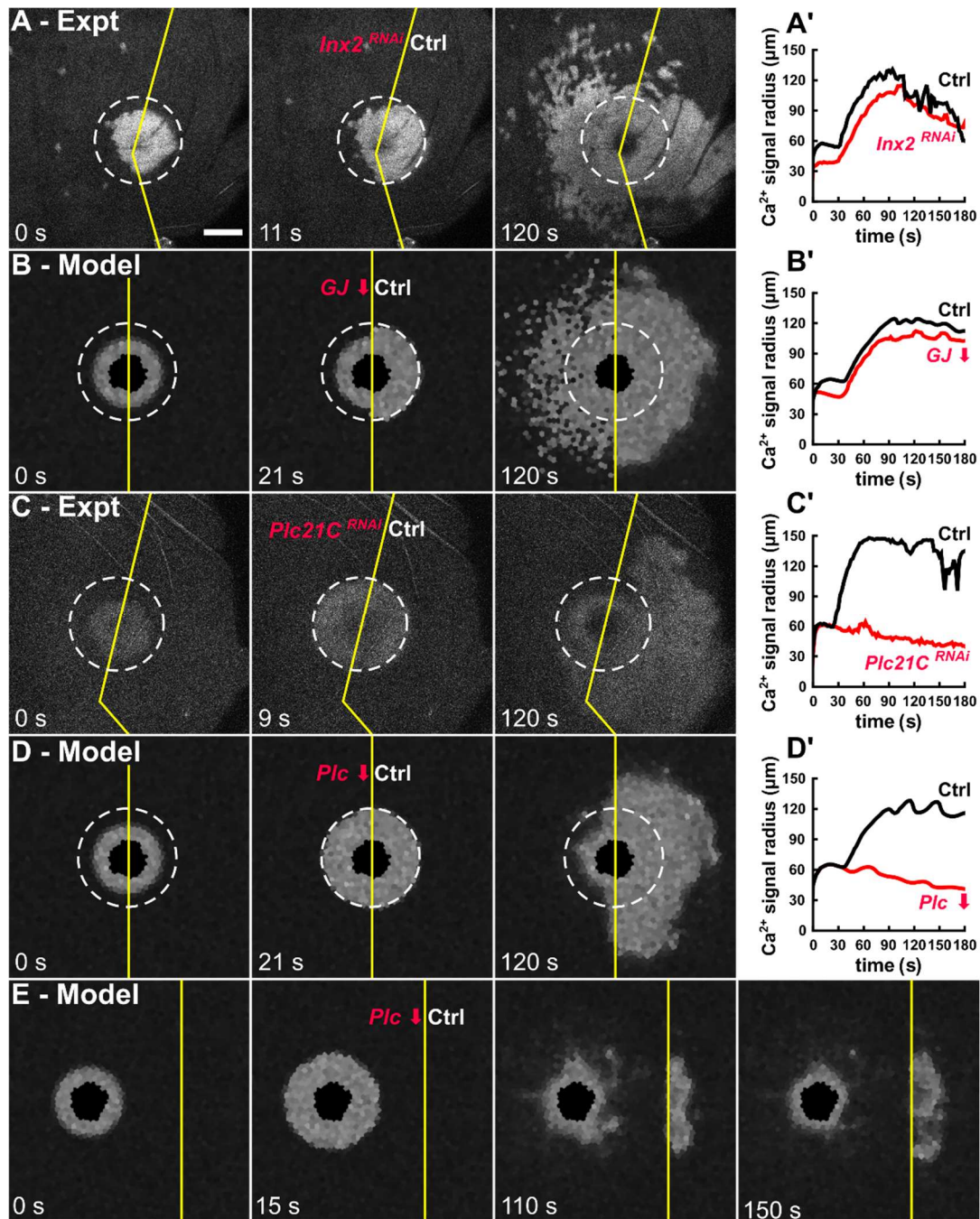
Figure 4-5: The mathematical model replicates knockdown experiments.

(A-D) Wound-induced calcium responses with gap junctions knocked down (A-B) and PLCβ knocked down (C-D) both *in vivo* (A, C) and *in silico* (B, D). Scale bar is 50 µm and applies to all images. **(A'-D')** Corresponding quantifications of the calcium signal radius on each side of the wound as a function of time. **(E)** Model replication of the "jump the gap" experiment; experimental data shown in Figure 3-1H, H'.

Knocking down gap junctions ($Inx2^{RNAi}$) has two effects on wound-induced calcium signals[113]. First, because calcium can no longer move between adjacent cells, the first expansion is prevented (Figure 4-5A, A'). In the experimental example shown, this effect is most evident via the asymmetry at 11 s after wounding. Second, the later, distal calcium response proceeds in a "speckled" pattern (Figure 4-5A, 120 s after wounding), i.e., the correlation between adjacent cells is greatly reduced. Nonetheless, the distal response still occurs on similar spatial and temporal scales in the knockdown and control sides of the wound (Figure 4-5A'). To model *in silico* knockdowns of gap junctions, we reduced the gap junction permeabilities $\eta_{GJ,Ca^{2+}}$ and η_{GJ,IP_3} by 90%. As shown in Figure 4-5B, B', this *in silico* gap junction knockdown produces the same two characteristic impacts. Gap junction fluxes in the model thus function to allow the first expansion and coordinate large-scale correlations in the distal calcium response.

Knocking down any component of the G-protein cascade – *mthl10*, $G_{\alpha q}$, or *PLCβ* – results in a loss of the distal calcium response[164]. An experimental example of one such knockdown of *PLCβ* ($Plc21C^{RNAi}$) is shown in Figure 4-5C, C'. The model contains a simplified version of the cascade that links the degree of Mthl10 activation to the downstream IP$_3$ production rate (Eq. (4-24)). A reduction of the parameter α in Eq. (4-24) is thus equivalent to a *PLCβ* knockdown; it could also be interpreted as a knockdown of $G_{\alpha q}$. In either case, an *in silico* knockdown that reduces α by 70% (similar to RNAi-mediated knockdown efficiency [179]) leaves the first expansion unchanged, but eliminates the distal calcium response (Figure 4-5D, D'). Direct knockdowns of the *IPR* also eliminate the distal calcium response in both experiments[164] and the model (Figure 3-1). These observations are all strong matches to experiments.

Further, when $G_{\alpha q}$ is knocked down experimentally and the tissue is wounded in the middle of the *pnr* domain rather than at the *pnr* border, the distal calcium signal appears to "jump the gap" into the control region. This experiment was performed by O'Connor et al. 2021[164] (Figure 3-1H, H') to demonstrate that the signal driving the distal calcium response is propagated extracellularly without the need for any bucket-brigade mechanism. As shown in Figure 4-5E, the "jump the gap" experiment is replicated in the model by simulating a wound inside a *pnr* domain where the parameter α has been reduced by 70% (Plc $\downarrow$). As expected, the distal calcium response skips over the cells with decreased α and appears at 110s after wounding only on the control side of the tissue. This match is not surprising given that the model's reaction-diffusion equations (Eqs. (4-2) - (4-5)) explicitly include extracellular diffusion of active GBP. Importantly, the distal signals in the control domain do not propagate back into the knockdown side in either the model or experiments. This lack of back propagation is a key check that the gap junction fluxes in the model are not too high.

Knocking down either the PMCA or the SOC does not have any noticeable effect on first/distal expansion in both experiments and model. However, these knockdowns respectively lead to higher or lower levels of calcium around the wound at later time points compared to control experiments (not shown), which is the motivation for including them in the model. Knockdowns of the SERCA pumps left many flies unhealthy and unviable for experiments, and in the model these knockdowns produce resting calcium levels way above typical physiological ranges. Therefore, the SERCA pump knockdowns were not considered for assessing the model.

4.4.2 New insights from the model

4.4.2.1 Free cytosolic calcium concentrations

Interpretation of calcium signals from experimental images is limited by the properties of the fluorescent reporter used. Given GCaMP's binding affinity for calcium (K_x = 0.167 μM), its fluorescence saturates at calcium concentrations well below those typically reached during physiological signaling events ($F - F_{\min} \geq 0.95(F_{\max} - F_{\min})$ when c ≥ 0.45 μM). Further, GCaMP's high level of cooperativity ($n_x = 2.96$) essentially gives a binary response of fluorescence "on" or "off". Therefore, although GCaMP is useful for indicating elevated cytosolic calcium, it has limited ability to differentiate just how elevated. Although ratiometric calcium indicator dyes are better able to quantify calcium concentrations[180], they cannot be used in the *Drosophila* pupal notum due to its impermeable cuticle.

The model reported here provides an alternate way to estimate the cytosolic levels of calcium around wounds. In fact, these levels are directly calculated in the model before using Eq. (4-30) to evaluate expected GCaMP fluorescence. Figure 4-6A, B respectively show the GCaMP fluorescence around a control *in silico* wound and a heat map of the corresponding cytosolic calcium concentrations. The calcium concentration heat map highlights two interesting details that are not evident from GCaMP fluorescence. First, regions of rather uniform GCaMP fluorescence can hide large gradients of calcium concentration. This effect is most evident at 60 s after wounding when the calcium signals are a mix of the initial influx through plasma membrane damage, the first expansion through gap junctions, and the beginnings of IP3-mediated release from intracellular stores. At this time, the model reports calcium

gradients between cells not adjacent to the wound as large as 1.5 $\mu M/\mu m$. Note that the scale of the heat map saturates at 1 µM. This choice of scale provides better visualization of distal calcium oscillations, but the calcium signals within the region of plasma membrane damage are then way off scale, reaching hundreds of µM. Second, one can observe the phasing of different parts of each calcium wave or flare. For example, there is an oscillation just trailing the front of the distal expansion that is not evident in the fluorescence signals. The model calculations provide a cautionary example that cells within the calcium signaling region can have similar GCaMP fluorescence levels and yet experience drastically different calcium concentration histories.
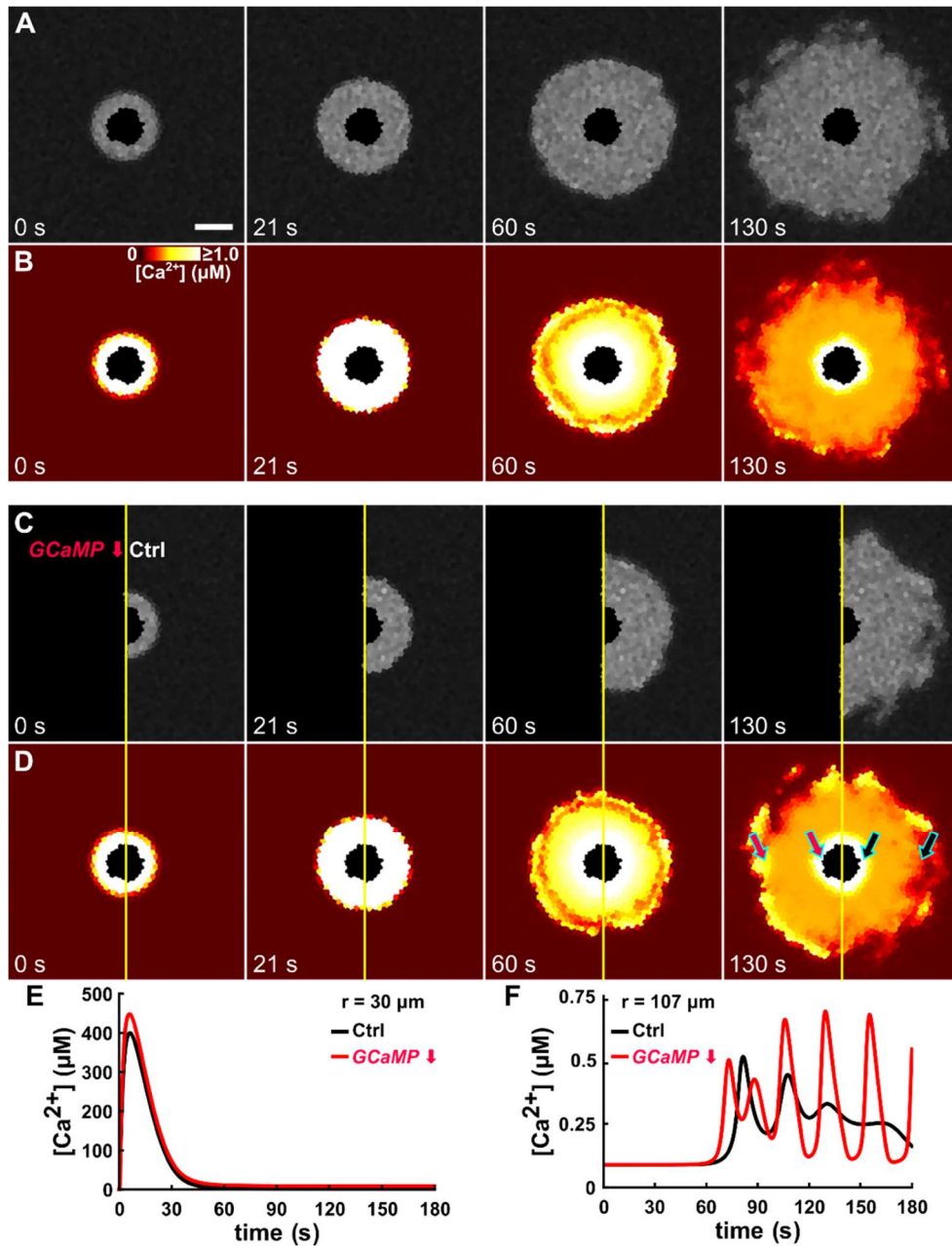
Figure 4-6: The model elucidates hidden structure in the free calcium concentrations.

(A-B) GCaMP fluorescence and corresponding free cytosolic calcium concentration in a control system. **(C-D)** Same in a GCaMP knockdown. Scale bar is 50 μm and applies to all images. The color scale for free cytosolic calcium is shown in B and applies to all images in B and D. Note that the scale saturates at 1.0 μM and that the wound region has been colored black since it is not cytosolic. **(E)** Free cytosolic calcium versus time for cells close to the wound; locations as marked by inner arrows in D. **(F)** Same for cells further from the wound; locations marked by outer arrows in D.

4.4.2.2 GCaMP's effect on calcium signals

The fluorescent calcium reporter GCaMP is also a buffer of calcium. The ability of buffers to impact calcium oscillations has been studied extensively both experimentally and theoretically; buffers decrease oscillation amplitude and frequency, even to the point of preventing calcium oscillations and waves altogether[22,172,181]. Given how information in calcium signals can be encoded by both amplitude and frequency[24,182], it is important to understand how the presence of GCaMP alters calcium signals following wounding.

We therefore ran an *in silico*, internally controlled knockout of GCaMP. Experimentally, this would be useless: no GCaMP would mean no fluorescent reporter of calcium; however, as shown in Figure 4-6C-D, the model can directly report the free cytosolic calcium concentration, with or without GCaMP. The absence of GCaMP as a buffer has three modest but discernable effects. First, the initial influx yields a ~10% higher peak of free cytosolic calcium levels (Figure 4-6E). Second, the distal calcium expansion occurs slightly earlier (Figure 4-6F). Third, the absence of GCaMP leads to distal calcium oscillations with a larger amplitude and frequency (Figure 4-6F). Consistent with observations of GCaMP expression not disrupting biological processes[173], the size of these impacts is small under the levels of GCaMP used here, but they would increase if GCaMP were expressed more strongly.

4.4.2.3 The roles of intercellular calcium and IP$_3$ transfer

Intercellular coupling of cells is a necessary condition for intercellular calcium waves to initiate and persist across a tissue[21]. The model presented here allows for the

gap-junction transfer of both cytosolic calcium and IP$_3$ (Eqs. (4-27) and (4-28)). Although knockdown experiments cannot individually determine the importance of each species' gap junction flux, the model presented here and matched to experiments does provide such insight.

During the first expansion, the amount of calcium moving through gap junctions is ~1000-fold higher than IP$_3$ (Figure 4-7A); however, during the distal expansion and subsequent flares, calcium and IP$_3$ have similarly sized fluxes (Figure 4-7B). This difference suggests that the relative importance of each flux may change with time after wounding. Nonetheless, the relative fluxes do not necessarily equate to importance. One must also consider how the fluxes change each species' concentration and how those concentrations compare to the half-maximal effect levels for downstream steps.
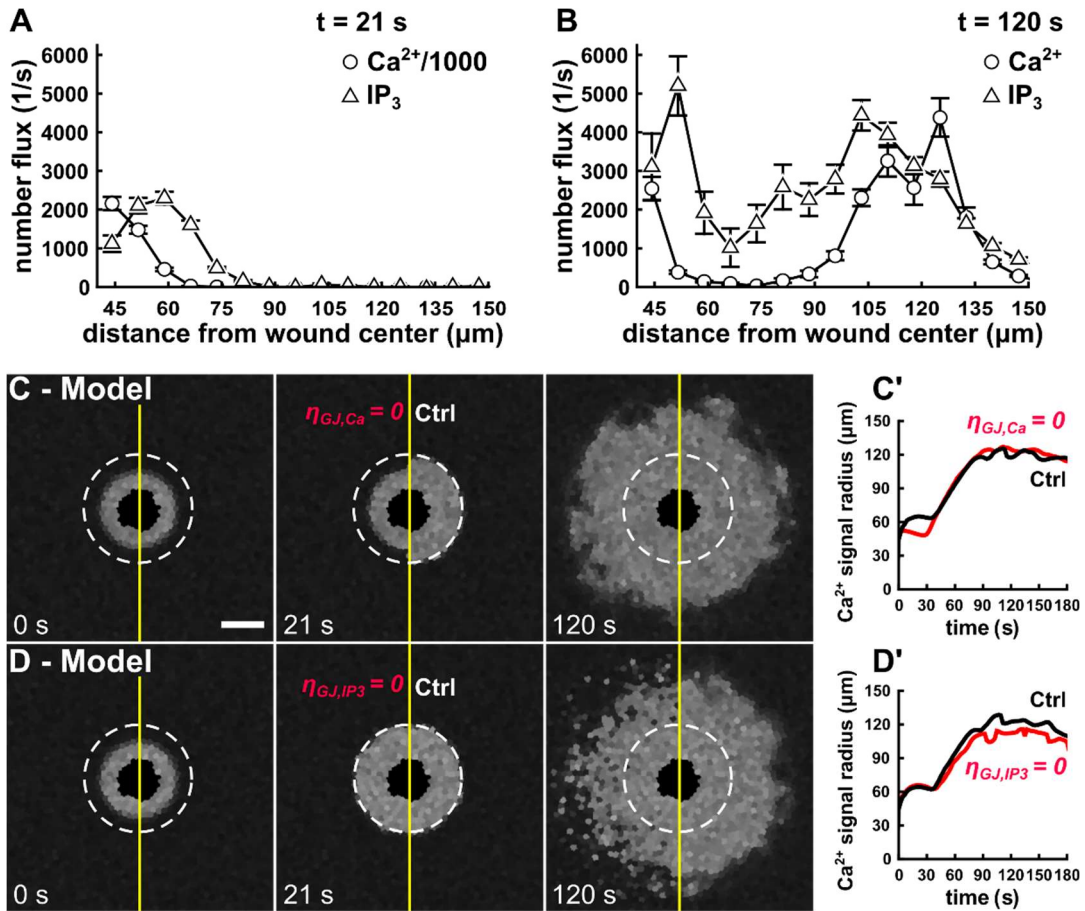
Figure 4-7: Model demonstrates different roles for gap-junction fluxes of calcium and IP₃.

(A-B) Quantification of average gap-junction fluxes, binned by distance from the wound center at both the maximum extent of the first expansion (21 s after wounding) and just after completion of the second distal expansion (120 s). Error bars denote standard error of the mean. Note that the calcium fluxes in A have been divided by a factor of 1000 to plot on the same scale as IP₃ fluxes. **(C-D)** Model responses after selective *in silico* knockdown of gap-junction fluxes for either calcium (C) or IP₃ (D). Scale bar is 50 μm and applies to all images. **(C'-D')** Corresponding quantifications of the calcium signal radius as a function of time.

The model does provide a path to exploration currently unavailable in experiments: we can run simulations in which one species' gap junction flux is eliminated but the other is left unchanged. To highlight the impact of each flux

elimination, we run the simulations as an internally controlled knockdown system. When only the calcium flux is eliminated, the first expansion is nonexistent (Figure 4-7C; $\eta_{GJ,Ca} = 0$). This result matches the effect of a full gap junction knockdown on the first expansion (Fig 3A,B, t = 11 or 21s). On the other hand, eliminating the calcium flux still allows for a coordinated distal expansion and flares. This result does not match the "speckled" pattern evident with a full gap junction knockdown (Figure 4-5A,B, t = 120 s). This speckled pattern can be reproduced if the gap junction fluxes are altered so that IP$_3$ fluxes are eliminated (Figure 4-7D; $\eta_{GJ,IP3} = 0$). These model results predict that intercellular transfer of calcium is necessary for the first expansion, while intercellular transfer of IP$_3$ coordinates multicellular calcium signaling during the later distal expansion and flares.

4.5 Discussion

We have developed a mathematical model to replicate and predict calcium signaling events following laser-induced wounding of the *Drosophila* pupal notum. At the tissue level, the model incorporates both a simple model of the physical damage and a reaction-diffusion model of biochemical damage signals. These damage models are applied across the field of cells which share a common calcium signaling toolkit (Figure 4-1). The calcium signaling toolkit elements and their associated parameters in Table 4-2 were chosen to replicate the spatiotemporal dynamics of calcium signaling events that follow wounding of wild-type tissues (Figure 4-3) and genetic knockdowns (Figure 4-5).

156

The model was then used to investigate the system in ways that are not currently experimentally accessible. First, the model reveals that many of the calcium signals are well above the K_d of the GCaMP sensor, and thus regions with rather uniform fluorescence can hide order-of-magnitude differences in cytosolic calcium concentration (Figure 4-6): cells within the first expansion experienced peak calcium levels of 100-400 µM, but cells within the distal expansion reached peaks around just 0.5 µM. Second, by running the model with or without the genetically-encoded calcium indicator GCaMP, we could show that GCaMP buffering has a small effect on the frequency and amplitude of calcium oscillations or flares, but has little to no effect on the spatial and temporal scales of the first and distal expansion. Third, by modeling selective gap junction knockdowns, i.e., allowing only calcium or IP$_3$ but not both to move between adjacent cells, the model shows that gap-junction fluxes of calcium play a key role in the first expansion, but it is the gap-junction transfer of IP$_3$ that couples and coordinates cells during the distal expansion and subsequent flares (Figure 4-7).

4.5.1 Cell-to-cell variability

Cell-to-cell variability across the tissue is a necessary condition for the model to break radial symmetry in the calcium flares (Figure 4-3C). We find that variations in two parameters could yield the appropriate broken symmetry without having other adverse effects: α, the parameter that controls the maximum IP$_3$ production rate (Eq. (4-24)); or h_{IPR}, the permeability of the fully open IPR (4-18). These two parameters respectively control how much IP$_3$ will be produced for a given level of damage signal Gbp and how much calcium is subsequently released from the ER, and thus they control the behavior

157

of the IP$_3$-dependent calcium flares (Figure 4-5C, D). Both parameters also had minimal impact on the resting calcium levels of modeled cells. We decided to move forward with variations in α because it represents the activity of an entire G-protein cascade, and the output of this multistep cascade would include the variability generated within each step of this signaling network.

A log-normal distribution was used to model cell-to-cell variability for several reasons. First, since the model parameters are nonnegative, the distribution needed to yield only positive values. Second, log-normal sampling has been shown to capture the impact of cell-to-cell variability on oscillatory calcium signaling[183]. And third, as the parameter α encompasses the activity of an entire G-protein cascade, the total variability in α consists of the product of the variabilities at each step, thus resulting in a multiplicative version of the central limit theorem where the result approaches a log-normal distribution[184].

The necessity of cell-to-cell variability begs a key question: is such variability simply noise or is it a key aspect of wound-induced calcium signaling? Analyses of other systems have shown that cell-to-cell variability is not intrinsic noise that obscures a signal, but instead increases the capacity of a group of cells to transmit information[185]. It has also been shown that variations in calcium responses can be explained by variations in the IPR response[186]. Further, as Yao et al. 2016[186] demonstrated, variations in cellular calcium responses can be explained by structured variability in cell state. Our model is thus far agnostic as to the role of cell-to-cell variability, but future investigations that link wound-induced calcium signals to downstream cellular behaviors should strive to discern whether the clearly present variability serves a functional role.

4.5.2 Intercellular calcium and IP$_3$ transfer have distinct roles

In the model, both calcium and IP$_3$ travel from a cell to its neighbors through gap junctions. By modeling "selective" gap junctions where only calcium or IP$_3$ is allowed to move intercellularly, we were able to tease apart separate roles for both fluxes. Given that the first expansion is caused by large amounts of calcium rushing in through plasma membrane damage, it is not surprising that intercellular calcium flux is necessary for the first expansion. Smaller calcium fluxes are still present during the distal calcium response and flares, but these fluxes are not sufficient to locally coordinate calcium responses. Instead, coordination of the distal expansion and flares is primarily driven by the gap-junction transfer of IP$_3$ (Figure 4-7C, D) – a result consistent with many other systems [21]. The selective gap junction simulations thus piece together the full gap junction knockdown experiments and simulations (Figure 4-5A, B): the first expansion is prevented due to a lack of calcium transfer, and the distal calcium response is altered due to a loss of IP$_3$ transfer.

Interestingly, the different roles for calcium and IP$_3$ transfer occur at later times in the simulations even though the radial fluxes of both species are similar. Obviously, the impacts of those fluxes are not equivalent. One reason is that cytosolic calcium concentrations are strongly buffered (Eq. (4-8)). This buffering reduces the impact of calcium fluxes unless they are large enough to overwhelm the cells buffering capacity, as is the case during the earlier first expansion. IP$_3$ has no such buffering present. In addition, small changes in IP$_3$ levels are leveraged into larger changes in cytosolic calcium through the Hill functions that link IP$_3$ to the opening of IPR and release of calcium from ER stores (Eqs. (4-18) and (4-19)).

4.5.3 Comparison to other calcium signaling models

The model developed here goes well beyond currently published models of wound-induced calcium signaling. Narciso et al. 2015[91] developed a calcium signaling model in the context of laser-ablation wounding of *Drosophila* wing discs; however, their wound is modeled only implicitly as a time-integrated IP_3 stimulus over a small circular area. Additionally, their model is implemented over a two-dimensional, homogenized continuum rather than over discrete cells in a tissue. A more recent model from the same lab investigates calcium signaling across a *Drosophila* wing disc, but with a focus on organ development and with the total IP_3 production rate in each cell being just a function of the cytosolic calcium concentration[187]. Donati et al. 2021[188] developed a model of calcium signals in mouse keratinocytes upon photodamage; however, instead of proteolytic activation driving the extracellular signaling mechanism, the damage signal in that system is ATP, which is released both from the wound site as well as from undamaged cells through connexin hemichannels. O'Connor et al. 2021[164] found that the adenosine receptor played no role in the wound-induced calcium response in the *Drosophila* notum.

Here we develop a more detailed model that can be used to describe calcium signaling around an explicit wound with both physical and biochemical damage signals. Further, our model is based on experiments in *Drosophila*. Although our chosen model components are not unique to *Drosophila*, a model that captures calcium signaling in this system is advantageous due to its utility. *Drosophila* has a well-established genetic toolkit, which provides an accessible route to discerning specific molecular mechanisms. Experimental genetic manipulations were key to outlining the components

needed in the model and provide a stringent test for evaluating the model's *in silico*

knockdowns. Continuing studies that tightly align expansions of the model presented

here with future genetic experiments should provide further insights linking calcium

signaling to wound responses and wound healing.

4.6 Conclusion

Laser-wounds in the *Drosophila* pupal notum give rise to a complex set of calcium

signaling events. These events are driven by at least two different aspects of the

wound, and yet interact with a common set of cellular components to generate

overlapping calcium signals. Here, we have developed a mathematical model that

includes both physical and chemical damage signals and integrates them with a single

calcium signaling toolkit at the cellular level. The model replicates experimental results

in wild-type and genetically manipulated tissues and yields key insights into cell-to-cell

variability, cytosolic free calcium behavior, and the roles of intercellular gap-junction

communication. It provides an important framework for future studies of both calcium

signaling and wound responses in the *Drosophila* system.

Chapter 5

Conclusions and future work

5.1 Conclusions

The work presented here displays impactful research that provides a deeper understanding of damage signals that arise around laser-induced epithelial wounds; the results and insights obtained would not have been possible without the interplay of both experiments and mathematical modeling.

5.1.1 Calcium signaling dynamics classification paired with diffusion models

In Chapter 2, multiple mechanisms were identified that produce distinct calcium signaling events around laser-induced epithelial wounds in *Drosophila* pupae. The experimentally observed calcium signaling events were 1) the initial calcium signal that begins within milliseconds after wounding within a region of radius 30-120 μm; 2) a calcium signal expansion over the next 10-20 s further out into one to two additional rows of cells; and 3) a distal calcium signal that appears ~40 s after wounding and spreads as far as 150 μm from the wound followed by stochastic calcium waves or flares that extend even further away from the wound. Further experimental investigations revealed that the initial calcium influx occurs exactly within the damage caused by laser-induced cavitation bubbles, that only the first calcium expansion requires gap-junction connections between adjacent cells, and that the distal calcium response requires sufficiently large wounds.

Diffusion models provided insight to the experimental observations. Calcium influx through the cavitation-induced plasma membrane micro-tears was modeled as

diffusion from a constant point source (Eq. (2-2)), and this model was fit to line-scan data of GCaMP fluorescence on millisecond timescales after wounding. It was found that the intracellular calcium diffusion rate on this timescale is much higher than that of buffered calcium in the typical cellular environment, suggesting that a sufficient amount calcium floods into damaged cells, exceeds the calcium buffering capacity, and thus is able to spread into undamaged cells. Additionally, a delayed-diffusion model was fit to both the first and distal calcium expansions. This analysis revealed that each expansion has distinct diffusive properties, suggesting separate mechanisms behind each signal, as well as revealed an inherent time delay in the distal calcium response should it be propagated by diffusion.

Paired together, the experimental evidence and mathematical modeling give a fuller picture of how calcium signals arise around laser-induced epithelial wounds. The initial influx is initiated by cavitation-induced shear stresses that physically create micro-tears in the cells' plasma membranes. Calcium then enters into cells in large enough amounts to overcome the buffering capacity and diffuse through gap junctions into undamaged cells. And finally, a second, separate diffusive signal drives the distal calcium response which depends on the amount of damage and only reaches signaling threshold at later times after wounding.

5.1.2 Identification of a protease-induced signal cascade paired with a reaction-diffusion model

In Chapter 3, the components of the diffusive signal behind the delayed, distal calcium response were identified through rigorous experimental testing in both

163

Drosophila pupae and larval wing discs. These experiments showed that the distal calcium response in pupae is dependent on the extracellular cytokines Gbps, which activate the GPCR Mthl10 to initiate the production of IP_3 and release of calcium from the ER. Further experiments in the wing discs revealed that Gbp must first be cleaved by proteases in order to initiate this signaling cascade.

With the identification of proteases, Gbp, and Mthl10, a reaction-diffusion model was developed that involved a protease source that builds up over time, cleavage of a diffusible ligand (Gbp), and binding between the ligand and the receptor (Mthl10). The reaction-diffusion model was fit to distal calcium response data and, despite "sloppy" parameter dependance, was able to provide robust results and predictions. Model analysis revealed that a slow protease buildup which activates a diffusible ligand is required in order to produce the delay in the distal calcium response. Additionally, this protease-initiated model is able to explain the distal calcium response's dependence of both diffusion rate and time delay on wound size.

Paired together, the experimental evidence and mathematical modeling give a fuller picture of the distal calcium response initiation. Gradual release of protease from lysed cells near the wound cleave and activate Gbps. The activated Gbps diffuse through the extracellular space and bind to the cell surface GPCR Mthl10 to trigger a canonical $G_{\alpha q}$/PLCβ/IPR cascade that releases calcium from the ER. This mechanism allows for the damage signal Gbp to both spread far beyond the protease source while also providing the experimentally observed wound-size dependence.

5.1.3 Experiments are used to validate model structure to provide new insights

In Chapter 4, a mathematical model was developed for wound-induced calcium signaling across an epithelium of thousands of coupled cells. The model incorporates both physical and chemical damage signals covered in previous chapters, along with experimentally identified and hypothesized cellular components that initiate and engage with calcium signals. While no new experimental evidence was presented here, the experiments still served as a way to validate the model structure and parameter selection. It was found that cell-cell variability in the model is required to replicate the asymmetric, distal calcium flares. Replication of various knockdown experiments with the model confirmed that gap junction connections between adjacent cells and IP_3 initiated calcium-release were playing their intended roles in the model.

Due to model validation from experiments, the model was then able to provide insights that are not experimentally accessible. Due to the high sensitivity and low-concentration saturation of calcium – GCaMP binding, calcium concentrations are not able to be quantified in our system. However, a direct output of the model is the cytosolic calcium concentration, and thus calcium dynamics not observable experimentally can be directly quantified with the model. Furthermore, the model is easily able to separate out the dependence of the calcium signals on the intercellular propagation of both calcium and IP_3, revealing that IP_3 transfer, but not calcium transfer, is sufficient to coordinate the distal calcium flares across the tissue.

Paired together, the experimental evidence and mathematical modeling produces a robust modeling framework from which future work in both *Drosophila* and wound signaling systems will greatly benefit.

5.2 Future work

5.2.1 Long-term calcium signals

The work presented here focuses on calcium signals around laser-induced epithelial wounds for times up to ~3 minutes after wounding. However, we observe repeated cycles of calcium signaling that persist for tens of minutes after wounding (Figure 2-10A). The mathematical modeling presented in Chapters 3 and 4 cannot explain this since the diffusive Gbp signal dies out once proGbp is depleted, and the micro-tears close on the order of seconds (τ_{heal} = 5.25 s, Table 4-2). This suggests that there are other mechanisms at play that enable calcium signals to persist past what is suggested by the model.

One possible mechanism that would allow calcium signals to persist could be inhibition of Gbp diffusion paired with more detailed receptor dynamics. Perhaps Gbp is too diffusive in the model, to where we have correctly captured the initiation of the signal, yet Gbp becomes too diffuse to stay above the signaling threshold. If instead of diffusing away the Gbp is somehow prevented from engaging in diffusion across large scales, the signal could persist above threshold for an extended time. This could be possible through some sort of Gbp buffering mechanism, which would allow a sufficient level of Gbp to persist in the extracellular space. Additionally, the ligand-receptor dynamics are greatly simplified in the reaction-diffusion model, being only represented by a reversible reaction. GPCRs actually have much more complicated dynamics that involve phosphorylation, uptake, and recycling[163]. This receptor recycling could give rise to periods of latency in the calcium signals despite persistent presence of a Gbp signal in the extracellular space.

166

Another possible mechanism that would allow calcium signals to persist for tens of minutes after wounding would be replenishment of Gbp itself. It has been shown in *Drosophila* that Gbp is produced by fat body cells[135], and that these cells also migrate to wounds in order to clear debris, seal the wound, and fight infection[189]. Perhaps fat body cells also release additional Gbp in order to maintain calcium signaling around the wound.

Whether or not the above mechanisms give rise to continued calcium signals around epithelial wounds, the modeling framework presented here can easily be adapted to investigate such hypotheses. The work would amount to incorporating additional species, reactions, and sources into the reaction-diffusion model, yet these new terms would be subject to similar derivations to what is already present. Exploration of these or other hypotheses with the model could help design future experiments that would validate or rule out the various proposed mechanisms.

5.2.2 Incorporation of tissue mechanics

When a tissue is wounded, the tension throughout the tissue changes[6,190]. Changes in tissue tension has been shown to initiate calcium signals in epithelial tissues[55,124], and calcium has also been shown to regulate the cytoskeleton[10,28,32,51]. Do tissue mechanics play a role in our wound responses, either through modulation of the resulting calcium signals or in their downstream effects? Kaori et al. 2019[191] developed a mathematical model in the context of *Xenopus* embryogenesis that incorporates a two-way mechanochemical feedback mechanism between calcium and cell contraction. Given how waves of cell contraction have been shown to exist around laser-induced

epithelial wounds in *Drosophila*[10], this mathematical model could be of great importance to understanding the interplay between calcium and tissue tension in our own system.

This particular model would be easy to implement into our current model. Due to the modular design of the calcium signaling model, incorporation of the model by Kaori et al. would simply amount to adding in an additional stretch-sensitive calcium channel flux along with this channel's calcium-dependent model that is described by its own first order, ordinary differential equation. This would produce an additional output of a dilation/compression factor, which would be easy to visualize around the wound similar to the model outputs present in Chapter 4.

5.2.3 Models of calcium signal decoding

The work presented here has focused on the initiation and persisting dynamics of calcium signals around laser-induced epithelial wounds, yet understanding how these calcium signals lead to downstream cellular behaviors is just as important in fully understanding the role of calcium signals around epithelial wounds. Unfortunately, compared to published models of calcium signal initiation and information encoding, models looking at calcium signal decoding are scarce[20]. Nevertheless, there are still places one can start. Noren et al. 2016[31] showed that calcium signals similar to those around our epithelial wounds give rise to distinct cellular behaviors in endothelial cells: large, constant calcium signals give rise to cell migration, whereas calcium oscillations give rise to cell proliferation. The location of these types of calcium signals around epithelial wounds match with migration and proliferation zones identified by Park et al. 2017[4]. Furthermore, a "ratchet model" has been identified wherein the kinetics of

calcium-mediated transcription factors determine whether they will respond to calcium signal amplitude or calcium signal frequency[20,31].

The modeling presented here could be incorporated into a separate model that focuses on calcium signal decoding. Since cytosolic calcium concentrations on the cellular-level are the primary output of the calcium signaling model, one could simply use this output as an input into any sort of calcium signal decoding model. Furthermore, the levels of damage signals are easily tunable through specific parameters in the model (Table 4-1), and thus one could also explore how levels of damage impact calcium oscillations, which in turn impact the downstream signals that are decoded.

Appendix A

Hydrodynamic Modeling of Laser-Induced Cavitation

A.1 Introduction

Upon laser-induced wounding of epithelial tissues, calcium enters cells from the extracellular space through plasma membrane micro-tears. These micro-tears are the result of fluid shear stresses exerted by a cavitation bubble that expands across the tissue. We have shown that the maximum radius of the cavitation bubble is equal to the initial radius of the calcium influx following wounding[113]. While this analysis shows that the damage within the cavitation bubble footprint is sufficient to cause extracellular calcium entry, it does not reveal further details of the damage distribution around the wound. In other words, how does cavitation-induced damage to the tissue vary with distance from the wound, and how much stress is required for micro-tear formation?

A.2 Hydrodynamic shear stress and shear impulse

Following laser-induced cavitation, cells experience a variety of outcomes depending on how far away they are from the wound, such as cell lysis, necrosis, or permeabilization[11,14]. Compton et al. 2013[12] showed that these cellular outcomes are determined by the time integral of the fluid shear stresses $\tau_w(r,t)$ exerted by the cavitation bubble, called the shear stress impulse $J(r)$:

$$J(r) = \int_0^{T_B} \tau_w(r,t)\, \mathrm{dt} \tag{A-1}$$

where r is the distance from the bubble center, t is time after bubble initiation, and T_{B} is the time it takes for the bubble wall to grow to a radius of r. In order to determine the shear stress, the velocity of the extracellular fluid outside of the cavitation bubble $V_{\infty}(r,t)$ must be known:

$$\tau_{\mathrm{w}}(r,t) = \rho\sqrt{\frac{\nu}{\pi}}\int_0^t \frac{\partial V_{\infty}(r,t')}{\partial t'}\cdot\frac{\mathrm{d}t'}{\sqrt{t-t'}} \tag{A-2}$$

where ρ and ν are the density and kinematic viscosity of the fluid medium. Assuming an incompressible surrounding fluid, the fluid velocity is related to the bubble wall radius $R(t)$ and velocity $V(t)$ by

$$V_{\infty}(r,t) = V(t)\cdot\left(\frac{R(t)}{r}\right)^2 \tag{A-3}$$

A.3 The Gilmore model

While quick time-resolved imaging can experimentally determine $R(t)$ and $V(t)$ for a given bubble[13], hydrodynamical modeling techniques can be employed to perform robust analysis across a wide variety of conditions. Here, we use the Gilmore model in order to determine $R(t)$ and $V(t)$ theoretically. In order allow for ease in replicating these results, the main equations and brief outline of the model are stated below, but further details and derivations can be found in the references[12,62,192]. The bubble wall position is determined by the differential equation

$$\ddot{R} = \left[-\frac{3}{2}\left(1-\frac{\dot{R}}{3C}\right)\dot{R}^2 + \left(1+\frac{\dot{R}}{C}\right)H + \frac{R}{C}\left(1-\frac{\dot{R}}{C}\right)\frac{\mathrm{d}H}{\mathrm{d}t}\right]\cdot\left[R\left(1-\frac{\dot{R}}{C}\right)\right]^{-1} \tag{A-4}$$

where C is the speed of sound in the fluid at the bubble wall, and H is the enthalpy difference between the pressure at the bubble wall P and the hydrostatic pressure p_∞ far from the bubble.

Assuming an ideal gas inside of the bubble, the pressure at the bubble wall is given by

$$P = \left(p_\infty + \frac{2\sigma}{R_n}\right)\left(\frac{R_n}{R}\right)^{3\kappa} - \frac{2\sigma}{R} - \frac{4\mu}{R}\dot{R} \tag{A-5}$$

where σ denotes the surface tension, μ is the dynamic shear viscosity, κ is the ratio between specific heat capacities at constant pressure and constant volume, and R_n is the equilibrium radius where the pressure inside the bubble is equal to the hydrostatic pressure. The Tait equation relates the pressure at the bubble wall to the fluid density ρ by

$$\frac{P + B}{p_\infty + B} = \left(\frac{\rho}{\rho_0}\right)^n \tag{A-6}$$

where ρ_0 is the fluid density without compression, and B and n are fluid-dependent parameters. This allows H and C to be determined as

$$H = \int_{p_\infty}^{P} \frac{dP'}{\rho} = \frac{n(p_\infty + B)}{(n-1)\rho_0}\left[\left(\frac{P + B}{p_\infty + B}\right)^{(n-1)/n} - 1\right] \tag{A-7}$$

and

$$C = (c_0^2 + (n-1)H)^{1/2} \tag{A-8}$$

Table A-1: Parameter values for the Gilmore model.

Symbol	Definition	Value
ρ_0	Density of water before compression	998 kg m^{-3}
σ	Surface tension	0.0726 N m^{-1}
κ	Ratio between specific heats at constant pressure and volume	4/3
μ	Dynamic shear viscosity	1.046 N ms m^{-3}
c_0	Speed of sound in water before compression	1483 m s^{-1}
p_∞	Static ambient pressure	100 x 10^3 Pa
B	Parameter for Tait equation for water	314 MPa
n	Parameter for Tait equation for water	7

A.4 Results

A.4.1 A linear relation exists between the lifetime and equilibrium radius of the bubble

Eqs. (A-4) - (A-8) along with parameters in Table A-1 determine the cavitation bubble wall position as a function of time $R(t)$ with the specification of three undetermined parameters: the initial bubble wall position and velocity, $R(0)$ and $V(0)$, and the equilibrium bubble radius, R_n (Figure A-1A). Our only direct measurement of the cavitation bubble is its lifetime as detected by hydrophone measurements[113]; therefore, none of these parameters are known for our cavitation bubbles. For simplicity, we assume $V(0) = 0$. Additionally, we determined that, for a given initial bubble radius, the bubble lifetime is proportional to the equilibrium radius (Figure A-1B). We can therefore determine the equilibrium radius corresponding to each measured bubble lifetime using linear relationships derived from repeated runs of the Gilmore model at a set initial bubble radius, thus making the initial bubble radius the only undetermined model parameter, which we take to be 5 μm (estimate from Hellman et al. 2008[14]).
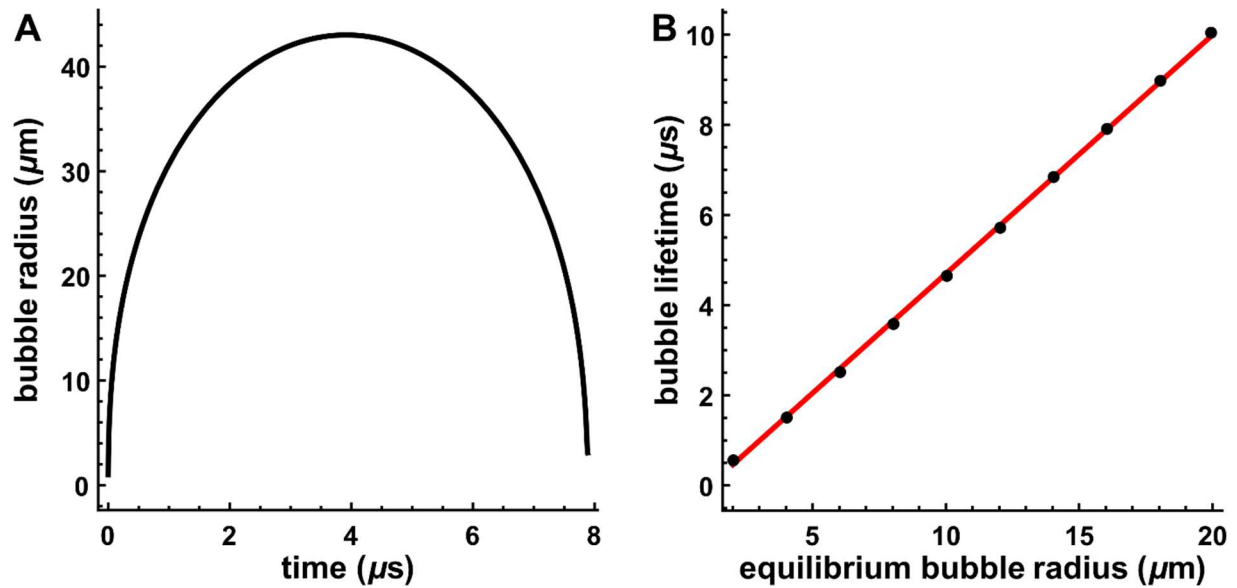
Figure A-1: Bubble lifetime is proportional to the equilibrium radius in the Gilmore model.

(A) Bubble radius as a function of time from the Gilmore model. Parameters are those in Table A-1 as well as $R(0)$ = 1 µm, $V(0)$ = 0 m/s, and R_n = 16 µm. The graph shows one bubble lifetime. **(B)** Bubble lifetime vs equilibrium bubble radius for initial bubble radius of $R(0)$ = 1 µm. Black points show bubble lifetime results from one model output using the corresponding equilibrium bubble radius, and the red line is a best fit line.

A.4.2 Shear impulse threshold for micro-tear formation

Results of the Gilmore model were applied to Eqs. (A-1) - (A-3) to determine the shear stress $\tau_w(r,t)$ and shear stress impulse $J(r)$ for each cavitation bubble. Examples of these functions for one bubble is show in Figure A-2A, B. By evaluating the shear stress impulse at the radius of initial calcium entry following wounding, we determined the required shear stress impulse required for micro-tear formation (Figure A-2C). After excluding outliers, the average shear stress impulse required for micro-tear formation is 5.5 mPa·s with a standard deviation of 1.5 mPa·s. It should be noted that this value is less than what is reported for cell permeability in Compton et al. 2013[12], but their

174

condition for cell permeability was entry of a 3 kDa dye, which is much larger than calcium ions. Therefore, dye entry would require larger holes in cell membranes than what would be needed for calcium entry, thus requiring a larger shear stress impulse threshold.
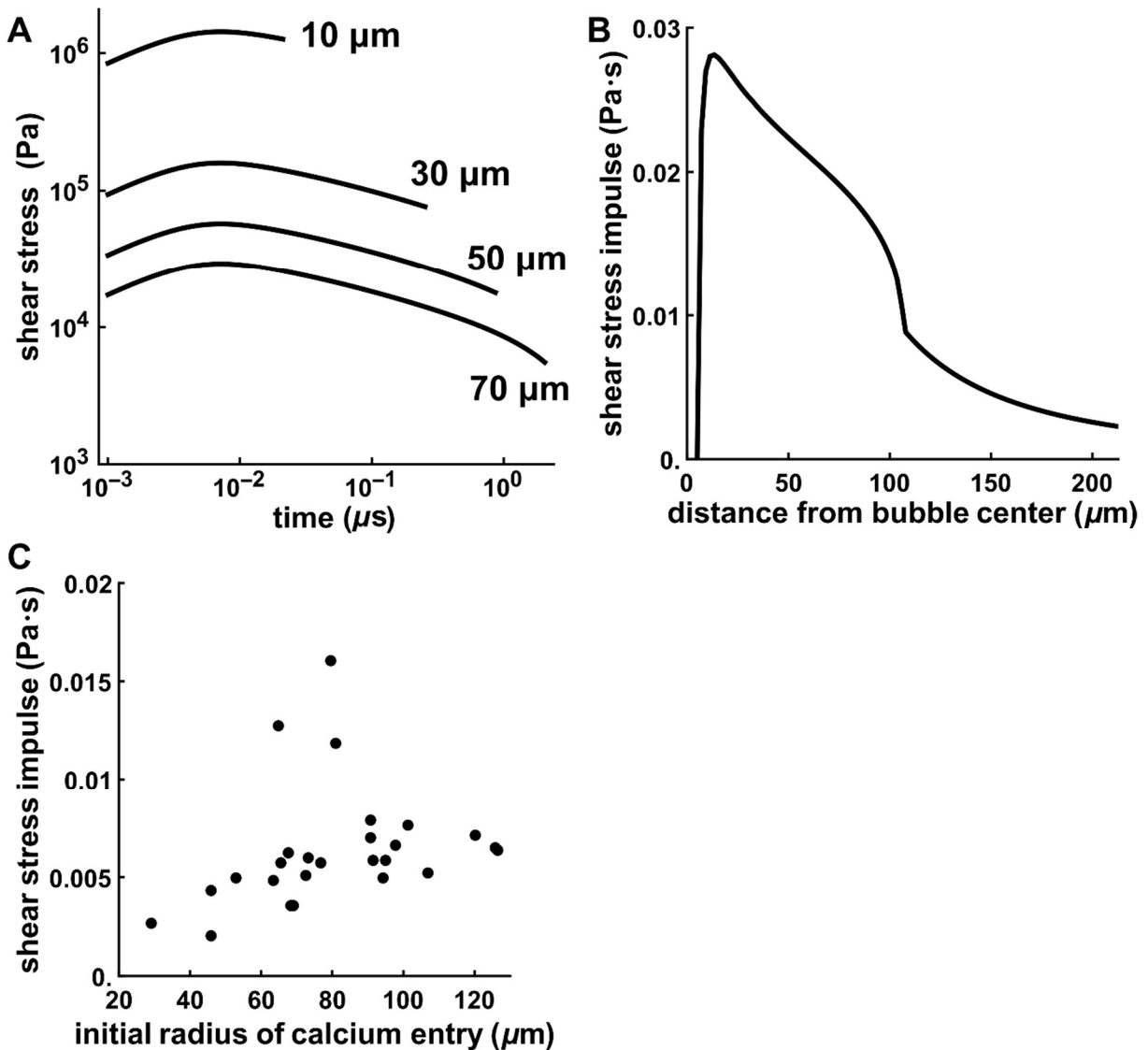
Figure A-2: Shear stress and shear stress impulse calculations.

(A) – (C) Calculations assume an initial bubble radius of 5 μm. **(A)** Shear stress vs time at specified distances from the bubble center. Each line is graphed up until the time at which the bubble wall reaches that position. **(B)** Shear stress impulse vs distance from the bubble center for a bubble whose lifetime is 20 μs. The discontinuity in the derivative

at ~100 µm occurs because this is the maximum radius of the cavitation bubble, and so past this distance the upper limit of the integral in Eq. (A-1) no longer changes with distance from the bubble center. **(C)** The shear stress impulse at the extent of the initial calcium entry for each bubble shown in Figure 2-1C.
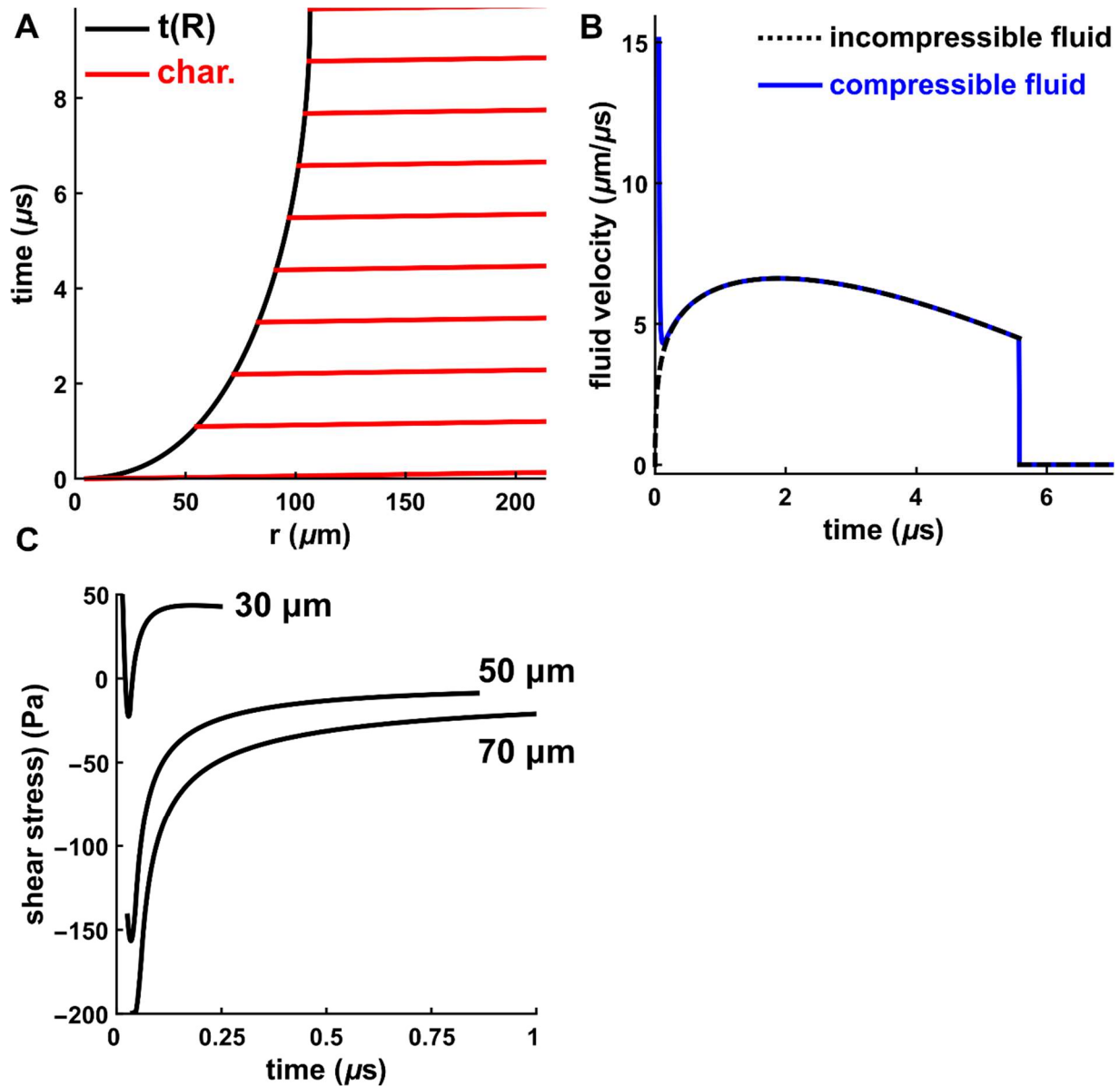
A.4.3 Shear stress calculations assuming a compressible surrounding fluid

There is a discrepancy between the Gilmore model and the use of Eq. (A-3) to determine the fluid velocity V_∞ outside of the bubble wall: the Gilmore model assumes a compressible fluid surrounding the bubble, whereas Eq. (A-3) assumes an incompressible fluid. To determine the fluid velocity in the case of a compressible fluid, one can employ the Kirkwood- Bethe hypothesis, which states that the quantity $y = r(h + V_\infty^2/2)$, where h is the enthalpy difference between the fluid at pressure p and at pressure p_∞, is constant along a path called a "characteristic" that is traced by a point moving with velocity $\dot{r} = C + V_\infty$. The Kirkwood-Bethe hypothesis therefore leads to coupled differential equations for the fluid velocity V_∞ as well as the characteristic along which the fluid velocity is determined, and the initial conditions for these differential equations are given by the bubble wall position and velocity. Figure A-3C shows examples of characteristics along with the bubble wall position in $t - r$ space. The choice in flipping the axes from the usual $r - t$ space is because it is easier to integrate $\dot{r} = C + V_\infty$ with respect to r instead of with respect to t (see Eq. 90 in Gilmore 1952[192]).

Computations along many characteristics can determine V_∞ across a lattice of (r, t) points (the details of these calculations can be found in the references[62,192]). Figure A-3B shows plots of the fluid velocity at a distance of 97.5 µm from the bubble center as a function of time determined by the Kirkwood-Bethe hypothesis for the case

of a compressible surrounding fluid as well as determined by Eq. (A-3) for the case of an incompressible surrounding fluid. The two methods give similar results at later times, but at early times the calculations for the compressible fluid case give very large fluid velocities that decay rapidly. The large negative derivative in the fluid velocity results in negative shear stress calculations from Eq. (A-2) (Figure A-3C). I suspect the reason for this velocity spike comes from improper initial conditions of the bubble wall in the Gilmore model, but further investigations need to be performed to determine why the solutions for the compressible fluid case have such large fluid velocity spikes and if a correction to this method would yield substantially different shear stress impulse results than the calculations for the incompressible fluid case.

Figure A-3: Fluid velocity and shear stress calculations for a compressible surrounding fluid.
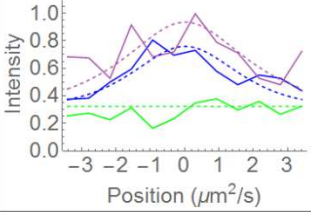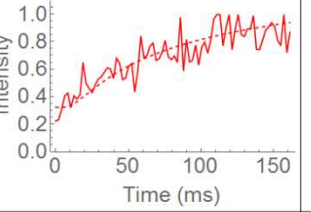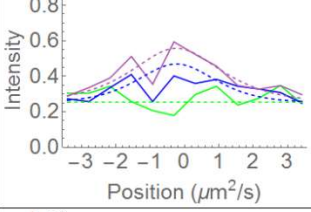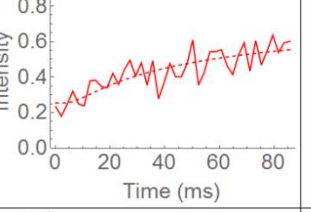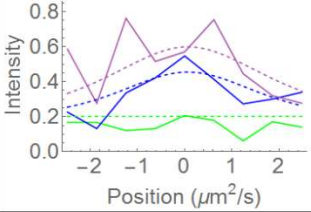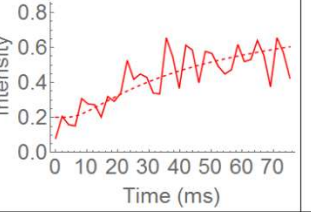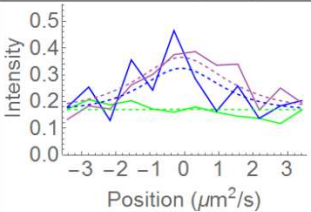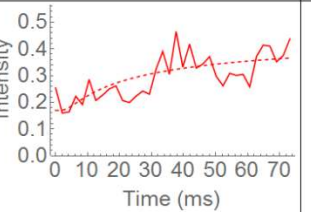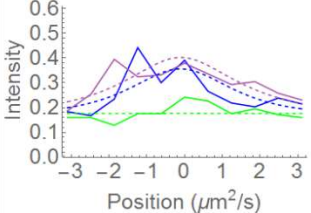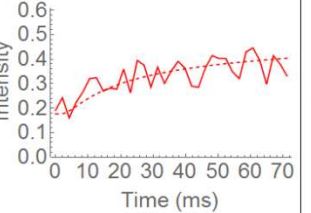
(A) The bubble wall position (black) along with examples of characteristics from the Kirkwood-Bethe hypothesis (red) plotted in t – r space. (B) Calculations of the fluid velocity for both an incompressible fluid (dashed, Eq. (A-3)) and a compressible fluid (blue) at a distance of 97.5 µm from the bubble center. The drop to 0 µm/µs in both cases indicates the time at which the bubble has grown to a radius of 97.5 µm. (C) Shear stress vs time for the compressible fluid case at specified distances from the bubble center. Each line is graphed up until the time at which the bubble wall reaches that position.

A.5 Conclusions

In our pulsed laser-ablation experiments, we are able to use a hydrophone to measure the lifetime of the resultant cavitation bubble in order to determine its maximum radius as well as the maximum radius of plasma membrane damage[113]. However, this does not reveal information about the damage distribution within the cavitation bubble footprint. This distribution can be determined theoretically by calculating the shear stress impulse (Eqs. (A-1) - (A-3)) from bubbles simulated using the Gilmore model (Eqs. (A-4) - (A-8)). The shear stress impulse, $J(r)$, determines the shape damage distribution around the wound[12], and the model predicts that a shear stress impulse of roughly 5.5 mPa·s is required to cause micro-tear damage and calcium entry. Further calculations were attempted to resolve the discrepancy between the Gilmore model and Eq. (A-3) with regard to fluid compressibility, but conclusive results were not obtained.

Appendix B

Complete set of fits from Figure 2-6 and Figure 2-11

Number	Rocket Density Plot	Fit Densiy Plot	Intensity v. Position	Intensity v. Time	Diffusion Constant
1					$32 \pm 2 \ \mu m^2/s$
2					$34 \pm 5 \ \mu m^2/s$
3					$51 \pm 8 \ \mu m^2/s$
4					$52 \pm 9 \ \mu m^2/s$
5					$68 \pm 11 \ \mu m^2/s$

Number	Rocket Density Plot	Fit Densiy Plot	Intensity v. Position	Intensity v. Time	Diffusion Constant
6					$71 \pm 12 \ \mu m^2/s$
7					$78 \pm 9 \ \mu m^2/s$
8					$81 \pm 9 \ \mu m^2/s$
9					$86 \pm 12 \ \mu m^2/s$
10					$89 \pm 14 \ \mu m^2/s$

Number	Rocket Density Plot	Fit Densiy Plot	Intensity v. Position	Intensity v. Time	Diffusion Constant
11					$104 \pm 17\ \mu m^2/s$
12					$108 \pm 9\ \mu m^2/s$
13					$123 \pm 13\ \mu m^2/s$
14					$123 \pm 13\ \mu m^2/s$
15					$126 \pm 22\ \mu m^2/s$

Number	Rocket Density Plot	Fit Densiy Plot	Intensity v. Position	Intensity v. Time	Diffusion Constant
16					$139 \pm 13\ \mu m^2/s$
17					$187 \pm 42\ \mu m^2/s$
18					$197 \pm 18\ \mu m^2/s$
19					$219 \pm 30\ \mu m^2/s$
20					$225 \pm 32\ \mu m^2/s$

Number	Rocket Density Plot	Fit Densiy Plot	Intensity v. Position	Intensity v. Time	Diffusion Constant
21					$260 \pm 33 \ \mu m^2/s$
22					$270 \pm 38 \ \mu m^2/s$
23					$286 \pm 45 \ \mu m^2/s$
24					$405 \pm 72 \ \mu m^2/s$
25					$474 \pm 57 \ \mu m^2/s$
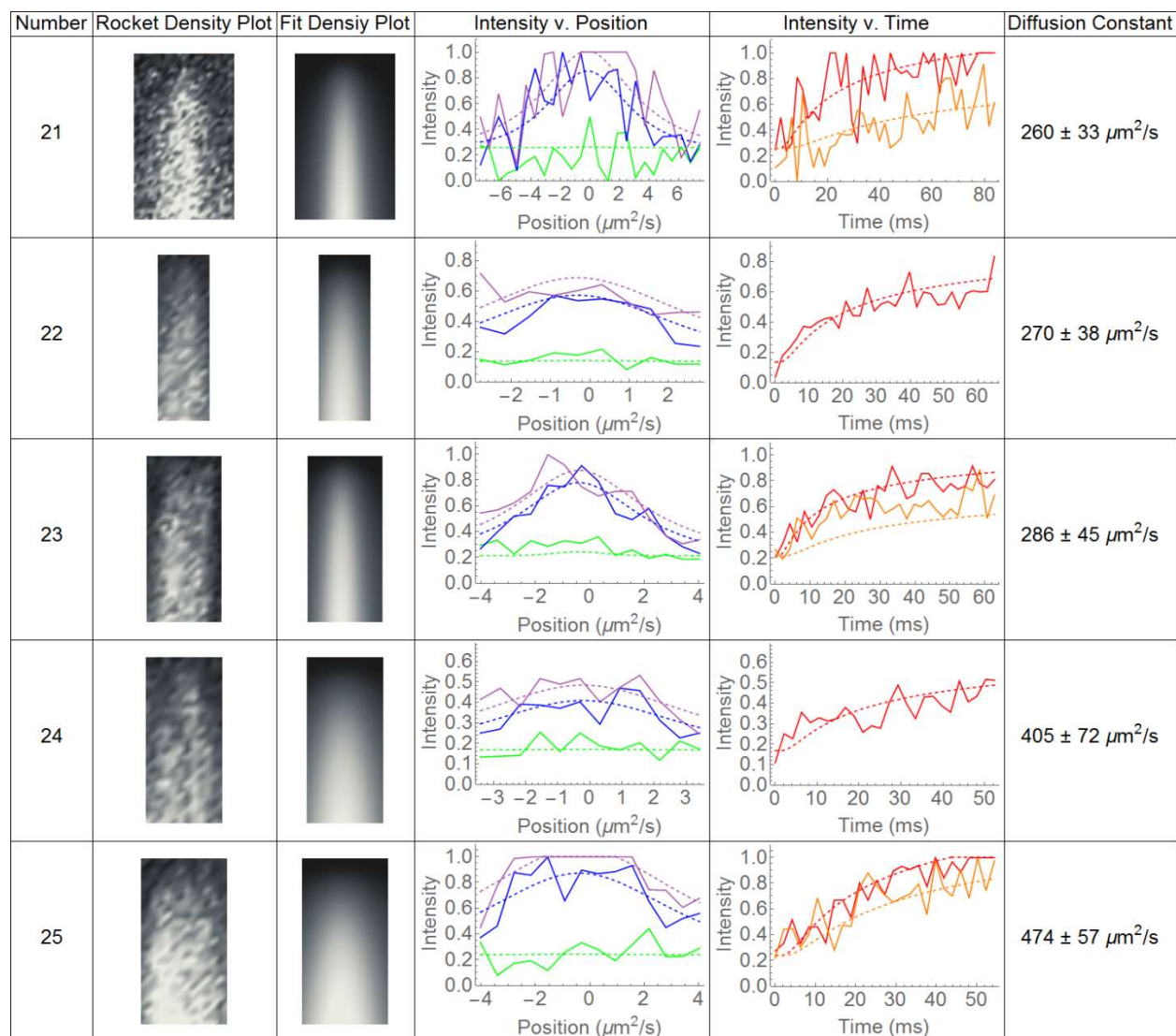
Figure B-1: Complete set of kymograph peak fits.

Complete set of 25 cropped kymograph peaks (or rockets) and their diffusion model fits sorted from smallest to largest diffusion constant. Data was fit to the diffusion of calcium continuously being released from a point source fixed in space. For the intensity vs position and intensity vs time plots, solid lines and dashed lines correspond to the data and fits respectively. The intensity vs position plots show data and fits at 2.1 ms after ablation (green), at the time half-way between the start and end of the image (blue), and at the time 4.2 ms before the end of the image (purple). The intensity vs time plots show data and fits along the midline of the image (red), and at a point half-way between the midline and the right edge of the image (orange, only shown if the image is wider than 13 pixels or 8.06 µm). Reported uncertainty for each diffusion is the standard error from the regression.
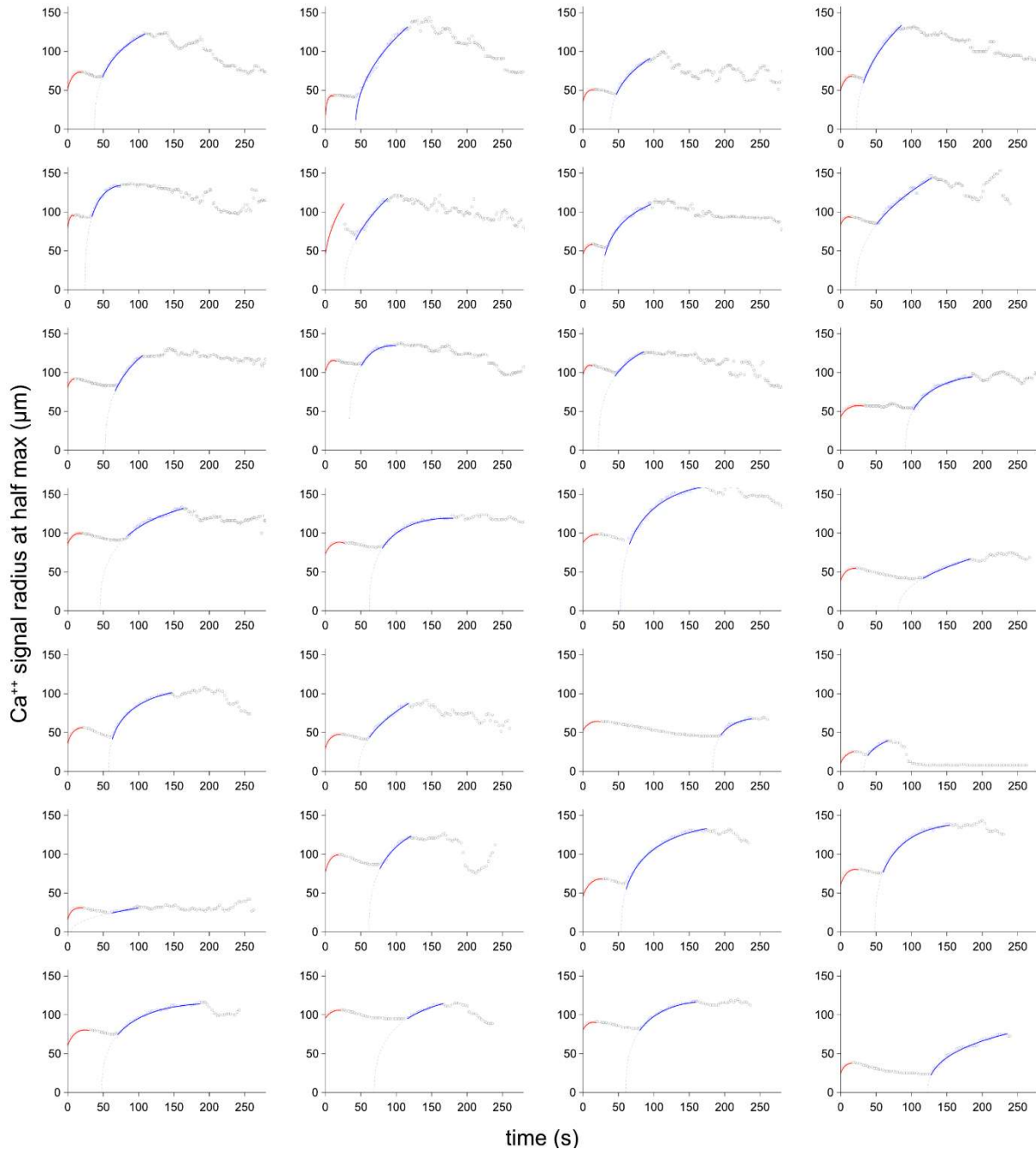
Figure B-2: Fitting calcium wave expansions to diffusion models.

Graphs show calcium signal expansion over time for 28 individual wounds, including the four shown in Figure 2-11. The first and second expansions are highlighted in red and blue respectively. The solid lines show nonlinear regression fits to each expansion using Eq. (2-1) in Section 2.4.5; the dashed blue lines show back-projections of fits to the second expansion. As a measure of goodness-of-fit, standard errors of the regressions for the first expansions range from 0.1 to 1.3 µm, with a median of 0.4 µm. Those for the second expansions range from 0.3 to 6.7 µm, with a median of 1.3 µm.

Appendix C

Materials and methods for Chapter 3

C.1 Resource availability

Materials availability

Fly lines generated in this study are available from the Bloomington Drosophila Stock Center or from the Lead Contact.

Data and code availability

Code generated for the Reaction-Diffusion Model has been deposited on Github (https://doi.org/10.5281/zenodo.4977106).

C.2 Experimental model and subject details

Drosophila melanogaster

The *Drosophila* lines used for this study are detailed in Table C-1. The complete genotype for each figure panel is provided in Table C-2. *Drosophila* were maintained on standard cornmeal-molasses media supplemented with dry yeast. With the exception of flies containing *Gal80*^{TS}, flies were housed in plastic tubes in incubators between 18˚C–25˚C.

Fly crosses where the progeny will express Gal80^{TS} were maintained at 18°C for 2 days to inhibit Gal4 activation during embryogenesis. Progeny were then incubated at 29°C to activate Gal4, where they remained until experimentation. Thus, 3rd instar larvae were incubated at 29°C for 3-4 days before wing disc dissections and pupae were incubated at 29°C for 4-5 days before wounding.

Table C-1: Complete genotype of source flies obtained for Chapter 3

Fly lines:	Complete genotype of source flies:
"ActinP-GCaMP6m"	*w[1118]; P{w[+mC]=ActinP-GCaMP6m}attp40* (This paper)
"pnr-Gal4"	*P{w[+mC]=UAS-Dcr-2.D}1, w[1118]; P{w[+mW.hs]=GawB}pnr[MD237]/TM3, Ser[1]* (FlyBase ID: FBst0025758)
"UAS-mCherry.NLS"	*w[*]; P{w[+mC]=UAS-mCherry.NLS}3* (FlyBase ID: FBst0038424)
"tubP-Gal80^{TS}*"*	*w[*]; P{w[+mC]=tubP-GAL80[ts]}2/TM2* (FlyBase ID: FBst0007017)
"UAS-GCaMP6m"	*w[1118]; P{y[+t7.7] w[+mC]=20XUAS-IVS-GCaMP6m}attP40* (FlyBase ID: FBst0042748)

"tubP-Gal4"	*y[1] w[*]; P{w[+mC]=tubP-GAL4}LL7/TM3, Sb[1] Ser[1]* (FlyBase ID: FBst0005138)
"UAS-Inx2 RNAi"	*y[1] v[1]; P{y[+t7.7] v[+t1.8]=TRiP.JF02446}attP2* (FlyBase ID: FBst0029306)
"UAS-IP$_3$ sponge"	*UAS-IP3-m49 sponge* (on 3rd) (Usui-Aoki et al., 2005)
	The *UAS-IP3-m49 sponge* line was obtained as a gift from Eric Baehrecke Lab, (University of Massachusetts Medical School, Worcester, MA)
"UAS-IP$_3$R RNAi#1"	*y[1] v[1]; P{y[+t7.7] v[+t1.8]=TRiP.JF01957}attP2* (FlyBase ID: FBst0025937)
"UAS-IP$_3$R RNAi#2"	*UAS-itpr RNAi (no. 1063R-1,* National Institute of Genetics, Japan)
"UAS-Plc21C RNAi#1"	*y[1] sc[*] v[1] sev[21]; P{y[+t7.7] v[+t1.8]=TRiP.HMS00600}attP2*
	(FlyBase ID: FBst0033719)
"UAS-Plc21C RNAi#2"	*y[1] v[1]; P{y[+t7.7] v[+t1.8]=TRiP.JF01211}attP2* (FlyBase ID: FBst0031270)
"UAS-Gαq RNAi#1"	*y[1] v[1]; P{y[+t7.7] v[+t1.8]=TRiP.JF01209}attP2/TM3, Ser[1]* (FlyBase ID: FBst0031268)
"UAS- Gαq RNAi#2"	*y[1] v[1]; P{y[+t7.7] v[+t1.8]=TRiP.JF02464}attP2* (FlyBase ID: FBst0033765)
"UAS-mthl10 RNAi#1"	*y[1] v[1]; P{y[+t7.7] v[+t1.8]=TRiP.HMJ23672}attP40/CyO* (FlyBase ID: FBst0062315)
"UAS-mthl10 RNAi#2"	*y[1] v[1]; P{y[+t7.7] v[+t1.8]=TRiP.HMC03304}attP2* (FlyBase ID: FBst0051753)
"UAS-AdoR RNAi"	*y[1] sc[*] v[1] sev[21]; P{y[+t7.7] v[+t1.8]=TRiP.HMC03684}attP2*
	(FlyBase ID: FBst0056866)
"UAS-Tre1 RNAi"	*y[1] v[1]; P{y[+t7.7] v[+t1.8]=TRiP.JF02751}attP2* (FlyBase ID: FBst0027672)
"UAS-TkR86C RNAi"	*y[1] v[1]; P{y[+t7.7] v[+t1.8]=TRiP.JF02160}attP2* (FlyBase ID: FBst0031884)
"UAS-Trpm RNAi#1"	*y[1] v[1]; P{y[+t7.7] v[+t1.8]=TRiP.JF01236}attP2* (FlyBase ID: FBst0031291)
"UAS-Trpm RNAi#2"	*y[1] v[1]; P{y[+t7.7] v[+t1.8]=TRiP.JF01465}attP2* (FlyBase ID: FBst0031672)
"ΔGbp1,2"	*Df(2R)Gbp-ex67* (Koyama and Mirth, 2016) *(obtained as a gift from Takashi Koyama, (IGC, Lisbon, Portugal))*
"Gbp1^Δ"	*w[1118]; Gbp1^Δ*
"Gbp2^{3ΔFS}"	*w[1118]; Gbp2^{3ΔFS}*
"vas-Cas9"	*w[1118]; PBac{y[+mDint2]=vas-Cas9}VK00027* (FlyBase ID: FBst0051324)

Table C-2: Complete genotype for each figure panel.

Figure	Full Genotype of Sample
Figure 3-1A'	*pnr-Gal4, UAS-mCherry.NLS, tubP-Gal80^{TS} / +*
Figure 3-1B-D, Figure 3-11H	*ActinP-GCaMP6m / + ; pnr-Gal4, UAS-mCherry.NLS, tubP-Gal80^{TS} / +*
Figure 3-1E	*ActinP-GCaMP6m / + ; pnr-Gal4, UAS-mCherry.NLS, tubP-Gal80^{TS} / UAS-IP$_3$R RNAi #1*
Figure 3-1F	*ActinP-GCaMP6m / + ; pnr-Gal4, UAS-mCherry.NLS, tubP-Gal80^{TS} / UAS-Plc21C RNAi #1*
Figure 3-1G-H	*ActinP-GCaMP6m / + ; pnr-Gal4, UAS-mCherry.NLS, tubP-Gal80^{TS} / UAS-Gαq RNAi #1*
Figure 3-3A	*ActinP-GCaMP6m / + ; pnr-Gal4, UAS-mCherry.NLS, tubP-Gal80^{TS} / UAS-Trpm RNAi #2*
Figure 3-3B	*ActinP-GCaMP6m / + ; pnr-Gal4, UAS-mCherry.NLS, tubP-Gal80^{TS} / UAS-AdoR RNAi*
Figure 3-3C, Figure 3-11B	*ActinP-GCaMP6m / UAS-Mthl10 RNAi #1 ; pnr-Gal4, UAS-mCherry.NLS, tubP-Gal80^{TS} / +*
Figure 3-4B, Figure 3-11D-F (+/+)	*ActinP-GCaMP6m / ActinP-GCaMP6m*
Figure 3-4C	*ActinP-GCaMP6m, Gbp1^Δ / ActinP-GCaMP6m, Gbp1^Δ*
Figure 3-4D	*ActinP-GCaMP6m, Gbp2^{3ΔFS} / ActinP-GCaMP6m, Gbp2^{3ΔFS}*

Figure 3-4E	*ActinP-GCaMP6m, ΔGbp1,2 / ActinP-GCaMP6m, ΔGbp1,2*	
Figure 3-5A-B, Figure 3-6	*ActinP-GCaMP6m / CyO*	
Figure 3-5C-D, F-G	*UAS-GCaMP6m / + ; tubP-Gal4, tubP-Gal80^{TS} / UAS-mCherry.NLS*	(White)
	UAS-GCaMP6m / UAS-Mthl10 RNAi #1 ; tubP-Gal4, tubP-Gal80^{TS} / +	(Red)
Figure 3-7A-F	*UAS-GCaMP6m / + ; tubP-Gal4, tubP-Gal80^{TS} / UAS-mCherry.NLS*	(White)
	ActinP-GCaMP6m, ΔGbp1,2 / ActinP-GCaMP6m, ΔGbp1,2	(Red)
Figure 3-11D-F	*ActinP-GCaMP6m, ΔGbp1,2 / ActinP-GCaMP6m, Gbp1^Δ*	
Figure 3-11D-F	*ActinP-GCaMP6m, ΔGbp1,2 / ActinP-GCaMP6m, Gbp2^{3ΔFS}*	
Figure 3-2A	*ActinP-GCaMP6m / + ; pnr-Gal4, UAS-mCherry.NLS, tubP-Gal80^{TS} / UAS-Inx2 RNAi #1*	
Figure 3-2B	*ActinP-GCaMP6m / + ; pnr-Gal4, UAS-mCherry.NLS, tubP-Gal80^{TS} / UAS-IP$_3$ sponge*	

Drosophila extract preparation

Fly and larval extract was made following a protocol adapted from Brodskiy et al. 2019[182] and Currie et al. 1988[193]. Briefly, 100 healthy adult flies with a female:male ratio of 3:1 or 100 healthy 3rd instar larvae, from non-overcrowded bottles, were homogenized in 750 µl of Schneider's *Drosophila* media (Thermo Fisher, #21720024). The resulting homogenates were centrifuged at 4°C for 20 minutes at 2600g. The supernatant was heat treated at 60°C for 5 minutes, before a second centrifugation at 4°C for 90 minutes at 2600g. The resulting supernatant – considered 100% extract – was aliquoted and stored at -20°C.

C.3 Method details

Pupal mounting

White prepupae were identified and aged for 12-18 hours After Puparium Formation (APF) at 29°C. Each pupa was placed ventral side down on a piece of double-sided tape (Scotch brand, catalog #665) adhered to a microscope slide, and the anterior pupal case was removed with fine tipped forceps to reveal the head and thorax. The entire piece of double-sided tape (with dissected pupa) was gently lifted off the microscope slide and adhered to a 35 mm x 50 mm coverslip (Fisherbrand, cat#125485R) so the pupa is laid against the coverslip notum-side down, with the pupa sandwiched between the coverslip and the tape layer. Then, an oxygen permeable membrane (YSI, standard membrane kit, cat#1329882) was applied over the pupa and secured to the coverslip with additional double-sided tape so the pupa would not become dehydrated or deprived of oxygen.

Pupal survival

When mounted as described above, pupae developed normally for the next 3-4 days until eclosion, whereupon the adult flies crawled out of their cases and became

stuck on the double-sided tape a few inches away. Pupal survival was measured as whether a pupa had developed into an adult fly and emerged from its case in this manner within 7 days after wounding (to ensure a pupa delayed in development was not accidentally miscounted as dead). Slides of pupae were returned to 29°C during this recovery phase after wounding to maintain Gal4 activation.

Live imaging

Live imaging of pupae was performed using a Zeiss (Oberkochen, Germany) LSM410 raster-scanning inverted confocal microscope with a 40X 1.3 NA oil-immersion objective. Raster-scans were performed with a 2.26 s scan time per image with no interval between scans. Live imaging of wing discs was performed on the same scope, with the confocal settings turned off to maximize imaging depth, using a 25X 0.8 NA air objective. Raster-scans were performed with a 2.26 s scan time per image with a 15 s interval between scans. Notum picture in Figure 3-1A' was taken on the same scope at 10X 0.50 NA air objective.

Images collected specifically for Figure 3-11C–F were captured on a Nikon Ti2 Eclipse with X-light V2 spinning disc (Nikon, Tokyo, Japan) with a 40X 1.3 NA oil-immersion objective.

Laser ablation

Laser ablation was performed using single pulses of the 3rd harmonic (355 nm) of a Q-switched Nd:YAG laser (5 ns pulse-width, Continuum Minilite II, Santa Clara, CA). Laser pulse energies were on the order of 1 µJ, but were varied day to day and based on focal plane of ablation in order to optimize consistent wound sizes. A separate computer-controlled mirror and custom ImageJ plug-in were used to aim and operate the ablation laser so that ablation could be performed without any interruption to live imaging. The frame during ablation was retroactively considered t = 0 s.

Puncture wounding

Multiple pupae were placed on a piece of double-sided tape (Scotch brand, catalog #665), ventral side down on a microscope slide, and each anterior pupal case was removed with fine tipped forceps to reveal the notum epithelium (as in Figure 3-1A). The slide was mounted on the stage of an upright epifluorescence microscope (Zeiss Axio M2) and imaged with a 1 s interval on a 5x objective (Zeiss EC Plan-NEOFLUAR 420330-9901). Pupae expressing GCaMP6m were manually punctured with an electrolytically sharpened tungsten needle (Fine Science Tools, No:10130) while imaging. The frame when the puncture occurred was retroactively considered t = 0 s. Unfortunately, many puncture wounds resulted in a bubble of hemolymph that pooled over the wound, obscuring the initial influx and first expansion from multiple samples. However, the distal calcium response was always speckled in gap-junction knockdowns and always absent in G_q-pathway knockdowns, recapitulating laser wounds.

189

Wing disc mounting

Wing discs from 3rd instar larvae were dissected in Schneider's *Drosophila* media (Gibco, Life Technologies, Ref:21720-024) and immediately mounted in a small bubble of Schneider's *Drosophila* media on coverslips (Fisherbrand, cat#125485R) for imaging. A pap pen (RPI, catalog #50-550-221) was used to trace a hydrophobic barrier around the wing discs on the coverslip. Two wing discs, control and experimental, were mounted side-by-side in the same media bubble. The control disc was identifiable by the presence of mCherry which was not present in the experimental disc. Images were taken to establish a baseline of GCaMP fluorescence, and then potential calcium activators were pipetted directly into the media bubble over the wing discs. The concentration of calcium activators in the text refers to the final concentration after addition to the media bubble. The image taken during pipetting was retroactively considered t = 0 s.

Protease inhibition experiments

To test whether ∆*Gbp1,2* Larval Extract elicits a calcium response in control wing discs via proteases, we pre-mixed protease inhibitor cocktails or vehicle-only controls either into the extract or media bubble before addition to the wing disc. Specifically, we used 1) Cell Signaling Technologies Protease inhibitor cocktail (Cell Signaling Technology, #5871S), which had no effect on the extract-mediated calcium response of ∆*Gbp1,2* Larval Extract when mixed at or below the 2x recommended concentration; at 3x recommended concentrations, the inhibitor itself elicited an ectopic calcium response on the discs, making it unusable for properly testing the extract-mediated calcium response. 2) MS-Safe Protease and Phosphatase inhibitor (Millipore Sigma, MSSAFE), which had no effect on the extract-mediated calcium response of ∆*Gbp1,2* Larval Extract when mixed at or below the 1x recommended concentration; at 1.5x recommended concentrations, the inhibitor itself elicited an ectopic calcium response on the discs, making it unusable for properly testing the extract-mediated calcium response. 3) Two other protease inhibitors tested (Millipore Sigma, 539134 and Millipore Sigma, 539133) used DMSO as a vehicle, which itself induces an ectopic calcium response in wing discs at even small concentrations (1% final v/v). Therefore, both of these protease inhibitors were not usable for properly testing the extract-mediated calcium response.

Peptide synthesis

The amino acid sequence for Growth-blocking peptides 1–5 is shown below (Tsuzuki et al., 2012).

Gbp1 (CG15917): ILLETTQKCKPGFELFGKRCRKPA

Gbp2 (CG11395): SLFNLDPKCAEGLKLMAGRCRKEA

Gbp3 (CG17244): MVAMIDFPCQPGYLPDHRGRCREIW

Gbp4 (CG12517): ILLDTSRKCRPGLELFGVRCRRRA

Gbp5 (CG14069): MLLEIQKRCWAGWGLLAGRCRKLA

These sequences were sent to Genscript (Piscataway, NJ. USA) for peptide synthesis under conditions to maintain the disulfide bond. The lyophilized peptide was reconstituted in ultrapure water, diluted to a concentration of 0.1 µM, aliquoted, and frozen at -80°C.

Protease preparation

Cysteine protease Clostripain (Alfa Aesar, Thermo Fisher, Stock: J61362) was reconstituted in a TBS solution (10 mM Tris, 1 mM $CaCl_2$, 50 mM NaCl, 2.5 mM beta-mercaptoethanol) to a final concentration of 1mg/mL (18.9 µM). This was aliquoted and frozen at -20°C. Serine protease trypsin (Gibco, Life Technologies, Ref: 25300-054) arrived at a concentration of 0.05% w/v (21.4 µM) and was refrigerated at 4°C.

ActinP-GCaMP6m generation

pBPw.Act5CP-GCaMP6m was generated from the GCaMP6m plasmid pGP-CMV-GCaMP6m (Addgene, originally in Chen et al. 2013[173]) and the Actin5c promoter[194]. Importantly, this construct features the full 4.4 Kb genomic enhancer sequence for actin, containing all the regulatory elements to drive ubiquitous expression, rather than the more commonly used 2.6 Kb actin promoter sequence which is not highly expressed in the pupal notum. This 4.4 Kb promoter was obtained as a gift from Gary Struhl (Columbia University, New York, NY). The *pBPw.Act5CP-GCaMP6m* construct was injected by BestGene (Chino Hills, CA. USA) into *Drosophila* using PhiC31 integrase at the attP40 site at 25C6 on Chromosome 2, generating the *ActinP-GCaMP6m* fly line.

Gbp1△ generation

The *Gbp1△* null mutant was created by targeting two CRISPR-mediated double-stranded breaks to the *Gbp1* gene locus (www.crisprflydesign.org). The following gRNAs were chosen:

#1) ATTTGCTCCCATCATTTATC

#2) CGGAAAACGATGCAGAAAGC

gRNAs sequences with extensions to allow for BbsI digestion were synthesized as single-stranded DNA oligos and annealed to form overhangs, then ligated to a pCFD5 vector (Addgene, #73914) digested with BbsI (NEB, #R3539S). Both plasmids were sequence-verified then injected by BestGene (Chino Hills, CA. USA) into *vas-Cas9* expressing *Drosophila* embryos (Bloomington Stock 51324). *vas-Cas9* was crossed out of progeny and mutants were identified by PCR for the presence of a *Gbp1* deletion.

On sequencing, *Gbp1*$^\Delta$ was found to be missing 282 nucleotides, spanning the coding region corresponding to 94 amino acids from A22 to K116. This includes the C-terminal active peptide of the Gbp1 protein, which spans I95 to A118.

Gbp2$^{3\Delta FS}$ generation

The *Gbp2*$^{3\Delta FS}$ null mutant was created by targeting two CRISPR-mediated double-stranded breaks in the *Gbp2* gene locus, using the protocol above. The following gRNAs were chosen:

#1) GAATATTCAACGCTGCCGTT

#2) AATTCCATACAACCGCGTCC

On sequencing, the *Gbp2*$^{3\Delta FS}$ allele was found to create multiple lesions: 8 missense mutations within the protein coding region generating the following amino acid substitutions: P41S, N42H, V51G, I61N, V94G, P150S, N192I, and S218P. Additionally, 3 small regions were deleted from the protein coding region: 30 nucleotides corresponding to Q236–Q246, 60 nucleotides corresponding to S252–T272, and 128 nucleotides corresponding to G284–R326. The last deletion induced a frameshift, creating multiple missense mutations and 4 stop codons in the final 391 nucleotides of the gene, thus preventing transcription of the region corresponding to the C-terminal active peptide of the Gbp2 protein, which spans S433 to A456.

C.4 Quantification and statistical analysis

Calcium signal intensity analysis

Fluorescence intensity of wing discs was measured using the Measure Stack plug-in in ImageJ. The region of interest was defined around the entire wing disc using the polygon selection tool. The mean fluorescence intensity for each disc was graphed in Microsoft Excel as a function of time, with 0 s corresponding to the frame when calcium activators were added to the wing disc media. The $\Delta F/F_0$ value for each experiment was defined as the disc's fluorescence intensity in the initial frame of the movie subtracted from the disc's maximum intensity, normalized to the initial frame intensity.

Calcium signal radius analysis

To quantify the spread of calcium signals from full-frame time-lapse images (Figure C-1A, A'), the ImageJ Radial Profile Angle Plot plug-in was used on each image to determine the average GCaMP6m intensity profile as a function of distance from the center of the wound (Figure C-1B, B'). A custom MATLAB script was then used to determine the distance from the wound at which the intensity dropped to half its maximum. This distance corresponds to the radius of the radially-averaged calcium

wave and plotting radius for each video frame yields a graph of calcium signal expansion over time, which was graphed in Microsoft Excel (Figure C-1A').
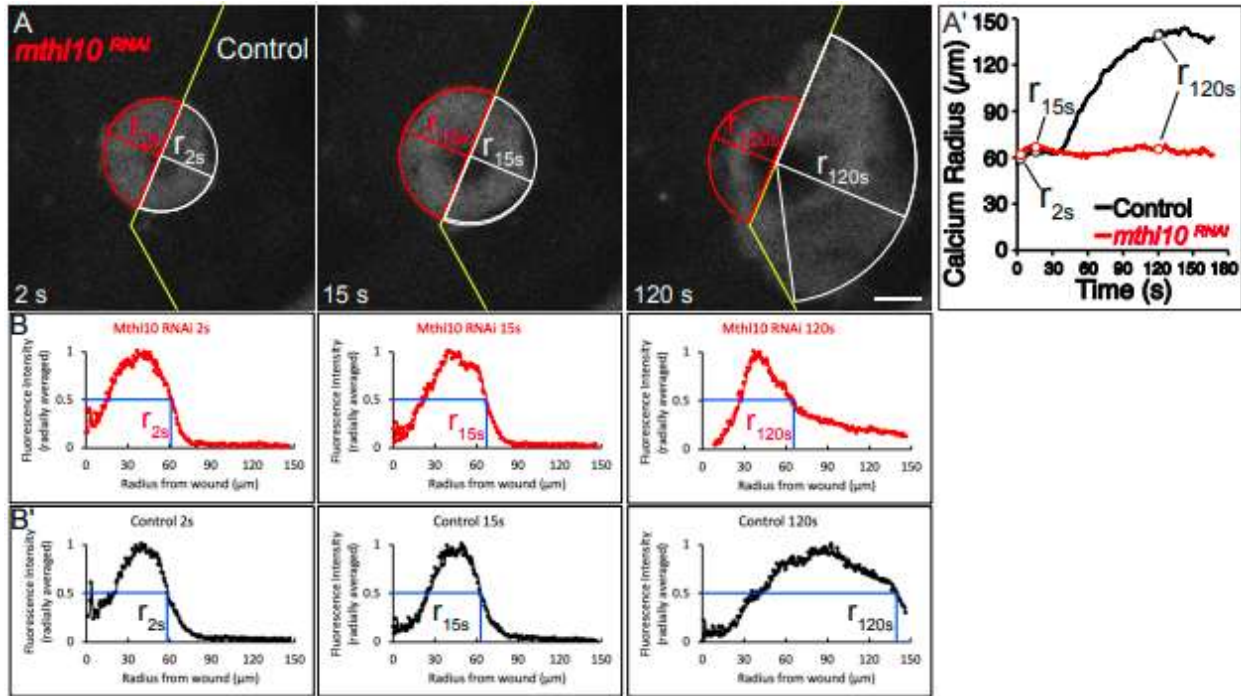
Figure C-1: Radial analysis of calcium signaling.

(**A**) Illustration of the radius analysis, applied to the sample shown in Figure 3-3C. The averaged calcium radius is defined for the knockdown and control sides at each time point independently, which can then be graphed as a function of time (**A'**). (**B, B'**) At each time point, the MATLAB program analyzes the radially averaged fluorescence intensity, and determines the upper radius of half maximum to define the calcium radius. The experimental domain (**B**) and internal-control domain (**B'**) are analyzed independently, delineated by *pnr>mCherry.NLS* (as in Figure 3-1B). Scale bar = 50 μm.

The only exception to this applies to the analysis for Figure 3-11D–F. Because these images were taken on a different scope, the custom MATLAB script was not optimized to determine radius vs time automatically, so these images were quantified by hand. Different control images were taken for this data-set than the controls in Figure 3-4, and this may explain any small discrepancies in spatial or temporal response values.

For all movies with an internal control, *pnr>mCherry.NLS* expression was used to define the experimental and control domains (as in Figure 3-1B). The average calcium signal within each domain was measured separately. After plotting calcium radius with respect to time, the Δradius value for each sample was defined as the maximum value of the control domain calcium radius minus the calcium radius of the *pnr*-expressing experimental domain at the same time point (as shown in Figure 3-1E').

For movies without an internal control, R_{Max} was defined as the maximum value of the calcium radius and R_{1st} as the value of the calcium radius at the first expansion local maximum. Duration of distal calcium response was defined by the duration the calcium response remained greater than R_{1st}. Movies cut off before the distal calcium response dipped below R_{1st} were excluded from duration analysis. Start time was defined as the time after wounding where the calcium radius value increased for at least three consecutive frames (excluding the first expansion increase). Movies where this never occurred were excluded from start time analysis.

Statistical analysis

All statistical analysis was performed in GraphPad Prism (San Diego, CA. USA). Δradius values for all samples of each genotype were graphed in Prism, and statistical analysis was performed by one-way ANOVA with multiple comparisons of each genotype from Figure 3-1, Figure 3-2, and Figure 3-3 simultaneously with respect to the control group from Fig. 1I. Values for radius, duration, and start time analyses in Figure 3-4G–I and Figure 3-11D–F were graphed in Prism and statistical analysis was performed by one-way ANOVA with multiple comparisons with respect to the control group. Similarly, $\Delta F/F_0$ values for all wing disc experiments were graphed in Prism, and statistical analysis was performed by Student's t-test in all cases except for Figure 3-7C which was analyzed by two-way ANOVA with multiple comparisons of each genotype with respect to the control extract + control disc group. Each scatterplot displays the value for each sample as a point, with bars representing mean and SEM.

References

1.   Honda, H. The world of epithelial sheets. *Dev Growth Differ* **59**, 306–316 (2017).

2.   Martini, E., Krug, S. M., Siegmund, B., Neurath, M. F. & Becker, C. Mend Your Fences: The Epithelial Barrier and its Relationship With Mucosal Immunity in Inflammatory Bowel Disease. *Cell Mol Gastroenterol Hepatol* **4**, 33–46 (2017).

3.   Gumbiner, B. M. Breaking through the tight junction barrier. *Journal of Cell Biology* vol. 123 Preprint at https://doi.org/10.1083/jcb.123.6.1631 (1993).

4.   Park, S. *et al.* Tissue-scale coordination of cellular behaviour promotes epidermal wound repair in live mice. *Nature Cell Biology 2017 19:3* **19**, 155–163 (2017).

5.   Enyedi, B. & Niethammer, P. Mechanisms of epithelial wound detection. *Trends in Cell Biology* vol. 25 Preprint at https://doi.org/10.1016/j.tcb.2015.02.007 (2015).

6.   Vogel, A. & Venugopalan, V. Mechanisms of pulsed laser ablation of biological tissues. *Chemical Reviews* vol. 103 577–644 Preprint at https://doi.org/10.1021/cr010379n (2003).

7.   Campbell, C. J., Noyori, K. S., Rittler, M. C. & Koester, C. J. Intraocular temperature changes produced by laser coagulation. *Acta Ophthalmol Suppl* (1963).

8.   Goldman, L., Blaney, D. J., Kindel, D. J. & Franke, E. K. Effect of the laser beam on the skin. Preliminary report. *J Invest Dermatol* **40**, (1963).

9.   Lynch, H. E. *et al.* Cellular mechanics of germ band retraction in Drosophila. *Dev Biol* **384**, 205–213 (2013).

10.   Antunes, M., Pereira, T., Cordeiro, J. v., Almeida, L. & Jacinto, A. Coordinated waves of actomyosin flow and apical cell constriction immediately after wounding. *Journal of Cell Biology* **202**, 365–379 (2013).

11.   O'Connor, J., Akbar, F. B., Hutson, M. S. & Page-McCaw, A. Zones of cellular damage around pulsed-laser wounds. *PLoS One* **16**, e0253032 (2021).

12.   Compton, J. L., Hellman, A. N. & Venugopalan, V. Hydrodynamic determinants of cell necrosis and molecular delivery produced by pulsed laser microbeam irradiation of adherent cells. *Biophys J* **105**, 2221–2231 (2013).

13.   Rau, K. R., Quinto-Su, P. A., Hellman, A. N. & Venugopalan, V. Pulsed Laser Microbeam-Induced Cell Lysis: Time-Resolved Imaging and Analysis of Hydrodynamic Effects. *Biophys J* **91**, 317–329 (2006).

14. Hellman, A. N., Rau, K. R., Yoon, H. H. & Venugopalan, V. Biophysical Response to Pulsed Laser Microbeam-Induced Cell Lysis and Molecular Delivery. *J Biophotonics* **1**, 24–35 (2008).

15. Horn, A. & Jaiswal, J. K. Cellular mechanisms and signals that coordinate plasma membrane repair. *Cellular and Molecular Life Sciences 2018 75:20* **75**, 3751–3770 (2018).

16. Chen, C., Smye, S. W., Robinson, M. P. & Evans, J. A. Membrane electroporation theories: A review. *Med Biol Eng Comput* **44**, 5–14 (2006).

17. McNeil, P. L. & Steinhardt, R. A. Plasma Membrane Disruption: Repair, Prevention, Adaptation. *http://dx.doi.org.proxy.library.vanderbilt.edu/10.1146/annurev.cellbio.19.111301.140101* **19**, 697–731 (2003).

18. Roh, J. S. & Sohn, D. H. Damage-Associated Molecular Patterns in Inflammatory Diseases. *Immune Netw* **18**, (2018).

19. Berridge, M. J., Bootman, M. D. & Roderick, H. L. Calcium signalling: dynamics, homeostasis and remodelling. *Nature Reviews Molecular Cell Biology 2003 4:7* **4**, 517–529 (2003).

20. Brodskiy, P. A. & Zartman, J. J. Calcium as a signal integrator in developing epithelial tissues. *Phys Biol* **15**, (2018).

21. Leybaert, L. & Sanderson, M. J. INTERCELLULAR Ca2 WAVES: MECHANISMS AND FUNCTION. *Physiol Rev* **92**, 1359–1392 (2012).

22. Skupin, A. *et al.* How does intracellular Ca2+ oscillate: By chance or by the clock? *Biophys J* **94**, 2404–2411 (2008).

23. Guisoni, N., Ferrero, P., Layana, C. & Diambra, L. Abortive and Propagating Intracellular Calcium Waves: Analysis from a Hybrid Model. *PLoS One* **10**, e0115187 (2015).

24. Thomas, A. P., Bird, G. St. J., Hajnóczky, G., Robb-Gaspers, L. D. & Putney, J. W. Spatial and temporal aspects of cellular calcium signaling. *The FASEB Journal* **10**, 1505–1517 (1996).

25. Berridge, M. J., Bootman, M. D. & Lipp, P. Calcium - a life and death signal. *Nature 1998 395:6703* **395**, 645–648 (1998).

26. de Koninck, P. & Schulman, H. Sensitivity of CaM Kinase II to the Frequency of Ca2+ Oscillations. *Science (1979)* **279**, 227–230 (1998).

27. Swulius, M. T. & Waxham, M. N. Ca2+/Calmodulin-dependent Protein Kinases. *Cellular and Molecular Life Sciences 2008 65:17* **65**, 2637–2657 (2008).

28. Xu, S. & Chisholm, A. D. A Gαq-Ca2+ signaling pathway promotes actin-mediated epidermal wound closure in C. elegans. *Current Biology* **21**, 1960–1967 (2011).

29. Razzell, W., Evans, I. R., Martin, P. & Wood, W. Calcium flashes orchestrate the wound inflammatory response through duox activation and hydrogen peroxide release. *Current Biology* **23**, 424–429 (2013).

30. Justet, C., Hernández, J. A., Torriglia, A. & Chifflet, S. Fast calcium wave inhibits excessive apoptosis during epithelial wound healing. *Cell Tissue Res* **365**, (2016).

31. Noren, D. P. *et al.* Endothelial cells decode VEGF-mediated Ca2+ signaling patterns to produce distinct functional responses. *Sci Signal* **9**, (2016).

32. Wales, P. *et al.* Calcium-mediated actin reset (CaAR) mediates acute cell adaptations. *Elife* **5**, (2016).

33. Landge, A. N., Jordan, B. M., Diego, X. & Müller, P. Pattern formation mechanisms of self-organizing reaction-diffusion systems. *Dev Biol* **460**, 2–11 (2020).

34. Boie, S., Kirk, V., Sneyd, J. & Wechselberger, M. Effects of quasi-steady-state reduction on biophysical models with oscillations. *J Theor Biol* **393**, 16–31 (2016).

35. Falcke, M. Reading the patterns in living cells —the physics of ca2+ signaling. *Adv Phys* **53**, (2004).

36. Dupont, G., Falcke, M., Kirk, V. & Sneyd, J. *Models of Calcium Signalling*. vol. 43 (Springer International Publishing, 2016).

37. Atri, A., Amundson, J., Clapham, D. & Sneyd, J. A Single-Pool Model for Intracellular Calcium Oscillations and Waves in the Xenopus laevis Oocyte. *Biophys J* **65**, 1727–1739 (1993).

38. Cao, P., Tan, X., Donovan, G., Sanderson, M. J. & Sneyd, J. A Deterministic Model Predicts the Properties of Stochastic Calcium Oscillations in Airway Smooth Muscle Cells. *PLoS Comput Biol* **10**, 1003783 (2014).

39. Han, J. M., Tanimura, A., Kirk, V. & Sneyd, J. A mathematical model of calcium dynamics in HSY cells. *PLoS Comput Biol* (2017) doi:10.1371/journal.pcbi.1005275.

40. Wagner, L. E. & Yule, D. I. Differential regulation of the InsP3 receptor type-1 and -2 single channel properties by InsP3, Ca2+ and ATP. *Journal of Physiology* **590**, (2012).

41. Sneyd, J. & Falcke, M. Models of the inositol trisphosphate receptor. *Prog Biophys Mol Biol* **89**, 207–245 (2005).

42. Li, Y. X. & Rinzel, J. Equations for InsP3 Receptor-mediated [Ca2+]i Oscillations Derived from a Detailed Kinetic Model: A Hodgkin-Huxley Like Formalism. *J Theor Biol* **166**, 461–473 (1994).

43. de Young, G. W. & Keizer, J. A single-pool inositol 1,4,5-trisphosphate-receptor-based model for agonist-stimulated oscillations in Ca2+ concentration. *Proc Natl Acad Sci U S A* **89**, (1992).

44. Abreu-Blanco, M. T., Verboon, J. M., Liu, R., Watts, J. J. & Parkhurst, S. M. Drosophila embryos close epithelial wounds using a combination of cellular protrusions and an actomyosin purse string. *J Cell Sci* **125**, (2012).

45. Matsubayashi, Y. & Millard, T. H. Analysis of the Molecular Mechanisms of Reepithelialization in Drosophila Embryos. *Advances in Wound Care* vol. 5 Preprint at https://doi.org/10.1089/wound.2014.0549 (2016).

46. Singer, A. J. & Clark, R. A. F. Cutaneous Wound Healing. *N Engl J Med* **341**, 738–746 (1999).

47. Stevens, L. J. & Page-McCaw, A. A secreted MMP is required for reepithelialization during wound healing. *Mol Biol Cell* **23**, 1068–1079 (2012).

48. Sammak, P. J., Hinman, L. E., Tran, P. O. T., Sjaastad, M. D. & Machen, T. E. How do injured cells communicate with the surviving cell monolayer? *J Cell Sci* **110**, (1997).

49. Shabir, S. & Southgate, J. Calcium signalling in wound-responsive normal human urothelial cell monolayers. *Cell Calcium* **44**, (2008).

50. Gao, K. *et al.* Traumatic scratch injury in astrocytes triggers calcium influx to activate the JNK/c-Jun/AP-1 pathway and switch on GFAP expression. *Glia* **61**, (2013).

51. Benink, H. A. & Bement, W. M. Concentric zones of active RhoA and Cdc42 around single cell wounds. *Journal of Cell Biology* **168**, (2005).

52. Klepeis, V. E., Weinger, I., Kaczmarek, E. & Trinkaus-Randall, V. P2Y receptors play a critical role in epithelial cell communication and migration. *J Cell Biochem* **93**, (2004).

53. Weinger, I., Klepeis, V. E. & Trinkaus-Randall, V. Tri-nucleotide receptors play a critical role in epithelial cell wound repair. *Purinergic Signal* **1**, (2005).

54. Chifflet, S. *et al.* Early and late calcium waves during wound healing in corneal endothelial cells. *Wound Repair and Regeneration* **20**, (2012).

55. Wood, W. Wound healing: Calcium flashes illuminate early events. *Current Biology* vol. 22 Preprint at https://doi.org/10.1016/j.cub.2011.11.019 (2012).

56. Restrepo, S. & Basler, K. Drosophila wing imaginal discs respond to mechanical injury via slow InsP 3 R-mediated intercellular calcium waves. *Nat Commun* **7**, (2016).

57. Colombelli, J., Reynaud, E. G., Rietdorf, J., Pepperkok, R. & Stelzer, E. H. K. In vivo selective cytoskeleton dynamics quantification in interphase cells induced by pulsed ultraviolet laser nanosurgery. *Traffic* **6**, (2005).

58. Khodjakov, A., Cole, R. W., Oakley, B. R. & Rieder, C. L. Centrosome-independent mitotic spindle formation in vertebrates. *Current Biology* **10**, (2000).

59. Abreu-Blanco, M. T., Verboon, J. M. & Parkhurst, S. M. Cell wound repair in Drosophila occurs through three distinct phases of membrane and cytoskeletal remodeling. *Journal of Cell Biology* **193**, (2011).

60. Greulich, K. O. *et al.* Micromanipulation by laser microbeam and optical tweezers: From plant cells to single molecules. *J Microsc* **198**, (2000).

61. Berns, M. W., Wright, W. H. & Steubing, R. W. Laser Microbeam as a Tool in Cell Biology. *Int Rev Cytol* **129**, (1991).

62. Vogel, A., Busch, S. & Parlitz, U. Shock wave emission and cavitation bubble generation by picosecond and nanosecond optical breakdown in water. *J Acoust Soc Am* **100**, 148 (1996).

63. Vogel, A. Nonlinear absorption: Intraocular microsurgery and laser lithotripsy. *Phys Med Biol* **42**, (1997).

64. Venugopalan, V., Guerra, A., Nahen, K. & Vogel, A. Role of laser-induced plasma formation in pulsed cellular microsurgery and micromanipulation. *Phys Rev Lett* **88**, (2002).

65. Hutson, M. S. & Ma, X. Plasma and cavitation dynamics during pulsed laser microsurgery in vivo. *Phys Rev Lett* **99**, (2007).

66. Zeitlinger, J. & Bohmann, D. Thorax closure in Drosophila: Involvement of Fos and the JNK pathway. *Development* **126**, (1999).

67. Tian, L. *et al.* Imaging neural activity in worms, flies and mice with improved GCaMP calcium indicators. *Nat Methods* **6**, (2009).

68. Allbritton, N. L., Meyer, T. & Stryer, L. Range of messenger action of calcium ion and inositol 1,4,5-trisphosphate. *Science (1979)* **258**, (1992).

69. Dijkink, R. *et al.* Controlled cavitation-cell interaction: Trans-membrane transport and viability studies. *Phys Med Biol* **53**, (2008).

70. Li, X. *et al.* Cell membrane damage is involved in the impaired survival of bone marrow stem cells by oxidized low-density lipoprotein. *J Cell Mol Med* **18**, (2014).

71. Fan, Z., Kumon, R. E., Park, J. & Deng, C. X. Intracellular delivery and calcium transients generated in sonoporation facilitated by microbubbles. *Journal of Controlled Release* **142**, (2010).

72. Kumon, R. E. *et al.* Ultrasound-induced calcium oscillations and waves in Chinese hamster ovary cells in the presence of microbubbles. *Biophys J* **93**, (2007).

73. Tsukamoto, A. *et al.* Stable cavitation induces increased cytoplasmic calcium in L929 fibroblasts exposed to 1-MHz pulsed ultrasound. *Ultrasonics* **51**, (2011).

74. Juffermans, L. J. M., Dijkmans, P. A., Musters, R. J. P., Visser, C. A. & Kamp, O. Transient permeabilization of cell membranes by ultrasound-exposed microbubbles is related to formation of hydrogen peroxide. *Am J Physiol Heart Circ Physiol* **291**, (2006).

75. Wright, S. H. Generation of resting membrane potential. *American Journal of Physiology - Advances in Physiology Education* **28**, (2004).

76. Cao, G. *et al.* Genetically targeted optical electrophysiology in intact neural circuits. *Cell* **154**, (2013).

77. Jin, L. *et al.* Single action potentials and subthreshold electrical events imaged in neurons with a novel fluorescent protein voltage probe. *Neuron* **75**, 779–785 (2012).

78. Davenport, N. R., Sonnemann, K. J., Eliceiri, K. W. & Bement, W. M. Membrane dynamics during cellular wound repair. *Mol Biol Cell* **27**, 2272–2285 (2016).

79. Bansal, D. *et al.* Defective membrane repair in dysferlin-deficient muscular dystrophy. *Nature* **423**, (2003).

80. Escoffre, J. M. *et al.* Membrane disorder and phospholipid scrambling in electropermeabilized and viable cells. *Biochim Biophys Acta Biomembr* **1838**, (2014).

81. McDade, J. R., Archambeau, A. & Michele, D. E. Rapid actin-cytoskeleton-dependent recruitment of plasma membrane-derived dysferlin at wounds is critical for muscle membrane repair. *FASEB Journal* **28**, (2014).

82. Thompson, G. L., Roth, C. C., Dalzell, D. R., Kuipers, M. A. & Ibey, B. L. Calcium influx affects intracellular transport and membrane repair following nanosecond pulsed electric field exposure. *J Biomed Opt* **19**, (2014).

83. McNeil, P. L., Miyake, K. & Vogel, S. S. The endomembrane requirement for cell surface repair. *Proc Natl Acad Sci U S A* **100**, (2003).

84. Defour, A., Sreetama, S. C. & Jaiswal, J. K. Imaging cell membrane injury and subcellular processes involved in repair. *Journal of Visualized Experiments* (2014) doi:10.3791/51106.

85.   Clementi, E. A., Marks, L. R., Roche-Håkansson, H. & Håkansson, A. P. Monitoring changes in membrane polarity, membrane integrity, and intracellular ion concentrations in Streptococcus pneumoniae using fluorescent dyes. *Journal of Visualized Experiments* (2014) doi:10.3791/51008.

86.   Cheng, J. P. X. *et al.* Caveolae protect endothelial cells from membrane rupture during increased cardiac output. *Journal of Cell Biology* **211**, (2015).

87.   Corrotte, M., Castro-Gomes, T., Koushik, A. B. & Andrews, N. W. Approaches for plasma membrane wounding and assessment of lysosome-mediated repair responses. *Methods Cell Biol* **126**, (2015).

88.   Marquez-Curtis, L. A., Sultani, A. B., McGann, L. E. & Elliott, J. A. W. Beyond membrane integrity: Assessing the functionality of human umbilical vein endothelial cells after cryopreservation. *Cryobiology* **72**, (2016).

89.   Meyers, J. R. *et al.* Lighting up the senses: FM1-43 loading of sensory cells through nonselective ion channels. *Journal of Neuroscience* **23**, (2003).

90.   Li, D., Hérault, K., Oheim, M. & Ropert, N. FM dyes enter via a store-operated calcium channel and modify calcium signaling of cultured astrocytes. *Proc Natl Acad Sci U S A* **106**, (2009).

91.   Narciso, C. *et al.* Patterning of wound-induced intercellular Ca2+ flashes in a developing epithelium. *Phys Biol* **12**, (2015).

92.   Balaji, R. *et al.* Calcium spikes, waves and oscillations in a large, patterned epithelial tissue. *Sci Rep* **7**, (2017).

93.   Stevenson, D. J., Gunn-Moore, F. J., Campbell, P. & Dholakia, K. Single cell optical transfection. *Journal of the Royal Society Interface* vol. 7 Preprint at https://doi.org/10.1098/rsif.2009.0463 (2010).

94.   Stracke, F., Rieman, I. & König, K. Optical nanoinjection of macromolecules into vital cells. *J Photochem Photobiol B* **81**, (2005).

95.   Clark, I. B. *et al.* Optoinjection for efficient targeted delivery of a broad range of compounds and macromolecules into diverse cell types. *J Biomed Opt* **11**, (2006).

96.   Rhodes, K. *et al.* Cellular Laserfection. *Methods in Cell Biology* vol. 82 Preprint at https://doi.org/10.1016/S0091-679X(06)82010-8 (2007).

97.   Baumgart, J., Bintig, W., Ngezahayo, A., Lubatschowski, H. & Heisterkamp, A. Fs-laser-induced Ca^2+ concentration change during membrane perforation for cell transfection. *Opt Express* **18**, (2010).

98.   Tao, W., Wilkinson, J., Stanbridge, E. J. & Berns, M. W. Direct gene transfer into human cultured cells facilitated by laser micropuncture of the cell membrane. *Proc Natl Acad Sci U S A* **84**, (1987).

99. Compton, J. L., Luo, J. C., Ma, H., Botvinick, E. & Venugopalan, V. High-throughput optical screening of cellular mechanotransduction. *Nat Photonics* **8**, (2014).

100. Yoo, S. K., Freisinger, C. M., LeBert, D. C. & Huttenlocher, A. Early redox, Src family kinase, and calcium signaling integrate wound responses and tissue regeneration in zebrafish. *Journal of Cell Biology* **199**, (2012).

101. Enyedi, B., Jelcic, M. & Niethammer, P. The Cell Nucleus Serves as a Mechanotransducer of Tissue Damage-Induced Inflammation. *Cell* **165**, (2016).

102. Arcuino, G. *et al.* Intercellular calcium signaling mediated by point-source burst release of ATP. *Proc Natl Acad Sci U S A* **99**, (2002).

103. Gomes, P., Srinivas, S. P., Vereecke, J. & Himpens, B. ATP-dependent paracrine intercellular communication in cultured bovine corneal endothelial cells. *Invest Ophthalmol Vis Sci* **46**, (2005).

104. Minns, M. S., Teicher, G., Rich, C. B. & Trinkaus-Randall, V. Purinoreceptor P2X7 regulation of Ca2+ mobilization and cytoskeletal rearrangement is required for corneal reepithelialization after injury. *American Journal of Pathology* **186**, (2016).

105. Berra-Romani, R. *et al.* Ca2+ signaling in injured in situ endothelium of rat aorta. *Cell Calcium* **44**, (2008).

106. Klepeis, V. E., Cornell-Bell, A. & Trinkaus-Randall, V. Growth factors but not gap junctions play a role in injury-induced Ca2+ waves in epithelial cells. *J Cell Sci* **114**, (2001).

107. Clark, A. G. *et al.* Integration of Single and Multicellular Wound Responses. *Current Biology* **19**, (2009).

108. Abreu-Blanco, M. T., Verboon, J. M. & Parkhurst, S. M. Coordination of Rho family GTPase activities to orchestrate cytoskeleton responses during cell wound repair. *Current Biology* **24**, (2014).

109. McNeil, P. L. & Ito, S. Molecular traffic through plasma membrane disruptions of cells in vivo. *J Cell Sci* **96**, (1990).

110. McNeil, P. L. & Steinhardt, R. A. Loss, restoration, and maintenance of plasma membrane integrity. *Journal of Cell Biology* vol. 137 Preprint at https://doi.org/10.1083/jcb.137.1.1 (1997).

111. Hunter, M. v., Lee, D. M., Harris, T. J. C. & Fernandez-Gonzalez, R. Polarized E-cadherin endocytosis directs actomyosin remodeling during embryonic wound repair. *Journal of Cell Biology* **210**, (2015).

112. Hunter, M. v., Willoughby, P. M., Bruce, A. E. E. & Fernandez-Gonzalez, R. Oxidative Stress Orchestrates Cell Polarity to Promote Embryonic Wound Healing. *Dev Cell* **47**, (2018).

113. Shannon, E. K. *et al.* Multiple Mechanisms Drive Calcium Signal Dynamics around Laser-Induced Epithelial Wounds. *Biophys J* **113**, (2017).

114. Stanisstreet, M. Calcium and wound healing in Xenopus early embryos. *J Embryol Exp Morphol* **Vol. 67**, (1982).

115. Celli, A., Tu, C., Chang, W. & Mauro, T. M. The calcium sensing receptor regulates epidermal intracellular Ca2+ signaling and re-epithelialization in aged epidermis. *Journal of Investigative Dermatology* **139**, (2019).

116. Hander, T. *et al.* Damage on plants activates Ca 2+ -dependent metacaspases for release of immunomodulatory peptides. *Science (1979)* **363**, (2019).

117. Wu, Y. *et al.* A Blood-Borne PDGF/VEGF-like Ligand Initiates Wound-Induced Epidermal Cell Migration in Drosophila Larvae. *Current Biology* **19**, (2009).

118. Kong, D. *et al.* In vivo optochemical control of cell contractility at single-cell resolution . *EMBO Rep* **20**, (2019).

119. Levy, H. M. & Ryan, E. M. Evidence that calcium activates the contraction of actomyosin by overcoming substrate inhibition [24]. *Nature* vol. 205 Preprint at https://doi.org/10.1038/205703b0 (1965).

120. Martin, P. & Lewis, J. Actin cables and epidermal movement in embryonic wound healing. *Nature* **360**, (1992).

121. Cooper, S. T. & McNeil, P. L. Membrane repair: Mechanisms and pathophysiology. *Physiol Rev* **95**, (2015).

122. D'Hondt, C., Himpens, B. & Bultynck, G. Mechanical stimulation-Induced calcium wave propagation in cell monolayers: The example of bovine corneal endothelial cells. *Journal of Visualized Experiments* (2013) doi:10.3791/50443.

123. Gomes, P., Malfait, M., Himpens, B. & Vereecke, J. Intercellular Ca2+-transient propagation in normal and high glucose solutions in rat retinal epithelial (RPE-J) cells during mechanical stimulation. *Cell Calcium* **34**, (2003).

124. Narciso, C. E., Contento, N. M., Storey, T. J., Hoelzle, D. J. & Zartman, J. J. Release of Applied Mechanical Loading Stimulates Intercellular Calcium Waves in Drosophila Wing Discs. *Biophys J* **113**, (2017).

125. Hanlon, C. D. & Andrew, D. J. Outside-in signaling - A brief review of GPCR signaling with a focus on the Drosophila GPCR family. *Journal of Cell Science* vol. 128 Preprint at https://doi.org/10.1242/jcs.175158 (2015).

126. Chang-Graham, A. L. *et al.* Rotavirus induces intercellular calcium waves through ADP signaling. *Science (1979)* **370**, (2020).

127. Thuma, L., Carter, D., Weavers, H. & Martin, P. Drosophila immune cells extravasate from vessels to wounds using Tre1 GPCR and Rho signaling. *Journal of Cell Biology* **217**, (2018).

128. Yang, L. *et al.* Substance P promotes diabetic corneal epithelial wound healing through molecular mechanisms mediated via the neurokinin-1 receptor. *Diabetes* **63**, (2014).

129. Sung, E. J. *et al.* Cytokine signaling through Drosophila Mthl10 ties lifespan to environmental stress. *Proc Natl Acad Sci U S A* (2017) doi:10.1073/pnas.1712453115.

130. Tsuzuki, S. *et al.* Drosophila growth-blocking peptide-like factor mediates acute immune reactions during infectious and non-infectious stress. *Sci Rep* **2**, (2012).

131. Hayakawa, Y. Mechanism of parasitism-induced elevation of haemolymph growth-blocking peptide levels in host insect larvae (Pseudaletia separata). **44**, 859–866 (1998).

132. Hayakawa, Y. Structure of a growth-blocking peptide present in parasitized insect hemolymph. *Journal of Biological Chemistry* **266**, (1991).

133. Matsumoto, Y., Oda, Y., Uryu, M. & Hayakawa, Y. Insect Cytokine Growth-blocking Peptide Triggers a Termination System of Cellular Immunity by Inducing Its Binding Protein *. **278**, 38579–38585 (2003).

134. Shears, S. B. & Hayakawa, Y. Functional multiplicity of an insect cytokine family assists defense against environmental stress. *Front Physiol* **10**, 222 (2019).

135. Koyama, T. & Mirth, C. K. Growth-Blocking Peptides As Nutrition-Sensitive Signals for Insulin Secretion and Body Size Regulation. *PLoS Biol* **14**, (2016).

136. Gasteiger, E. *et al.* ExPASy: The proteomics server for in-depth protein knowledge and analysis. *Nucleic Acids Res* **31**, (2003).

137. Guruharsha, K. G. *et al.* A protein complex network of Drosophila melanogaster. *Cell* **147**, (2011).

138. Gutenkunst, R. N. *et al.* Universally Sloppy Parameter Sensitivities in Systems Biology Models. *PLoS Comput Biol* **3**, 1871–1878 (2007).

139. Frank, D. & Vince, J. E. Pyroptosis versus necroptosis: similarities, differences, and crosstalk. *Cell Death and Differentiation* vol. 26 Preprint at https://doi.org/10.1038/s41418-018-0212-6 (2019).

140. Boucher, I., Rich, C., Lee, A., Marcincin, M. & Trinkaus-Randall, V. The P2Y2 receptor mediates the epithelial injury response and cell migration. *Am J Physiol Cell Physiol* **299**, (2010).

141. Gault, W. J., Enyedi, B. & Niethammer, P. Osmotic surveillance mediates rapid wound closure through nucleotide release. *Journal of Cell Biology* **207**, (2014).

142. Sieger, D., Moritz, C., Ziegenhals, T., Prykhozhij, S. & Peri, F. Long-Range Ca2+ Waves Transmit Brain-Damage Signals to Microglia. *Dev Cell* **22**, (2012).

143. Zimmermann, H., Zebisch, M. & Sträter, N. Cellular function and molecular structure of ecto-nucleotidases. *Purinergic Signal* **8**, (2012).

144. Bement, W. M., Mandato, C. A. & Kirsch, M. N. Wound-induced assembly and closure of an actomyosin purse string in Xenopus oocytes. *Current Biology* **9**, (1999).

145. Wood, W. *et al.* Wound healing recapitulates morphogenesis in Drosophila embryos. *Nat Cell Biol* **4**, (2002).

146. Tsuzuki, S. *et al.* Switching between humoral and cellular immune responses in Drosophila is guided by the cytokine GBP. (2014) doi:10.1038/ncomms5628.

147. Cvejic, S., Zhu, Z., Felice, S. J., Berman, Y. & Huang, X. Y. The endogenous ligand Stunted of the GPCR Methuselah extends lifespan in Drosophila. *Nat Cell Biol* **6**, (2004).

148. Lin, Y. J., Seroude, L. & Benzer, S. Extended life-span and stress resistance in the Drosophila mutant methuselah. *Science (1979)* **282**, (1998).

149. Franceschi, C., Garagnani, P., Vitale, G., Capri, M. & Salvioli, S. Inflammaging and 'Garb-aging'. *Trends in Endocrinology and Metabolism* vol. 28 Preprint at https://doi.org/10.1016/j.tem.2016.09.005 (2017).

150. Gredilla, R. & Barja, G. The role of oxidative stress in relation to caloric restriction and longevity. *Endocrinology* vol. 146 Preprint at https://doi.org/10.1210/en.2005-0378 (2005).

151. McCay, C. M., Crowell, M. F. & Maynard, L. A. The effect of retarded growth upon the length of life span and upon the ultimate body size. *Nutrition* **5**, (1989).

152. Zeng, Y. *et al.* Novel loci and pathways significantly associated with longevity. *Sci Rep* **6**, (2016).

153. Chasan, R., Jin, Y. & Anderson, K. v. Activation of the easter zymogen is regulated by five other genes to define dorsal-ventral polarity in the Drosophila embryo. *Development* **115**, (1992).

154. Morisato, D. & Anderson, K. v. The spätzle gene encodes a component of the extracellular signaling pathway establishing the dorsal-ventral pattern of the Drosophila embryo. *Cell* **76**, (1994).

155. Valanne, S., Wang, J.-H. & Rämet, M. The Drosophila Toll Signaling Pathway . *The Journal of Immunology* **186**, (2011).

156. Macfarlane, R. G. A. The blood clotting mechanism. The development of a theory of blood coagulation. *Proc R Soc Lond B Biol Sci* **173**, (1969).

157. Schmidt, A. Neue Untersuchungen über die Faserstoffgerinnung. *Pflüger, Archiv für die Gesammte Physiologie des Menschen und der Thiere* **6**, (1872).

158. Torbet, J. The thrombin activation pathway modulates the assembly, structure and lysis of human plasma clots in vitro. *Thromb Haemost* **73**, (1995).

159. Bergsbaken, T., Fink, S. L. & Cookson, B. T. Pyroptosis: Host cell death and inflammation. *Nature Reviews Microbiology* vol. 7 Preprint at https://doi.org/10.1038/nrmicro2070 (2009).

160. Fantuzzi, G. & Dinarello, C. A. Interleukin-18 and Interleukin-IB : Two Cytokine Substrates for. *J Clin Immunol* **19**, 1–11 (1999).

161. Fink, S. L. & Cookson, B. T. Apoptosis, pyroptosis, and necrosis: Mechanistic description of dead and dying eukaryotic cells. *Infection and Immunity* vol. 73 Preprint at https://doi.org/10.1128/IAI.73.4.1907-1916.2005 (2005).

162. Beloshistov, R. E. *et al.* Phytaspase-mediated precursor processing and maturation of the wound hormone systemin. *New Phytologist* **218**, (2018).

163. Lemon, G., Gibson, W. G. & Bennett, M. R. Metabotropic receptor activation, desensitization and sequestration - I: Modelling calcium and inositol 1,4,5-trisphosphate dynamics following receptor activation. *J Theor Biol* **223**, 93–111 (2003).

164. O'Connor, J. T. *et al.* Proteolytic activation of Growth-blocking peptides triggers calcium responses through the GPCR Mthl10 during epithelial wound detection. *Dev Cell* **56**, 2160-2175.e5 (2021).

165. Enyedi, B. & Niethammer, P. Mechanisms of epithelial wound detection. *Cell Press* **5**, 398–407 (2015).

166. Dupont, G., Combettes, L. & Leybaert, L. Calcium Dynamics: Spatio-Temporal Organization from the Subcellular to the Organ Level. *Int Rev Cytol* **261**, 193–245 (2007).

167. Dupont, G. *et al.* Ca2+ oscillations in hepatocytes do not require the modulation of InsP3 3-kinase activity by Ca2+. *FEBS Lett* **534**, 101–105 (2003).

168. Williams, G. S. B., Smith, G. D., Sobie, E. A. & Jafri, M. S. Models of cardiac excitation-contraction coupling in ventricular myocytes. *Math Biosci* **226**, 1–15 (2010).

169. Graupner, M. & Brunel, N. Mechanisms of induction and maintenance of spike-timing dependent plasticity in biophysical synapse models. *Front Comput Neurosci* **4**, 136 (2010).

170. Thurley, K. *et al.* Timescales of IP 3-evoked Ca 2+ spikes emerge from Ca 2+ puffs only at the cellular level. *Biophys J* **101**, 2638–2644 (2011).

171. Hellman, A. N., Rau, K. R., Yoon, H. H. & Venugopalan, V. Biophysical response to pulsed laser microbeam-induced cell lysis and molecular delivery. *J Biophotonics* 24–35 (2007) doi:10.1002/jbio.200710010.

172. Wagner, J. & Keizer, J. Effects of rapid buffers on Ca2+ diffusion and Ca2+ oscillations. *Biophys J* **67**, 447–456 (1994).

173. Chen, T. W. *et al.* Ultra-sensitive fluorescent proteins for imaging neuronal activity. *Nature* **499**, 295 (2013).

174. Balasubramaniam, S. L., Gopalakrishnapillai, A., Gangadharan, V., Duncan, R. L. & Barwe, S. P. Sodium-calcium exchanger 1 regulates epithelial cell migration via calcium-dependent extracellular signal-regulated kinase signaling. *Journal of Biological Chemistry* **290**, 12463–12473 (2015).

175. Dupont, G. & Sneyd, J. Recent developments in models of calcium signalling. *Curr Opin Syst Biol* **3**, 15–22 (2017).

176. Siekmann, I., Wagner, L. E., Yule, D., Crampin, E. J. & Sneyd, J. A Kinetic Model for Type I and II IP3R Accounting for Mode Changes. *Biophys J* **103**, 658 (2012).

177. Cao, P., Tan, X., Donovan, G., Sanderson, M. J. & Sneyd, J. A Deterministic Model Predicts the Properties of Stochastic Calcium Oscillations in Airway Smooth Muscle Cells. *PLoS Comput Biol* **10**, e1003783 (2014).

178. Kusters, J. M. A. M. *et al.* Stabilizing role of calcium store-dependent plasma membrane calcium channels in action-potential firing and intracellular calcium oscillations. *Biophys J* **89**, 3741–3756 (2005).

179. Ramos-Lewis, W., LaFever, K. S. & Page-McCaw, A. A scar-like lesion is apparent in basement membrane after wound repair in vivo. *Matrix Biology* **74**, 101–120 (2018).

180. Grynkiewicz, G., Poenie, M. & Tsienb, R. Y. THE JOURNAL OF BIOLOGICAL CHEMISTRY A New Generation of Ca2+ Indicators with Greatly Improved Fluorescence Properties*. *Journal of Biological Chemistry* **260**, 3440–3450 (1985).

181. Nuccitelli, R., Yim, D. L. & Smart, T. The Sperm-Induced Ca2+ Wave Following Fertilization of the Xenopus Egg Requires the Production of Ins(1,4,5)P3. *Dev Biol* **158**, 200–212 (1993).

182. Brodskiy, P. A. *et al.* Decoding Calcium Signaling Dynamics during Drosophila Wing Disc Development. *Biophys J* **116**, 725–740 (2019).

183. Estrada, J. *et al.* Cellular Interrogation: Exploiting Cell-to-Cell Variability to Discriminate Regulatory Mechanisms in Oscillatory Signalling. *PLoS Comput Biol* **12**, e1004995 (2016).

184. Limpert, E., Stahel, W. & Abbt, M. Log-normal Distributions across the Sciences : Keys and Clues. *Bioscience* **51**, 341–352 (2001).

185. Wada, T., Hironaka, K. ichi & Kuroda, S. Cell-to-cell variability serves as information not noise. *Curr Opin Syst Biol* **27**, 100339 (2021).

186. Yao, J., Pilko, A. & Wollman, R. Distinct cellular states determine calcium signaling response. 1–12 (2016) doi:10.15252/msb.20167137.

187. Soundarrajan, D. K., Huizar, F. J., Paravitorghabeh, R., Robinett, T. & Zartman, J. J. From spikes to intercellular waves: Tuning intercellular calcium signaling dynamics modulates organ size control. *PLoS Comput Biol* **17**, e1009543 (2021).

188. Donati, V. *et al.* Calcium Signaling in the Photodamaged Skin : In Vivo Experiments and Mathematical Modeling. **3**, 1–21 (2021).

189. Franz, A., Wood, W. & Martin, P. Fat Body Cells Are Motile and Actively Migrate to Wounds to Drive Repair and Prevent Infection. *Dev Cell* **44**, (2018).

190. Ma, X., Lynch, H. E., Scully, P. C. & Hutson, M. S. Probing embryonic tissue mechanics with laser hole drilling. *Phys Biol* **6**, (2009).

191. Kaouri, K., Maini, P. K., Skourides, P. A., Christodoulou, N. & Chapman, S. J. A simple mechanochemical model for calcium signalling in embryonic epithelial cells. *J Math Biol* **78**, 2059–2092 (2019).

192. Gilmore, F. The growth or collapse of a spherical bubble in a viscous compressible liquid. *Calf. Inst. Tech. Rep.* https://authors.library.caltech.edu/561/ (1952).

193. Currie, D. A., Milner, M. J. & Evans, C. W. The growth and differentiation in vitro of leg and wing imaginal disc cells from Drosophila melanogaster. *Development* **102**, (1988).

194. Struhl, G. & Basler, K. Organizing activity of wingless protein in Drosophila. *Cell* **72**, (1993).